

The Pennsylvania State University  
The Graduate School  
Eberly College of Science

## **4 DEVELOPMENT OF SCALABLE APPROACHES TO NEUTRINO MASS 5 MEASUREMENT WITH THE PROJECT 8 EXPERIMENT**

A Thesis in  
The Physics Department  
by  
Andrew Douglas Ziegler

10 © 2023 Andrew Douglas Ziegler

Submitted in Partial Fulfillment  
of the Requirements  
for the Degree of

14 Doctor of Philosophy

15 December 2023

<sup>16</sup> The thesis of Andrew Douglas Ziegler was reviewed and approved\* by the following:

Luiz de Viveiros Souza  
Assistant Professor of Physics  
Thesis Advisor  
Chair of Committee

Carmen Carmona  
Assistant Professor of Physics

<sup>17</sup> Doug Cowan  
Professor of Physics and Astrophysics

Xingjie Ni  
Associate Professor of Electrical Engineering

<sup>18</sup> Stephanie Wissel  
Associate Professor of Physics

<sup>19</sup> \*Signatures are on file in the Graduate School.

# <sup>20</sup> Abstract

<sup>21</sup> Neutrinos are fundamental particles in the standard model and play an important role  
<sup>22</sup> in the current understanding of the universe, however, the masses of the neutrinos, one  
<sup>23</sup> of the most fundamental parameters for any particles, is currently unknown. This fact  
<sup>24</sup> represents a gaping hole in our current knowledge of the universe that may provide clues  
<sup>25</sup> to the energy scale of possible physics beyond the standard model. This dissertation  
<sup>26</sup> summarizes research and development as a member of the Project 8 collaboration towards  
<sup>27</sup> an experiment to measure the neutrino mass to a sensitivity below  $50 \text{ meV}/c^2$ , which  
<sup>28</sup> is an order of magnitude below the most sensitive direct measurements of the neutrino  
<sup>29</sup> mass to date. Project 8 will perform this measurement using Cyclotron Radiation  
<sup>30</sup> Emission Spectroscopy (CRES) to measure the beta-decay endpoint spectrum of atomic  
<sup>31</sup> tritium. I present an analysis of the signal reconstruction performance of an antenna  
<sup>32</sup> array system designed to perform large-scale CRES measurements. Next, I discuss an  
<sup>33</sup> approach to calibrating an antenna array CRES experiment using a unique probe antenna  
<sup>34</sup> designed to mimic radiation from CRES events. Finally, I present design studies for a  
<sup>35</sup> resonant cavity that could be used to perform a CRES experiment with atomic tritium  
<sup>36</sup> at multi-cubic-meter scales.

# Table of Contents

38	<b>List of Figures</b>	viii
39	<b>List of Tables</b>	xxvii
40	<b>Acknowledgments</b>	xxviii
41	<b>Chapter 1</b>	
42	<b>Introduction</b>	1
43	1.1 Summary . . . . .	1
44	1.2 Outline . . . . .	4
45	<b>Chapter 2</b>	
46	<b>Neutrinos and Neutrino Masses</b>	6
47	2.1 Introduction . . . . .	6
48	2.2 Neutrinos and Beta-decay . . . . .	6
49	2.3 Neutrino Oscillations . . . . .	8
50	2.4 Neutrino Masses in the Standard Model . . . . .	11
51	2.5 Neutrino Absolute Mass Scale . . . . .	13
52	2.5.1 Limits from Cosmology . . . . .	13
53	2.5.2 Limits from Neutrinoless Double Beta-decay Searches . . . . .	15
54	2.5.3 Limits from Beta-decay . . . . .	17
55	<b>Chapter 3</b>	
56	<b>Direct Measurement of the Neutrino Mass with Project 8</b>	21
57	3.1 Introduction . . . . .	21
58	3.2 Project 8 and Cyclotron Radiation Emission Spectroscopy . . . . .	22
59	3.2.1 Cyclotron Radiation Emission Spectroscopy — CRES . . . . .	22
60	3.2.2 Project 8 . . . . .	26
61	3.2.3 The Project 8 Phased Development Plan . . . . .	30
62	3.3 Phase II: First Tritium Beta Decay Spectrum and Neutrino Mass Measurement with CRES . . . . .	34
63	3.3.1 The Phase II CRES Apparatus . . . . .	34
64	3.3.2 CRES Track and Event Reconstruction . . . . .	38
65	3.3.3 Results from Phase II . . . . .	42
66	3.4 Phase III R&D: Antenna Array CRES . . . . .	46

68	3.4.1	The Basic Approach . . . . .	47
69	3.4.2	The FSCD: Free-space CRES Demonstrator . . . . .	48
70	3.5	Pilot-scale Experiments . . . . .	53
71	3.5.1	Choice of Frequency . . . . .	54
72	3.5.2	Pilot-scale Experiment Concepts . . . . .	56
73	3.6	Phase IV . . . . .	59

## 74 Chapter 4

### 75 Signal Reconstruction Techniques for Antenna Array CRES and the 76 FSCD 61

77	4.1	Introduction . . . . .	61
78	4.2	FSCD Simulations . . . . .	62
79	4.2.1	Kassiopeia . . . . .	63
80	4.2.2	Locust . . . . .	67
81	4.2.3	CRESana . . . . .	71
82	4.3	Signal Detection and Reconstruction Techniques for Antenna Array CRES . . . . .	71
83	4.3.1	Digital Beamforming . . . . .	76
84	4.3.2	Matched Filtering . . . . .	85
85	4.3.3	Machine Learning . . . . .	97
86	4.4	Analysis of Signal Detection Algorithms for the FSCD . . . . .	102
87	4.4.1	Introduction . . . . .	103
88	4.4.2	Signal Detection with Antenna Array CRES . . . . .	104
89	4.4.2.1	Antenna Array and Data Rate Estimates . . . . .	104
90	4.4.2.2	Real-time Signal Detection . . . . .	106
91	4.4.3	Signal Detection Algorithms . . . . .	109
92	4.4.3.1	Power Threshold . . . . .	110
93	4.4.3.2	Matched Filtering . . . . .	112
94	4.4.3.3	Machine Learning . . . . .	116
95	4.4.4	Methods . . . . .	118
96	4.4.4.1	Data Generation . . . . .	118
97	4.4.4.2	Template Number and Match Estimation . . . . .	119
98	4.4.4.3	CNN Training and Data Augmentation . . . . .	120
99	4.4.5	Results and Discussion . . . . .	121
100	4.4.5.1	Trigger Classification Performance . . . . .	121
101	4.4.5.2	Computational Cost and Hardware Requirements . . . . .	123
102	4.4.6	Conclusion . . . . .	125

## 103 Chapter 5

### 104 Antenna and Antenna Measurement System Development for the 105 Project 8 Experiment 127

106	5.1	Introduction . . . . .	127
107	5.2	Antenna Measurements for CRES experiments . . . . .	128
108	5.2.1	Antenna Parameters . . . . .	128
109	5.2.1.1	Radiation Patterns . . . . .	128

110	5.2.1.2	Directivity and Gain . . . . .	129
111	5.2.1.3	Far-field and Near-field . . . . .	130
112	5.2.1.4	Polarization . . . . .	131
113	5.2.1.5	Antenna Factor and Effective Aperture . . . . .	132
114	5.2.2	Antenna Measurement Fundamentals . . . . .	134
115	5.2.2.1	Friis Transmission Equation . . . . .	134
116	5.2.2.2	S-Parameters and Network Analyzers . . . . .	135
117	5.2.2.3	Antenna Array Commissioning and Calibration Measurements . . . . .	136
119	5.2.3	The Penn State Antenna Measurement System . . . . .	137
120	5.3	Development of a Synthetic Cyclotron Antenna (SYNCA) for Antenna Array Calibration . . . . .	140
121	5.3.1	Introduction . . . . .	141
123	5.3.2	Cyclotron Radiation Phenomenology . . . . .	143
124	5.3.3	SYNCA Simulations and Design . . . . .	149
125	5.3.4	Characterization of the SYNCA . . . . .	155
126	5.3.5	Beamforming Measurements with the SYNCA . . . . .	159
127	5.3.6	Conclusions . . . . .	163
128	5.4	FSCD Antenna Array Measurements with the SYNCA . . . . .	164
129	5.4.1	Introduction . . . . .	164
130	5.4.2	Measurement Setups . . . . .	165
131	5.4.2.1	FSCD Array Setup . . . . .	165
132	5.4.2.2	Synthetic Array Setup . . . . .	167
133	5.4.3	Simulations, Analysis, and Results . . . . .	167
134	5.4.3.1	Simulations . . . . .	168
135	5.4.3.2	Phase Analysis . . . . .	169
136	5.4.3.3	Magnitude Analysis . . . . .	173
137	5.4.3.4	Beamforming Characterization . . . . .	174
138	5.4.4	Conclusions . . . . .	176

139	<b>Chapter 6</b>		
140	<b>Development of Resonant Cavities for Large Volume CRES Measurements</b>	<b>182</b>	
141	6.1	Introduction . . . . .	182
142	6.2	Cylindrical Resonant Cavities . . . . .	183
143	6.2.1	General Field Solutions . . . . .	183
144	6.2.2	TE and TM Modes . . . . .	184
145	6.2.3	Resonant Frequencies of a Cylindrical Cavity . . . . .	186
146	6.2.4	Cavity Q-factors . . . . .	188
147	6.3	The Cavity Approach to CRES . . . . .	192
148	6.3.1	A Sketch of a Molecular Tritium Cavity CRES Experiment . . . . .	192
149	6.3.2	Magnetic Field, Cavity Geometry, and Resonant Modes . . . . .	194
150	6.3.3	Trade-offs Between the Antenna and Cavity Approaches . . . . .	197
152	6.4	Single-mode Resonant Cavity Design and Simulations . . . . .	199

153	6.4.1	Open Cylindrical Cavities with Coaxial Terminations . . . . .	199
154	6.4.2	Mode Filtering . . . . .	203
155	6.4.3	Simulations of Open, Mode-filtered Cavities . . . . .	204
156	6.5	Single-mode Resonant Cavity Measurements . . . . .	207
157	6.5.1	Cavities and Setup . . . . .	207
158	6.5.2	Results and Discussion . . . . .	210
159	<b>Chapter 7</b>		
160	<b>Conclusion and Future Prospects</b>		<b>214</b>
161	<b>Bibliography</b>		<b>217</b>

# **List of Figures**

162	2.1	A diagram of two different neutrino mass ordering scenarios [1]. In the inverted hierarchy (inverted mass ordering) the lightest neutrino mass is $m_3$ , whereas, in the normal hierarchy (normal mass ordering) $m_1$ is the lightest neutrino. What cannot be measured by neutrino oscillations is the neutrino absolute mass scale, which is essentially the mass of the lightest neutrino mass eigenstate. . . . .	9
163	2.2	The masses of the neutrinos as a function of the lightest neutrino mass in both the normal (a) and inverted (b) mass ordering regimes. . . . .	10
164	2.3	The neutrino mass observable measured by cosmology as a function of the lightest neutrino mass eigenstate. . . . .	14
165	2.4	Feynman diagrams for double beta-decay (a) and $0\nu\beta\beta$ (b). . . . .	15
166	2.5	The discovery probabilities for the future generation of $0\nu\beta\beta$ experiments as a function of $m_{\beta\beta}$ and $m_{least}$ . Figure from [2]. . . . .	16
167	2.6	A Feynman diagram of beta decay . . . . .	17
168	2.7	A figure from Fermi's 1934 paper on a theory of beta-decay depicting the kinetic energy spectrum of the emitted electron. The effect of the neutrino mass, written as $\mu$ , is to distort the shape of the spectrum near the endpoint from the zero-mass spectrum. . . . .	17
169	2.8	The tritium beta-decay spectrum. The effect of a massive neutrino on the spectrum is to change its shape near the endpoint by an amount proportional to the size of the neutrino mass. A sufficiently high-statistic and high-resolution measurement of the spectrum endpoint would be able to measure the neutrino mass. . . . .	19
170			
171			
172			
173			
174			
175			
176			
177			
178			
179			
180			
181			
182			
183			
184			
185			

186	3.1	A cartoon illustration of the CRES technique. An electron is contained in 187 a magnetic trap, which is a local minimum in the magnetic field, so that 188 its cyclotron radiation can be detected by an array of antennas. Detecting 189 the cyclotron radiation allows one to measure its cyclotron frequency and 190 determine its kinetic energy. . . . .	23
191	3.2	An illustration of an electron in a bathtub magnetic trap generated by 192 two well-separated coils. . . . .	24
193	3.3	A plot of the main components of an electron's trajectory in a cylindrically 194 symmetric trap. . . . .	25
195	3.4	A plot of the final state distributions of atomic and molecular tritium. The 196 final state distribution provides the primary contribution to the width of 197 the molecular spectrum whereas thermal doppler broadening is responsible 198 for the width of the atomic spectrum. . . . .	27
199	3.5	Neutrino mass exclusion plot including limits from cosmological measure- 200 ments and the KATRIN experiment. Allowed ranges for neutrino masses 201 under the normal and inverted hierarchies are shown as the blue and 202 orange lines respectively. The black dashed line shows Project 8's goal 203 neutrino mass sensitivity for the Phase IV experiment. . . . .	30
204	3.6	Sensitivity calculations for a cavity based CRES experiment that demon- 205 strate the neutrino mass measurement goals of Project 8 throughout the 206 phased development plan. The blue curves indicate molecular tritium 207 sources and the red curves indicate atomic tritium sources. In the current 208 plan, Phase III contains two tritium experiments. The first is the Low- 209 frequency Apparatus (LFA), which is a molecular tritium experiment, and 210 the second is the atomic tritium pilot-scale experiment that officially ends 211 Phase III. The sensitivity of these experiments is primarily a function 212 of statistics, however, there is a critical density beyond which CRES 213 electrons do not have enough time to radiate between collisions for a 214 high-resolution frequency measurement leading to worse sensitivity. . . .	31
215	3.7	The Phase II CRES apparatus used to perform the first measurement of 216 the tritium beta-decay spectrum using CRES. . . . .	35
217	3.8	Diagram of the CRES cell portion of the Phase II apparatus. . . . .	36
218	3.9	RF system diagram for the Phase II apparatus. . . . .	37

219	3.10 The time-frequency spectrogram of a tritium CRES event in the Phase II 220 apparatus. . . . .	39
221	3.11 The sparse spectrogram obtained by placing a power cut on the raw 222 spectrogram shown in Figure 3.10. . . . .	41
223	3.12 Fits to the measured 17.8-keV $^{83m}\text{Kr}$ conversion line using the deep and 224 shallow trap configurations. . . . .	43
225	3.13 Measurements of the 17.8-keV $^{83m}\text{Kr}$ line using the deep trap configuration 226 for different values of the magnetic field from the field shifting solenoid. .	44
227	3.14 The measured tritium spectrum from Phase II with Bayesian and frequen- 228 tist fits. . . . .	45
229	3.15 A cartoon illustration of the basics of the antenna array CRES technique.	47
230	3.16 An image of the MRI magnet installed in the Project 8 laboratory at the 231 University of Washington, Seattle. . . . .	49
232	3.17 (a) A model of the FSCD antenna array, magnetic trap, and tritium 233 containment vessel design.(b) A more detailed model of a prototype 234 design for the 5-slot waveguide antenna design. . . . .	50
235	3.18 (a) A plot of the decay rate for the two-body dipolar spin exchange 236 interaction for cc and dd state. (b) A plot of the decay rate of the dipolar 237 spin exchange interaction for d+d states as a function of magnetic field 238 magnitude. Lowering the magnetic field is key for reducing the losses 239 from this interaction. . . . .	55
240	3.19 A conceptual sketch of a large-volume antenna array based CRES experi- 241 ment to measure the neutrino mass. . . . .	56
242	3.20 A conceptual sketch of a pilot-scale cavity CRES experiment with an 243 atomic tritium beamline. . . . .	58

244	3.21 An illustration of a possible arrangement of ten pilot-scale cavity experiments for Phase IV. The experiments are arranged in a circle with an approximate diameter of 50 meters. Each atomic beamline connected to the bottom of each cavity is approximately 10 m in length. The cavities themselves are designed to operate at 325 MHz and are approximately 11 m tall. The circular arrangement of cavities has some advantages when it comes to cancellation of fringe fields from neighboring magnets, which is important due to the small magnetic field magnitudes consistent with these CRES frequencies. The advantage of ten independent atomic sources and cavities is that there is no single point of failure for the experiment. If an experiment goes down for repairs the other nine may continue running. Figure courtesy of Michael Huehn at UW-Seattle. . . . .	60
256	4.1 The geometry and parameters of the coils used to simulate the FSCD magnetic trap in Kassiopeia. Some axial profiles of the magnetic trap at different radial positions are shown to demonstrate the shape of the magnetic field and trap depth as a function of position. Calculation of the magnetic field profiles was graciously done by René Reimann. . . . .	64
261	4.2 A map of the average $\nabla B$ -drift frequency for electrons trapped in the prototype FSCD trap shown in Figure 4.1. Negative drift frequencies indicate electrons that are drifting opposite to the standard direction, which means that they are close to escaping the magnetic trap. . . . .	66
265	4.3 The receiver chain used by Locust when simulating CRES events in the FSCD. . . . .	69
267	4.4 A high-level diagram depicting the process of CRES event reconstruction. The first step consists of identifying the presence of a signal in the data. This step is necessary to avoid the danger of performing a reconstruction of a false event, which would constitute a background contribution to the tritium spectrum measured by CRES. . . . .	73
272	4.5 An illustration of two PDFs associated a binary hypothesis test. The decision threshold is represented by the vertical line that partitions both distributions. The orange and red areas correspond to the true negative and false positive probabilities and the blue and green areas correspond to the false negative and true positive probabilities respectively. To decide between the two hypotheses the likelihood ratio test specified by the Neyman-Pearson theorem is applied. This approach achieves the highest true positive probability for a given false positive probability. . . . .	74

280	4.6 An example ROC curve formed by computing the $P_{\text{FP}}$ and the $P_{\text{TP}}$ for 281 a given likelihood ratio test. As the decision threshold is increased $P_{\text{FP}}$ 282 decreases at the expense of a lower $P_{\text{TP}}$ . The black dashed line indicates 283 the lower bound ROC curve obtained by randomly deciding between $\mathcal{H}_0$ 284 and $\mathcal{H}_1$ . . . . .	75
285	4.7 An illustration of the constructive interference condition which is the 286 operating principle of digital beamforming using a uniform linear array 287 as an example. . . . .	77
288	4.8 A system level diagram of the laboratory setup used for beamforming 289 demonstrations at Penn State. For more information on this system see 290 Chapter 5. Signals near 26 GHz are fed to a dipole antenna using an 291 arbitrary waveform generator (AWG) and vector network analyzer (VNA), 292 which drive a mixer. The dipole radiation is collected by an array of 293 antennas connected to the digitizer data acquisition (DAQ) system. . . . .	78
294	4.9 Photographs of the beamforming demonstration setup. In (a) I show a 295 top-down view of the dipole antenna and the array of eight horn antennas. 296 Manual repositioning of the horn antennas allows one to synthesize a full- 297 circular antenna array. The dipole antenna is mounted on a camera tripod 298 mount that allows for manual position tuning. (b) is a close up image of 299 the dipole, which is manufactured from two segments of semi-rigid coaxial 300 cable. (c) is another image of the dipole and array. . . . .	79
301	4.10 An example of digital beamforming reconstruction of a dipole antenna 302 using a synthetic array of horn antennas. The beamforming image on 303 the right is constructed by computing the time-averaged power of the 304 summed signals for a two-dimensional grid of beamforming positions. In 305 the image, one can see a clear maximum that corresponds to the position 306 of the dipole antenna. On the left I show the frequency spectrum of the 307 time-series at the maximum power pixel. White Gaussian noise is added 308 to the signal to mimic a more realistic signal-to-noise-ratio. The signal 309 emitted by the dipole is clearly visible as the high power peak in the 310 frequency spectrum. . . . .	80
311	4.11 Beamforming images visualizing the reconstruction of an electron without 312 (a) and with (b) the cyclotron phase correction. The images were generated 313 using data from Locust simulations. The cyclotron phase refers to a phase 314 offset equal to the relative azimuthal position of an antenna in the array. 315 This phase offset is caused by the circular electron orbit and must be 316 corrected for during reconstruction. . . . .	81

317	4.12 Beamforming images visualizing the reconstruction of an electron located 318 off the central axis of the FSCD trap. In (a) beamforming is being 319 performed without the $\nabla B$ -drift correction, and in (b) it is included. . . . .	82
320	4.13 A plot of a typical frequency spectrum obtained by applying a Fourier 321 transform to the time-series obtained from beamforming. The frequency 322 spectra are plotted without noise on top of an example of a typical noise 323 spectrum to visualize a realistic signal-to-noise ratio. In the example, 324 without beamforming it would not be possible to detect anything since 325 the signal amplitudes would be reduced by a factor of sixty relative to 326 the noise. Additionally, it is clear the $\nabla B$ -drift correction is needed to 327 detect this electron in the presence of noise. . . . .	84
328	4.14 A plot of the total signal power received by the FSCD array from trapped 329 electrons with different radial positions and pitch angles generated using 330 Locust simulations. The lines on the plot indicate a 10 dB detection 331 threshold above the mean value of the noise in the frequency spectrum. 332 With static beamforming electrons with radial positions larger than about 333 two centimeters are undetectable due to the change in the electron's 334 position over time causing losses from beamforming phase mismatch. This 335 is corrected by including $\nabla B$ -drift frequencies in the beamforming phases. 336 Both beamforming techniques fail to detect electrons below $\approx 88.0^\circ$ , since 337 these signals are composed of several relatively weak sidebands that are 338 comparable to the noise. . . . .	85
339	4.15 Example of a convolution of a CRES signal template with a segment of 340 noisy data. A simulated CRES signal was simulated using Locust and 341 normalized to create a matched filter template. When this template is 342 convolved with noisy data the convolution output increases dramatically compared to data with only noise. 343 The decreasing convolution output as the time offset of the convolution 344 increases is caused by zero-padding of the data and template. . . . .	86
345	4.16 An example two-dimensional parameter distribution of a matched filter 346 template bank and random test signals. $\theta$ refers to the pitch angle of 347 the electron and $E$ is the kinetic energy. The template bank forms a 348 regular grid of in pitch angle and energy; whereas, the test signals are 349 uniformly distributed in pitch angle and follow the tritium beta-decay 350 kinetic energy distribution. This is why there are fewer test signals at 351 higher energies. The need for high match across the full parameter space 352 prevents one from reducing the density of templates in this low activity 353 region. A zoomed in version of the template bank illustrates the relative 354 density of templates and signals needed for match > 90%. . . . .	89

356	4.17 The matched filter scores of a dense grid of templates in pitch angle energy 357 space. Dense template grids allow one to estimate the kinetic energy of 358 the electron by identifying the best matching template. The uncertainty 359 on this value is proportional to the space of templates that also match 360 the test signal well. In the worst case matched filter templates can be 361 completely degenerate where templates with different parameters match 362 a signal with equal likelihood. . . . .	90
363	4.18 The mean match of the dense template grid shown in Figure 4.17 for 364 different numbers of templates. Grids of different sizes were obtained by 365 decimating a dense grid of templates and the average match for each grid 366 was computed using the same set of randomly distributed test signals. 367 Plotting the mean match against the size of the grid allows one to visualize 368 the exponential relationship between match and template bank size. The 369 noise in each curve is caused by sampling effects from the decimation 370 algorithm. In general, longer templates are harder to match than shorter 371 templates. . . . .	91
372	4.19 Matched filter template bank ROC curves as a function of mean match. 373 One can see that for low match a matched filter is on average worse than 374 the more straight forward beamforming detection approach. . . . .	91
375	4.20 Boundaries of detectable electrons in pitch angle kinetic energy space 376 for a series of different signal detection algorithms. A detectable signal 377 is defined as a signal that is above a consistent decision with at least 378 50% probability. This non-rigorous treatment of detection probability is 379 primarily useful for the visualization the relative increases in detection 380 performance provided by the different algorithms. The static beamforming 381 (Static-BF) algorithm is the digital beamforming algorithm introduced 382 above without the $\nabla B$ -drift correction. The DNN algorithm refers to a 383 convolutional neural network classifier trained to detect CRES signals 384 (see Section 4.3.3). . . . .	92
385	4.21 Two example illustrations of the correlation between kinetic energy and 386 pitch angle imparted by the shape of the FSCD magnetic trap. The 387 correlations manifest themselves as degeneracies in the matched filter 388 score where multiple matched filter templates have the same matched filter 389 for a particular signal. These degeneracies are a sign that the magnetic 390 trap must be redesigned in order to break the correlation between pitch 391 angle and kinetic energy. . . . .	96

392	4.22 A visualization of the correlation between energy and pitch angle in the FSCD magnetic trap. The image is formed by computing the match of the best template from a grid consisting of pitch angles from 84 to 90 degrees in steps of 0.05 degrees, kinetic energies from 17574 to 18574 eV, located at 2 cm from the central axis, and simulated for a length of three FSCD time-slices. The signals used to compute the best matching template consisted of a grid from 84 to 90 degrees in steps of 0.05 degrees, kinetic energies from 18550 to 18575 eV in steps of 0.25 eV, located 2 cm from the central axis, and simulated for three FSCD time-slices. The colored regions of the plot show how well signals with lower energy can match those of higher energy for the FSCD magnetic trap, which is proportional to the achievable energy resolution of the FSCD design. . . . .	97
404	4.23 A representation of a matched filter template bank as a convolutional neural network. The network has a single layer composed of the templates, which act as convolutional filters. The activation of the neural network is an absolute value followed by a max operator. . . . .	100
408	4.24 A graphical depiction of CRES signal detection using a CNN. A noisy segment of data is converted to a frequency series using digital beamforming and a FFT. The complex-valued frequency series is input into a trained CNN model that classifies the data as signal or noise using a decision threshold on the CNN output. . . . .	101
413	4.25 The detection efficiency and false alarm rate (false positive rate) as a function of the decision threshold for different values of the noise temperature. The model is trained to output a value close to one for data that contains a signal and outputs a value near zero when the data contains only noise. One sees that a lower decision threshold will have a high detection efficiency at the cost of a high rate of false alarms. . . . .	102
419	4.26 ROC curves for a CNN model classifying CRES signals. One can see that the area under the curve, which is a figure of merit that describes the performance of the classifier, is roughly linearly dependent with the noise temperature. . . . .	103

423	4.27 An illustration of the conceptual design for an antenna array CRES	
424	tritium beta-decay spectrum measurement. The antenna array geometry	
425	consists of a 20 cm interior diameter with 60 independent antenna channels	
426	arranged evenly around the circumference. The nominal antenna design	
427	is sensitive to radiation in the frequency range of 25-26 GHz, which	
428	corresponds to the cyclotron frequency of electrons emitted near the	
429	tritium beta-spectrum endpoint in a 0.96 T magnetic field. The array is	
430	located at the center of the magnetic trap produced by a set of current-	
431	carrying coils. The nominal magnetic trap design is capable of trapping	
432	electrons up to 5 cm away from the central axis of the array and traps	
433	electrons within an approximately 6 cm long axial region centered on the	
434	antenna array. . . . .	105
435	4.28 A block diagram illustration of the real-time triggering algorithm proposed	
436	for antenna array CRES reconstruction. . . . .	106
437	4.29 An illustration of the digital beamforming procedure. The blue lines	
438	indicate the distances from the beamforming position to each antenna.	
439	In the situation depicted the actual position of the electron matches the	
440	beamforming position; therefore, one expects constructive interference	
441	when the phase shifted signals are summed. To prevent the electron's	
442	$\nabla B$ -motion from moving the electron off of the beamforming position,	
443	the beamforming phases include time-dependence to follow the trajectory	
444	of the electron in the magnetic trap. . . . .	107
445	4.30 Frequency spectra of simulated CRES events in the FSCD magnetic	
446	trap after beamforming. The signal of a 90° electron consists of a single	
447	frequency component that is clearly detectable using a power threshold	
448	on the frequency spectrum. This power threshold remains effective for	
449	signals with relatively large pitch angles such as 89.0° and 88.75°, which	
450	are composed of a main carrier and a few small sidebands. Signals with	
451	smaller pitch angles, below about 88.5°, are dominated by sidebands such	
452	that no single frequency component can be reliably distinguished from	
453	the noise with a power threshold. . . . .	109
454	4.31 PDFs of the power threshold test statistic for CRES signals with various	
455	pitch angles as well as the PDF for the noise-only signal case. The average	
456	PDF computed for pitch angles ranging from 85.5 to 88.5° is also shown.	
457	As the pitch angle is decreased the signal PDF converges towards the	
458	noise PDF which indicates that the power threshold trigger is unable to	
459	distinguish between small pitch angle signals and noise. . . . .	112

460	4.32 Plots of PDFs that describe the matched filter template bank test statistic for CRES signals with various pitch angles, as well as the estimated PDF for the noise only case. $10^5$ matched filter templates are used and perfect match between signal and template i.e. $\Gamma_{\text{best}} = 1$ is assumed. The mean PDF includes signals ranging from $85.5 - 88.5^\circ$ in pitch angle. There is a larger distinction between the signal PDFs at small pitch angles compared to the power threshold, which indicates a higher detection efficiency for these signals. . . . .	116
468	4.33 The mean match of the matched filter template bank to a test set of randomly parameterized signals as a function of the number or density of templates. The parameter space includes pitch angles from $85.5 - 88.5^\circ$ and energies from $18575 - 18580$ eV. . . . .	119
472	4.34 Histograms of the trained CNN model output from the test dataset. The blue histogram shows the model outputs for signal data. The oddly shaped peak near the end is the result of the softmax function mapping the long tail of the raw output distribution to the range $[0, 1]$ . . . . .	121
476	4.35 ROC curves describing the detection efficiency or true positive rates for the three signal classification algorithms examined in this paper. The matched filter (MF) and Power Threshold curves are computed analytically using the distribution functions introduced in Section 4.4.3, and the CNN curve is computed numerically using the classification results on the test dataset. The percent match indicated in the legend refers to the mean match of the classifier. . . . .	122
483	5.1 An example radiation pattern generated using HFSS simulations. The color and radial distance of the surface from the origin indicate the relative magnitude of radiation power emitted by the antenna in that direction. The primary goal of most antenna measurements is typically to measure the antenna pattern, which is used to derive many useful antenna performance parameters. . . . .	128

489	5.2 An illustration of the three field regions important for the analysis of 490 an antenna system. Very close to the antenna the electric fields are 491 primarily reactive so there is no radiation. If a receiving antenna were 492 placed in this region most of the energy would be reflected back to the 493 transmitter. Outside of the reactive near-field is the radiative near field. 494 At these distances the antenna does radiate, but the radiation pattern is 495 not well-defined since it changes based on the distance of the receiving 496 antenna. It is only in the far-field region where the radiation pattern 497 becomes constant as a function of distance, which is where the majority 498 of antenna engineering is assumed to take place. The antenna arrays 499 developed by Project 8 for CRES measurements operate in the radiative 500 near-field due to the importance of limiting power loss from free-space 501 propagation, which complicates the design of the antenna system. . . . .	130
502	5.3 An illustration of the Friis measurement technique commonly used for 503 antenna characterization measurements. . . . .	134
504	5.4 Illustration of a two-port S-parameter measurement setup. S-parameters 505 characterize how incoming waves of voltage or power scatter off of the RF 506 device under test. This allows you to measure important properties of the 507 device. In particular, this framework can be used to model a two antenna 508 radiation pattern measurement, which can be automated using a VNA. . .	135
509	5.5 Two measurement approaches to characterizing an antenna array for CRES 510 measurements. The full-array approach (a) requires a complete antenna 511 array with all the associated hardware. The synthetic array approach 512 (b) utilizes a single antenna and a set of rotation/translation stages to 513 reposition the transmitter or the receiving antenna to synthesize the signals 514 that would be received by the full-array. This approach reduces the cost 515 and complexity of array measurements. A down-side of the synthetic 516 array approach is that multi-channel effects such as reflections cannot 517 be measured. Utilizing both the full-array and the synthetic array is a 518 powerful way to quantify the impact of errors from the multi-channel array.	136
519	5.6 Illustration of the antenna measurement system developed for the Project 520 8 Collaboration. The reference and test antennas can be connected to 521 different data acquisition configurations depending on the measurement 522 goals. The reference antenna is typically a standard horn antenna and 523 the test antenna is mounted on a set of translation stages for positioning. 524 Automated translation stages allow for relatively painless data-taking enabling 525 synthetic antenna array measurements using only a single receiving 526 antenna. Anechoic form designed to mitigate RF reflections surrounds 527 the setup. . . . .	138

528	5.7	Diagrams of two measurement system configurations. Configuration (a) utilizes a VNA and is more suited to antenna characterization. Configuration (b) utilizes an AWG (arbitrary waveform generator) and VNA as a signal generation system and digitizer to collect measurement data, which is more suited to simulating CRES measurements. The transmission chain utilizes a quadrature hybrid and a pair of baluns to drive the cross-dipole variant test antenna developed for synthetic CRES measurements. . . . .	139
535	5.8	A sketch of an antenna array large-volume CRES experiment. Electrons from $\beta$ -decays are confined in a magnetic field using a set of trap coils. The cyclotron radiation produced by the motion of the trapped electrons can be detected by a surrounding antenna array to determine the electron energies. Measuring the energies of many electrons produces a $\beta$ -decay spectrum. . . . .	141
541	5.9	A schematic of the antenna array test stand. The circular antenna array has a radius of 10 cm with 60 independent channels (limited number shown for clarity). The test stand includes an arbitrary waveform generator (AWG), local oscillator (LO), and data acquisition (DAQ) hardware. Finally, a specialized Synthetic Cyclotron Antenna (SYNCA) is used to inject signals to test the antenna array. . . . .	142
547	5.10	An electron (red dot) performing cyclotron motion in the x-y plane. The resulting cyclotron radiation is observed by an antenna located at the field point of interest. . . . .	143
550	5.11	A plot of the numeric solution to Equation 5.30. The time-domain representation of the signal (a) is composed of a zero frequency term and a series of harmonics separated by the main cyclotron frequency as shown in the plot of the frequency spectrum (b). We can see that the relative amplitude of the harmonics beyond $k = 7$ are smaller than the main carrier by a factor of about $10^{-5}$ and are completely negligible. . . . .	146
556	5.12	The amplitude maxima of the cyclotron radiation form an Archimedean spiral as the radiation propagates outward from the cyclotron orbit center (a). A circular antenna array located at a fixed radius from the orbit center will receive electric fields with equal magnitude in each of its channels, but the phase of the electric field incident on each array channel will be linearly out of phase from its neighbor antennas by an amount equal to the angular separation of the two channels (b). . . . .	148

563	5.13 Images of an early prototype crossed-dipole antenna manufactured by hand and the first measurement setup. The antenna was constructed by hand using four stripped coaxial cables. The antenna was connected to one port of the VNA, and the remaining three ports on the VNA were connected to horn antenna arranged with 90 deg offsets around the crossed-dipole. The measured unwrapped S-parameter phases exhibit the desired relative phase behavior for a SYNCA. These early measurements were the first laboratory proof-of-principle for the crossed-dipole SYNCA.	150
571	5.14 An early iteration of a crossed-dipole SYNCA antenna simulated in HFSS. The antenna is electrically small at 26 GHz, which requires dipole arms on the order of 1 mm long. This design is limited by the minimum achievable distance between the dipole arms caused by the available diameters of coaxial cables. The assumed termination scheme for the coaxial cables to the antenna is hand-soldering, which introduces random variation in the antenna pattern from the inevitable blobs of solder left on the surface of the PCB.	151
579	5.15 An idealized crossed-dipole antenna consists of two electric dipole antennas oriented perpendicular to each other and is fed with four signals with a quadrature phase relationship. An example antenna feed circuit is shown which is composed of a chained combination of a quadrature hybrid-coupler (Quad) and two baluns.	152
584	5.16 A model of the PCB crossed-dipole antenna with dimensions. The design has an inside diameter of 2.16 mm for the central circular trace, which is 0.13 mm wide. The dipole arms each have a width of 1.27 mm and protrude beyond the circular trace by 1.40 mm, which gives an overall width of 4.96 mm for the length of the antenna PCB trace from end-to- end. The overall size of the antenna is 20.0 mm the majority of which is the PCB dielectric material. This design was observed in simulation to maintain the field characteristics of the idealized crossed-dipole while being simpler to fabricate due to the increased size of the antenna.	153
593	5.17 A comparison of the electric field magnitudes, normalized by the maximum value of the electric field in each simulation, plotted on a 10 cm square to visualize the Archimedean spirals formed by the electron (a), the crossed- dipole antenna (b), and a PCB crossed-dipole antenna (c). The matching patterns indicate that the electric fields have similar phase characteristics. These images were generated using Locust simulations for the electron and ANSYS HFSS for both antennas.	154

600	5.18 A comparison of the normalized electric field magnitudes for the ideal		
601	crossed-dipole, PCB crossed-dipole, and a simulated electron as a function		
602	of the polar angle ( $\theta$ ). (a) Shows the total electric field, (b) shows the		
603	$\phi$ -polarized electric field component, and (c) shows the $\theta$ -polarized electric		
604	field component. These images were generated using Locust simulations		
605	for the electron and ANSYS HFSS for both antennas. . . . .	155	
606	5.19 A comparison of the normalized electric field magnitudes for the crossed-		
607	dipole, PCB crossed-dipole, and a simulated electron as a function of the		
608	azimuthal angle ( $\phi$ ) evaluated at $\theta = 90^\circ$ . This image was generated using		
609	Locust simulations for the electron and ANSYS HFSS for both antennas.	156	
610	5.20 (a) A cartoon schematic which highlights the routing of the semi-rigid		
611	coax transmission lines. (b) A photograph of a SYNCA constructed		
612	using the modified crossed-dipole PCB antenna design. Visible in the		
613	photograph of the SYNCA are four blobs of solder which are an artifact		
614	of the SYNCA's hand-soldered construction. These solder blobs are the		
615	most significant deviation from the SYNCA design shown in Figure 5.16		
616	and are responsible for a significant fraction of the irregularities seen in		
617	the antenna pattern. . . . .	157	
618	5.21 A schematic of the VNA characterization measurements (a). This setup		
619	allows for antenna gain and phase measurements across a full $360^\circ$ of		
620	azimuthal angles using a motorized rotation stage and control of the radial		
621	position of the SYNCA using a translation stage. A photo of the setup in		
622	the lab is shown in (b). . . . .	158	
623	5.22 Linear interpolations of the measured electric field magnitude (a) and		
624	phase (b). The data was acquired using a VNA at 120 points spaced		
625	by 3 degrees from 0 to $357^\circ$ of azimuthal angle. The different		
626	color lines indicate the vertical offset of the horn antenna relative to the		
627	SYNCA PCB and the dashed line shows the expected shape from electron		
628	simulations. No significant difference in the antenna pattern is observed		
629	for the measured vertical offsets. . . . .	159	
630	5.23 (a) A depiction of the relative phase differences for signals received by a		
631	circular antenna array from an isotropic source. The phases correspond to		
632	a unique spatial position. (b) A schematic of the setup used to perform		
633	digital beamforming. . . . .	160	

634	5.24 Digital beamforming maps generated using a simulated 60 channel array and electron simulated using the Locust package. (a) and (b) show the beamforming maps for simulated electrons without the cyclotron spiral phases and with the cyclotron spiral phases respectively. (c) and (d) show the beamforming maps produced from SYNCA measurements. We observe good agreement between simulated electrons and the SYNCA measurements. . . . .	161
641	5.25 A plot of the SYNCA's reconstructed position using the synthesized horn- antenna array and digital beamforming. (a) Shows the reconstructed position of the SYNCA compared with the target position indicated by the positioning system readout. (b) Shows the reconstruction error, which is the difference between the target and reconstructed positions. The error bars in (b) are the uncertainty in the mean position of the 2D Gaussian used to fit the digital beamforming reconstruction peak obtained from the fit covariance matrix. The mean fit position uncertainty of 0.02 mm is an order of magnitude smaller than the typical reconstruction error of 0.3 mm obtained by calculating the standard deviation of the difference between the reconstructed and target position. . . . .	162
652	5.26 A diagram of the array measurement system used to test the prototype FSCD antenna array. A VNA is used as the primary measurement tool, which is connected to the array through a series of switches. The other port of the VNA connects to the SYNCA through the quad-balun chain used to provide the SYNCA feed signals. During measurements the SYNCA is positioned inside the center of the antenna array and translated to different radial and axial positions using a 3-axis manual translation stage setup. . . . .	164
660	5.27 Photos of the prototype FSCD antenna (a), the FSCD array and SYNCA (b), and the translation stages and coordinate system used to position the SYNCA (c). . . . .	166
663	5.28 A photo of the FSCD antenna and the SYNCA in the synthetic array measurement setup at Penn State. . . . .	168
665	5.29 The unwrapped phases of signals received by the FSCD antenna array from an electron with a 90° pitch angle located in the plane of the antenna array. The data points indicated the phases extracted from simulation and the dashed lines show the model predictions. . . . .	169

669	5.30 Plots of the measured unwrapped phases from the FSCD array (a) and the 670 synthetic array (b) compared to the model predictions for a series of radial 671 positions. The different phases of the sinusoidal phase oscillations in the 672 two plots reflects differences in the coordinate systems of the measurements.	170
673	5.31 The phase errors between the measurement and model for the synthetic 674 array (blue) and the FSCD array (orange) for a series of radial positions. 675 The label JUGAAD refers to an alternative name for the FSCD array 676 setup. As the SYNCA is translated off-axis phase errors with progressively 677 higher oscillation frequency enter into the measurements. . . . .	171
678	5.32 Two dimensional plots of the phase errors for the synthetic array (a) 679 and the FSCD (JUGAAD) array (b). In both plots there is evidence 680 of a similar diffraction pattern with bilateral symmetry, but the FSCD 681 array measurments have an additional phase error contribution from the 682 different antennas and paths through the switch network. . . . .	177
683	5.33 The amplitude of the signals from CREsana for the FSCD array from a 684 $90^\circ$ electron. As the electron is moved from $R = 0$ the signals begin to 685 have unequal amplitudes depending on the distance from the electron to 686 the antenna. . . . .	178
687	5.34 The normalized magnitudes of the S21 parameters measured in the FSCD 688 (orange) and synthetic array (blue) setups. The dominant observed 689 behavior as a function of radius is the increase in the number of magnitude 690 peaks, which was noted in the phase error curves. There does not appear 691 to be a strong change in the relative amplitude of a group of antennas as 692 predicted by CREsana. . . . .	178
693	5.35 . . . . .	179
694	5.36 Beamforming images from the synthetic array (a) and FSCD array (b) 695 setups with the SYNCA positioned 15 mm off the central axis. In both 696 images, there is a clear maxima that corresponds to the true SYNCA 697 position. However, in the FSCD array there is an additional faint peak 698 located at the opposite position of the beamforming maximum. This 699 additional peak is the mirror of the true peak and is the result of reflections 700 between antennas in the FSCD array. . . . .	180

701	5.37 A comparison of the maximum signal amplitude obtained by beamforming 702 to the signal amplitude obtained with an ideal summation as a function of 703 the radial position of the SYNCA. The amplitudes for the synthetic array 704 are shown in (a) and the FSCD array are shown in (b). In both setups, 705 the signal amplitudes obtained from beamforming are smaller than the 706 signal amplitude that could be attained with the ideal summation without 707 phase mismatch. . . . .	180
708	5.38 The ratio of the beamforming signal amplitude to the ideal signal ampli- 709 tude for the FSCD and synthetic arrays. The FSCD array has a larger 710 power loss from phase error compared to the synthetic array which indi- 711 cates that calibration errors associated with the multiple channels as well 712 as reflections are impacting the signal reconstruction. . . . .	181
713	6.1 Geometry of a cylindrical waveguide with radius $b$ . . . . .	183
714	6.2 The geometry of a cylindrical cavity with length $L$ and radius $b$ . . . . .	186
715	6.3 Relation of mode frequency to cavity length for a cylindrical cavity with 716 a radius of 18.32 cm. . . . .	187
717	6.4 A series RLC circuit. . . . .	188
718	6.5 Illustration of the behavior of the input impedance of the series RLC 719 circuit as a function of the driving frequency. The BW is proportion to 720 the width of the resonance, which is inversely proportional to Q. . . . .	190
721	6.6 A series RLC circuit coupled to an external circuit with input impedance 722 $R_L$ . . . . .	191
723	6.7 A cartoon depiction of a cavity CRES experiment. A metallic cavity filled 724 with tritium gas is inserted into a uniform background magnetic field 725 to perform CRES measurements. Electrons from beta-decays inside the 726 cavity can be trapped and used to excite a resonant mode(s). By coupling 727 to the cavity mode with a suitable probe one can measure the cyclotron 728 frequency of the electron and perform CRES. . . . .	192

729	6.8 Examples of the resonant mode frequencies of a cylindrical cavity. This 730 cavity has a radius of 18.32 cm and a length to diameter ratio of 4.55. Sev- 731 eral families of resonant modes are relevant in the $\approx 800$ MHz bandwidth 732 of (a); however, after zooming in to a $\sim 80$ MHz bandwidth centered 733 on TE011 one sees that only a handful of resonant modes have frequen- 734 cies close to TE011. Since the bandwidth required for a cavity CRES 735 experiment is $O(10)$ 's MHz, a significant number of resonant modes can 736 be safely ignored since their resonant frequencies are far from the CRES 737 bandwidth. . . . .	196
738	6.9 An image of an open cavity with coaxial terminations used for dielectric 739 constant measurements. Figure from [3]. . . . .	200
740	6.10 The simplified geometry of an open cavity with coaxial terminations. 741 Figure from [4]. . . . .	201
742	6.11 Electric field regions for the open cavity boundary value problem. Figure 743 from [4]. . . . .	201
744	6.12 Two mode filtering concepts to break the degeneracy of TE <sub>01</sub> and TM <sub>11</sub> 745 modes. The resistive approach uses dielectric materials to impede currents 746 that travel vertically along the cavity while leaving azimuthal currents 747 unperturbed. An alternative approach is to impede the currents using 748 grooves cut into the cavity wall, which achieve the same effect with an 749 inductive impedance. . . . .	204
750	6.13 Four cavity design variations. (a) is a standard sealed cylindrical cavity, 751 (b) is an open cavity with smooth walls, (c) is an open cavity with walls 752 made of alternating conductor and dielectric, and (d) is an open cavity 753 with grooved walls. The main cavity and coaxial terminator parameter 754 are identical for all four cavities. . . . .	205
755	6.14 The frequencies and Q-factors of the resonant modes identified by HFSS 756 for the cavity variations shown in Figure 6.13. The fully-sealed cavity with 757 smooth walls has several high-Q modes near the TE <sub>011</sub> resonance. Intro- 758 ducing the open-termination preserves the Q-factors of the TE <sub>01ℓ</sub> modes 759 and suppresses the Q-factors of the modes whose boundary conditions do 760 not match the cylindrical partition. Both the resistive and grooved wall 761 perturbations shift the resonant frequencies of the TM modes away from 762 the TE <sub>011</sub> mode. By properly tuning the geometry of the grooves or the 763 resistive spacers several MHz of frequency separation can be achieved. . .	206

764	6.15 A cartoon depicting the design of the open-ended cavity prototype designed 765 to operate at approximately 6 GHz. The main cavity wall was composed of 766 a single copper pipe. A mode-filtered version of this cavity was constructed 767 by . . . . .	208
768	6.16 Images depicting the measurement of the filtered and non-filtered open 769 cavities using the VNA. The coupling loop in the figure is shown in the 770 TE orientation. . . . .	209
771	6.17 HFSS simulation results for a the as-built cavity with the coaxial termi- 772 nators removed. The $TE_{011}/TM_{111}$ frequency is approximately 5.78 GHz. . . . .	210
773	6.18 Measurements of the filtered and non-filtered prototype cavities acquired 774 with the VNA. . . . .	211

# **List of Tables**

775	4.1	A summary of the CNN model layers and parameters. The output of each 1D-Convolution and Fully Connected layer is passed through a LeakyReLU activation function and re-normalized using batch normalization before being passed to the next layer in the model. The output of the final Fully Connected layer in the model is left without activation so that the model outputs can be directly passed to the Binary Cross-entropy loss function used during training. The first layer in the network has two input channels for the real and imaginary components of the spectrum. . .	117
784	6.1	A table of the values of $p'_{nm}$ . . . . .	185
785	6.2	A table of the values of $p_{nm}$ . . . . .	186
786	6.3	A table of cavity design parameters used for HFSS simulations. . . . .	205
787	6.4	A table of parameters describing the cavity prototypes. Certain values such as the cavity length and the distance between dielectric spacers are approximate due to variation in the machining of the copper. In particular, the filtered cavity was constructed from conducting copper segments that varied in size from 1.50" to 1.85". . . . .	208

## <sup>792</sup> **Acknowledgments**

<sup>793</sup> First, thank you to my advisor, Luiz de Viveiros. During these past years I have been  
<sup>794</sup> deeply grateful for the freedom to pursue my own research paths, his patience and support  
<sup>795</sup> when, inevitably, things do not go right the first time, and the reminders to keep the big  
<sup>796</sup> picture in mind.

<sup>797</sup> Second, thank you to my friends in colleagues in the Project 8 Collaboration, who  
<sup>798</sup> have been a genuine pleasure to work with and have contributed in enumerable ways to  
<sup>799</sup> my dissertation and ability as a scientist. I am honored to have been a member of this  
<sup>800</sup> team.

<sup>801</sup> **Dedication**

<sup>802</sup> To my parents, Chris and Doug, and my sister, Hannah. And to all those friends and  
<sup>803</sup> mentors who have shared this strange and beautiful thing called "life" with me.

804 **Chapter 1** |  
805 **Introduction**

806 **1.1 Summary**

807 Neutrinos are one of the fundamental particles that comprise the standard model of  
808 particle physics and account for a significant fraction of the matter in the universe.  
809 Neutrinos are the most abundant fermions in the universe, but due to their weak  
810 interactions neutrinos seldom interact with other particles. Regardless, neutrinos play a  
811 unique role in the evolution of the early-universe, and a detailed understanding of the  
812 properties of the neutrino is key to understanding the universe at the cosmological scale  
813 as well as the smallest particle physics regime.

814 It was uncertain that neutrinos had nonzero mass until vacuum neutrino flavor  
815 oscillations were observed in the late 90's and early 00's. A simple relativistic argument  
816 as to why oscillations are evidence for neutrino masses is that oscillations imply neutrinos  
817 experience time, which means that they do not propagate at the speed of light, therefore  
818 the masses of the neutrinos must be non-zero. Current neutrino oscillation data supports  
819 that neutrino flavor states are actually a superposition of three separate neutrino states  
820 with well-defined masses. Measurements of neutrino oscillations that have taken place  
821 over the past couple of decades have measured the differences between neutrino mass  
822 eigenstates with increasing precision. However, oscillation measurements cannot tell  
823 us the mass scale of the neutrinos, which is required in order to measure the absolute  
824 neutrino masses.

825 The neutrino mass scale remains an unknown quantity in the standard model of  
826 particle physics. The value of the neutrino mass influences the evolution of the early  
827 universe and is likely relevant to the energy-scale of new physics responsible for the factor  
828 of  $10^{-6}$  difference between the neutrino and electron masses. A model-independent way  
829 to measure the neutrino mass is to measure the tritium beta-decay spectrum near its  
830 endpoint. Energy conservation requires that the neutrino mass carry away some kinetic

831 energy from the beta-decay electron in the form of its mass, which causes a distortion in  
832 the shape of the tritium beta-decay spectrum near the endpoint. The isotope tritium has  
833 many advantages for this measurement, and has been used by the KATRIN collaboration  
834 to perform the most sensitive direct neutrino mass measurement to date.

835 KATRIN represents the state-of-the-art in the current generation of neutrino mass  
836 direct measurement experiments with a projected neutrino mass sensitivity of  $m_\nu < 200$  meV.  
837 This sensitivity does not fully exhaust the allowed parameter space of neutrino  
838 masses under the normal and inverted neutrino mass ordering scenarios, which motivates  
839 the development of a next generation of neutrino mass measurement experiments.

840 The Project 8 collaboration is developing a next-generation neutrino mass experiment  
841 with a goal neutrino mass sensitivity of  $m_\nu < 40$  meV. This sensitivity is sufficient to  
842 exhaust the range of neutrino masses allowed under the inverted mass ordering regime.  
843 Project 8 intends to achieve its sensitivity goal utilizing two technologies that are novel  
844 to the space of direct neutrino mass measurements — atomic tritium and cyclotron  
845 radiation emission spectroscopy (CRES). Atomic tritium is required in order to avoid  
846 systematic broadening the tritium beta-decay spectrum caused by the final state of the  
847  $^3\text{He}^+ \text{-T}$  molecule, and the CRES technique enables a differential measurement of the  
848 tritium spectrum that is background-free and able to be directly integrated with the  
849 atomic tritium source.

850 The Project 8 collaboration is currently engaged in a research and development  
851 program intended to simultaneously develop the atomic tritium and CRES technologies  
852 so that they can be combined in a next-generation experiment. This past year (2022)  
853 Project 8 has used the CRES technique to measure the molecular tritium beta-decay  
854 spectrum and place an upper limit on the neutrino mass:  $m_\beta \leq 152$  eV. This measurement,  
855 while not competitive scientifically, represents the first proof-of-principle that the CRES  
856 technique can be used to measure the neutrino mass.

857 The future goals of the Project 8 collaboration are to develop the technologies  
858 and techniques necessary to scale-up the volume in which CRES measurements can  
859 be performed. Project 8's first neutrino mass measurement with CRES utilized a  
860 measurement volume on the cubic-centimeter scale, however, sensitivity calculations  
861 estimate that an experiment sensitive to neutrino masses of 40 meV will require several  
862 tens of cubic-meters of experiment volume filled with atomic tritium. Developing a new  
863 approach to performing CRES measurements that can be successfully scaled to these  
864 volumes is a necessary step towards Project 8's neutrino mass measurement goal, and is  
865 the primary topic of my dissertation research.

866 A parallel development is the technology necessary to produce, cool, trap, and  
867 recirculate a supply of atomic tritium that is compatible with CRES measurements. The  
868 atomic tritium system is equally important as the large-volume CRES measurement  
869 technology, but will not be discussed at depth here.

870 The Project 8 collaboration has identified two scalable approaches to neutrino mass  
871 measurement using the CRES technique. One approach is to use an array of antennas  
872 that surrounds a volume of trapped atomic tritium that can perform CRES measurements  
873 by collection the cyclotron radiation emitted by beta-decay electrons into free-space. The  
874 other approach uses a resonant cavity filled with atomic tritium to perform CRES by  
875 measuring the excitation of resonant cavity modes caused by the motion of electrons  
876 trapped inside the cavity volume.

877 The cavity and antenna approaches to CRES have been studied in detail over the past  
878 five years, and, while both approaches offer a physically viable path towards a 40 meV  
879 neutrino mass measurement, the collaboration has elected to pursue the cavity approach  
880 for the foreseeable future. The major advantage of the cavity approach is a significant  
881 reduction in the cost and complexity of the experiment design and data analysis, which  
882 provides a lower risk path to Project 8’s scientific goals.

883 In this dissertation I summarize my most impactful contributions to the research and  
884 development of antenna array and cavity CRES. In short these contributions are

- 885 • the development and analysis of signal reconstruction algorithms for antenna array  
886 CRES, which provide key inputs to sensitivity analyses of antenna array CRES  
887 experiments.
- 888 • The development of a specialized antenna, designed to synthesize fake CRES  
889 radiation, which enables bench-top testing and validation of the antenna array  
890 CRES technique.
- 891 • The development of an open-cavity design for CRES measurement, whose mode  
892 structure can be tuned using perturbations that modify the impedance of the cavity  
893 walls. The development of this cavity concept was one of many developments that  
894 eventually lead to the adoption of cavities as the CRES technology of choice for  
895 the future of Project 8.

## 896 1.2 Outline

897 The outline of this dissertation is as follows. In Chapter 2 I provide an introduction to  
898 the basic physics of neutrinos and beta-decay, which provides context for a discussion of  
899 various methods to measure the neutrino absolute mass scale.

900 Chapter 3 is an overview of the CRES technique and the Project 8 collaboration.  
901 Project 8's experimental program is organized into four phases. The first phase completed  
902 in 2015 before I began my dissertation work, so begin by highlighting the Project 8's first  
903 measurement of the tritium beta-decay spectrum with CRES. Next, I discuss the planned  
904 research and development for an antenna array CRES experiment for the upcoming phase  
905 of Project 8's experimental program. I end Chapter 3 with a discussion of Project 8's  
906 pilot-scale and final phase experiments, that will combine a scalable CRES measurement  
907 technology with atomic tritium and measure the neutrino mass with 40 meV sensitivity.

908 Chapter 4 discusses the first of my contributions mentioned above, which is the  
909 development of signal reconstruction techniques for antenna array CRES and an antenna  
910 array demonstrator experiment called the FSCD. I discuss the key tools that Project 8  
911 uses to simulate antenna array CRES before introducing signal reconstruction algorithms  
912 that can be used to detect CRES signals using the array. I end Chapter 4 with a  
913 detailed analysis and comparison of the signal detection performance of each algorithm,  
914 as reported in a paper I have authored.

915 Chapter 5 describes my contributions to the development of antennas and an antenna  
916 measurement system for Project 8, which is the second major contribution of this  
917 dissertation. I begin with a general overview of basic principle of antennas and antenna  
918 measurements, and describe the development, as reported in another paper I have  
919 authored, of unique antenna designed to mimic the cyclotron radiation emitted by  
920 electrons in free-space. I call this antenna the synthetic cyclotron radiation antenna  
921 (SYNCA) and its main purpose is to serve as a fake electron for laboratory validation  
922 measurements of Project 8's antenna array CRES simulations. Chapter 5 ends with an  
923 overview of laboratory measurements of a prototype antenna array using the SYNCA,  
924 which were compared with simulations to provide upper bounds on reconstruction errors  
925 caused by imperfections in real-life measurements.

926 Chapter 6 discusses the cavity approach to CRES, which was adopted as the preferred  
927 CRES technology for Phase IV late into my dissertation work. The chapter starts by  
928 discussing resonant cavities in general before introducing the operating principles of the  
929 cavity approach to CRES. I end the chapter by discussing a study of and open-cavity

<sup>930</sup> design that could be used for CRES measurements and integrated with atomic tritium  
<sup>931</sup> and an electron gun calibration source for the pilot-scale and Phase IV experiments.

<sup>932</sup> Finally, in Chapter 7 I conclude by briefly discussing the future directions of Project  
<sup>933</sup> 8 as development proceeds towards a direct measurement of the neutrino mass.

934 **Chapter 2 |**

935 **Neutrinos and Neutrino Masses**

936 **2.1 Introduction**

937 In this chapter I provide a cursory overview of background information relevant to  
938 neutrinos and neutrino mass measurements.

939 In Section 2.2 I provide background information on the history of neutrinos and beta-  
940 decay. In Section 2.3 I describe the discovery of neutrino oscillations, which demonstrated  
941 unambiguously that neutrinos have non-zero masses. In Section 2.4 I discuss the current  
942 state of the theoretical understanding of neutrino masses in the standard model. Lastly,  
943 in Section 2.5 I discuss a few methods for measuring the absolute scale of the neutrino  
944 mass.

945 **2.2 Neutrinos and Beta-decay**

946 Late in the 19th century the phenomena of radioactivity was first observed in experiments  
947 performed by Henri Becquerel with uranium, and further studied using thorium and  
948 radium by Marie and Pierre Curie [5,6]. Early work in radioactivity classified different  
949 forms of radiation based on it's ability to penetrate different materials. Rutherford was  
950 the first to separate radioactive emissions into two types, alpha and beta radiation [7].  
951 Alpha rays were easily stopped by a piece of paper or thin foil of metal, whereas beta  
952 radiation could penetrate metal several millimeters thick. Later a third form of radiation  
953 was identified by Villard [8], which was still more penetrating, later termed gamma  
954 radiation by Rutherford.

955 When these forms of radioactivity were first discovered, it was unclear what physically  
956 constituted an alpha, beta, or gamma particle. Experiments with radioactivity in magnetic  
957 fields were eventually able to identify the charge composition of the different forms of

radiation. In particular, experiments by Becquerel identified [9] that beta radiation had an identical charge-to-mass ratio to the electron. This was strongly suggestive that beta particles were indeed electrons.

Studies of beta radiation lead to the discovery that radioactivity resulted in the transmutation of elements [10] caused by the decay of a heavier nucleus to a lighter species. A decay that produces beta-radiation is called a beta-decay. One feature of beta radiation that differentiated it from alpha and gamma radiation is that the electrons produced by beta-decay have a continuous spectrum of kinetic energies, whereas, alpha and gamma particles are emitted with discrete energies. This feature of beta-decay was first observed by Chadwick in 1914 [11], and was extremely puzzling at the time, since the continuous spectrum apparently violates energy conservation [12].

Famously, in 1930 Pauli proposed the existence of a new neutral particle, which he termed the "neutron", that was also produced during beta-decay to resolve the missing energy problem posed by the beta-decay spectrum [13]. Because this particle carried no charge, it was hypothesized that it had simply not been observed in any previous experiments. This "neutron", which was initially estimated to have a mass no larger than that of an electron, was eventually renamed the "neutrino" by Fermi [14] after the discovery of the neutron by Chadwick in 1932 [15]. Later, in 1933, Fermi developed a quantum mechanical theory for beta-decay in which an electron and neutrino are produced by the decay of a neutron to a proton inside the radioactive nucleus [16].

Little more than a speculation when first introduced, indirect evidence for the existence of neutrinos was obtained in 1938 by the simultaneous observation of the electron and recoiling nucleus in cloud chambers by Crane and Halpern [17]. However, it wasn't until the Cowan-Reines experiment [18] in 1956 that direct evidence for the existence of neutrinos was observed through the observation of inverse beta-decays caused by neutrinos from a nuclear reactor interacting with protons contained in water molecules. The difficulty in detecting neutrinos is caused by their weak interactions with other particles. Later experiments revealed the existence of different types or flavors of neutrinos based on the nature of the leptons produced in neutrino charged-current interactions [19], but the existence of a neutrino mass remained an open question that would take more than 40 years to resolve.

## 989 2.3 Neutrino Oscillations

990 One of the first clues that neutrino flavor transitions or neutrino oscillations were occurring  
 991 was the solar neutrino problem. The solar neutrino problem is a discrepancy between  
 992 the measured and predicted flux of  $\nu_e$  from the sum. The solar neutrino problem was  
 993 famously observed by Ray Davis Jr. and collaborators in the 1960's [20] at the Homestake  
 994 mine in South Dakota. In the early 2000's, the SNO experiment was able to resolve the  
 995 solar neutrino problem by identifying neutrino oscillations as the cause of the observed  
 996 deficit [21]. Furthermore, measurements of the atmospheric flux of neutrinos by the  
 997 Super-Kamiokande experiment and others revealed that fewer muon-type neutrinos  
 998 survived passage through the earth than expected providing strong evidence for neutrino  
 999 oscillations for both flavors [22].

1000 Neutrino oscillations occur because the neutrino flavor eigenstates are distinct from  
 1001 the mass eigenstates [23]. The neutrino mass eigenstates represent physical particles in  
 1002 that they are solutions to the free-particle Hamiltonian, whereas, the neutrino flavor  
 1003 eigenstates correspond to the neutrino states that interact via the weak charged-current  
 1004 interaction. The neutrino flavor eigenstates are a linear superposition of the neutrino  
 1005 mass eigenstates

$$1006 \nu_\ell = \sum_i U_{\ell i} \nu_i, \quad (2.1)$$

1007 where  $\ell = e, \mu, \tau$  and  $i = 1, 2, 3$ . The matrix elements  $U_{\ell i}$  are the elements of the  
 1008 Pontecorvo-Maki-Nakagawa-Sakata (PMNS) matrix that describes the mixing between  
 the neutrino flavor and mass states.

1009 A standard parameterization [24] of the PMNS matrix is

$$1010 U_{PMNS} = \begin{bmatrix} U_{e1} & U_{e2} & U_{e3} \\ U_{\mu 1} & U_{\mu 2} & U_{\mu 3} \\ U_{\tau 1} & U_{\tau 2} & U_{\tau 3} \end{bmatrix} \\ = \begin{bmatrix} 1 & 0 & 0 \\ 0 & c_{23} & s_{23} \\ 0 & -s_{23} & c_{23} \end{bmatrix} \begin{bmatrix} c_{13} & 0 & s_{13}e^{-i\delta} \\ 0 & 1 & 0 \\ -s_{13}e^{i\delta} & 0 & c_{13} \end{bmatrix} \begin{bmatrix} c_{12} & s_{12} & 0 \\ -s_{12} & c_{12} & 0 \\ 0 & 0 & 1 \end{bmatrix} \quad (2.2) \\ \times \begin{bmatrix} e^{i\alpha_1/2} & 0 & 0 \\ 0 & e^{i\alpha_2/2} & 0 \\ 0 & 0 & 1 \end{bmatrix},$$

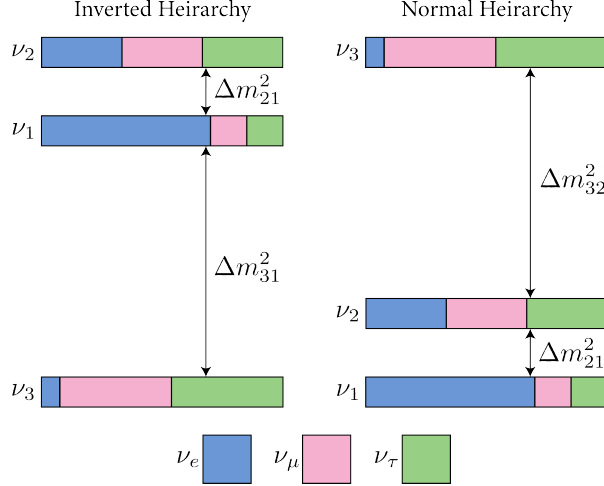


**Figure 2.1.** A diagram of two different neutrino mass ordering scenarios [1]. In the inverted hierarchy (inverted mass ordering) the lightest neutrino mass is  $m_3$ , whereas, in the normal hierarchy (normal mass ordering)  $m_1$  is the lightest neutrino. What cannot be measured by neutrino oscillations is the neutrino absolute mass scale, which is essentially the mass of the lightest neutrino mass eigenstate.

where  $c_{ij} = \cos \theta_{ij}$  and  $s_{ij} = \sin \theta_{ij}$ . The parameters  $\alpha_1$  and  $\alpha_2$  are only included in the PNMS matrix if neutrinos are Majorana particles, something which represents a current area of research in neutrino physics. The phase  $\delta$  quantifies the degree of CP-violation in the neutrino sector. Including the Majorana phases the PMNS matrix contains six independent parameters. Neutrino oscillation probabilities also depend on the squared mass differences between neutrino mass eigenstates

$$\Delta m_{ij}^2 = m_i^2 - m_j^2, \quad (2.3)$$

where  $ij = 12, 32, 31$  respectively. Because  $\Delta m_{32}^2 = \Delta m_{31}^2 - \Delta m_{21}^2$ , this adds an additional two parameters that must be constrained by neutrino oscillations.

A large experimental effort over the past couple decades has greatly contained the majority of parameters in the PMNS matrix, many to relative uncertainties of only a few percent. However, certain ambiguities remain, which is the origin of the current uncertainty in the ordering of the neutrino masses (see Figure 2.1). The neutrino masses can be arranged by their relative masses. Current neutrino oscillation data supports that  $m_2 > m_1$ , however, the sign of  $\Delta m_{32}^2$  is still unknown. Therefore, two mass-ordering scenarios are allowed, one where neutrino masses are arranged  $m_3 > m_2 > m_1$ , which is called the normal mass ordering (NMO), or alternatively neutrino masses may be ordered  $m_2 > m_1 > m_3$ , which is called the inverted mass ordering (IMO). Next-

1027 generation neutrino oscillation experiments such as JUNO [25], Hyper-Kamiokande [26],  
1028 and DUNE [27] are poised to resolve this ambiguity in the coming years.

1029 Neutrino oscillation probabilities are sensitive to the neutrino masses via the squared  
1030 mass differences. Therefore, oscillation probabilities are unaffected by the absolute scale  
1031 of the neutrino mass. However, oscillations can be used to obtain a lower bound on the  
1032 neutrino masses by setting the mass of the lightest neutrino mass state to zero. This  
1033 results in different lower limits depending on the ordering of the neutrino mass states.  
1034 Current best-fit values [24] with  $1\sigma$ -uncertainties for the squared mass differences are

$$\Delta m_{21}^2 = (7.42^{+0.21}_{-0.20}) \times 10^{-5} \text{ eV}^2, \quad (2.4)$$

$$\Delta m_{31}^2 = (2.5176^{+0.026}_{-0.028}) \times 10^{-3} \text{ eV}^2 \text{ (NMO)}, \quad (2.5)$$

1035 for the normal mass ordering, and for the inverted ordering the limit is

$$\Delta m_{32}^2 = (-2.498^{+0.028}_{-0.028}) \times 10^{-3} \text{ eV}^2 \text{ (IMO).} \quad (2.6)$$

1036 The parameter  $\Delta m_{21}^2$  is the same in the NMO and the IMO. Allowing the lightest neutrino  
1037 mass in each ordering scenario ( $m_{\text{least}}$ ) to take on a range of values, one can visualize the  
1038 relative masses of the neutrinos as a function of  $m_{\text{least}}$  (see Figure 2.2). The absolute  
1039 neutrino mass scale is effectively the value of this  $m_{\text{least}}$  parameter.

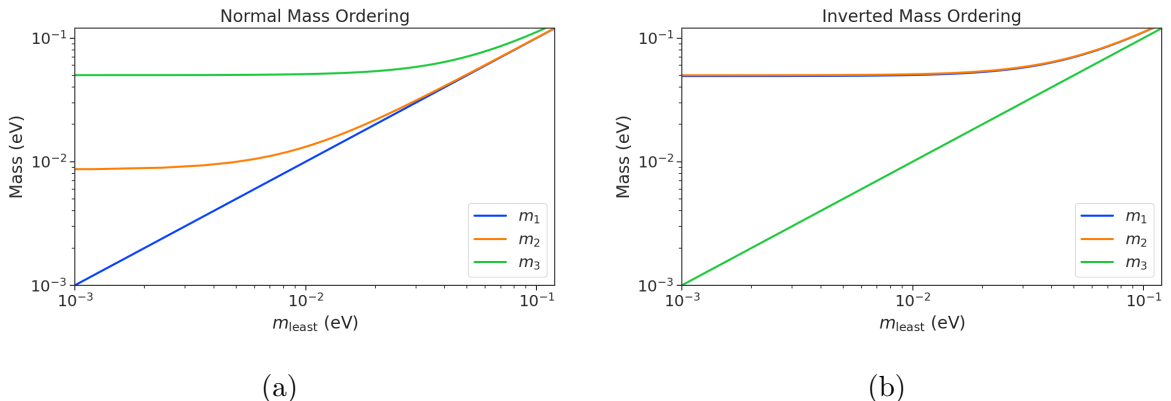


**Figure 2.2.** The masses of the neutrinos as a function of the lightest neutrino mass in both the normal (a) and inverted (b) mass ordering regimes.

## 2.4 Neutrino Masses in the Standard Model

In this section, I briefly summarize the current theoretical understanding of neutrino masses in the standard model [28–30]. Neutrinos are spin 1/2 particles, which are described using the Dirac equation.

$$(i\hbar\gamma^\mu\partial_\mu - mc)\psi(x) = 0, \quad (2.7)$$

where the field that describes the particle is denoted as  $\psi(x)$ . In the standard model fermions acquire mass through the Yukawa interaction, which add to the standard model Lagrangian terms of the form

$$\mathcal{L}_{\text{Yukawa}} = -Y_{ij}^\ell \bar{L}_{Li} \phi E_{Rj} + \text{h.c.}, \quad (2.8)$$

where  $Y_{ij}^\ell$  is an element of the  $3 \times 3$  Yukawa coupling matrix for leptons,  $L_{Li}$  is the left-handed lepton doublet for generation  $i$ ,  $\phi$  is the Higgs doublet, and  $E_{Rj}$  is the right-handed lepton field for generation  $j$ . Neutrinos are represented only as left-handed neutrinos and right-handed antineutrinos in the standard model, which is consistent with experimental observations. Since there are no right-handed neutrino singlet fields, there are no Yukawa interaction terms, thus neutrinos in the standard model are strictly massless. Therefore, non-zero neutrino mass is evidence for physics beyond the standard model.

For the charged leptons, the Yukawa interaction leads to masses of the form

$$m_{ij}^\ell = Y_{ij}^\ell \frac{v}{\sqrt{2}}, \quad (2.9)$$

where  $v$  is the Higgs vacuum expectation value. The observation of massive neutrinos motivates the extension of the standard model to explain the origin of neutrino masses, which can be approached in different ways, but all approaches add additional degrees of freedom to the standard model.

One approach is to introduce to the standard model a right-handed neutrino field that allows one to include Yukawa terms of the form

$$\mathcal{L}_{\nu \text{Yukawa}} = -Y_{ij}^\ell \bar{L}_{Li} \phi \nu_{Rj} + \text{h.c.} \quad (2.10)$$

where  $\nu_{Rj}$  is the right-handed neutrino singlet. Because experimental evidence strongly

1063 predicts only three active neutrinos, these additional neutrinos are "sterile", in that they  
1064 do not interact via the strong, weak, or electromagnetic interactions. After spontaneous  
1065 symmetry breaking, the Yukawa interaction leads to mass terms given by

$$\mathcal{L}_D = -M_{Dij}\bar{\nu}_{Ri}\nu_{Lj} + \text{h.c.}, \quad (2.11)$$

1066 which is called a Dirac mass term. One of the issues with constructing neutrino masses  
1067 in this way is that the required Yukawa couplings are at least a factor of  $10^6$  smaller than  
1068 that of an electron, which begs the question: why are the Yukawa couplings so small for  
1069 the neutrinos?

1070 An alternative approach is to allow the neutrinos to have a Majorana mass, which is  
1071 possible because neutrinos are electrically neutral particles. The Majorana mass terms  
1072 for neutrinos have the form

$$\mathcal{L}_M = -\frac{1}{2}(M_{Rij}\bar{\nu}_{Ri}\nu_{Rj}^c M_{Lij}\bar{\nu}_{Li}\nu_{Lj}^c) + \text{h.c.}, \quad (2.12)$$

1073 where  $M_{Rij}$  and  $M_{Lij}$  are right-handed and left-handed Majorana mass matrices. A  
1074 consequence of neutrinos being Majorana particles is lepton number violation, which  
1075 predicts the occurrence of neutrino-less double beta-decay at a rate proportional to the  
1076 neutrino mass.

1077 In the most general case neutrinos have both Dirac and Majorana mass terms, which  
1078 allows one to generate neutrino masses with Yukawa couplings similar to the rest of the  
1079 standard model. Considering a single generation of neutrinos for demonstration, the  
1080 combined neutrino mass Lagrangian can be written as

$$\mathcal{L}_{D+M} = -m_D\bar{\nu}_R\nu_L - \frac{1}{2}(m_L\bar{\nu}_L\nu_L^c + m_R\bar{\nu}_R\nu_R^c) + \text{h.c.}, \quad (2.13)$$

1081 or equivalently,

$$\mathcal{L}_{D+M} = -\frac{1}{2} \begin{bmatrix} \bar{\nu}_L & \bar{\nu}_R^c \end{bmatrix} \begin{bmatrix} m_L & m_D \\ m_D & m_R \end{bmatrix} \begin{bmatrix} \nu_L^c \\ \nu_R \end{bmatrix} + \text{h.c..} \quad (2.14)$$

1082 An example mass generation mechanism with this approach is the Type-I see-saw  
1083 mechanism [31], in which one takes  $m_L = 0$  and  $m_R \gg m_D$ . By diagonalizing Equation  
1084 2.14 one obtains the mass eigenvalues that represent the physical masses of the neutrinos.  
1085 The light neutrino mass eigenstate, which represents the observed neutrino mass, has a  
1086 mass given by

$$m_1 \approx \frac{m_D^2}{m_R}, \quad (2.15)$$

1087 and the heavy neutrino mass eigenstate, which represents the unobserved sterile neutrino,  
1088 has a mass

$$m_2 \approx m_R. \quad (2.16)$$

1089 For  $m_D$  similar to the other quark or lepton masses, one obtains physical neutrino masses  
1090 consistent with observations from sterile neutrino masses of  $m_R \approx O(10^{15})$  GeV. This  
1091 mass scale is well beyond the capabilities of modern particle accelerators to probe.

## 1092 2.5 Neutrino Absolute Mass Scale

1093 The neutrino absolute mass scale or simply "neutrino mass" cannot be probed with  
1094 neutrino oscillations, since oscillation probabilities are determined by the squared mass  
1095 differences between neutrino mass eigenstates, therefore, alternative techniques are needed  
1096 to perform an effective measurement of the neutrino mass.

### 1097 2.5.1 Limits from Cosmology

1098 The  $\Lambda$ CDM model summarizes the current cosmological understanding of the universe [24].  
1099  $\Lambda$ CDM predicts that the universe originated from a single expansion event colloquially  
1100 called the "Big Bang". During the Big Bang, the universe originated as a hot spacetime  
1101 singularity, which abruptly experienced rapid expansion in a process known as inflation.  
1102 After expansion the inflationary field eventually decayed into a population of quarks,  
1103 gluons, leptons, and photons, which were kept in thermal equilibrium by the high-  
1104 temperatures of the early universe.

1105 As the universe continued to expand it's density and temperature decreased until  
1106 the formation of neutral atoms, primarily hydrogen, was possible. At which point the  
1107 population of photons produced during the Big Bang decoupled from the primordial  
1108 universe and began to freely propagate. A direct prediction of the  $\Lambda$ CDM model is that  
1109 this population of photons is still present, but with a significantly reduced temperature  
1110 due to the subsequent expansion of the universe. This is consistent with the observation of  
1111 the CMB (cosmic microwave background), which is a population of microwave radiation  
1112 with a blackbody temperature of 2.7 K. The CMB is extremely uniform in all directions  
1113 with slight anisotropies that can be analyzed to study the evolution of the early universe.  
1114 A series of experiments have measured the CMB with increasing levels of precision, which  
1115 has lead to a significant increase in our current understanding of cosmology.

1116 In addition to the CMB, inflation predicts the existence of a  $C\nu B$  (cosmic neutrino

background) [32], which are the remnant neutrinos produced during the Big Bang. Since neutrinos only interact via the weak force, they decouple from the Big Bang plasma at an earlier time than the CMB photons. The temperature at which the C $\nu$ B decouples depends on the neutrino rest mass. Neutrinos play a unique role in the  $\Lambda$ CDM model, due to the fact that neutrinos act as radiation early in the universe but as matter in the late universe. This leads to specific signatures that impact the expected anisotropies of the CMB as well as the distribution of matter in the universe [33]. By combining measurements of the CMB with measurements of the large-scale structure (LSS) of the universe one can constrain the neutrino mass scale by fitting these datasets with the  $\Lambda$ CDM model. This analysis results in some of the most stringent constraints on the neutrino mass. Recent analyses [24] have been able to constrain the neutrino mass scale to

$$\Sigma_{m_\nu} \equiv \sum_i m_i < 0.11 \text{ eV}, \quad (2.17)$$

where  $m_i$  are the neutrino mass eigenstates.

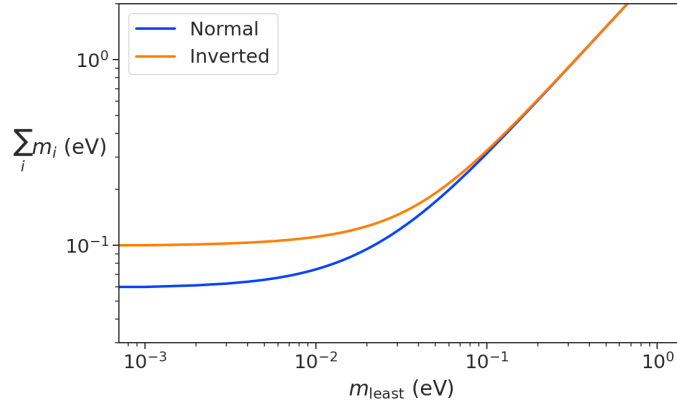


**Figure 2.3.** The neutrino mass observable measured by cosmology as a function of the lightest neutrino mass eigenstate.

The observable  $\Sigma_{m_\nu}$  constrains the neutrino mass by setting the mass of the lightest neutrino mass eigenstate ( $m_{\text{least}}$ ) (see Figure 2.3). In the normal mass ordering  $\Sigma_{m_\nu}$  can be rewritten in the form

$$\Sigma_{m_\nu} = m_{\text{least}} + \sqrt{\Delta m_{21}^2 + m_{\text{least}}^2} + \sqrt{\Delta m_{32}^2 + m_{\text{least}}^2}, \quad (2.18)$$

where it is clear that a measurement of  $\Sigma_{m_\nu}$  effectively sets the neutrino mass scale

1134 through  $m_{\text{least}}$ . The analogous formula for the inverted mass ordering is

$$\Sigma_{m_\nu} = m_{\text{least}} + \sqrt{-\Delta m_{32}^2 + m_{\text{least}}^2} + \sqrt{-\Delta m_{31}^2 + m_{\text{least}}^2}. \quad (2.19)$$

1135 Upcoming experiments [34] are planned to refine measurements of the CMB, LSS,  
1136 and other cosmological observables. With this additional data it is possible that in the  
1137 near future cosmological measurements will be able to positively constrain the neutrino  
1138 absolute mass scale. However, the strength of these limits strictly depend on the accuracy  
1139 of the  $\Lambda$ CDM model, which highlights the need for direct experimental measurements of  
1140 the neutrino mass to confirm the predictions of cosmology and to fix the neutrino mass  
1141 parameter in future cosmological analyses.

### 1142 2.5.2 Limits from Neutrinoless Double Beta-decay Searches

1143 If neutrinos are Majorana fermions, then the neutrino is equivalent to its own antiparticle  
1144 and lepton conservation is not an exact law of nature [35]. Limits on the rate of  
1145 neutrinoless double beta-decay ( $0\nu\beta\beta$ ), are some of the most powerful current tests of  
1146 lepton number conservation [24]. If  $0\nu\beta\beta$  were observed, it would be direct evidence that  
1147 neutrinos are Majorana fermions and provide a method for measuring the neutrino mass  
1148 scale.

1149 Standard double beta-decay occurs when two neutrons in an unstable nucleus spon-  
1150 taneously decay into two protons, which results in the production of two electrons and  
 two neutrinos (see Figure 2.4). Whereas, during  $0\nu\beta\beta$  the two neutrinos self-annihilate

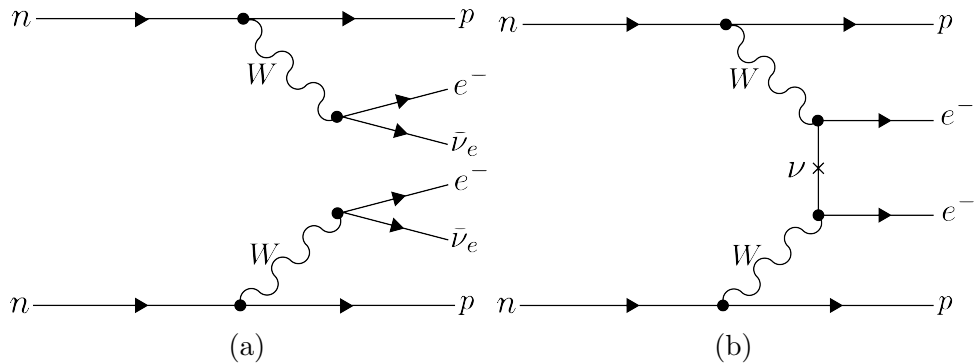


**Figure 2.4.** Feynman diagrams for double beta-decay (a) and  $0\nu\beta\beta$ (b).

1151  
1152 producing only two electrons, which violates lepton number by two.

1153 Assuming that the exchange of two Majorana neutrinos is the dominant channel for  
1154  $0\nu\beta\beta$ , then a measurement of the  $0\nu\beta\beta$  half-life for a particular isotope can be used to

1155 set the neutrino absolute mass scale [36]. The half-life is written in terms of the effective  
 1156 neutrino mass for  $0\nu\beta\beta$  ( $m_{\beta\beta}$ ) using the equation

$$T_{1/2}^{0\nu} = \frac{1}{G|\mathcal{M}|^2 m_{\beta\beta}^2}, \quad (2.20)$$

1157 where  $G$  is the phase-space factor for the decay and  $\mathcal{M}$  is the relevant nuclear matrix  
 1158 element.  $m_{\beta\beta}$  is given by an incoherent sum of the neutrino mass eigenstates weighted  
 1159 by the PMNS mixing matrix parameters,

$$m_{\beta\beta} = \left| \sum_i U_{ei}^2 m_i \right|. \quad (2.21)$$

1160 The information provided from  $0\nu\beta\beta$  on the neutrino mass scale can be visualized by  
 1161 expressing the value of  $m_{\beta\beta}$  in terms of  $m_{\text{least}}$  and two relative Majorana phases [2]. The  
 1162 allowed regions for  $m_{\beta\beta}$  as a function of  $m_{\text{least}}$  are shown in Figure 2.5 as the regions  
 1163 bounded by the black curves overlayed with the discovery probabilities of future  $0\nu\beta\beta$   
 decay experiments based on current neutrino data.

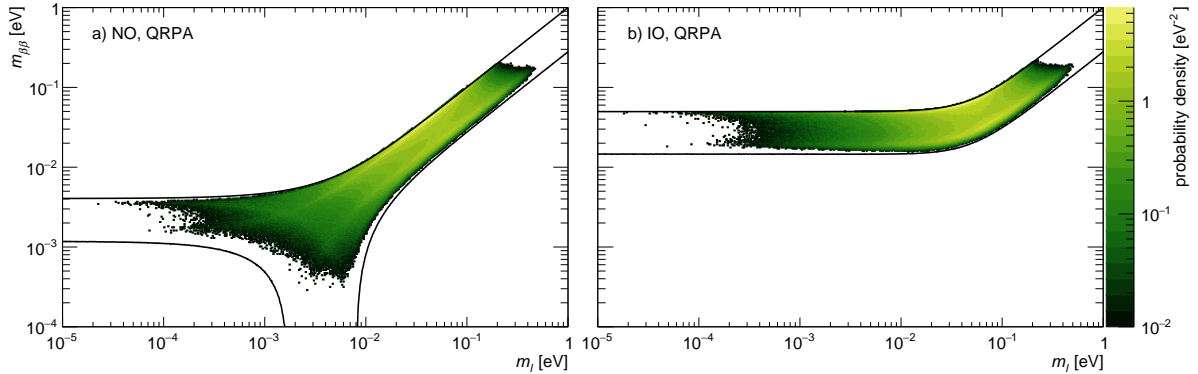


**Figure 2.5.** The discovery probabilities for the future generation of  $0\nu\beta\beta$  experiments as a function of  $m_{\beta\beta}$  and  $m_{\text{least}}$ . Figure from [2].

1164  
 1165 Because of the possibility of cancellation due to the unknown Majorana phases included  
 1166 in the sum specified by Equation 2.21, the neutrino mass information gained from  $0\nu\beta\beta$   
 1167 is necessarily imperfect. Additionally, theoretical uncertainties in the calculation of the  
 1168 nuclear matrix elements complicates the calculation of  $m_{\beta\beta}$  from a measurement of  $0\nu\beta\beta$   
 1169 half-life. Similar to cosmology, there is a high degree of complementarity between direct  
 1170 measurements of the neutrino mass and  $0\nu\beta\beta$ . In particular, a measurement of  $m_{\text{least}}$  to  
 1171 less than 0.1 eV sensitivity provides significant information for  $0\nu\beta\beta$  searches based on  
 1172 the discovery probabilities displayed in Figure 2.5.

### 2.5.3 Limits from Beta-decay

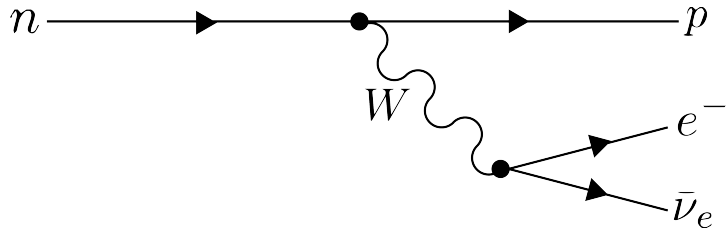


**Figure 2.6.** A Feynman diagram of beta decay

Certain processes involving neutrinos, in particular beta-decay (see Figure 2.6), have initial states with well-defined total energies and final states that can be measured with high accuracy and precision. Beta-decay involves the decay of an unstable isotope where a neutron spontaneously converts to a proton and emits an electron and anti-neutrino ("neutrino" for brevity) to conserve charge and lepton number [5]. Therefore, by applying the principles of energy and momentum conservation, a measurement of the kinematics of the final state can be used to constrain the neutrino mass [37].

Using beta-decay to measure the neutrino mass can be tied back to Fermi's original 1934 theory of nuclear beta-decay [16] (see Figure 2.7). Because the constraints on the

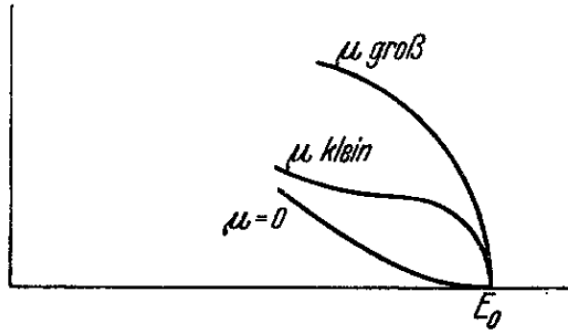


**Figure 2.7.** A figure from Fermi's 1934 paper on a theory of beta-decay depicting the kinetic energy spectrum of the emitted electron. The effect of the neutrino mass, written as  $\mu$ , is to distort the shape of the spectrum near the endpoint from the zero-mass spectrum.

neutrino mass from beta-decay depend only on the final state measurement capabilities and the principles of energy and momentum conservation, neutrino mass measurements with beta-decay are called direct measurements. A direct measurement like beta-decay contrasts with other neutrino mass measurements approaches that are model-dependent such as cosmology and  $0\nu\beta\beta$ , which provide complementary ways to study the physics of massive neutrinos.

1189     The isotope of choice for direct neutrino mass measurements with beta-decay has  
 1190     been tritium ( ${}^3H_2$ ) for many decades, because it conveniently fulfills many experimental  
 1191     requirements. Of upmost importance is a decay with a low Q-value, which is the available  
 1192     kinetic energy based on the mass difference between the initial and final states. The  
 1193     effect of a massive neutrino on the shape of the spectrum is magnified for low Q-values  
 1194     and tritium has an unusually low Q-value of 18.6 keV.

1195     Additionally, tritium beta-decay is super-allowed, which results in a relatively short  
 1196     half-life of 12.3 years. Therefore, high source activity can be obtained with a relatively  
 1197     small source mass. High-activity is desirable because of the low-activity near the tritium  
 1198     spectrum endpoint. For tritium beta-decays, only a factor of  $3 \times 10^{-13}$  of the decays  
 1199     occur in the last 1 eV of the spectrum. Isotopes with Q-values lower than tritium are  
 1200     known [37], but this is outweighed by exceedingly long half-lives leading to unobtainable  
 1201     source masses.

1202     The endpoint measurement approach involves quantifying the effect of the neutrino's  
 1203     mass on shape of the electron's kinetic energy spectrum near the endpoint. The shape of  
 1204     the kinetic energy spectrum (see Figure 2.8) is given by

$$\frac{d\Gamma}{dE} = \frac{G_F^2 |V_{ud}|^2}{2\pi^3} (G_V^2 + 3G_A^2) F(Z, \beta) \beta (E + m_e)^2 (E_0 - E) \\ \times \sum_{i=1,2,3} |U_{ei}|^2 [(E_0 - E)^2 - m_i^2]^{1/2} \Theta(E_0 - E - m_i), \quad (2.22)$$

1205     where  $G_F$  is the Fermi coupling constant,  $V_{ud}$  is an element of the CKM matrix,  $E$   
 1206     is the kinetic energy of the electron,  $\beta$  is the velocity of the electron divided by the  
 1207     speed of light,  $E_0$  is the endpoint energy assuming zero neutrino mass,  $F(Z, \beta)$  is the  
 1208     Fermi function, and  $\Theta(E_0 - E - m_i)$  is the Heaviside function, which enforces energy  
 1209     conservation. One can see that the decay spectrum is actually a combination of three  
 1210     spectra with different endpoints based on the values of the neutrino mass eigenstates,  $m_i$ .  
 1211     This produces "kinks" in the spectrum shape due to overlapping spectra with different  
 1212     endpoint values, but such an effect would be nearly impossible to resolve given the finite  
 1213     energy resolution of a real experiment.

1214     The neutrino mass scale variable measured by beta-decay is given by

$$m_\beta^2 = \sum_i |U_{ei}|^2 m_i^2, \quad (2.23)$$

1215     where  $m_\beta$  is the electron-weighted neutrino mass or simply "neutrino mass" for brevity.

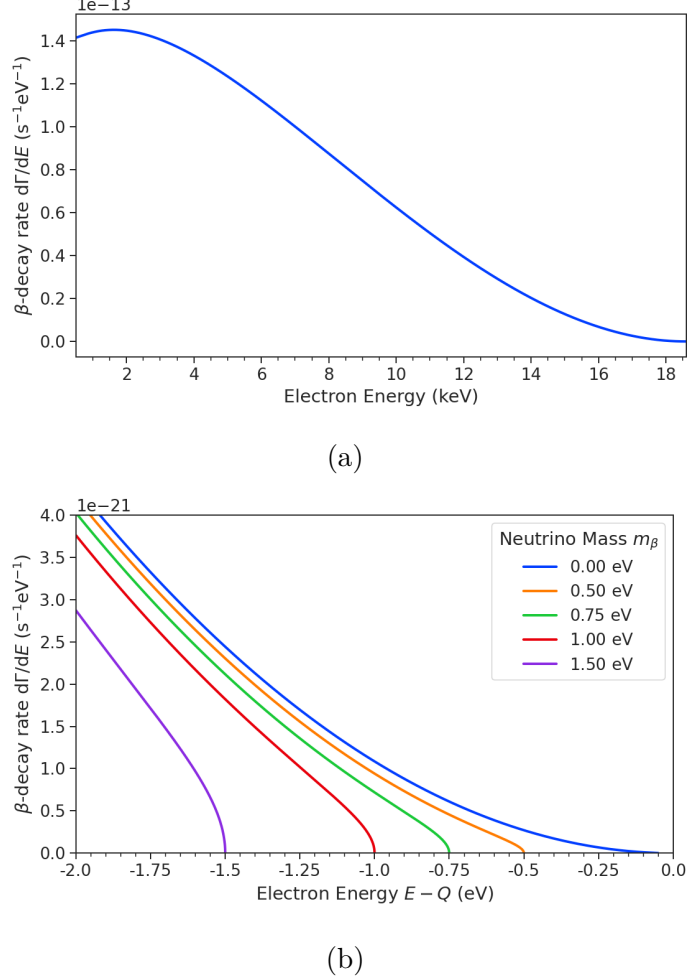


**Figure 2.8.** The tritium beta-decay spectrum. The effect of a massive neutrino on the spectrum is to change its shape near the endpoint by an amount proportional to the size of the neutrino mass. A sufficiently high-statistic and high-resolution measurement of the spectrum endpoint would be able to measure the neutrino mass.

The quantity  $m_\beta$  corresponds to a particular weighted sum of the neutrino masses, which is distinct from effective neutrino masses such as  $m_{\beta\beta}$  [37]. Assuming unitarity, the neutrino mass can be expressed in terms of the PMNS matrix elements, squared mass differences, and the lightest neutrino mass eigenstate. For the normal mass ordering the equation is

$$m_\beta^2 = m_{\text{least}}^2 + |U_{e2}|^2 \Delta m_{21}^2 + |U_{e3}|^2 \Delta m_{31}^2, \quad (2.24)$$

and for the inverted ordering the equation is

$$m_\beta^2 = m_{\text{least}}^2 + |U_{e1}|^2 (-\Delta m_{32}^2 - \Delta m_{21}^2) + |U_{e2}|^2 (-\Delta m_{32}^2). \quad (2.25)$$

1222 Therefore, a measurement of the neutrino mass in combination with neutrino mixing  
1223 parameters is effectively a measurement of  $m_{\text{least}}$ .

1224 Since the neutrino mass is small ( $< 1$  eV), its effect on the spectrum is limited to the  
1225 endpoint region. The affect of a non-zero neutrino mass on the endpoint spectrum is  
1226 plotted for the reader in Figure 2.8. Resolving the small changes in the spectrum shape  
1227 requires an experimental technique with high statistics, excellent energy resolution, and  
1228 low background activity.

1229 **Chapter 3 |**

1230 **Direct Measurement of the Neutrino Mass**

1231 **with Project 8**

1232 **3.1 Introduction**

1233 A promising technique for direct measurements of the neutrino mass beyond the projected  
1234 200 meV limit of the KATRIN experiment [38] is tritium beta-decay spectroscopy with  
1235 an atomic tritium source [39]. Atomic tritium, combined with a large-volume, high-  
1236 resolution energy measurement technique, is capable of measuring the neutrino mass  
1237 with sensitivity below the 50 meV, which exhausts the range of neutrino masses allowed  
1238 under the inverted hierarchy.

1239 Cyclotron Radiation Emission Spectroscopy (CRES) is a high-resolution energy  
1240 measurement technique compatible with atomic tritium production and storage that can  
1241 enable the next-generation of neutrino mass direct measurement experiments [40]. The  
1242 Project 8 collaboration is currently engaged in a program of research and development  
1243 (R&D) aimed at developing the technology necessary for a measurement of the neutrino  
1244 mass using CRES and atomic tritium with a sensitivity of 40 meV [41].

1245 In Section 3.2 I provide an introduction to the basics of the CRES technique as well as  
1246 the goals of the Project 8 experiment. Additionally, I sketch out the phased experiment  
1247 development plan being implemented by Project 8 to build towards a next-generation  
1248 neutrino mass experiment.

1249 In Section 3.3 I give an overview of Phase II of the Project 8 experiment [42,43], which  
1250 completed early in 2023. Although the bulk of the work presented in this dissertation is  
1251 relevant to designs of future Project 8 experiments, a description of the work in Phase II  
1252 provides useful context.

1253 In Section 3.4 I introduce a CRES measurement concept based on antenna arrays [44],  
1254 which could be the basis for the ultimate Project 8 neutrino mass experiment. A

1255 significant portion of the R&D efforts of Project 8 in Phase III were directed towards  
1256 simulating and modeling this experimental concept in order to understand the achievable  
1257 sensitivity to the neutrino mass.

1258 Lastly, in Section 3.5 I introduce conceptual designs of pilot-scale experiments and  
1259 Phase IV that combine atomic CRES with a large-volume CRES detection technique.  
1260 This includes a design concept for an antenna array based experiment, but also a design  
1261 for a resonant cavity based experiment. Resonant cavities are discussed in more depth in  
1262 Chapter 6 and have become the default choice for the Phase IV experiment.

## 1263 **3.2 Project 8 and Cyclotron Radiation Emission Spectroscopy**

1264

### 1265 **3.2.1 Cyclotron Radiation Emission Spectroscopy — CRES**

1266 Time and frequency are two of the most precisely measured quantities in physics. Atomic  
1267 clocks, which operate by measuring the frequencies of various atomic transitions, have  
1268 been used to measure time with astounding relative uncertainties of  $10^{-18}$  seconds [45].  
1269 The extreme precision possible with frequency measurements is often summarized using  
1270 the a quote from the Physicist Arthur Schawlow who said advise his students to "Never  
1271 measure anything but frequency!" [46].

1272 Neutrino mass measurements using tritium beta-decay require the measurement  
1273 of perturbations to the 18.6-keV tritium endpoint with a precision as small as 0.1 eV.  
1274 Therefore, a spectroscopic technique with extremely high resolution is required. Frequency  
1275 measurements are capable of such high-resolutions for the intuitive reason that they are  
1276 essentially digital counting measurements, which average the number of oscillations of a  
1277 physical system over time. By observing a rapidly oscillating system over a sufficient  
1278 length of time one can obtain essentially arbitrary precision on a frequency limited only  
1279 by the measurement time and signal-to-noise ratio (SNR) of the system.

1280 A method is required for translating an electron kinetic energy measurement into a  
1281 frequency measurement. A straightforward way to accomplish this is to place a gaseous  
1282 supply of tritium into a magnetic field, therefore, when a beta-decay occurs the resulting  
1283 electron will immediately begin to orbit around a magnetic field line at the cyclotron  
1284 frequency, proportional to its kinetic energy (see Figure 3.1). The acceleration caused  
1285 by the orbit leads to the emission of cyclotron radiation that can be detected using an  
1286 array of antennas or resonant cavity. The starting frequency of the radiation gives the

1287 electron's initial kinetic energy, which is used to build the beta-decay spectrum and  
 1288 measure the neutrino mass. The name for this measurement technique is Cyclotron  
 1289 Radiation Emission Spectroscopy or CRES [40].

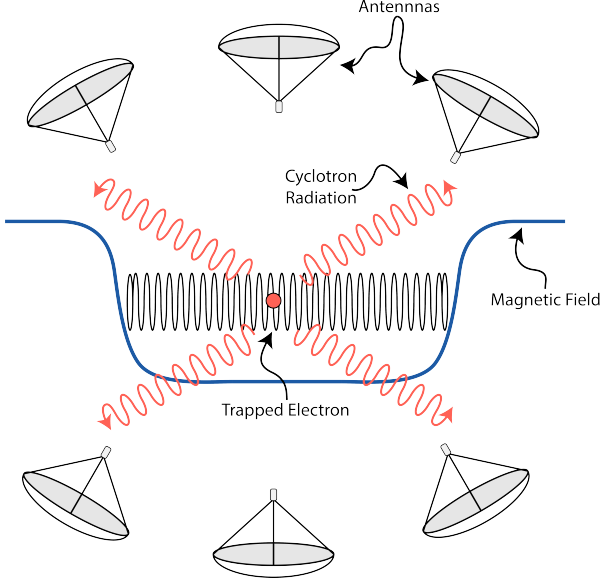


**Figure 3.1.** A cartoon illustration of the CRES technique. An electron is contained in a magnetic trap, which is a local minimum in the magnetic field, so that its cyclotron radiation can be detected by an array of antennas. Detecting the cyclotron radiation allows one to measure its cyclotron frequency and determine its kinetic energy.

1290 In the non-relativistic case, the cyclotron frequency is simply a function of the  
 1291 charge-to-mass ratio of the particle, however, the relativistic correction to the cyclotron  
 1292 frequency

$$f_c = \frac{qB}{2\pi m_e \gamma} = \frac{1}{2\pi} \frac{qB}{m_e + E_{\text{kin}}/c^2}, \quad (3.1)$$

1293 introduces a dependence of the kinetic energy ( $E_{\text{kin}}$ ) to the inverse of the cyclotron  
 1294 frequency ( $f_c$ ). Electrons with kinetic energies of 18.6 keV are in the weakly relativistic  
 1295 regime with  $\beta = \frac{v}{c} = 0.263$  and  $\gamma = 1.036$ .

1296 The frequency resolution of a CRES measurement can be estimated by differentiating  
 1297 Equation 3.1,

$$\frac{df_c}{dE_{\text{kin}}} = \frac{1}{2\pi} \frac{-qBc^2}{(m_e c^2 + E_{\text{kin}})^2}, \quad (3.2)$$

1298 from which one obtains the relationship between fractional differences in energy and  
 1299 frequency,

$$\frac{df_c}{f_c} = \frac{1 - \gamma}{\gamma} \frac{dE_{\text{kin}}}{E_{\text{kin}}}. \quad (3.3)$$

1300 Therefore, an energy precision of 1 eV for an 18.6 keV electron can be achieved with a  
 1301 frequency precision of approximately 2 ppm.

1302 The minimum observation time required to achieve this resolution can be estimated  
 1303 using the uncertainty principle as formulated by Gabor [47]. Electrons from tritium  
 1304 beta-decay experience random collisions with the background gas particles, which limits  
 1305 the uninterrupted radiation lifetime. The time between collision events, referred to as  
 1306 "track length", is an exponentially distributed variable. Differences in the track lengths  
 1307 of a population of mono-energetic electrons leads to an uncertainty or broadening in the  
 1308 distribution of measured frequencies, which is proportional to the mean track length,  $\tau_\lambda$ .  
 1309 The resulting frequency distribution has a Lorentzian profile, whose width is given by  
 1310 the Gabor limit,

$$\tau_\lambda \Delta f_c = \frac{1}{2\pi} \implies \Delta f_c = \frac{1}{2\pi\tau_\lambda}. \quad (3.4)$$

1311 The cyclotron frequency for a 18.6-keV electron in a 1 T field is approximately  
 1312 27 GHz, consequently, the minimum observation time for a frequency resolution of 2 ppm  
 1313 is approximately 3  $\mu$ sec. The Gabor limit is not the true lower bound on the frequency  
 1314 resolution for a CRES signal, since it derives from the Fourier representation of a fixed  
 1315 length time-series using a basis of infinite duration sinusoids. If one takes the approach of  
 1316 fitting the CRES signal in the time-domain, then the lower limit on frequency precision  
 1317 is given by the Cramér-Rao lower bound (CRLB) [48], which depends on the track length  
 1318 and SNR. The CRLB is the minimum variance achievable by an unbiased estimator  
 1319 for an unknown but deterministic parameter. In general, the CRLB allows for better  
 1320 precision on the cyclotron frequency.

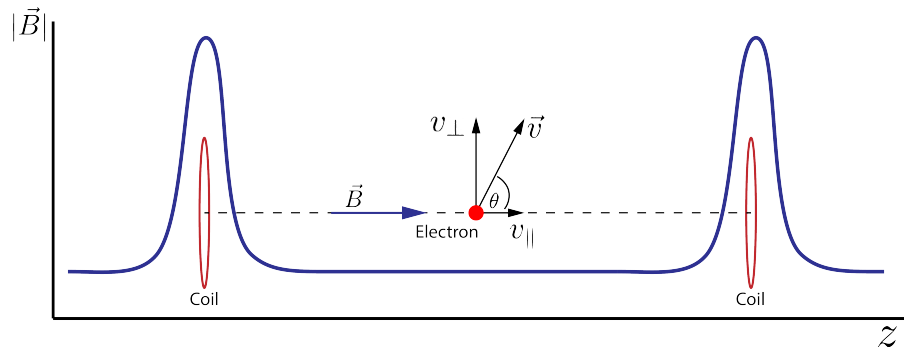


**Figure 3.2.** An illustration of an electron in a bathtub magnetic trap generated by two well-separated coils.

1321 Ensuring that an electron remains under observation long enough so that its frequency  
 1322 can be precisely measured can be achieved using a magnetic trap. A magnetic trap is a

local minimum in a background magnetic field generated an appropriate configuration of electromagnetic coils. Since magnetic fields can do no work, there is no danger of the magnetic trap affecting the kinetic energy of the electron after it is emitted from the beta-decay. One common approach to creating a magnetic trap is the "bathtub" trap configuration, which can be produced using two magnetic pinch coils aligned on a central axis that are separated by a distance that is large compared to the coil radius (see Figure 3.2). This configuration produces a trap with a uniform bottom and relatively steep walls, which is ideal for CRES measurements.

The electron's pitch angle is a useful parameter for describing its motion in the magnetic trap. Pitch angle is defined in terms of the ratio between the component of the electron's velocity perpendicular to the magnetic field and the component parallel to the magnetic field

$$\tan \theta_p = \frac{v_{\perp}}{v_{\parallel}}. \quad (3.5)$$

Electrons with pitch angles less than  $90^{\circ}$  oscillate back and forth in the magnetic trap, which leads to variations in the cyclotron frequency caused by the changing value of the magnetic field along the electron's path. This leads to frequency modulation that produces sidebands in the cyclotron radiation spectrum. Resolving these sideband frequency components is necessary for a complete reconstruction of the CRES signal in the experiment.

Electrons trapped in a cylindrically symmetric trap have three primary components of motion (see Figure 3.3). The dominant component, typically with the highest frequency,

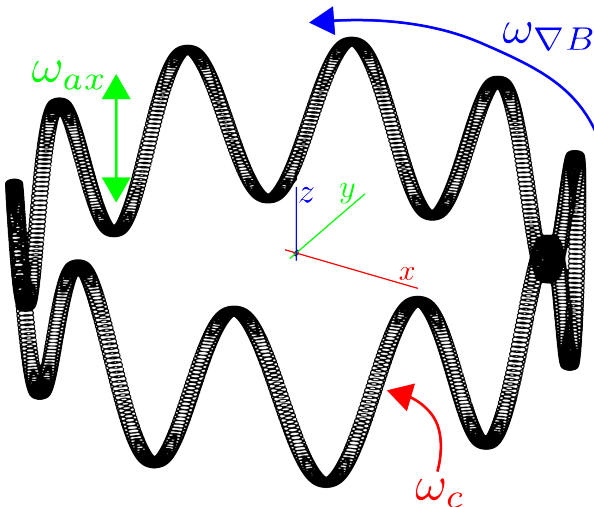


**Figure 3.3.** A plot of the main components of an electron's trajectory in a cylindrically symmetric trap.

1342

1343 is the electron's cyclotron orbit, which encodes information on the electron's kinetic  
 1344 energy. Axial motion from the electron's pitch angle leads to frequency modulation,  
 1345 and a shift in the average magnetic field experienced by an electron. This leads to a  
 1346 correlation between the kinetic energy of the electron and the pitch angle depending on  
 1347 the particular shape of the magnetic trap, which can negatively impact energy resolution.  
 1348 Generally, more variation in the magnetic field along the electron's trajectory leads to  
 1349 a worse energy resolution. The magnetic trap can be engineered to have a flat bottom  
 1350 with very steep walls to mitigate this effect. A bathtub trap design, where the distance  
 1351 between the coils is much greater than the coil radius, is the trap that best approximates  
 1352 this ideal design. Radial gradients in the trap leads to a third component of motion  
 1353 called grad-B drift [49]. The equation for the drift velocity is

$$\mathbf{v}_{\nabla B} = \frac{m_e v_{\perp}^2}{2qB} \frac{\mathbf{B} \times \nabla B}{B^2}. \quad (3.6)$$

1354 The total power of the radiation emitted by an electron in a free-space environment  
 1355 is given by the Larmor equation [50]

$$P(\gamma, \theta_p) = \frac{1}{4\pi\epsilon_0} \frac{2}{3} \frac{q^2 \omega_c^2}{c} (\gamma^2 - 1) \sin^2 \theta_p, \quad (3.7)$$

1356 where  $\omega_c$  is the cyclotron frequency multiplied by  $2\pi$  and  $\theta_p$  is the pitch angle to distinguish  
 1357 it from the spherical angle coordinate. A single electron with a  $90^\circ$  pitch angle and  
 1358 18.6 keV of kinetic energy in a 1 T magnetic field emits a total radiation power of 1.2 fW.  
 1359 Furthermore, one is typically only able to receive a fraction of this total power with an  
 1360 antenna or other detection system. Therefore, RF (radio-frequency) systems in CRES  
 1361 experiments must be operated at cryogenic temperatures to limit the noise power such  
 1362 that adequate SNR can be achieved for signal detection and reconstruction. Alternatively,  
 1363 longer tracks enable detection of weaker signals due to the increase in the total signal  
 1364 energy available for the detection algorithm.

### 1365 3.2.2 Project 8

1366 The Project 8 collaboration<sup>1</sup> is a group of institutions in the United States and Germany  
 1367 building an experiment to measure the neutrino mass by developing a novel spectrometer  
 1368 technology based on CRES. In the ultimate Project 8 experiment, the CRES technique  
 1369 will be used to measure the beta-decay spectrum using a large source of atomic tritium

---

<sup>1</sup><https://www.project8.org/>

1370 sufficient to achieve the required statistics in the last  $O(10)$  eV of the decay spectrum.  
1371 Project 8 is targeting a neutrino mass sensitivity below 50 meV [51], which exhausts the  
1372 range of possible neutrino masses under the inverted hierarchy and is a factor of four less  
1373 than sensitivity projections for the ongoing KATRIN experiment.

1374 Project 8's proposed experiment requires the development of two novel technologies:  
1375 the production and trapping of a source of atomic tritium on cubic-meter scales and  
1376 technology to enable CRES measurements of individual electrons in the same volume.

### 1377 Atomic Tritium

1378 Previous measurements of the tritium beta-decay spectrum for neutrino mass measure-  
1379 ments have relied on sources of molecular tritium for their measurements [38, 52, 53] due  
1380 to the technical challenges associated with the production and storage of atomic tritium.

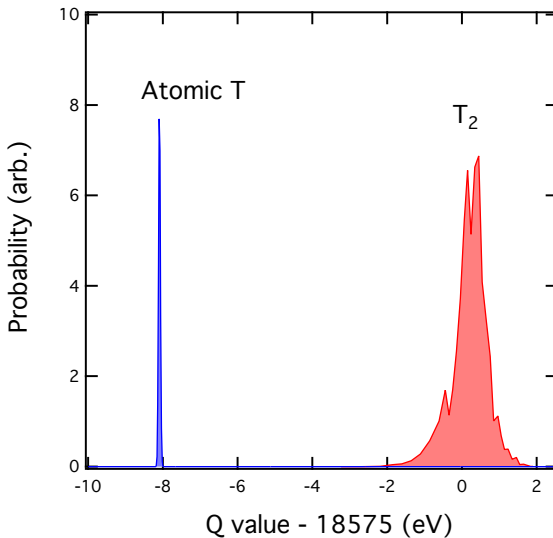


**Figure 3.4.** A plot of the final state distributions of atomic and molecular tritium. The final state distribution provides the primary contribution to the width of the molecular spectrum whereas thermal doppler broadening is responsible for the width of the atomic spectrum.

1381 One must supply sufficient energy to the tritium molecules to break the molecular  
1382 bond and create atomic tritium. Common approaches include the use of hot coaxial  
1383 filament atom crackers as well as plasma sources. Both involve heating the tritium atoms  
1384 to temperatures of  $> 2500$  K, which must then be cooled to temperatures on the order  
1385 of a few mK so that the tritium atoms can be trapped. Cooling the atoms requires the  
1386 construction of a large tritium infrastructure and cooling system that can supply a source  
1387 of cold atoms to the trap.

1388 Once cold tritium atoms are produced they cannot make contact with any surfaces  
1389 to avoid recombination of the atoms to molecules. Therefore, a magnetic trap is required  
1390 to store the atoms for a sufficient length of time that they have a chance to decay before  
1391 escaping the trap. Trapping the atoms requires the construction of a large and complex  
1392 magnet system that must be cooled to cryogenic temperatures.

1393 The significant experimental complexity caused by atomic tritium makes a molecular  
1394 source the obvious choice from practical considerations. However, the drawback of  
1395 molecular tritium for neutrino mass measurement is the irreducible broadening in the  
1396 electron's kinetic energy due to the final state spectrum of molecular tritium (see Figure  
1397 3.4). The broadening of the final state spectra has a RMS amplitude of 436 meV [54, 55]  
1398 caused by variation in the final vibrational state of the daughter molecule.

1399 For atomic tritium, the primary sources of broadening in the final state spectrum are  
1400 magnetic hyperfine splittings (magnitude of  $O(10^{-5})$  eV) and thermal Doppler broadening  
1401 caused by the motion of the trapped atom. Atomic tritium at a temperature of 1 mK  
1402 has a broadening which is dominated by thermal Doppler broadening, providing about  
1403 1 meV RMS of broadening to the electron's kinetic energy.

1404 The larger energy broadening with molecular tritium leads to an irreducible statistical  
1405 uncertainty that limits the achievable sensitivity to approximately 100 meV at 90%  
1406 confidence. For previous direct measurements of the neutrino mass, this uncertainty is  
1407 an insignificant contribution to the overall uncertainty budget. However, for experiments  
1408 like Project 8 atomic tritium is a key component to the success of the experiment.

## 1409 **CRES for Neutrino Mass Measurement**

1410 Several features of the CRES technique make it an attractive choice for a next generation  
1411 neutrino mass measurement experiment. Because CRES is a remote-sensing technique,  
1412 it is possible to observe the kinetic energy of the electron without altering its trajectory  
1413 or directly interacting with the particle, therefore, in a CRES experiment the source  
1414 gas volume can be the same as the CRES spectrometer volume. Tritium gas is also  
1415 transparent to cyclotron radiation, which means that the kinetic energies of electrons can  
1416 be measured using a cavity or antenna array, located directly outside the atom trapping  
1417 volume.

1418 Because source and spectrometer can be colocated, CRES experiments have an  
1419 advantageous scaling law relative to the current state-of-the-art beta-decay spectroscopy  
1420 experiment, KATRIN. KATRIN utilizes the magnetic adiabatic collimation with an  
1421 electrostatic filter (MAC-E filter) technique to measure the beta-decay spectrum of

1422 molecular tritium. In this approach, a source of molecular tritium is located outside the  
1423 spectrometer. When a beta-decay occurs the electron is guided out of the tritium source  
1424 using a magnetic field and is transported through the MAC-E filter before it is detected  
1425 on the other side of the filter using a charge sensor. The measurement statistics of the  
1426 MAC-E filter are limited by the transverse area of the tritium source and filter due to the  
1427 need to travel through the experiment without scattering. This scaling is less favorable  
1428 than the volumetric scaling of CRES due to the ability to colocate source and detector.

1429 Another promising aspect of the CRES technique is the inherently high precision  
1430 of frequency based measurements. The endpoint of the molecular tritium beta-decay  
1431 spectrum is approximately 18.6 keV, which dwarfs the neutrino mass scale of  $< 1 \text{ eV}/c^2$   
1432 by at least a factor of  $10^5$ . Measuring the effect of such a small mass on a high energy  
1433 electron requires excellent energy resolution. Since frequency measurements are essentially  
1434 counting measurements they are intrinsically quite accurate due to the ability to measure  
1435 the cyclotron frequency by effectively averaging over millions of cyclotron orbits. It  
1436 is possible to achieve part-per-million accuracy on the kinetic energy with the CRES  
1437 technique using the off-the-shelf RF components.

1438 CRES is also nearly immune to typical sources of backgrounds that can plague other  
1439 experiments. Since CRES operates via a non-destructive measurement of the electron's  
1440 cyclotron frequency, sources of background electrons are effectively filtered out by limiting  
1441 the frequency bandwidth of the measurement. The fiducial volume of the experiment is  
1442 free from any surfaces that could introduce stray electrons, and electrons from sources  
1443 outside the fiducial volume can be prevented from entering the experiment.

## 1444 Neutrino Mass Sensitivity Goals

1445 Project 8's ultimate goal is to combine CRES with atomic tritium to measure the neutrino  
1446 mass with 40 meV sensitivity at the 90% confidence level (see Figure 3.5). This sensitivity  
1447 is sufficient to fully exhaust the range of allowable neutrino masses under the inverted  
1448 neutrino mass ordering regime and is approximately an order of magnitude less than the  
1449 projected final sensitivity of the KATRIN experiment. Excluding the full neutrino mass  
1450 parameter space would require a sensitivity an order of magnitude lower than what is  
1451 proposed by Project 8, which would require an experiment whose size and complexity  
1452 are currently well beyond proposals for the next-generation of neutrino mass direct  
1453 measurement experiments.

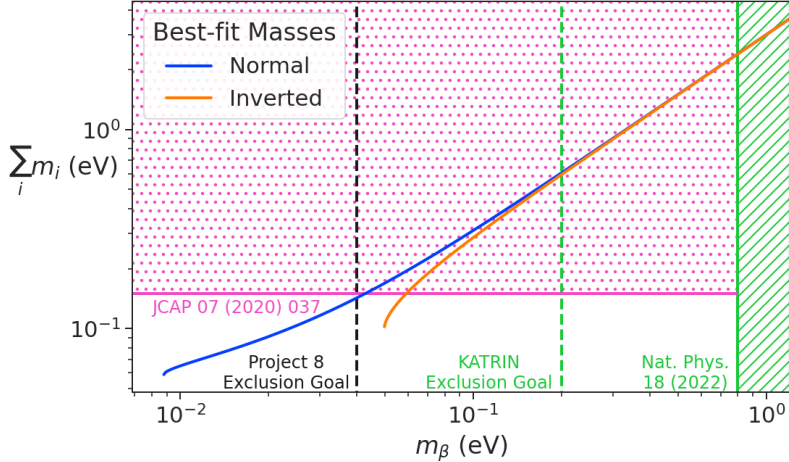


**Figure 3.5.** Neutrino mass exclusion plot including limits from cosmological measurements and the KATRIN experiment. Allowed ranges for neutrino masses under the normal and inverted hierarchies are shown as the blue and orange lines respectively. The black dashed line shows Project 8’s goal neutrino mass sensitivity for the Phase IV experiment.

### 1454    3.2.3 The Project 8 Phased Development Plan

1455    Reaching 40 meV sensitivity requires the simultaneous development and eventually  
 1456    combination of CRES and atomic tritium. These technologies require a significant up-front  
 1457    R&D investment to build-out the required capabilities for a 40 meV CRES experiment.  
 1458    Therefore, Project 8 is following a phased experiment plan in which incremental progress  
 1459    can be made towards the ultimate goal of a 40 meV neutrino mass measurement with  
 1460    CRES.

1461    Project 8’s experiment plan is divided into four phases. The first phase, called  
 1462    Phase I, consisted of a demonstration of the CRES technique and a measurement of the  
 1463    internal conversion spectrum of  $^{83m}\text{Kr}$ . Phase II was the first measurement of the tritium  
 1464    beta-decay spectrum and neutrino mass measurement with CRES. Currently, Project 8  
 1465    is engaged in Phase III, which is research and development towards a scalable CRES  
 1466    measurement technique and atomic tritium source for the final Project 8 experiment in  
 1467    Phase IV. Phase IV is the ultimate experiment by Project 8 that will combine CRES  
 1468    with atomic tritium to measure the neutrino mass with a sensitivity of 40 meV.

#### 1469    Phase I and II: Proof of Principle and First Tritium Measurements

1470    The earlier phases of the Project 8 experiment, Phase I and II, were focused on demon-  
 1471    stration and development of the CRES technique itself as well as a proof-of-principle

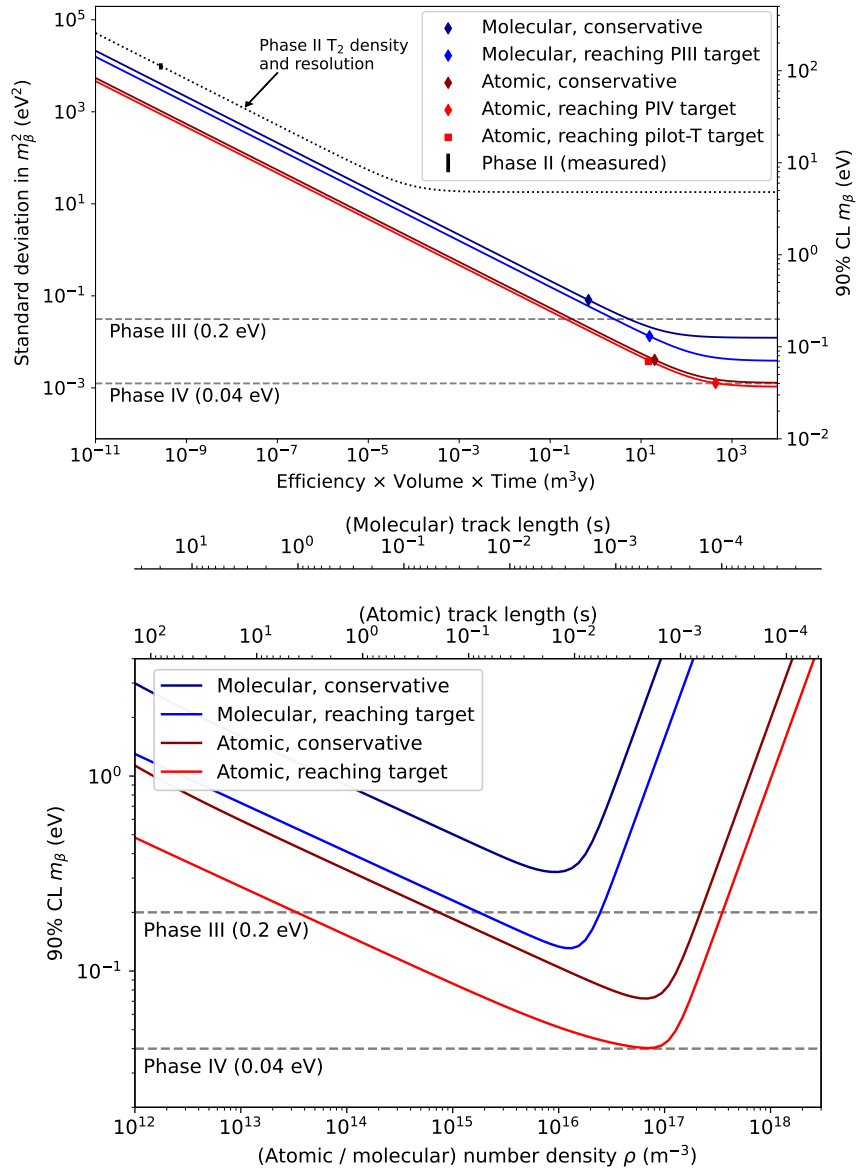


**Figure 3.6.** Sensitivity calculations for a cavity based CRES experiment that demonstrate the neutrino mass measurement goals of Project 8 throughout the phased development plan. The blue curves indicate molecular tritium sources and the red curves indicate atomic tritium sources. In the current plan, Phase III contains two tritium experiments. The first is the Low-frequency Apparatus (LFA), which is a molecular tritium experiment, and the second is the atomic tritium pilot-scale experiment that officially ends Phase III. The sensitivity of these experiments is primarily a function of statistics, however, there is a critical density beyond which CRES electrons do not have enough time to radiate between collisions for a high-resolution frequency measurement leading to worse sensitivity.

<sup>1472</sup> measurement of the neutrino mass using the CRES technique.

<sup>1473</sup> In Phase I, Project 8 performed a proof-of-principle measurement of the  $^{83m}\text{Kr}$   
<sup>1474</sup> spectrum using CRES, which marked the first ever kinetic energy spectrum measurement  
<sup>1475</sup> with CRES. The experiment included all the components of a basic CRES experiment.  
<sup>1476</sup> An electron source consisting of a gas of  $^{83m}\text{Kr}$  was supplied to a waveguide gas cell  
<sup>1477</sup> constructed out of a segment of WR-42 waveguide and sealed with Kapton windows at  
<sup>1478</sup> the top and bottom. A magnetic trapping region was created in the waveguide cell using  
<sup>1479</sup> a single electromagnetic coil wrapped around the waveguide which provided a trapping  
<sup>1480</sup> volume on the order of a few cubic-millimeters. Detection of the cyclotron radiation was  
<sup>1481</sup> performed by connecting the waveguide cell to an additional segment of waveguide that  
<sup>1482</sup> transmitted the radiation to a cryogenic amplifier.

<sup>1483</sup> Success in Phase I was achieved with the 2014 publication of the measured  $^{83m}\text{Kr}$   
<sup>1484</sup> conversion spectrum [56], which contains a mono-energetic 17.8-keV line as well as several  
<sup>1485</sup> other conversion lines at higher energies. Publication of this result marked the official  
<sup>1486</sup> end of Phase I and the start of Phase II, in which Project 8 shifted its focus to the  
<sup>1487</sup> demonstration of the first tritium beta-decay spectrum using CRES. Phase II is described  
<sup>1488</sup> below in Section 3.3.

### <sup>1489</sup> **Phase III: Research and Development and a Pilot-scale Experiment**

<sup>1490</sup> After completing Phase II, Project 8 has shifted focus towards R&D aimed at the  
<sup>1491</sup> construction of an experiment that demonstrates all the technologies required for a  
<sup>1492</sup> 40 meV measurement of the neutrino mass. The culmination of Phase III is a pilot-scale  
<sup>1493</sup> experiment that successfully retires all technological and engineering risks associated  
<sup>1494</sup> with the Phase IV experiment, while also being a scientifically interesting experiment in  
<sup>1495</sup> its own right. Sensitivity estimates of the pilot-scale experiment predict a neutrino mass  
<sup>1496</sup> sensitivity on par with the projected sensitivity of the KATRIN experiment.

<sup>1497</sup> Phase III R&D is divided into two main efforts — atomic tritium and CRES detection  
<sup>1498</sup> techniques. Atomic tritium development in Phase III must retire all risks associated  
<sup>1499</sup> with the atomic tritium system. This includes the production of tritium atoms, atomic  
<sup>1500</sup> cooling and recirculation systems, purity and isotope concentration monitoring, and  
<sup>1501</sup> atom trapping. Currently, Project 8 is operating small scale atom cracking demonstrator  
<sup>1502</sup> systems to show that atom production at the estimated rates needed for Phase IV is  
<sup>1503</sup> achievable. Future efforts will continue the current developments on atom production  
<sup>1504</sup> and expand to include demonstrations of atomic cooling with an evaporative beam line  
<sup>1505</sup> as well as atom trapping using Halbach magnet arrays.

1506        The need for new CRES detection techniques is driven by the drastic increase in scale  
1507        from Phase II to the pilot-scale experiments. The physical volume used for CRES in  
1508        Phase II was on the order of a few cubic-centimeters, and achieving Project 8’s sensitivity  
1509        target of 40 meV requires an experiment volume on the multi-cubic meter scale. Therefore,  
1510        the waveguide gas cell CRES detection technique used in Phase II is not a feasible option  
1511        for the future of Project 8 due to its inability to scale to the required size.

1512        Two alternative CRES detection techniques have been proposed for the pilot-scale  
1513        experiment — antenna arrays and resonant cavities (see Section 3.4 and Chapter 6).  
1514        Both approaches have relative advantages and disadvantages, however, the improved  
1515        understanding of the antenna array and cavity approaches to CRES in the recent years  
1516        has led to cavities being the preferred technology for the pilot-scale experiment and  
1517        Phase IV due to the estimated reduced cost and complexity of this approach. Since  
1518        a large degree of the work presented in this dissertation is focused specifically on the  
1519        development of the antenna array CRES technique as well as the design of demonstrator  
1520        experiments, I describe the proposed R&D plan for antenna array CRES in Section 3.4.  
1521        A description of the cavity approach to CRES can be found in Chapter 6.

1522        Cavity CRES R&D consists of a series of demonstrator experiments intended to  
1523        demonstrate cavity CRES at a variety of scales and magnetic fields. Radioactive sources  
1524        gases include  $^{83m}\text{Kr}$  and molecular tritium, as well as electrons produced by an electron-  
1525        gun, which is a key calibration tool for future CRES experiments. The near-term cavity  
1526        effort in Project 8 is the cavity CRES apparatus (CCA), which is a small-scale cavity  
1527        experiment operating near 26 GHz. The CCA will perform the first CRES measurements  
1528        using a small cavity, and will pave the way towards larger scale cavity experiments in  
1529        preparation for the eventual pilot-scale tritium experiment.

1530        The pilot-scale experiment will be the first experiment to combine atomic tritium and  
1531        large-volume CRES detection. It will directly demonstrate all the technologies required  
1532        for Phase IV such that no technical risks remain for scaling the experiment to required  
1533        scale. A robust approach to scaling the pilot-scale experiment is to simply build multiple  
1534        copies of it for the Phase IV experiment.

#### 1535        **Phase IV: Project 8’s Ultimate Neutrino Mass Experiment**

1536        The design of Phase IV should be a direct extension of the pilot-scale CRES experiment  
1537        that marks the official end of Phase III (see Section 3.5). The Phase IV experiment  
1538        represents the final experiment in the Project 8 neutrino mass measurement experiment  
1539        plan and will have sensitivity to neutrino masses of 40 meV.

### **3.3 Phase II: First Tritium Beta Decay Spectrum and Neutrino Mass Measurement with CRES**

In Phase II, Project 8 demonstrated the first ever measurement of the tritium beta-decay spectrum endpoint using the CRES technique, which lead to the first neutrino mass measurement by Project 8. This milestone was made possible by many improvements in the CRES technique and in the understanding of CRES systematics, which takes an important first step towards larger scale measurements of the tritium beta-decay spectrum with CRES. In this section, I briefly describe some important elements of the Phase II experiment, with the goal of contextualizing the research and development efforts for Phases III and IV of Project 8. For more complete descriptions of the work that lead to Project 8's Phase II results please refer to the relevant publications by the collaboration [42, 43].

#### **3.3.1 The Phase II CRES Apparatus**

##### **Magnet and Cryogenics**

The magnetic field for the Phase II experiment is provided by a nuclear magnetic resonance (NMR) spectroscopy magnet with a central bore diameter of 52 mm (see Figure 3.7). The magnet produces a background magnetic field with an average value of 0.959 T with a 10 ppm variation across the bore diameter achieved using several shim coils built into the magnet. Using an external NMR field probe, the variation of the magnetic field along the vertical axis of the magnet bore was measured to obtain an accurate model of the magnetic field so that the CRES cell could be positioned for optimal magnetic field uniformity.

An external solenoid magnet was installed inside the magnet bore to provide the ability to shift the magnitude of the background magnetic field by a few mT. The solenoid has inside diameter of 46 mm and a length of 350 mm, which terminates in a vacuum flange that allows it to be inserted into the NMR magnet bore from the bottom. By shifting the value of the magnetic field by a few mT, the cyclotron frequencies of electrons produced by the 17.8 keV  $^{83m}\text{Kr}$  internal-conversion line [57] can be shifted by frequencies of  $\pm 100$  MHz. This allows one to study the frequency dependent behavior of several CRES systematics, such as detection efficiency, that directly affect the measured shape of the tritium spectrum.

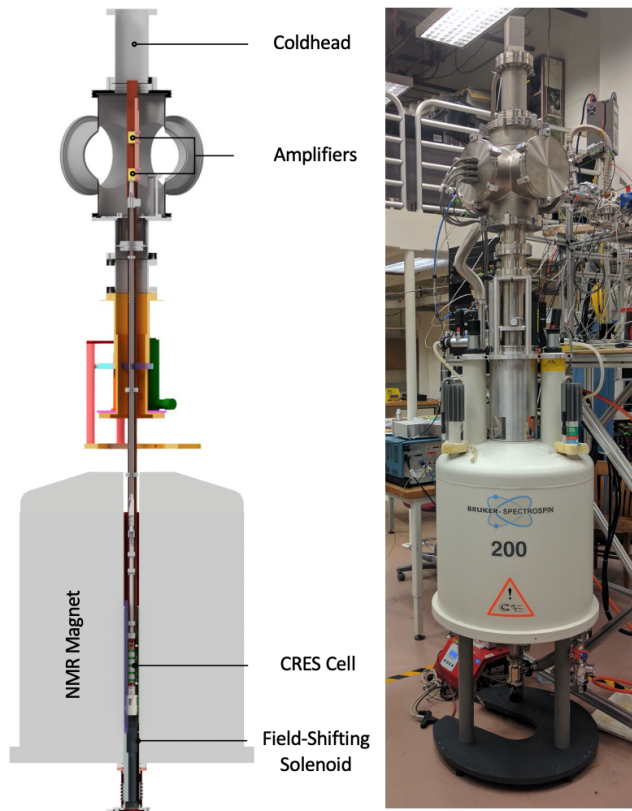


**Figure 3.7.** The Phase II CRES apparatus used to perform the first measurement of the tritium beta-decay spectrum using CRES.

1571        The inside of the magnet bore diameter was pumped down to a vacuum of less than  
 1572      10  $\mu$ torr using a turbomolecular pump, which allows for cryogenic cooling of the CRES  
 1573      cell and RF system. Cooling power was supplied to the Phase II apparatus using a  
 1574      cryopump with its coldhead mounted above the primary magnet and CRES cell. This  
 1575      arrangement allowed for sufficient cooling power to be delivered to the amplifiers to cool  
 1576      them to a temperature of  $\approx 40$  K, while keeping the amplifiers far enough from the  
 1577      magnet so as not to be damaged by the large field strength. Thermal contact between  
 1578      the coldhead, amplifiers, RF system, and CRES cell is achieved using a copper bar that  
 1579      runs the full length of the apparatus. To prevent freeze-out of  $^{83m}\text{Kr}$  on the walls of the  
 1580      CRES cell a separate heater was installed to keep the CRES cell near a temperature of  
 1581      85 K during the operation of the experiment.

1582    **CRES Cell**

1583    Located in the most uniform region of the magnetic field is the CRES cell, which is  
1584    the region of the apparatus where radioactive decays of  $^{83m}\text{Kr}$  and  $T_2$  produce electrons  
that can be trapped and measured using CRES (see Figure 3.8). The CRES cell is

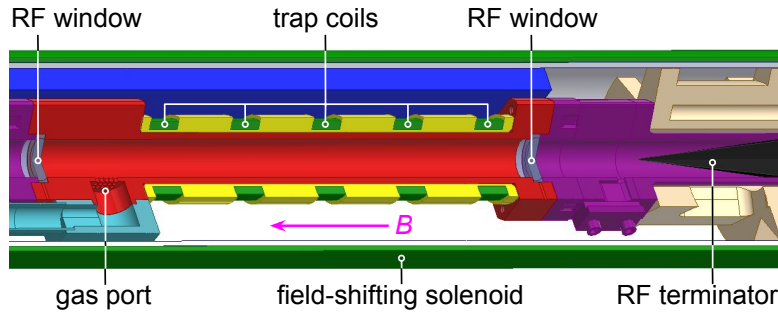


Figure 3.8. Diagram of the CRES cell portion of the Phase II apparatus.

1585  
1586    manufactured from a segment of cylindrical waveguide designed to operate at K-band  
1587    frequencies near 26 GHz. The diameter of the waveguide determines which resonant  
1588    modes of the waveguide will couple to the electron and transmit its radiation to the  
1589    amplifiers. For Phase II a waveguide diameter of 1 cm was selected, which allows electrons  
1590    to couple to the  $\text{TE}_{11}$  and  $\text{TM}_{01}$  cylindrical waveguide modes. To reduce complexity in  
1591    modeling and analyzing the CRES data, it is ideal to select a diameter that prevents  
1592    electrons from coupling to higher-order waveguide modes beyond the fundamental  $\text{TE}$   
1593    and  $\text{TM}$  modes.

1594    Around the exterior of the cylindrical waveguide are several magnetic coils used to  
1595    produce magnetic traps inside the CRES cell volume. Without a magnetic trap electrons  
1596    produced from decays inside the CRES cell quickly impact the cell wall, which prevents  
1597    a measurement of their cyclotron frequency using CRES. Each coil along the length of  
1598    the waveguide produces a separate trap that is approximately harmonic in shape. By  
1599    independently controlling the currents provided to each coil, the traps can be configured  
1600    to have equal values of the magnetic field at the trap bottom despite a non-uniform field  
1601    from the NMR magnet.

1602    Two primary magnetic trap configurations were used during the Phase II experiment.  
1603    The first was a shallow trap configuration used primarily for its high energy resolution to  
1604    study systematics using  $^{83m}\text{Kr}$  decays, and the second was a deeper trap that could trap a  
1605    higher percentage of pitch angles. The trade-off with this trap is that the higher trapping  
1606    efficiency comes at the cost of lower energy resolution due to the greater variation in  
1607    pitch angle (see Section 3.2.1). The deep trap was the trap used to measure the tritium

1608 beta-decay spectrum in Phase II.

1609 The source gases were delivered into the CRES cell through a gas port located near the  
1610 top end of the cylindrical waveguide. To prevent the gases from escaping the cell, vacuum  
1611 tight RF transparent windows are needed to contain the tritium and krypton source  
1612 gas across a 1 atm pressure differential, while still transmitting the cyclotron radiation  
1613 without distortion. The crystalline material, CaF<sub>2</sub>, which has a thermal expansion  
1614 coefficient similar to that of copper, was used for this purpose in the CRES cell. Two  
1615 windows, each 2.4 mm thick, were used to seal off the ends of the CRES cell. The  
1616 thickness of 2.4 mm corresponds to half of a cyclotron wavelength when one accounts for  
1617 the permittivity of CaF<sub>2</sub>.

## 1618 RF System

1619 The RF system in the Phase II apparatus propagates the cyclotron radiation from the  
1620 CRES cell to the receiver chain. The receiver chain performs the down-conversion and  
1621 digitization required to obtain signals that can be analyzed to determine the cyclotron  
frequencies of electrons in the CRES cell (see Figure 3.9).

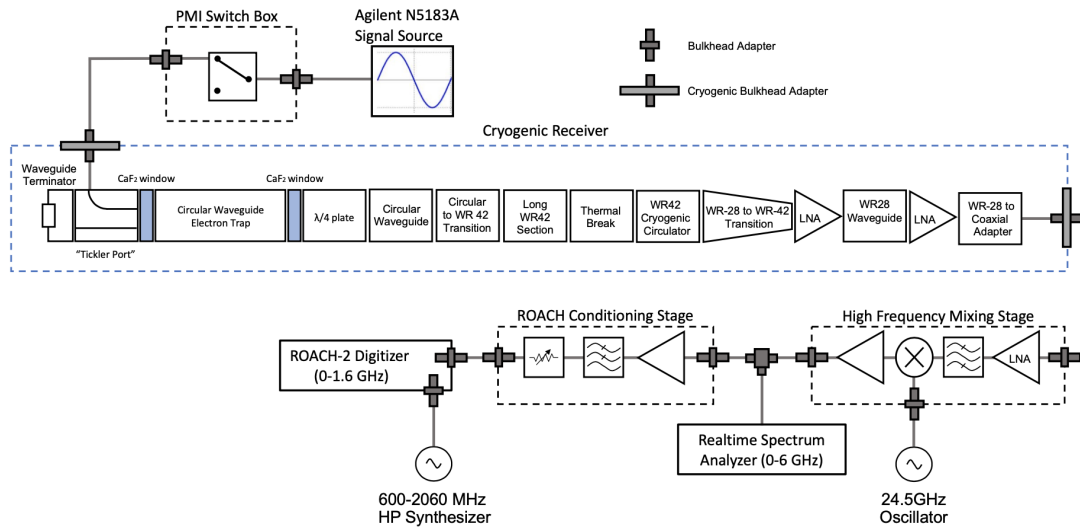


Figure 3.9. RF system diagram for the Phase II apparatus.

1622  
1623 Below the CRES cell, at the bottom of the Phase II apparatus, is a tickler port and  
1624 waveguide terminator. The tickler port is used to inject signals into the CRES cell and  
1625 RF system for testing and calibration purposes. The waveguide terminator is designed to  
1626 absorb cyclotron radiation emitted by electrons that transmits out of the bottom of the  
1627 CRES cell. This lowers the total power received from electrons in the CRES cell, since all

1628 the energy radiated downwards is absorbed into the terminator. Earlier iterations of the  
1629 Phase II apparatus used an RF short in this location that reflected this power up towards  
1630 the amplifiers, however, interference between the upward traveling and reflected radiation  
1631 led to a disappearance in the signal carrier that made reconstruction impossible.

1632 Radiation traveling upward passes through the CaF<sub>2</sub> window passes and a λ/4 plate,  
1633 which transforms the circularly polarized cyclotron radiation into linear polarization.  
1634 The linearly polarized fields next travel through a segment of circular waveguide that  
1635 transitions into a long segment of WR-42 waveguide that carries the fields out of the  
1636 high magnetic field region. A thermal break segment is included, which consists of a  
1637 segment of gold-plated stainless steel WR-42 waveguide, to help thermally isolate the  
1638 relatively warm CRES cell from the colder amplifiers. The radiation then passes through  
1639 a cryogenic circulator, which prevents signals reflected from the amplifiers from interfering  
1640 with the CRES cell before a WR-42 to WR-28 transition connects the waveguide to the  
1641 first of the cyrogenic amplifiers. The radiation passes through two cyrogenic amplifiers  
1642 before being coupled to a coaxial termination at the top of the Phase II apparatus.

1643 The coaxial cable transfers the cyclotron radiation signals to a high-frequency mixing  
1644 stage that performs an analog frequency down-conversion using a 24.5 GHz LO. Two forms  
1645 of digitization can be used at this stage to readout the CRES data. One is a real-time  
1646 spectrum analyzer that digitizes the CRES signal data in time-domain and computes the  
1647 frequency spectrum in real-time, which allows for direct visualization of CRES signal  
1648 spectrograms as the experiment is running. The real-time spectrum analyzer is most  
1649 useful for taking small amount of streamed data for debugging and analysis of the system.  
1650 The other method, which was used to collect the majority of the CRES data in Phase II,  
1651 is a ROACH-2 FPGA and digitizer system. The ROACH system consists of a fast ADC  
1652 that samples the CRES signal data at 3.2 GSps. Internal digital down-conversion stages  
1653 implemented in the FPGA perform a mixing operation that reduces the bandwidth of the  
1654 CRES signals to 100 MHz. The FPGA implements a 4096 sample FFT and packetizes  
1655 time and frequency domain records in parallel. The packetized data is then transferred  
1656 from the ROACH to be analyzed by the data-processing pipeline.

### 1657 **3.3.2 CRES Track and Event Reconstruction**

#### 1658 **Time-Frequency Spectrogram**

1659 The online data-processing software uses a real-time triggering algorithm that identifies  
1660 interesting data that could contain CRES signals. Triggered data are collected into files

1661 that are transferred to a server for offline processing and analysis. The data files contain  
1662 a continuous series of time-domain samples, broken into a set of records, which are 4096  
1663 samples long. The time-series is made up of 8-bit IQ samples acquired at 100 MHz.

1664 Each time-series record is accompanied by an associated frequency spectrum consisting  
1665 of 4096 frequency bins approximately 24.4 kHz wide, which is represented as a power  
1666 spectral density. The individual frequency spectra can be organized temporally to create  
1667 a time-frequency spectrogram that represents the evolution of the cyclotron frequency  
spectrum over the course of the CRES event (see Figure 3.10). The time-frequency

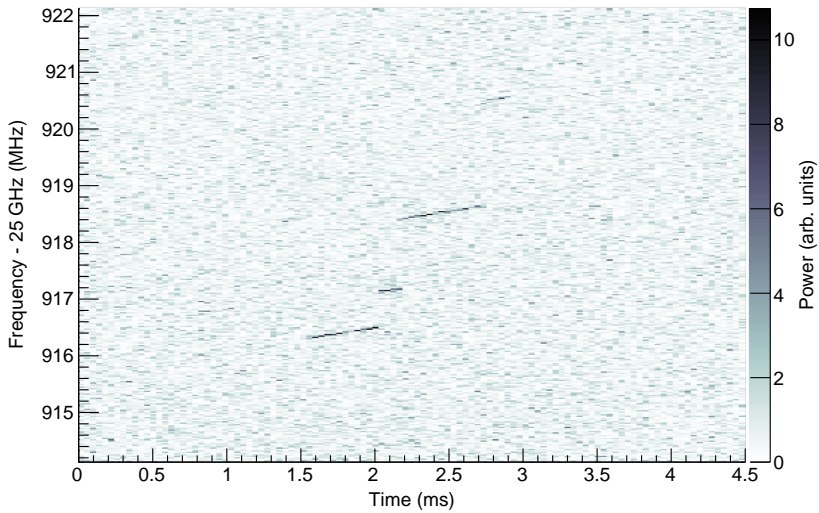


**Figure 3.10.** The time-frequency spectrogram of a tritium CRES event in the Phase II apparatus.

1668  
1669 spectrogram is represented as a two-dimensional image where the color of each pixel is  
1670 proportional to the power spectral density. Each vertical slice of pixels in the image  
1671 represents a frequency spectrum, therefore, each horizontal bin represents the data  
1672 obtained over a duration of  $4096 \times 0.01 \text{ MHz}^{-1} = 40.96 \mu\text{sec}$ .

### 1673 CRES Event Data Features

1674 Phenomenologically, a CRES signal appears as a sinusoidal signal whose frequency slowly  
1675 increases over time in what is called a frequency "chirp". Axial motion of the electron in  
1676 the trap leads to the formation of frequency sidebands that surround the more powerful  
1677 carrier frequency. The critical piece of information that must be extracted from the track  
1678 and event reconstruction procedure is the carrier frequency, since it is this frequency that  
1679 gives the cyclotron frequency and thus the kinetic energy. Axial motion from non-90°

1680 pitch angles changes the average magnetic field experienced by an electron, because  
1681 the electron effectively samples the magnetic field along its trajectory. The change in  
1682 the average magnetic field with pitch angle leads to different cyclotron frequencies that  
1683 correspond to the same kinetic energy. However, because of the low-SNR in Phase  
1684 II, sidebands were unable to be observed, so no attempt to correct for this effect was  
1685 attempted. The effect of different pitch angles is to broaden the peak of a monoenergetic  
1686 electron line, which can be quantified by measuring the instrumental resolution of the  
1687 Phase II apparatus.

1688 In the time-frequency spectrogram representation, the chirping carrier frequency  
1689 appears as a linear track of high-power frequency bins (see Figure 3.10). The vertical  
1690 slope of the tracks is caused by the emission of energy from the electron in the form of  
1691 cyclotron radiation, therefore, the size of the slope parameter is directly proportional  
1692 to the Larmour power. The continuous track is periodically interrupted by random  
1693 jumps to higher frequency (lower energy) caused by random inelastic collisions with  
1694 background gas molecules. The length of a track is an exponentially distributed variable  
1695 whose mean value is inversely proportional to the gas density. The size of the frequency  
1696 discontinuities is directly proportional to the energies of the rotational and vibrational  
1697 states of background gas molecules.

1698 A CRES event refers to the collection of tracks produced by a trapped electron until  
1699 it inevitably scatters into a pitch angle that can no longer be trapped. The goal of track  
1700 and event reconstruction is to identify the set of tracks in a time-frequency spectrogram  
1701 that represents a segment of data acquired in the Phase II apparatus. These tracks must  
1702 be clustered into events, from which one can determine the first track produced by the  
1703 electron and thus estimate its starting cyclotron frequency and kinetic energy.

## 1704 **Track Reconstruction**

1705 The first step in CRES event reconstruction is the identification of tracks in the time-  
1706 frequency spectrogram, which is essentially an image processing task. Track finding  
1707 starts by normalizing the power spectral density based on the average noise power. Next  
1708 a power threshold is applied to the normalized spectrogram where only bins that have a  
1709 SNR ratio greater than five are selected to build tracks. In this case SNR is defined as the  
1710 ratio between the normalized, unitless power of a bin divided by the average normalized  
1711 power across the full frequency spectrum.

1712 The sparse spectrogram produced by this power cut consists only of a sparse collection  
1713 of high-power frequency bins that could be part of a CRES signal track (see Figure

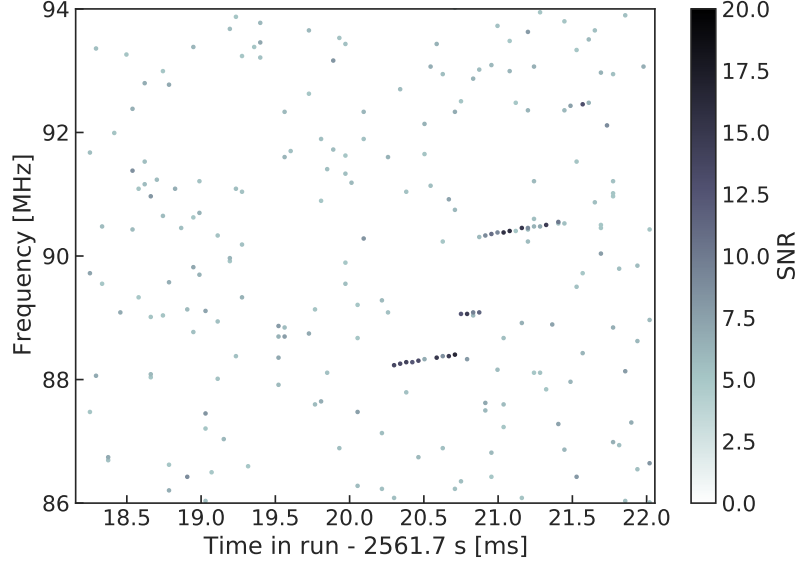


**Figure 3.11.** The sparse spectrogram obtained by placing a power cut on the raw spectrogram shown in Figure 3.10.

1714 3.11). In this form is it much easier to identify tracks "by eye", however, for the Phase II  
 1715 analysis Project 8 developed its own custom-made track finding algorithm, called the  
 1716 sequential track finder (STF).

1717 The STF algorithm processes the sparse spectrogram in sequential fashion, processing  
 1718 each time-slice one-by-one until the end of the spectrogram is reached. Tracks are found  
 1719 by searching for points in the sparse spectrogram that appear to fall on a straight line.  
 1720 Multiple configurable parameters are built into the STF algorithm that allow the user to  
 1721 tune the criteria for adding a point to an existing track or creating a new track. These  
 1722 include parameters such as maximum time and frequency differences between subsequent  
 1723 points in a track as well as minimum SNR values for the start and endpoints of the track.  
 1724 Additionally, tracks are required to have a minimum length and slope to be considered  
 1725 potential CRES tracks rather than random noise fluctuations.

1726 The resulting output of the STF is a collection of track objects that consist of the track  
 1727 point objects and their properties. The final step is to calculate track-level properties and  
 1728 apply cuts to reject false tracks found by the STF. This involves the fitting of a line to  
 1729 the collection of track points as well as the total and average power of the track obtained  
 1730 by computing the sum and mean of the points powers. The starting frequency of the  
 1731 track is determined by calculating the time coordinate that intersects with the linear fit.  
 1732 A cut is then performed to remove all tracks that do not have a specified average power  
 1733 over their duration, which helps to remove the majority of noise fluctuations that have

<sup>1734</sup> passed all previous cuts up to this point.

### <sup>1735</sup> Event Reconstruction

<sup>1736</sup> After track reconstruction comes event reconstruction, where the identified tracks are  
<sup>1737</sup> grouped into events that correspond to the trajectory of a single electron in the trap.  
<sup>1738</sup> This procedure attempts to match tracks head to tail by checking if the start and end  
<sup>1739</sup> times of a pair of tracks falls within a certain tolerance. This tolerance is a configurable  
<sup>1740</sup> parameter that can be tuned to an optimal value using Monte Carlo simulations of events  
<sup>1741</sup> in the Phase II apparatus.

<sup>1742</sup> After the event building procedure has completed, there remains a small likelihood  
<sup>1743</sup> that false tracks have made it through to the event reconstruction stage. Typically, cuts  
<sup>1744</sup> at the track level are able to remove 95% of the false tracks identified by the STF, which  
<sup>1745</sup> leads to a significant number of false tracks at the event building stage. However, the  
<sup>1746</sup> additional event-level information makes it possible to reject events that contain these  
<sup>1747</sup> false tracks with a high degree of confidence.

<sup>1748</sup> Two event level features are associated with events caused by real electrons — the  
<sup>1749</sup> duration of the first track as well as the number of tracks in the event. Real electrons  
<sup>1750</sup> tend to have event structures with longer first tracks and a higher number of total tracks.  
<sup>1751</sup> Based on the values of these two criteria, a minimum threshold on the average power in  
<sup>1752</sup> the first track was configured to reject false events. The average power in the first track  
<sup>1753</sup> was chosen due to the critical nature of the starting frequency of the first track in an  
<sup>1754</sup> event to the krypton and tritium spectrum analyses.

### <sup>1755</sup> 3.3.3 Results from Phase II

<sup>1756</sup> The main result from Phase II was the measurement of the tritium beta-decay spectrum  
<sup>1757</sup> using CRES, which lead to the first neutrino mass limit with CRES. However, Phase  
<sup>1758</sup> II also included a significant  $^{83m}\text{Kr}$  measurement campaign to understand important  
<sup>1759</sup> systematics relevant to the tritium spectrum measurement and the fundamentals of  
<sup>1760</sup> the CRES technique itself. This required high-resolution measurements of the  $^{83m}\text{Kr}$   
<sup>1761</sup> internal-conversion spectrum [57], which is an interesting science result in its own right.

<sup>1762</sup> The results from Phase II represents a significant effort from entire Project 8 over  
<sup>1763</sup> several years. Because the focus of my contributions to Project 8 is directed towards the  
<sup>1764</sup> research and development efforts for the Phase III experiments, the goal in this section  
<sup>1765</sup> is not to provide a detailed description of the analyses that lead to the Phase II results.

1766 Rather, I will provide brief descriptions of a few plots representative of the main results  
1767 from Phase II as reported in [42, 43].

## 1768 Measurements with Krypton

1769 Measurements with krypton were a key calibration tool for Phase II of the experiment  
1770 and will continue to be useful in Phase III. Krypton measurements refers to CRES  
1771 measurements of the internal-conversion spectrum of the metastable state of krypton-83,  
1772  $^{83m}\text{Kr}$ , produced by electron capture decays of  $^{83}\text{Rb}$ . A supply of  $^{83}\text{Rb}$  was built into the  
1773 Phase II apparatus gas system that supplied the CRES cell with  $^{83m}\text{Kr}$  via emanation.

1774 The  $^{83m}\text{Kr}$  internal-conversion spectrum consists of several lines based on the orbital  
1775 of the electron ejected during the decay. The conversion lines useful to Project 8 are  
1776 those that emit electrons with kinetic energies that fall inside the detectable frequency  
1777 bandwidth of the Phase II apparatus. These are the K; L2 and L3; M2 and M3; and N2  
1778 and N3 lines; with kinetic energies of 17.8 keV,  $\approx$  30.4 keV,  $\approx$  31.9 keV, and  $\approx$  32.1 keV,  
1779 respectively. The different energies of the lines allows one to test the linearity of the  
1780 relationship between kinetic energy and frequency across the range of frequencies covered  
1781 by the continuous tritium spectrum.

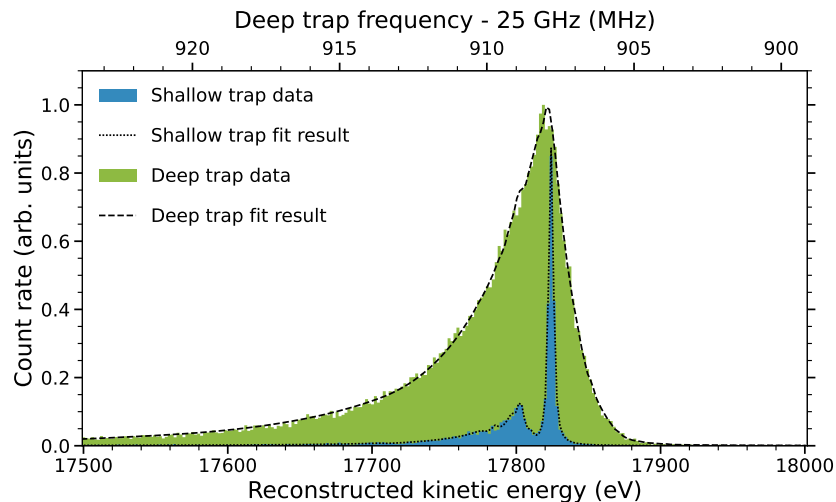


**Figure 3.12.** Fits to the measured 17.8-keV  $^{83m}\text{Kr}$  conversion line using the deep and shallow trap configurations.

1782 Numerous detector-related effects relevant to the tritium analysis can be characterized  
1783 by measuring the shape of the krypton spectrum. Specific examples include variations  
1784 in the magnetic field as a function of the radial position of the electron, variation in  
1785 the magnetic field caused by the trap shape, variation in the average magnetic field for

1786 electrons with different pitch angles, and the effect of missing tracks due to scattering.  
 1787 These spectrum shape measurements focused on the 17.8-keV krypton line and utilized  
 1788 different trap geometries based on the particular goal of the dataset (see Figure 3.12).

1789 Krypton measurements with a shallow trap allow for high energy resolution, since  
 1790 variation in frequency due to pitch angle differences is sharply reduced in the shallow  
 1791 trap configuration. With this trap the main 17.8-keV peak of the conversion spectrum is  
 1792 clearly visible along with additional satellite peaks at lower energy, which correspond to  
 1793 the shakeup/shakeoff spectrum of the decay. The high accuracy of the fit demonstrates a  
 1794 high degree of understanding of the CRES systematics.

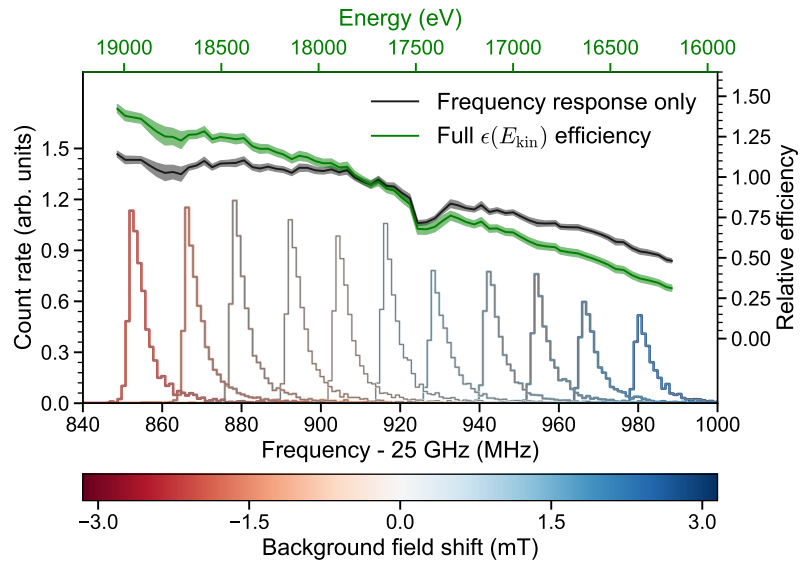


**Figure 3.13.** Measurements of the 17.8-keV  $^{83m}\text{Kr}$  line using the deep trap configuration for different values of the magnetic field from the field shifting solenoid.

1795 The broadening of the krypton spectrum seen for the deeper track is due to the large  
 1796 range of electron pitch angles that can be trapped. Furthermore, with a deeper trap  
 1797 there is a larger parameter space of electron that could be produced with pitch angles  
 1798 that are trappable but not visible in the time-frequency spectrogram. These electrons  
 1799 remain in the trap and can scatter multiple times before randomly scattering to a visible  
 1800 pitch angle. This leads to one or more missing tracks earlier in the event, which leads to  
 1801 a misreconstruction of the true starting frequency. By measuring the krypton spectrum  
 1802 shape in the same trap used to detect tritium events, the effect this has on the spectrum  
 1803 shape can be characterized to mitigate its impact on the tritium measurements.

1804 Changes in the Krypton spectrum shape as a function of CRES frequency were

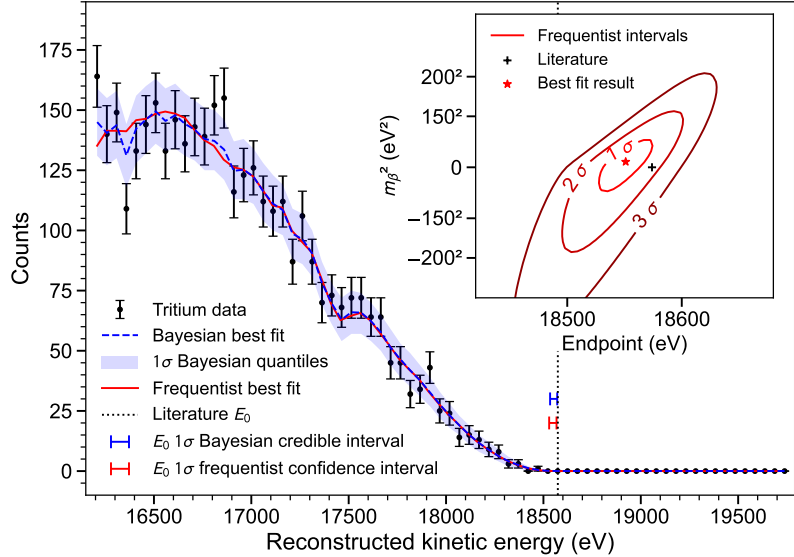


**Figure 3.14.** The measured tritium spectrum from Phase II with Bayesian and frequentist fits.

used to study the detection efficiency of the Phase II apparatus. Variations in the detection efficiency as a function of frequency directly influences the measured shape of the continuous tritium spectrum, which can lead to errors in the neutrino mass estimate if not modeled appropriately. Using the field-shifting solenoid (FSS) the cyclotron frequency of the krypton 17.83 keV line was shifted across the full frequency range of the tritium spectrum data (see Figure 3.13). The FSS is a wound copper solenoid magnet that surrounds the CRES cell. Controlling the current through this magnet allows one change the value of the background magnetic field and the frequency of the krypton conversion lines. Variations in the deep trap krypton spectrum shape can be used to infer the detection efficiency as a function of frequency and correct for this affect in the tritium measurements.

### 1816 Tritium Spectrum and Neutrino Mass Results

1817 The tritium measurement campaign resulted in the collection of 82 days of detector  
 1818 live time during which 3770 total tritium events were detected. The track and event  
 1819 reconstruction analysis extracted the starting frequencies of these tritium events, which  
 1820 were used to build a frequency spectrum of tritium beta-decays. The resulting frequency  
 1821 spectrum was then converted to an energy spectrum using the information gleaned from  
 1822 the krypton measurement campaign to obtain the tritium beta-decay spectrum (see  
 1823 Figure 3.14).

1824 CRES is inherently a very low background technique with the dominant source of noise  
1825 being random RF fluctuations. Monte Carlo simulations, validated using measurements  
1826 of the RF noise background, were used to set track and event cuts to guarantee that  
1827 zero false events would occur over the duration of the experiment with 90% confidence.  
1828 Notably, the measured spectrum has zero events beyond the tritium spectrum endpoint,  
1829 which allows one to constrain the background rate in the Phase II apparatus to less than  
1830  $3 \times 10^{-10}$  counts/ev/s. Achieving a low background is critical for future neutrino mass  
1831 experiments that seek to measure the neutrino mass with less than 100 meV sensitivity.

1832 Bayesian and frequentist based fits to the measured tritium spectrum, incorporating  
1833 information gained about CRES systematics from the krypton measurements, were  
1834 performed to extract upper limits on the tritium beta-decay spectrum endpoint as well as  
1835 the neutrino mass. The estimated spectrum endpoints are  $18553^{+18}_{-19}$  eV for the Bayesian  
1836 analysis and  $18548^{+19}_{-19}$  eV for the frequentist analysis. The quoted uncertainties are  
1837  $1-\sigma$ , and both results are within  $2-\sigma$  of the literature endpoint value of 18574 eV. The  
1838 estimated neutrino mass for both results is consistent with  $m_\beta^2 = 0$ . The 90% confidence  
1839 upper limits for the Bayesian analysis is  $m_\beta < 155$  eV/c<sup>2</sup> and  $m_\beta < 152$  eV/c for the  
1840 frequentist analysis.

1841 Though the neutrino mass results from Phase II are not competitive with KATRIN,  
1842 the experiment was a promising first step towards the development of more precise  
1843 neutrino mass measurements using CRES. The low-background and high-resolution  
1844 achievable with krypton measurements are promising features of the technique that were  
1845 demonstrated with the Phase II apparatus. As new technologies are developed to enable  
1846 CRES measurements in larger volume, many of the lessons learned from Phase II will  
1847 continue to influence the operation and design of future experiments.

### 1848 **3.4 Phase III R&D: Antenna Array CRES**

1849 The goal of Phase III in the Project 8 experimental program is to develop the technologies  
1850 and expertise required to build an experiment that uses CRES to measure the neutrino  
1851 mass with a target sensitivity of 40 meV. One of the key technologies is a method for  
1852 performing high resolution CRES measurements in a large volume, which allows one to  
1853 observe a sufficient quantity of tritium to measure the low-activity endpoint region of  
1854 the tritium spectrum.

### 1855 3.4.1 The Basic Approach

1856 One possible approach, suggested in the original CRES publication [40], is to use many  
1857 antennas to surround a volume of tritium gas in a magnetic field (see Figure 3.15). When  
1858 a decay occurs the electron will emit cyclotron radiation that can be collected by the array  
and used to perform CRES. Each antenna in the array collects only a small fraction of

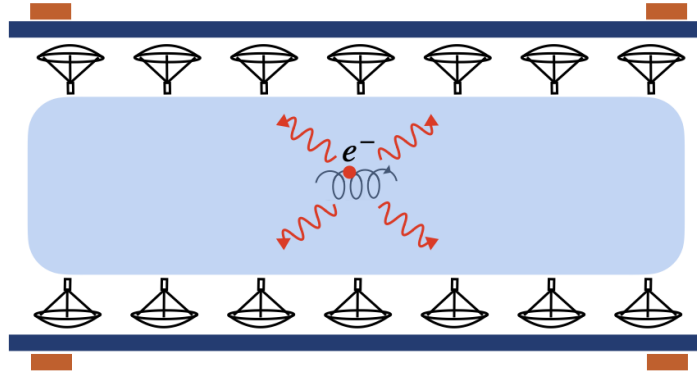


Figure 3.15. A cartoon illustration of the basics of the antenna array CRES technique.

1859  
1860 the electron's signal power, which is less than 1 fW for a 18.6 keV kinetic energy electron  
1861 in a 1 T magnetic field. Scaling to large volumes with the antenna array approach is  
1862 accomplished by increasing the number of antennas in the array, which increases the  
1863 volume available for CRES measurements.

1864 Several features of the antenna array approach make it an attractive candidate technol-  
1865 ogy for a large volume experiment. One example is the accurate position reconstruc-  
1866 tion possible with a multichannel antenna array. Using techniques like digital beamforming,  
1867 it is possible to estimate the radial and azimuthal positions of the electron in the mag-  
1868 netic trap with a precision significantly less than the size of the cyclotron wavelength.  
1869 This capability allows one to perform event-by-event estimations of the magnetic fields  
1870 experienced by an electron, which helps achieve high energy resolution with the CRES  
1871 technique.

1872 The easy availability of position information with the antennas array approach  
1873 is potentially a unique advantage that provides significant flexibility in the magnetic  
1874 field uniformity requirements compared to other proposed approaches to large volume  
1875 CRES (see Chapter 6). Spatial discrimination using digital beamforming leads to pileup  
1876 reduction, which helps to reduce the potential of background events caused by missing  
1877 tracks or by incorrectly clustering a group of tracks into an event. Limits on the  
1878 background rate for a neutrino mass measurement with 40 meV sensitivity are stringent

1879 and the total activity of the tritium source is gigantic relative to the activity near the  
1880 endpoint. Thus, pileup discrimination could be an important tool for a large scale CRES  
1881 experiment.

1882 Another beneficial quality of antenna arrays is that the volume of the experiment can  
1883 be scaled independent of frequency by simply adding more antennas to the array (see  
1884 Figure 3.19). Resonant cavities, the proposed alternative large volume CRES technology,  
1885 are ideally operated in magnetic fields that cause electrons to move with cyclotron  
1886 frequencies near the fundamental cavity resonance, to avoid complex coupling of the  
1887 electron to multiple cavity modes simultaneously. This leads to a coupling between the  
1888 cavity volume and the magnetic field magnitude, which forces one to lower the magnetic  
1889 field in order to increase the experiment scale. Whereas, for antenna arrays, in principle  
1890 there is no physical limitation on the size of the antenna array that can be used at a  
1891 particular magnetic field. However, this approach to scaling an antenna array experiment  
1892 leads to rapidly increasing cost and complexity due to the large number of antennas,  
1893 amplifiers, and data streams, which require substantial computer processing power to  
1894 effectively utilize. The link between array size and computational cost will be explored  
1895 in Section 4.3.

### 1896 **3.4.2 The FSCD: Free-space CRES Demonstrator**

1897 The complexity of the antenna array CRES technique requires the construction of a  
1898 small scale demonstration experiment to develop an understanding of technique itself and  
1899 relevant systematics. Without a demonstrator experiment it is not possible to sufficiently  
1900 retire the technical risks associated with the full-scale experiment. Therefore, Phase  
1901 III of the Project 8 experimental program is primarily focused on the development and  
1902 operation of demonstrator experiments to inform the design of the Phase IV experiment.

1903 The Phase III demonstrator experiment for antenna array CRES is called the Free-  
1904 space CRES Demonstrator or FSCD. The FSCD is also a capable neutrino mass mea-  
1905 surement experiment in its own right, with a target neutrino mass sensitivity of a few  
1906 eV using a molecular tritium source. The higher-costs associated with antenna-based  
1907 CRES, which were identified over the course of the development of the FSCD, have lead  
1908 to the adoption of resonant cavities as the technology of choice for Phase III. Therefore,  
1909 all future development of the FSCD and antenna-based CRES in Project 8 has been  
1910 suspended.

1911 **Magnetic Field**

1912 The background magnetic field for the FSCD is provided by a hospital-grade MRI magnet  
1913 (see Figure 3.16). The magnet produces a magnetic field of approximately 0.958 T, which corresponds to a tritium spectrum endpoint frequency of approximately 25.86 GHz. The



**Figure 3.16.** An image of the MRI magnet installed in the Project 8 laboratory at the University of Washington, Seattle.

1914  
1915 magnet is installed in the Project 8 laboratory located at the University of Washington,  
1916 Seattle, and is shimmed to produce a uniform magnetic field with variations on the  
1917 ppm-level. Measurements of the magnetic field non-uniformities are performed using a  
1918 NMR probe and rotational gantry to capture measurements of the magnetic field around  
1919 an elliptical surface in the center of the MRI magnet. During the operation of the FSCD  
1920 an array of Hall or NMR magnetometers would be used to periodically measure the  
1921 magnetic field to monitor its time stability.

1922 Inside the field of the MRI additional electromagnets would be installed that provide  
1923 the capability to shift the value of the background magnetic field and produce a magnetic  
1924 trap. Shifting the background magnetic field by a few  $\mu$  T lets one control the cyclotron  
1925 frequencies of electrons with a fixed kinetic energy, which is key to an effective calibration  
1926 of the FSCD. The preferred calibration method for the FSCD is a mono-energetic electron  
1927 gun that can inject electrons into the magnetic trap with a known kinetic energy. In  
1928 combination with the field shifting magnet, one can vary the cyclotron frequencies of the  
1929 electrons to measure the response of the antenna array as a function of the radiation  
1930 frequency and electron position. This procedure characterizes the response of the antenna

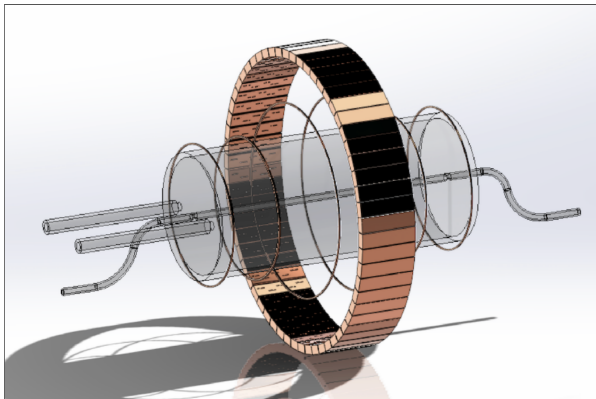
array and provides further information on magnetic field uniformity, which is important to achieving good energy resolution.

The design of the magnetic trap is absolutely critical to the success of a CRES experiment. The ideal shape is the perfect magnetic box, which has a flat bottom and step function walls. Any variation in the average magnetic field experienced by an electron leads to changes in the cyclotron frequency that can make determining the true starting kinetic energy more difficult. This includes changes in the magnetic field caused by the walls of the magnetic trap as well as radial magnetic field variations.

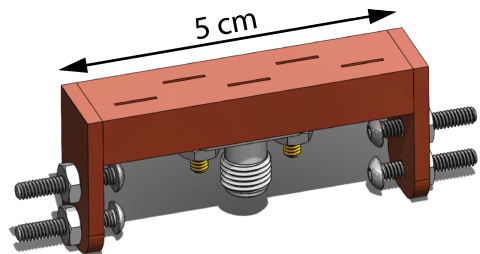
The ideal box trap is completely uniform and has infinitely steep walls that cause no change in the electron's cyclotron frequency as it is reflected from the trap wall. However, such a trap cannot be made from any combination of magnetic coils since it violates Maxwell's equations. One of the goals of magnetic trap design is to identify the configuration of coils that produces a trap that approximates the perfect box trap as closely as possible.

## Antenna Array

The canonical antenna array design for CRES is a uniform cylindrical array of antennas that surrounds the magnetic trap volume. Since the FSCD is a demonstrator experiment, the antenna array design is the simplest form of the uniform cylindrical array, which is a single circular ring of antennas with a diameter of 20 cm (see Figure 3.17). Along



(a)



(b)

**Figure 3.17.** (a) A model of the FSCD antenna array, magnetic trap, and tritium containment vessel design.(b) A more detailed model of a prototype design for the 5-slot waveguide antenna design.

1949

1950 this circle are sixty slotted waveguide antennas that fully populate the available space

1951 around the array circumference. It is optimal to cover as large a fraction of the solid  
1952 angle around the magnetic trap as possible in order to maximize the power collected  
1953 from each electron .

1954 The distance between antennas around the circumference of the array is proportional  
1955 to the wavelength of the cyclotron radiation. Therefore, maximizing the solid angle  
1956 coverage of the array, while minimizing channel count to keep the hardware and data  
1957 acquisition costs manageable, biases one towards smaller array diameters. Antenna  
1958 near-field effects limit the minimum diameter of the array for a given antenna design,  
1959 since the radiation from electrons that are too close to the array cannot be detected due  
1960 to destructive interference.

1961 Slotted waveguide antennas are used in the FSCD antenna array due to their high  
1962 efficiency and low loss, which comes from the lack of dielectric materials in the antenna  
1963 structure. Coupling to the waveguide is performed with a coaxial cable connected at the  
1964 center of the antenna. One of the drawbacks of waveguide antennas is the large amount  
1965 of space required to fit them inside the limited MRI magnet volume. Alternative antenna  
1966 designs, constructed from microstrip printed circuit boards require significantly less space  
1967 at the cost of slightly higher energy losses in the antenna structure.

1968 The FSCD antenna design is a 5 cm long segment of WR-34 waveguide with 5 vertical  
1969 slots cut into the side. The distance between slots along the length of the waveguide is  
1970 a half wavelength for optimal power combination between the individual antenna slots.  
1971 Each slot is offset from the center of the antenna face a small distance in order to most  
1972 effectively couple the slot to waveguide modes inside the antenna.

1973 The passive power combination achieved by placing 5 slots in a single waveguide is a  
1974 compromise intended to reduce the cost and complexity of the antenna array system.  
1975 Each additional channel in the array requires its own cryogenic amplifier and also increase  
1976 the required computer power to process the raw data collected by digitizing each channel.  
1977 Passive summation, achieved by combining antennas into arrays axially, reduces the  
1978 array channel count at the cost of losses from imperfect passive combination.

1979 Interference and re-radiation eventually limit the axial extent of passive power combi-  
1980 nation. The 5-slot designed developed for the FSCD is optimized to minimize the impact  
1981 of these losses while achieving the maximum amount of axial coverage with a single ring  
1982 of antennas. Scaling beyond the volume covered by a single ring of antennas is achieved  
1983 by stacking additional rings of antennas together to cover a larger trap volume. A likely  
1984 scenario for the FSCD experiment involves a staged experiment approach, where first  
1985 a series of measurements is performed using only a single ring of antennas followed by

1986 experiments that add additional rings to the FSCD. The goal would be to first understand  
1987 the principles of antenna array CRES using the simplest possible experiment, before  
1988 attempting to scale the technique by expanding the antenna array size.

1989 **Tritium Source**

1990 While the primary purpose of the FSCD is as a technology demonstrator, it is impossible to  
1991 retire all risks with the Phase IV experiment without an intermediate scale measurement  
1992 of the neutrino mass. Therefore, the FSCD has the scientific goal of measuring the  
1993 neutrino mass with a rough sensitivity goal in the range of a few eV. This level of precision  
1994 is achievable using a molecular tritium source with a volume of approximately 1 L at a  
1995 density comparable to potential Phase IV scenarios.

1996 Unlike previous CRES experiments, where the tritium source could be colocated  
1997 with the receiving antenna inside a waveguide transmission line, the tritium source  
1998 in the FSCD is thermally isolated from the antenna array to avoid freeze-out of the  
1999 tritium molecules. The tiny radiation power emitted by electrons requires a system noise  
2000 temperature of  $\approx 10$  K or less, in order to detect events at a high enough efficiency to  
2001 reach the neutrino mass sensitivity goals of the experiment. Achieving a system noise of  
2002 10 K requires that the antenna array and amplifiers operate at liquid helium temperatures  
2003 of  $\approx 4$  K, which significantly lowers the vapor pressure of molecular tritium. By keeping  
2004 the molecular tritium isolated in an RF-transparent vessel the tritium gas can be kept  
2005 at a relatively warmer temperature in the range of 30 K to avoid the accumulation of  
2006 tritium on the experiment surfaces.

2007 **Data Acquisition and Reconstruction**

2008 A fundamental change in the data acquisition system for the FSCD is the shift from  
2009 single to multichannel reconstruction. This transition results in a significant increase in  
2010 the data-generation rate, which is linearly related to the number of independent channels  
2011 in the array. The larger data volume coincides with an increased demand for computer  
2012 processing power based on the need for more precise signal reconstruction algorithms  
2013 driven by the FSCD and Phase IV sensitivity goals. Therefore, the data acquisition  
2014 system for the FSCD is likely to represent a significantly larger fraction of the experiment  
2015 cost and complexity than in Phase II.

2016 Each antenna is connected to a cryogenic amplifier and down-converted from the  
2017 26 GHz CRES frequency using an IQ-mixer to reduce the size of the analysis window.  
2018 Using an LO with a frequency of approximately 25.80 GHz the antenna array signals can

2019 be digitized at a rate of 200 MHz, which is sufficient bandwidth to resolve the complete  
2020 sideband spectrum produced by axial oscillations of electrons in the FSCD magnetic  
2021 trap.

2022 Direct storage of the raw FSCD antenna array data is undesirable, since the estimated  
2023 amount of raw data generated is  $O(1)$  exabyte per year. The storage of such a large  
2024 dataset is infeasible for a demonstrator experiment like the FSCD, since it would represent  
2025 a disproportionate fraction of the total experiment budget in Phase III and Phase IV.  
2026 Therefore, a goal of the FSCD experiment is the development of real-time reconstruction  
2027 methods that could reduce the raw data volume by detecting and reconstructing CRES  
2028 events in real-time. Ultimately, a real-time CRES reconstruction pipeline is desired, which  
2029 takes raw voltages samples from the antenna array and converts them into measured  
2030 starting kinetic energy values for electrons.

2031 The feasibility of a real-time reconstruction pipeline rests on the development of  
2032 computationally efficient algorithms that can be implemented without the need for  
2033 enormous computing resources. One challenge with the antenna array approach is that  
2034 the small radiation power of a single electron is distributed among all channels in the array,  
2035 such that reconstruction using only the information in a single channel is not possible.  
2036 Therefore, simply performing the initial step in reconstruction — signal detection —  
2037 requires orders of magnitude more computational power than previous CRES experiments.  
2038 This operation will then be followed by other, potentially more expensive, reconstruction  
2039 steps that are required in order to determine the kinetic energy of the electron.

## 2040 **3.5 Pilot-scale Experiments**

2041 The Project 8 pilot-scale experiment represents the experiment that retires all technical  
2042 and engineering risks with Project 8’s neutrino mass measurement approach, by combining  
2043 all the required components of Phase IV in a multi-cubic-meter experiment. The larger  
2044 scope and complexity of the pilot-scale experiment requires a careful choice of magnetic  
2045 field and cyclotron frequency since this directly affects the design of nearly all parts of  
2046 the experiment. Currently, designs for the pilot-scale experiment are in the conceptual  
2047 stage, but a goal of Phase III is to translate these design concepts into detailed technical  
2048 designs and specifications.

2049 **3.5.1 Choice of Frequency**

2050 The optimal CRES frequency for Project 8 is that which reaches the target sensitivity of  
2051 40 meV, while minimizing the cost and complexity of the overall experiment. The CRES  
2052 frequency is directly linked to the magnetic field, which is coupled to nearly all aspects  
2053 of the experiment design, therefore, an optimization of CRES frequency is effectively an  
2054 optimization of the sensitivity of the overall experiment.

2055 **Frequency Scaling Laws**

2056 The Phase I and II experiments utilized a background magnetic field of 0.959 T provided  
2057 by an NMR magnet. Since this magnet was already available, the 0.959 T background  
2058 field was selected for convenience. However, one additional reason to use this background  
2059 field is that the cyclotron frequencies for electrons near the tritium endpoint in a 0.959 T  
2060 field are approximately 26 GHz, which is within the standard RF Ka-band. Therefore,  
2061 microwave electronics specialized for these frequencies are obtainable for relatively low  
2062 cost. The operating frequency for the large-scale experiments must be selected in a more  
2063 rigorous manner due to the increased scale and complexity of the systems as well as the  
2064 requirements of the 40 meV neutrino mass science goal.

2065 There is a bias towards lower frequencies in a large-volume experiment, due to the  
2066 direct relationship between wavelength and the physical size of the compatible RF  
2067 components like antennas and cavities. With a longer wavelength more volume can  
2068 be surrounded by an array with fewer antennas, which reduces hardware and data-  
2069 processing costs. Additionally, the size of a cavity experiment is directly proportional to  
2070 the wavelength, since this sets the physical dimensions of the cavity. It is also simpler to  
2071 engineer a magnet that provides a uniform magnetic field across several cubic-meters of  
2072 space at lower magnetic fields, which provides advantages in terms of cost-reduction.

2073 A concern with lower magnetic fields and frequencies is the power scaling as described  
2074 by the Larmour equation, in which power is proportional to the square of the frequency.  
2075 Naively, one would predict that the SNR would decrease with lower fields, however, two  
2076 additional scaling laws that affect the noise power also come into play. Noise power  
2077 is directly proportional to the required bandwidth, which decreases linearly with the  
2078 magnetic field. Furthermore, at lower frequencies it is possible to purchase amplifiers with  
2079 lower noise temperatures until approximately 300 MHz, at which point this relationship  
2080 tends to flatten. Therefore, it is expected that the SNR remains approximately constant  
2081 as the frequency decreases.

2082 The facts that large-volume experiments are simpler to achieve at lower frequencies  
 2083 and SNR is expected to be approximately the same together motivate the usage of lower  
 2084 magnetic fields in the large-scale experiments. This is simply because a low-frequency  
 2085 experiment is less costly than a high-frequency experiment and there is little to no penalty  
 2086 in SNR or detection efficiency at these fields.

2087 One drawback of lower magnetic fields is the increased influence of external magnetic  
 2088 fields on the experiment. This includes magnetic fields from the building materials as well  
 2089 as variations in the earth's magnetic field. A suitable magnetic field correction system  
 2090 will need to be devised to deal with these effects, which includes constant monitoring of  
 2091 external fields.

## 2092 Atomic Tritium Considerations

2093 The pilot-scale experiments will be the first Project 8 experiments to combine CRES with  
 2094 atomic tritium, therefore, the optimal frequency should take into account the affect of the  
 background magnetic field on the atom trap. The primary influence of the background

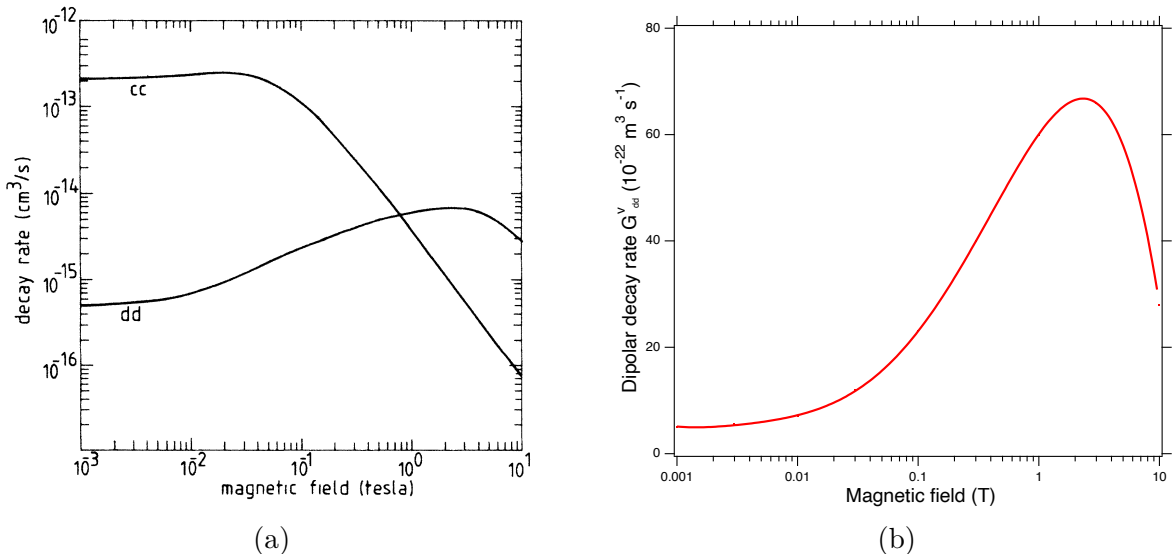


**Figure 3.18.** (a) A plot of the decay rate for the two-body dipolar spin exchange interaction for cc and dd state. (b) A plot of the decay rate of the dipolar spin exchange interaction for d+d states as a function of magnetic field magnitude. Lowering the magnetic field is key for reducing the losses from this interaction.

2095 field magnitude is through the rate of dipolar spin-flips caused by a spin exchange  
 2096 interaction between trapped atoms [58].

2098 Atomic tritium is a simple quantum system with a hyperfine structure given by the  
 2099 addition of the nuclear and atomic spins. The addition of two spins leads to a hyperfine

structure with four states in the  $(m_s, m_I)$  basis [59]. The states with atomic spins directed anti-parallel to the magnetic field have  $m_s = -1/2$  and are labeled as the a and b states. The a and b states are colloquially known as high-field seeking states, since their energy is minimized when in regions of higher magnetic field. This leads to losses in the magnetic trap as these atoms are drawn to higher fields away from the trap center. Alternatively, the c and d states, with atomic spin  $m_s = +1/2$ , minimize their energy in low magnetic fields because of the parallel alignment between spin and the magnetic field. Therefore, these low-field seeking states tend to stay trapped significantly longer than the high-field seeking states.

It would be advantageous to prepare tritium atoms in purely c and d states before trapping, however, even in this case losses still occur due to dipolar interactions between pairs of c and d states leading to flipped atomic spins and subsequent losses from high-field seeking atoms. The rate of these interactions depends on the magnitude of the background magnetic field and is maximal for dd interactions around 1 T (see Figure 3.18). The rate of losses from these interactions at 1 T requires atomic tritium production at a rate two orders of magnitude larger than at 0.1 T, thus, requirements on the whole atomic tritium system are significantly relaxed at lower magnetic fields, which provides powerful argument for moving to lower frequencies with the pilot-scale experiments and Phase IV.

### 3.5.2 Pilot-scale Experiment Concepts

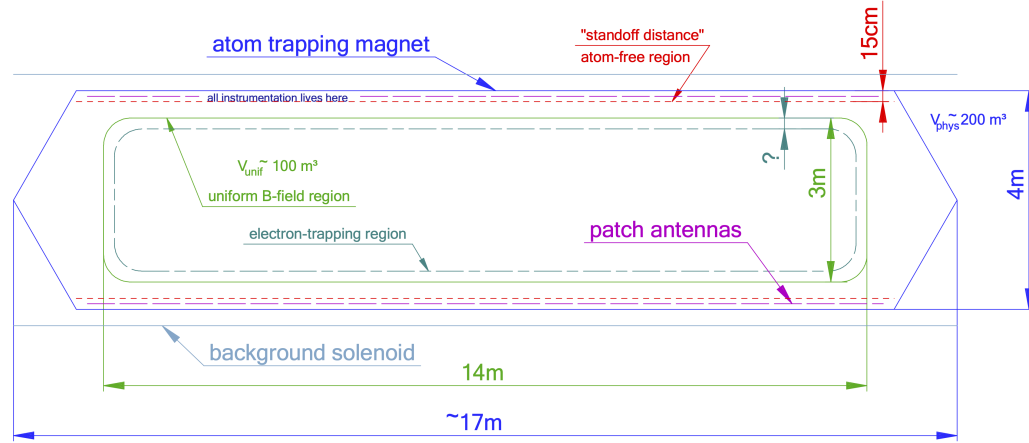


**Figure 3.19.** A conceptual sketch of a large-volume antenna array based CRES experiment to measure the neutrino mass.

While the pilot-scale experiments are still in the early stages, enough is known to

2121 sketch the general features of these experiments at the conceptual level. Development of  
2122 the antenna-based experiment has been suspended in favor of the cavity-based experiment.

### 2123 **Pilot-scale Antenna Array CRES Experiment Concept**

2124 A conceptual design for an antenna-based CRES experiment is shown in Figure 3.19. A  
2125 large solenoid magnet provides a uniform background magnetic field less than 0.1 T in  
2126 magnitude. Inside this region is the atom trapping magnet that generates a high magnetic  
2127 field at the walls, which decays exponentially towards the central region. Known magnet  
2128 designs that produce suitable atom trapping fields include Ioffe-Pritchard traps [60],  
2129 which use conducting coils, as well as a Halbach array [61] made from permanent magnets.  
2130 Either magnet choice produces a region of high magnetic fields, which excludes atoms  
2131 and allows for the placement of antennas inside the experiment.

2132 Inside this region an array of microstrip patch antennas is inserted to collect the  
2133 cyclotron radiation without providing a surface for atomic tritium recombination. Due  
2134 to the lower frequency of cyclotron radiation antennas of a larger size can be used,  
2135 which lowers the total number of antennas required to observe the experiment volume.  
2136 Because of this scaling, the lower frequency experiment uses a similar number of antennas  
2137 compared to a much smaller demonstrator experiment with a 1 T magnetic field.

2138 The atomic tritium beamline that supplies fresh tritium atoms to the experiment is  
2139 not shown in the figure. The general configuration would matches the one shown for the  
2140 pilot-scale cavity experiment (see Figure 3.20).

### 2141 **Pilot-scale Cavity CRES Experiment Concept**

2142 The pilot-scale cavity experiment includes both an atomic tritium system and cavity  
2143 CRES system. The atomic system consists of a thermal atom cracker located at the  
2144 start of an evaporatively cooled atomic beamline. The atomic tritium system provides a  
2145 supply of tritium atoms to the trap with temperatures on the order of a few mK. Atoms  
2146 at this temperature can be trapped magneto-gravitationally, which is the reason for the  
2147 vertical orientation of the cavity. At these low magnetic fields the trapping requirements  
2148 for electrons and atoms differ enough such that it is advantageous to decouple the the  
2149 trapping potentials to avoid radioactive heating of the tritium atoms from excess trapped  
2150 electrons. Electron trapping is provided by a set of magnetic pinch coils at the top and  
2151 bottom of the cavity and a multi-pole Ioffe or Halbach magnet serves to contain the  
2152 atoms.

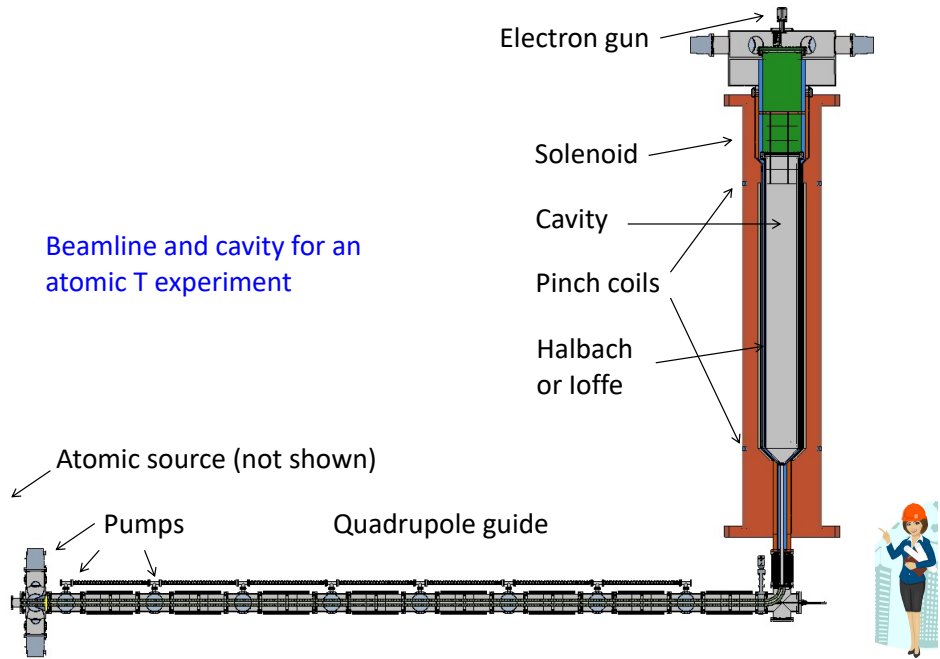


**Figure 3.20.** A conceptual sketch of a pilot-scale cavity CRES experiment with an atomic tritium beamline.

2153      The cavity design for the pilot-scale experiment consists of a large cylindrical cavity  
 2154     with a TE011 resonance of 325 MHz. Such a cavity is truly enormous, with a diameter of  
 2155     approximately 1.2 m and a height of 11 m. When an electron is produced inside the cavity  
 2156     with a cyclotron frequency that matches the TE011 resonant frequency, its cyclotron  
 2157     orbit couples the electron to the TE011 mode, which drives a resonance in the cavity.  
 2158     These resonant fields can be read-out using an appropriate cavity coupling mechanism  
 2159     located at the center of the cavity. For more information on the cavity approach to  
 2160     CRES see Chapter 6.

2161      The bottom of the cavity has a cone termination to match the contour of the atom  
 2162     trapping magnet. This shape still allows for TE011 resonances with high internal Qs,  
 2163     which are required for good SNR in the cavity experiment. A small opening in the bottom  
 2164     of the cone serves as an entry point for the tritium atoms. To allow for calibration of  
 2165     the magnetic field inhomogeneities with an electron gun, the top of the cavity is left  
 2166     nearly completely open. Normally, this would drastically lower the Q-factor of the TE011  
 2167     mode, but a specially configured coaxial partition is inserted at the top. This termination  
 2168     scheme is designed to act as a perfect short for the TE011 mode since the circular shape  
 2169     of the partition matches the electric field boundary conditions for the TE011 mode.  
 2170     Simulations with HFSS have confirmed that this design results in a high quality TE011

<sup>2171</sup> resonance despite the nearly completely open end.

## <sup>2172</sup> 3.6 Phase IV

<sup>2173</sup> The baseline CRES technology being pursued by Project 8 are resonant cavities, which,  
<sup>2174</sup> due to their geometric properties, simple CRES signal structure, and low channel  
<sup>2175</sup> count, appear to be the better option for Phase IV. The current knowledge of the  
<sup>2176</sup> antenna array CRES approach reveals no technical obstacles that would preclude it  
<sup>2177</sup> as a baseline technology for Phase IV, though it would certainly be significantly more  
<sup>2178</sup> expensive. Therefore, antenna arrays represent a fallback approach if resonant cavities  
<sup>2179</sup> prove infeasible.

<sup>2180</sup> The sensitivity of the pilot-scale atomic tritium experiment is estimated to be on  
<sup>2181</sup> the order of 0.1 eV, which means that increasing the sensitivity to reach the Phase IV  
<sup>2182</sup> goal will require an even larger experiment. Because of the direct coupling between the  
<sup>2183</sup> RF characteristics of a cavity and its geometry, the baseline plan is to build multiple  
<sup>2184</sup> copies of the pilot-scale experiment (see Figure 3.21) to obtain the required amount of  
<sup>2185</sup> volume rather than increase the size of the cavity beyond the pilot-scale. The built-in  
<sup>2186</sup> redundancy of this approach is useful in the sense that the experiment has no single  
<sup>2187</sup> point of failure, additionally, building several copies of the a pilot-scale experiment will  
<sup>2188</sup> minimize new engineering and design effort.

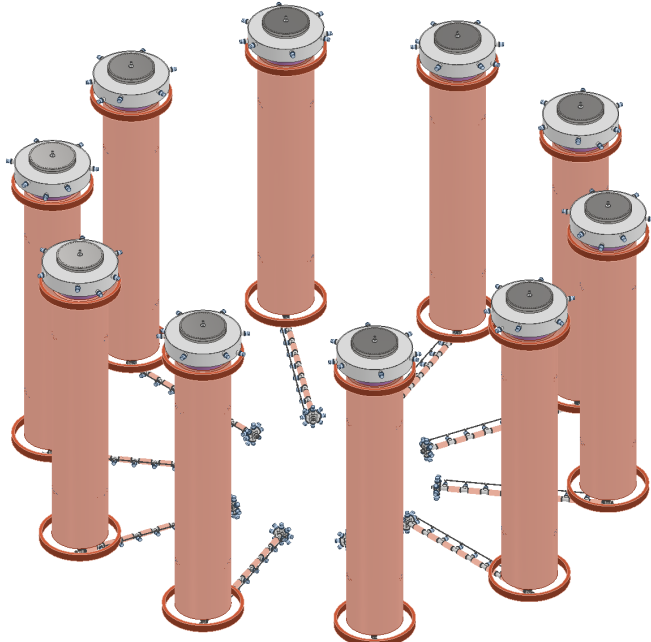


**Figure 3.21.** An illustration of a possible arrangement of ten pilot-scale cavity experiments for Phase IV. The experiments are arranged in a circle with an approximate diameter of 50 meters. Each atomic beamline connected to the bottom of each cavity is approximately 10 m in length. The cavities themselves are designed to operate at 325 MHz and are approximately 11 m tall. The circular arrangement of cavities has some advantages when it comes to cancellation of fringe fields from neighboring magnets, which is important due to the small magnetic field magnitudes consistent with these CRES frequencies. The advantage of ten independent atomic sources and cavities is that there is no single point of failure for the experiment. If an experiment goes down for repairs the other nine may continue running. Figure courtesy of Michael Huehn at UW-Seattle.

## **Chapter 4**

# **Signal Reconstruction Techniques for Antenna Array CRES and the FSCD**

### **4.1 Introduction**

An antenna array CRES (Cyclotron Radiation Emission Spectroscopy) experiment introduces new challenges related to data acquisition, signal detection, and signal reconstruction caused by the multi-channel nature of the data. The development of signal reconstruction algorithms [62] is crucial for the design of antenna array based experiments like the FSCD (Free Space CRES Demonstrator, described in Section 3.4.2), because these algorithms directly influence the detection efficiency and energy resolution of the CRES experiment. In this Chapter I summarize my contributions to the development and analysis of signal reconstruction and detection algorithms for the FSCD experiment.

In Section 4.2 I discuss the primary tool for this work, which is the Locust simulations package developed by the Project 8 experiment. Locust is used to simulate CRES events in the detector, which begins with calling a second software package — Kassiopeia — to calculate particle trajectory solutions for electrons in the magnetic trap. The trajectories are subsequently used to calculate the response of the antenna array to the cyclotron radiation produced by the electron, which results in signals that can be used to analyze the performance of different signal reconstruction algorithms. More recently, Project 8 has developed CREsana, which is a new simulations package that takes an analytical approach to CRES signal simulations. Although CREsana signals were not used for the signal reconstruction algorithm development, I introduce the software as it is the simulation software used to model the antenna array measurements presented in Section 5.4 in the next chapter.

In Section 4.3 I discuss the signal reconstruction and detection approaches analyzed for the FSCD experiment. In general there are two steps to signal reconstruction — detection

and parameter estimation. With signal detection one is concerned with distinguishing between data that contains a signal versus data that contains only noise; whereas, with parameter estimation one extracts the kinematic parameters of the electron encoded in the cyclotron radiation signal shape. Due to the low signal power of electrons near the spectrum endpoint in the FSCD experiment, signal detection is a non-trivial problem. This is magnified by the need to maximize the detection efficiency of the experiment in order to achieve the neutrino mass sensitivity goals. My contributions to signal reconstruction analyses for the FSCD are focused on the signal detection component of reconstruction.

After discussing various signal detection approaches, in Section 4.4 I present a detailed analysis of the detection performance of three algorithms, which could be used to signal detection in the FSCD. This section was prepared for publication in JINST as a separate paper. The algorithms include a digital beamforming algorithm, a matched filter algorithm, and a neural network algorithm, which I analyze in terms of classification accuracy and estimated computational cost.

## 4.2 FSCD Simulations

Antenna array CRES and the FSCD require a combination of different capabilities not often found in a single simulation tool. In particular, accurate calculations of the magneto-static fields produced by current-carrying coils are needed to accurately model the magnetic trap and background magnets. The resulting magnetic fields must then be used to calculate the exact relativistic trajectory of electrons. The electron trajectories are required to calculate the electro-magnetic (EM) fields produced by the acceleration of the electron. Finally, the simulation must model the interaction of the antenna and RF (radio-frequency) receiver chain with the EM-fields in order to yield the simulated voltage signals from the antenna array. No available simulation tools adequately perform these combined functions; therefore, Project 8 developed a custom simulation framework to simulate the FSCD and CRES. This simulation framework includes custom simulation tools developed by Project 8, as well as open-source and proprietary software developed by third-parties.

### 2244 4.2.1 Kassiopeia

2245 Kassiopeia<sup>1</sup> is a particle tracking and static EM-field solver developed by the KATRIN  
2246 collaboration for simulations of their spectrometer based on the MAC-E (magnetic  
2247 adiabatic collimation with electrostatic) filter technique [63]. Unfortunately, Kassiopeia is  
2248 not designed to solve for the EM-fields radiated by electrons in magnetic fields. However,  
2249 it does provide efficient solvers for static electric and magnetic fields and charged particle  
2250 trajectory solvers. Because of this, Project 8 has incorporated parts of Kassiopeia into  
2251 the Locust simulation framework.

### 2252 Magnetostatic Field Solutions

2253 The solutions to the electric and magnetic fields generated by a static configuration of  
2254 charges and currents is given by Maxwell's equations in the limit where the time-dependent  
2255 terms go to zero. In their static form Maxwell's equations [49] are

$$\nabla \cdot \mathbf{E} = \frac{\rho}{\epsilon_0} \quad (4.1)$$

$$\nabla \times \mathbf{E} = 0 \quad (4.2)$$

$$\nabla \cdot \mathbf{B} = 0 \quad (4.3)$$

$$\nabla \times \mathbf{B} = \mu_0 \mathbf{J}, \quad (4.4)$$

2256 where it can be seen that the electric and magnetic fields are completely decoupled from  
2257 one another. The solution for the magnetic field in this boundary value problem is given  
2258 by the Biot-Savart law

$$\mathbf{B}(\mathbf{r}) = \frac{\mu_0}{4\pi} \int dr' \frac{r'^3 \mathbf{J}(\mathbf{r}') \times (\mathbf{r} - \mathbf{r}')}{|\mathbf{r}' - \mathbf{r}|^3}, \quad (4.5)$$

2259 which Kassiopeia can use a variety of numeric integration techniques to solve for a  
2260 particular current distribution.

### 2261 Kassiopeia Simulation of the FSCD Magnetic Trap

2262 The trap developed for the FSCD experiment utilizes six current carrying coils, which  
2263 surround a cylindrical tritium containment vessel (see Figure 4.1). Some important  
2264 aspects of the trap design include the total trapping volume, the maximum trap depth,

---

<sup>1</sup><https://github.com/KATRIN-Experiment/Kassiopeia>

the steepness of the trap walls, as well as the radial and azimuthal uniformity of the magnetic fields.

The volume of the FSCD trap is a cylindrically shaped region with a radius of 5 cm and a length of 15 cm resulting in a roughly 1 L total trap volume. The trap volume is an important design feature, because it sets the volume of the experiment that is potentially usable for CRES measurements. Trapping a larger volume allows one to observe a larger number of tritium atoms, which increases the statistical power and sensitivity of the neutrino mass measurement. Due to the cost of constructing magnets with large and uniform magnetic fields it is important that the trap use as much of the available volume as possible to limit the overall cost of the experiment.

Coil	Radius (mm)	Z Pos. (mm)	Current (Amp. $\times$ Turns)
1	50.0	-92.3	750.0
2	50.1	-56.9	-220.3
3	68.5	-19.5	-250.0
4	68.5	19.5	-250.0
5	50.1	56.9	-220.3
6	50.0	92.3	750.0

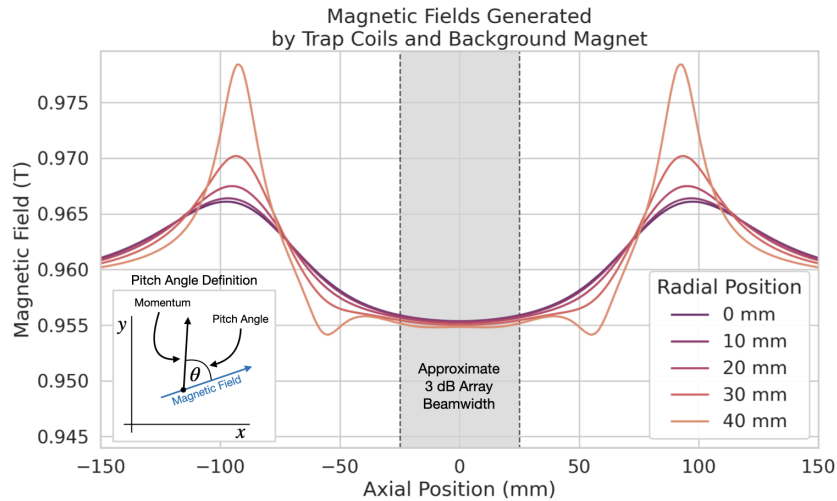
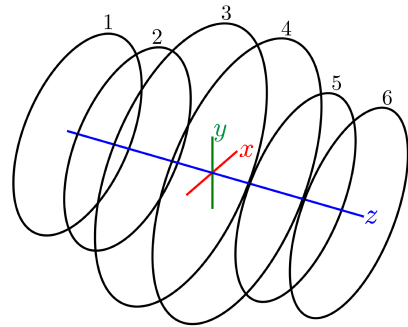


**Figure 4.1.** The geometry and parameters of the coils used to simulate the FSCD magnetic trap in Kassiopeia. Some axial profiles of the magnetic trap at different radial positions are shown to demonstrate the shape of the magnetic field and trap depth as a function of position. Calculation of the magnetic field profiles was graciously done by René Reimann.

The depth of the FSCD trap is approximately 10 mT when measured along the central axis, which is sufficient to trap electrons with pitch angles as small as 84°. The trap depth influences the efficiency of the experiment by directly controlling the range of

2278 electron pitch angles that can be trapped. If a higher fraction of pitch angles are trapped,  
2279 in principle, more decay events can be observed. However, the signals from electrons  
2280 with small pitch angles are significantly harder to detect in the FSCD than large pitch  
2281 angles, which increases the likelihood of not detecting the first track of the CRES event  
2282 and harms the energy resolution of the experiment.

2283 The steepness of the trap walls as well as non-uniformities in the magnetic field  
2284 contribute to the total energy resolution of the CRES measurement by causing uncertainty  
2285 in the relationship between an electron's kinetic energy and its cyclotron frequency. When  
2286 an electron is trapped, it oscillates back and forth along the trap z-axis (see Figure 4.1)  
2287 unless it has a pitch angle of exactly 90° [64]. As the electron is reflected from the trap  
2288 walls it experiences a change in the total magnetic field, which causes a modulation in the  
2289 cyclotron frequency. This change in magnetic field from the trap introduces a correlation  
2290 between the pitch angle and kinetic energy parameters of the electron that can reduce  
2291 energy resolution. In order to mitigate this effect it is important to make the trap walls  
2292 as steep as possible.

## 2293 Particle Trajectory Solutions

2294 The magnetic fields solved by direct integration of the coil current densities are used to  
2295 calculate the trajectories of electrons based on user specified initial conditions. Various  
2296 statistical distributions are available, which can be sampled to replicate realistic event  
2297 statistics. These include uniform, Gaussian, and Lorentzian distributions among others.  
2298 In general, an electron has six kinematic parameters that define its trajectory, which are  
2299 the three-dimensional coordinates of the initial position and the three components of the  
2300 electron's momentum vector. However, when simulating CRES events it is common to  
2301 parameterize the electron's trajectory in terms of the initial position, kinetic energy, pitch  
2302 angle, and initial direction of the component of the electron's momentum perpendicular  
2303 to the magnetic field. This parameterization is completely equivalent to specifying the  
2304 starting position and momentum vectors.

2305 From the initial parameters of the electron and the magnetic field, Kassiopeia solves  
2306 for the trajectory of the electron. The direct approach proceeds by solving the motion of  
2307 the electron using the Lorentz force equation, which takes the form of a set of differential  
2308 equations

$$\frac{d\mathbf{r}}{dt} = \frac{\mathbf{p}}{\gamma m} \quad (4.6)$$

$$\frac{d\mathbf{p}}{dt} = e(\mathbf{E} + \frac{\mathbf{p} \times \mathbf{B}}{\gamma m}), \quad (4.7)$$

where  $\mathbf{r}$  is the position of the electron,  $\mathbf{p}$  is the electron's momentum,  $e$  is the charge of the electron,  $m$  is the electron's mass, and  $\gamma$  is the relativistic Lorentz term. Kassiopeia solves this pair of differential equations using numerical integration, however, the exact trajectory can be computationally intensive to solve. If the adiabatic approximation can be applied, then Kassiopeia can make use of a simpler set of equations that can be more readily solved numerically.

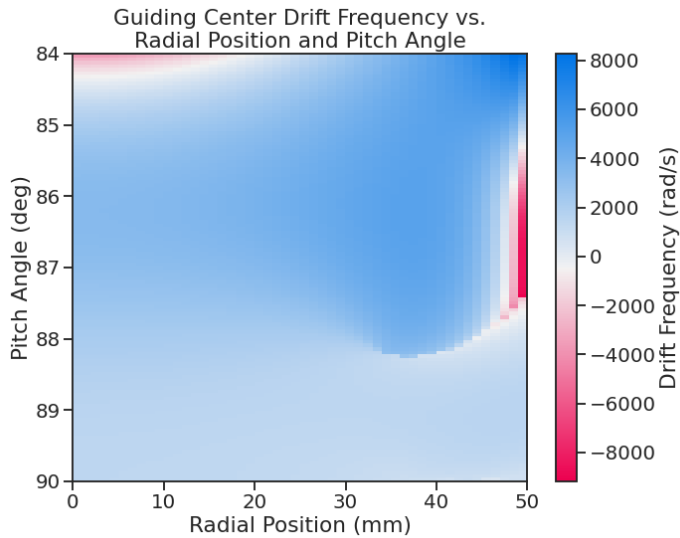


**Figure 4.2.** A map of the average  $\nabla B$ -drift frequency for electrons trapped in the prototype FSCD trap shown in Figure 4.1. Negative drift frequencies indicate electrons that are drifting opposite to the standard direction, which means that they are close to escaping the magnetic trap.

Though Kassiopeia is not directly capable of simulating the cyclotron radiation, it is an invaluable CRES simulation tool. With Kassiopeia it is possible to test the efficiency of a particular trap design, and analyze features of the electron trajectories that are important to the position, track, and event reconstruction (see Section 4.3). An example is the analysis of the average  $\nabla B$ -drift frequency as a function of the electrons radial position and pitch angle in the FSCD trap (see Figure 4.2). Radial gradients in the trap cause the guiding center of the electron to drift around the center of the magnetic trap with an average frequency on the order of  $10^3$  rad/s. This frequency, while slow compared to the length of a typical CRES time-slice, is large enough to cause a significant loss in efficiency of certain signal reconstruction algorithms. Therefore, it is important to model

2325 the drift of the electron in the reconstruction algorithm in order to mitigate the effects  
2326 of this motion on the reconstruction.

## 2327 4.2.2 Locust

2328 The Locust<sup>2</sup> software package [65] is the primary simulation tool developed and used  
2329 by the Project 8 collaboration for CRES experiments. Locust simulates the responses  
2330 of antennas and receiver electronics chain to rapidly time-varying electric fields using  
2331 a flexible approach that allows one to choose from a variety of electric field sources  
2332 and antennas. Similarly, one can simulate the receiver chain using a series of modular  
2333 generators that include standard signal processing operations such as down-mixing and  
2334 fast Fourier transforms (FFT). Since the primary focus of this chapter is the application  
2335 of Locust to analyses of the FSCD, I shall describe only the most relevant aspects of the  
2336 software rather than provide a comprehensive description.

## 2337 Cyclotron Radiation Field Solutions

2338 Simulating CRES events in the FSCD requires one to calculate the electric fields produced  
2339 by the acceleration of the electron. In the general case, this can be a complicated  
2340 computation, due to back-reaction forces on the electron. However, in the case of the  
2341 FSCD it is possible to ignore such effects and approximate the electron as radiating into  
2342 a free-space environment.

2343 The equations that describe the EM fields from a relativistic moving point particle  
2344 are the Liénard-Wiechert equations [66, 67], which are obtained by differentiating the  
2345 Liénard-Wiechert potentials. In their full form, the Liénard-Wiechert field equations are

$$\mathbf{E} = e \left[ \frac{\hat{n} - \boldsymbol{\beta}}{\gamma^2(1 - \boldsymbol{\beta} \cdot \hat{n})^3 |\mathbf{R}|^2} \right]_{t_r} + \frac{e}{c} \left[ \frac{\hat{n} \times [(\hat{n} - \boldsymbol{\beta}) \times \dot{\boldsymbol{\beta}}]}{(1 - \boldsymbol{\beta} \cdot \hat{n})^3 |\mathbf{R}|} \right]_{t_r} \quad (4.8)$$

$$\mathbf{B} = [\hat{n} \times \mathbf{E}]_{t_r}, \quad (4.9)$$

2346 where  $e$  is the charge of the particle,  $\hat{n}$  is the unit vector pointing from the particle to  
2347 the position where the fields are calculated,  $\boldsymbol{\beta}$  and  $\dot{\boldsymbol{\beta}}$  are the velocity and acceleration  
2348 of the particle divided by the speed of light ( $c$ ),  $\mathbf{R}$  is the distance from the particle to  
2349 the field calculation position, and  $\gamma$  is the relativistic Lorentz term. The subscript  $t_r$   
2350 indicates that the equations are evaluated at the retarded time so that the time-delay  
2351 from the travel time of the electromagnetic radiation is taken into account.

---

<sup>2</sup>[https://github.com/project8/locust\\_mc/tree/master](https://github.com/project8/locust_mc/tree/master)

2352        The only required input to calculate the electric field at the position of an FSCD  
 2353      antenna is the velocity and acceleration of the electron, which can be obtained from  
 2354      Kassiopeia simulations. Therefore, when simulating a CRES event Locust first runs  
 2355      a Kassiopeia simulation of the electron and subsequently calculates the electric field  
 2356      incident on the antenna. This requires one to calculate the retarded time. The retarded  
 2357      time corresponds to the time that a photon, which has just arrived at an antenna at  
 2358      the space-time position  $(t, \mathbf{r})$ , was actually emitted by the electron at the space-time  
 2359      position of  $(t_r, \mathbf{r}_e(t_r))$ . To calculate the retarded time one solves

$$c(t - t_r) = |\mathbf{r} - \mathbf{r}_e(t_r)|, \quad (4.10)$$

2360      where the distance traveled by the photon between the measurement and retarded times  
 2361      is equal to the distance between the antenna and the electron at the retarded time.  
 2362      Locust solves Equation 4.10 using root finding algorithm to calculate the retarded time,  
 2363      which yields the electric field emitted by the electron, at the position of each antenna in  
 2364      the FSCD array.

### 2365      Antenna Response Modeling

2366      The electric field solutions are used to calculate the resulting voltages produced in the  
 2367      antenna. However, direct simulation of the antenna itself is computationally expensive,  
 2368      since it requires modeling the complex interactions of the electron's electric fields with  
 2369      charge carriers in the antenna. Direct simulation of the antenna in Locust is avoided by  
 2370      modeling the antenna response using the antenna factor, or antenna transfer function.  
 2371      The antenna factor defines the voltage produced in the antenna terminal for an incident  
 2372      electric field [68],

$$A_F = \frac{V}{|\mathbf{E}|}, \quad (4.11)$$

2373      where  $V$  is the voltage and  $|\mathbf{E}|$  is the magnitude of the incident electric field. To obtain the  
 2374      antenna factor for the antennas developed for the FSCD Project 8 employs Ansys HFSS.  
 2375      HFSS is a commercially available finite element method electromagnetic solver widely  
 2376      used throughout the antenna engineering industry [69]. HFSS is capable of calculating  
 2377      the antenna factor and gain patterns for complex antenna designs and outputting the  
 2378      resulting quantities in the form of a text file that can be used as a configuration input to  
 2379      Locust.

2380      The antenna factor defines the steady-state response of the antenna to electromagnetic

2381 plane waves in the frequency-domain. Since the antenna response is calculated in the  
 2382 time-domain Locust models the antenna as a linear time-invariant system [70]. In this  
 2383 formalism the response of the system to the driving force is given by

$$y[n] = h * x = \sum_k h[k]x[n - k], \quad (4.12)$$

2384 where  $y[n]$  is the discretely sampled response,  $x$  is the driving force stimulus, and  $h$  is  
 2385 the finite impulse response (FIR) filter. When applied to the FSCD array, this formalism  
 2386 calculates the voltage time-series produced in each antenna by convolving the electric  
 2387 field time-series with the antenna FIR filter, which is obtained by performing an inverse  
 2388 Fourier transform on the transfer function from HFSS.

### 2389 Radio-frequency Receiver and Signal Processing

2390 After obtaining the voltage time-series by computing the electron trajectory and antenna  
 2391 response, Locust simulates the signal processing performed by the RF receiver chain.  
 2392 The simulated Locust receiver chain includes all operations that would be performed by  
 2393 the RF hardware (see Figure 4.3).

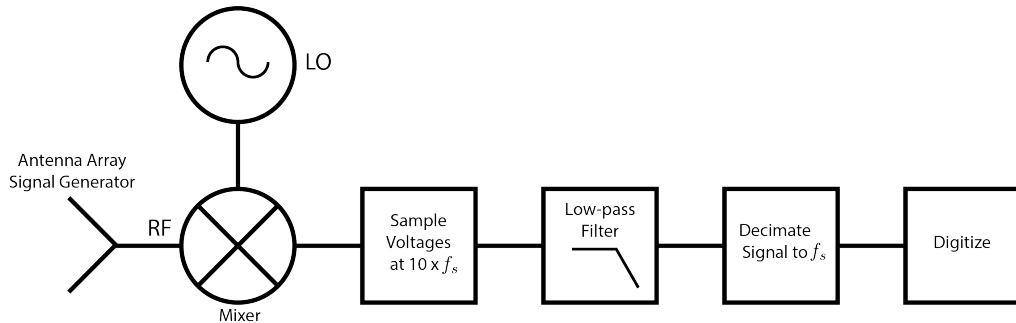


**Figure 4.3.** The receiver chain used by Locust when simulating CRES events in the FSCD.

2394 Frequency down-conversion reduces the digitization bandwidth required to read-out  
 2395 CRES data. According to the Nyquist sampling theorem [71], the minimal sampling rate  
 2396 that guarantees no information loss for a signal with a bandwidth  $\Delta f$  is given by

$$f_{\text{Nyq}} = 2\Delta f. \quad (4.13)$$

2397 The total bandwidth for CRES events ranges from 0 to 26 GHz in a 0.95 T magnetic field;  
 2398 therefore, direct digitization of CRES signals from the FSCD would require sampling  
 2399 frequencies greater than 50 GHz, which is infeasible for a real experiment. However, one

2400 need only measure the shape of the spectrum in the last 100 eV, which corresponds to a  
2401 frequency bandwidth of 5 MHz, to effectively measure the neutrino mass.

2402 Down-conversion is a technique for reducing the base frequencies of signals in a  
2403 bandwidth given by  $[f_{\text{LO}}, f_{\text{LO}} + \Delta f]$  to the bandwidth  $[0, \Delta f]$ , by performing the following  
2404 multiplication

$$x(t) \rightarrow x(t)e^{-2\pi f_{\text{LO}} t}. \quad (4.14)$$

2405 The signal,  $x(t)$ , is multiplied by a sinusoidal signal with frequency  $f_{\text{LO}}$  to reduce the  
2406 absolute frequencies of the signals in the bandwidth. In the FSCD, this allows one to  
2407 detect events in the last 100 eV of the tritium spectrum, while sampling the data far  
2408 below 50 GHz. The standard bandwidth used in the FSCD is 200 MHz, which allows for  
2409 higher frequency resolution than the minimum sampling frequency for 100 eV of energy  
2410 bandwidth.

2411 Directly simulating down-conversion with a frequency multiplication in Locust requires  
2412 sampling the electric fields at each antenna in the FSCD array with a period of  $\approx 20$  ps,  
2413 which is extremely slow computationally. To avoid this, Locust performs the down-  
2414 conversion by intentionally under-sampling the electric fields with a frequency of 2 GHz.  
2415 Sampling below the Nyquist limit causes the higher frequency components of the CRES  
2416 signal to alias, however, Locust can remove these aliased frequency peaks using a  
2417 combination of low-pass filtering and decimation to recreate frequency down-conversion.  
2418 After filtering and decimation, Locust simulates digitization by an 8-bit digitizer at a  
2419 sampling frequency of 200 MHz to recreate the conditions of the FSCD. The voltage  
2420 offset and digitizer range must be configured by the user based on the characteristics of  
2421 the simulation.

## 2422 Data

2423 The output of Locust simulations for the FSCD primarily consists of two data files. The  
2424 first is the electron trajectory information calculated by Kassiopiea, which is output in  
2425 the form of a `.root` file [72]. This file contains important kinematic information about  
2426 the electron such as its position and pitch angle as a function of time. The other file  
2427 is produced by Locust and contains the digitized signals acquired from each antenna  
2428 in the array. The Locust output files conform to the Monarch specification<sup>3</sup> developed  
2429 by Project 8, which is based on the commonly used HDF5 file format, and matches the  
2430 format of the files produced by the Project 8 data acquisition software. This makes it

---

<sup>3</sup><https://github.com/project8/monarch>

2431 possible to use the same data analysis code to analyze both simulated and real data.

### 2432 4.2.3 CRESana

2433 Locust is the primary simulation tool used by Project 8 in the development and simulation  
2434 of the FSCD. However, simulations of CRES events in larger antenna arrays ( $\geq 100$   
2435 antennas) can take several hours to complete, which is prohibitively long when one is  
2436 performing a sensitivity analysis and optimization. One reason for Locust's slow operation  
2437 is that the electric fields from the electron must be solved numerically for each time-step  
2438 for all antennas in the array. These numerical solutions allow Locust to accurately  
2439 simulate the electric fields from arbitrarily complicated electron trajectories at the cost  
2440 of more computations and slower simulations. Therefore, an additional simulation tool  
2441 that sacrifices the accuracy of numerical approaches for computational efficiency is a  
2442 useful tool for studying large antenna array experiments.

2443 Recently, Project 8 has developed a new simulations package called CRESana<sup>4</sup>, specif-  
2444 ically designed to perform analytical simulations of antenna-based CRES experiments.  
2445 CRESana provides a significant increase in simulation speed by using well-justified an-  
2446 alytical approximations of the electrons motion and electric fields in a magnetic trap.  
2447 The electric fields and signals generated by CRESana are consistent with theoretical  
2448 calculations of the electron's radiation, and are tested for accuracy using well-known  
2449 test-case simulations and consistency checks.

## 2450 4.3 Signal Detection and Reconstruction Techniques for 2451 Antenna Array CRES

### 2452 Antenna Array CRES Signal Reconstruction

2453 Antenna array CRES requires one to use the multichannel time-series obtained by  
2454 digitizing the array to estimate the starting kinetic energies of electrons produced in  
2455 the magnetic trap using CRES signal reconstruction algorithm. This procedure consists  
2456 of a multi-stage process of detecting a CRES signal followed by an estimation of the  
2457 electron's parameters.

2458 Antenna array CRES requires a significantly different approach to signal reconstruction  
2459 than previous Project 8 experiments. In Phases I and II, CRES was performed using a

---

4<https://github.com/MCflowMace/CRESana>

2460 waveguide gas cell directly integrated into a waveguide transmission line. The transmission  
2461 line efficiently propagates the cyclotron radiation along its length to an antenna at the  
2462 ends of the waveguide. However, with an antenna array the electron is radiating into  
2463 free-space; therefore, the cyclotron radiation power collected by the array is directly  
2464 proportional to the solid angle surrounding the electron that is covered with antennas.  
2465 Because it is not practical to fully surround the magnetic trap with antennas, some of the  
2466 cyclotron radiation power that would have been collected by the waveguide escapes into  
2467 free-space. Furthermore, the power that is collected by the antenna array is split between  
2468 every channel in the antenna array, which significantly lowers the signal-to-noise ratio  
2469 (SNR) of CRES signals in a single antenna channel compared to a waveguide apparatus.  
2470 Therefore, a suite of completely new signal reconstruction techniques are needed in order  
2471 to perform CRES in the FSCD.

2472 Changes to the approach to CRES signal reconstruction are also motivated by the  
2473 scientific goals of Project 8. A measurement of the tritium beta-decay spectrum that is  
2474 sensitive to neutrino masses as small as 40 meV requires that we measure the kinetic  
2475 energies of individual electrons with a total energy broadening of 115 meV [73]. This  
2476 resolution includes all sources of uncertainty in the electron's kinetic energy such as  
2477 magnetic field inhomogeneities. This precise energy resolution is only achieved by an  
2478 event-by-event signal reconstruction approach where the kinetic energies, pitch angles,  
2479 and other parameters of the CRES events are estimated for individual electrons before  
2480 constructing the beta-decay spectrum.

2481 The event-by-event approach is distinct from the analysis done for the Phase I  
2482 and Phase II experiments, where the starting cyclotron frequency of the event was  
2483 measured by analyzing the tracks formed by the electron's carrier in a time-frequency  
2484 spectrogram. These frequencies were then combined into a frequency beta-spectrum,  
2485 which was converted to the beta-decay energy spectrum using an ensemble approach that  
2486 averaged over all other event parameters. The ensemble approach to signal reconstruction  
2487 results in poor energy resolution because other kinematic parameters such as pitch angle  
2488 change the cyclotron carrier frequency due to changes in the average magnetic field  
2489 experience by the electron.

## 2490 Components of Reconstruction: Signal Detection and Parameter Estimation

2491 CRES signal reconstruction is a two-step procedure consisting of signal detection followed  
2492 by parameter estimation. In the former, one is concerned with identifying CRES signals  
2493 in the data regardless of the signal parameters; whereas, in the latter one operates under

2494 the assumption that a signal is present and then estimates it's parameters.

2495 More formally, signal detection can be posed as a binary hypothesis test between  
2496 the signal and noise data classes, and parameter estimation is a process of fitting a  
2497 signal model to the observed data. While both of these are required for a complete  
2498 reconstruction (see Figure 4.4), the focus of my work and this chapter is on the signal  
2499 detection aspect of antenna array CRES signal reconstruction.

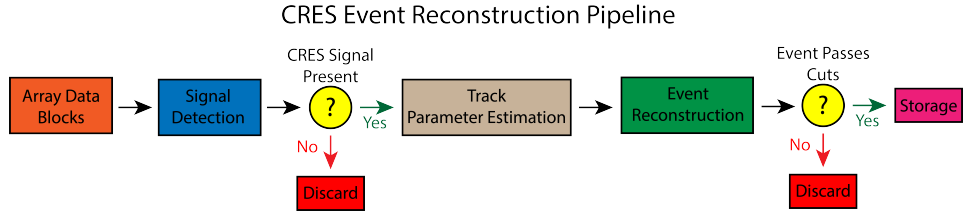


**Figure 4.4.** A high-level diagram depicting the process of CRES event reconstruction. The first step consists of identifying the presence of a signal in the data. This step is necessary to avoid the danger of performing a reconstruction of a false event, which would constitute a background contribution to the tritium spectrum measured by CRES.

## 2500 Detection Theory

2501 Signal detection is the process of deciding whether noisy data contains signal or noise,  
2502 which can be posed as a statistical hypothesis test [74]. For CRES signals, which are  
2503 represented by signal vectors with added white Gaussian noise (WGN), one needs to  
2504 choose between

$$\mathcal{H}_0 : \mathbf{y} = \boldsymbol{\nu} \quad (4.15)$$

$$\mathcal{H}_1 : \mathbf{y} = \mathbf{x} + \boldsymbol{\nu}, \quad (4.16)$$

2505 where  $\mathbf{y}$  is the CRES data vector,  $\boldsymbol{\nu}$  is a sample of WGN, and  $\mathbf{x}$  represents the CRES  
2506 signal. The hypothesis that the data contains only noise is labeled  $\mathcal{H}_0$  and the hypothesis  
2507 that the data contains a signal is labeled  $\mathcal{H}_1$ .

2508 For illustrative purposes, it is useful to study the case where only the first sample of  
2509 data is used to distinguish between  $\mathcal{H}_0$  and  $\mathcal{H}_1$ . The value of the first data sample is  
2510 distributed according to two possible Gaussian distributions(see Figure 4.5). By setting a  
2511 decision threshold on the value of this sample, one can choose the correct hypothesis with  
2512 a probability given by the area underneath the probability distribution curves. A true  
2513 positive corresponds to correctly identifying that the data contains signal; whereas, a true  
2514 negative means that one has correctly identified the data as noise. The rate at which the

2515 detector performs a true positive classification is given by the green region underneath  
 2516  $p(\mathbf{y}[0]; \mathcal{H}_0)$ , and the rate at which the detector performs a true negative classification is  
 given by the orange region underneath  $p(\mathbf{y}[0]; \mathcal{H}_1)$ . Two types of misclassifications are

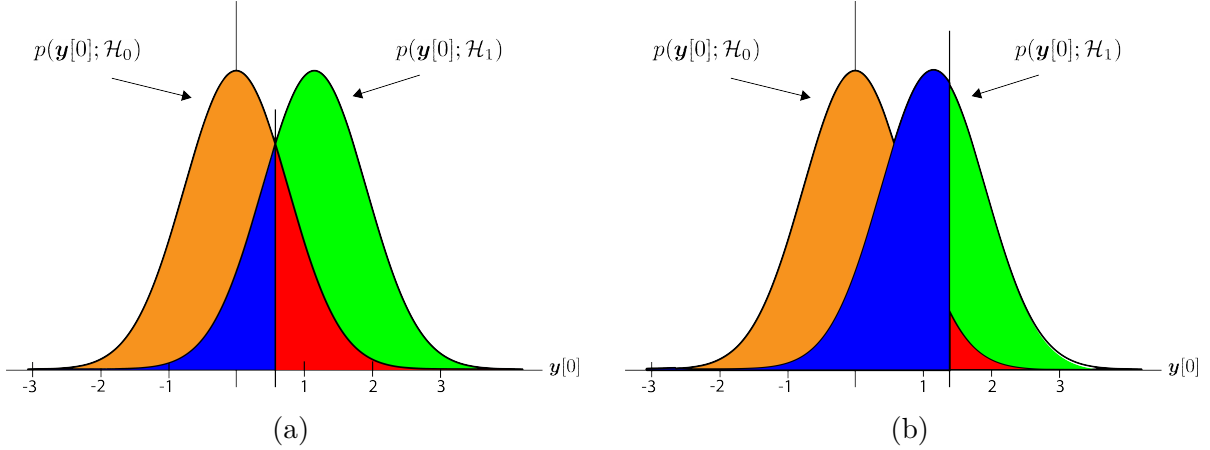


**Figure 4.5.** An illustration of two PDFs associated with a binary hypothesis test. The decision threshold is represented by the vertical line that partitions both distributions. The orange and red areas correspond to the true negative and false positive probabilities and the blue and green areas correspond to the false negative and true positive probabilities respectively. To decide between the two hypotheses the likelihood ratio test specified by the Neyman-Pearson theorem is applied. This approach achieves the highest true positive probability for a given false positive probability.

2517  
 2518 possible. Either one declares noise data as signal, which is called a false positive, or one  
 2519 declares signal data as noise, which is a false negative. Note that it is only possible to  
 2520 trade off these two types of errors by tuning the detection threshold. One cannot reduce  
 2521 the rate of false positives without also increasing the rate of false negatives.

2522 The approach taken with CRES signals is to fix the rate of false positives by setting  
 2523 a minimum decision threshold value. The rate of false positives that is acceptable at the  
 2524 detection stage depends upon the total rate of background events compatible with the  
 2525 sensitivity goals of the experiment. The ultimate goal of a neutrino mass measurement  
 2526 with 40 meV sensitivity in general has strict requirements on the number of background  
 2527 events, which requires a relatively high detection threshold to achieve. Consequently,  
 2528 the ideal signal detection algorithm is the one that achieves the maximum rate of true  
 2529 positives for a fixed rate of false positives, so that the detection efficiency of the experiment  
 2530 is maximized and potential sources of background are kept to a minimum.

2531 According to the Neyman-Pearson theorem [75], the statistical hypothesis test that  
 2532 maximizes the probability of detection for a fixed rate of false positives is the likelihood  
 2533 ratio test, which is formed by computing the ratio of the signal likelihood to the noise

2534 likelihood,

$$L(x) = \frac{P(\mathbf{y}; \mathcal{H}_1)}{P(\mathbf{y}; \mathcal{H}_0)} > \gamma. \quad (4.17)$$

2535 Here, the likelihood of the hypotheses  $\mathcal{H}_0$  and  $\mathcal{H}_1$  are described by the probability  
2536 distributions  $P(\mathbf{y}; \mathcal{H}_0)$  and  $P(\mathbf{y}; \mathcal{H}_1)$  respectively, and  $\gamma$  is the threshold for deciding  $\mathcal{H}_1$ .

2537 The decision threshold is determined by integrating  $P(\mathbf{y}; \mathcal{H}_0)$  such that

$$P_{FP} = \int_{\gamma}^{\infty} P(\tilde{\mathbf{y}}; \mathcal{H}_0) d\tilde{\mathbf{y}} = \alpha, \quad (4.18)$$

2538 where  $\alpha$  is the desired false positive detection rate given by the red colored areas shown  
2539 in Figure 4.5. The true positive detection rate is given by the similar integral

$$P_{TP} = \int_{\gamma}^{\infty} P(\tilde{\mathbf{y}}; \mathcal{H}_1) d\tilde{\mathbf{y}}, \quad (4.19)$$

2540 which corresponds to the green areas in Figure 4.5.

2541 Changing the decision threshold allows one to trade-off between  $P_{TP}$  and  $P_{FP}$  as  
2542 appropriate for the given situation. It is standard to summarize the relationship between  
2543  $P_{TP}$  and  $P_{FP}$  using the receiver operating characteristic (ROC) curve, which is obtained  
2544 by evaluating the true positive and false positive probabilities as a function of the decision  
threshold value (see Figure 4.6). The ROC curve provides a convenient way to compare

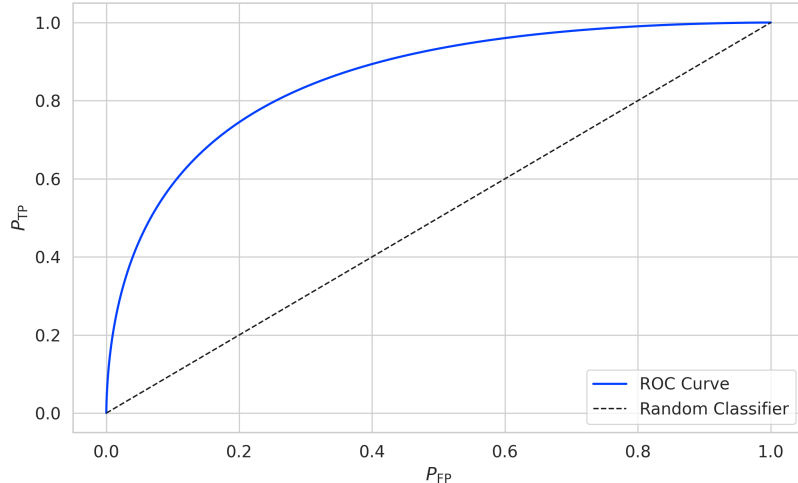


**Figure 4.6.** An example ROC curve formed by computing the  $P_{FP}$  and the  $P_{TP}$  for a given likelihood ratio test. As the decision threshold is increased  $P_{FP}$  decreases at the expense of a lower  $P_{TP}$ . The black dashed line indicates the lower bound ROC curve obtained by randomly deciding between  $\mathcal{H}_0$  and  $\mathcal{H}_1$ .

2545

2546 the performance of different signal detection algorithms. In general, a classifier with  
2547 a higher the  $P_{TP}$  as a function of  $P_{FP}$  is desirable, which corresponds to a larger area  
2548 underneath the respective ROC curve. A perfect classifier has an area underneath the  
2549 curve of 1.0, however, such a classifier is never achieved in practice.

### 2550 4.3.1 Digital Beamforming

#### 2551 Introduction to Beamforming

2552 Beamforming is an antenna array signal processing technique designed to enhance the  
2553 radiation of the array in a particular direction and suppress it in other directions [68].  
2554 Beamforming is of interest to Project 8 as a first level of signal reconstruction for the  
2555 FSCD and other antenna array CRES experiments, which operates at the signal detection  
2556 stage of reconstruction.

2557 Beamforming is performed using a phased summation of the signals received by the  
2558 antenna array. The beamforming phases are selected such that the signals emitted by  
2559 the array will constructively interfere at the point of interest (see Figure 4.7). As a  
2560 consequence of the principle of reciprocity [76], when the array is operating in receive  
2561 mode, the signals emitted from a source at the same point will constructively interfere  
2562 when summed. The origin of the phase delays in beamforming is the path-length difference  
2563 to the beamforming point between different antennas in the array. The relationship  
2564 between the phase delay and the path-length difference is given by the familiar equation

$$\phi = \frac{2\pi d}{\lambda}, \quad (4.20)$$

2565 where  $\phi$  is the phase delay,  $d$  is the path-length difference, and  $\lambda$  is the wavelength of  
2566 the radiation. In practice, one chooses the values of  $d$  by specifying the beamforming  
2567 positions of interest and then calculates the beamforming phases using Equation 4.20,  
2568 which is guaranteed to follow the constructive interference condition shown in Figure 4.7.

2569 Beamforming can be neatly expressed mathematically using the vector equation

$$y[n] = \Phi^T[n] \mathbf{x}[n], \quad (4.21)$$

2570 where  $\mathbf{x}[n]$  is the array snapshot vector,  $\Phi[n]$  is a vector of beamforming shifts, and  
2571  $y[n]$  is the resulting summed signal. The beamforming shifts consist of a set of complex

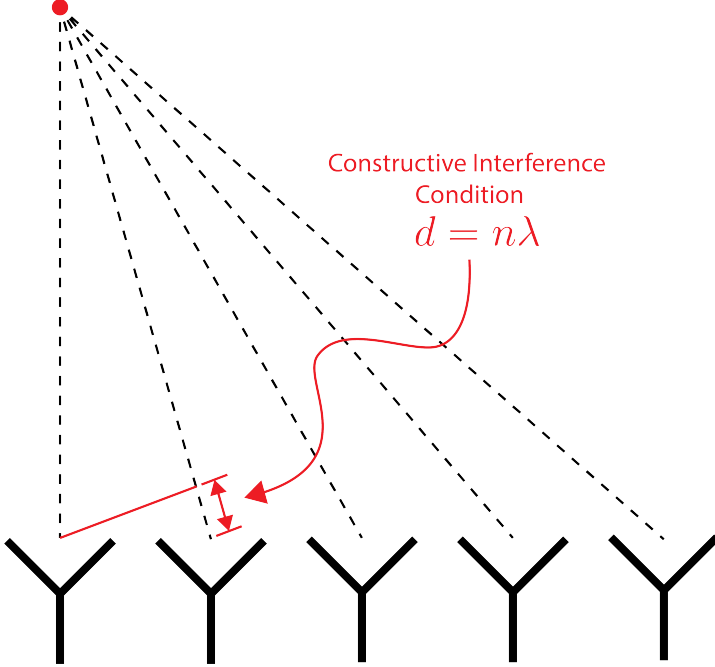


**Figure 4.7.** An illustration of the constructive interference condition which is the operating principle of digital beamforming using a uniform linear array as an example.

2572 numbers that contain the beamforming phase shift and an amplitude weighting factor,

$$\Phi[n] = [A_0[n]e^{-2\pi i \phi_0[n]}, A_1[n]e^{-2\pi i \phi_1[n]}, \dots, A_{N-1}[n]e^{-2\pi i \phi_{N-1}[n]}], \quad (4.22)$$

2573 where the set of magnitudes  $A_i[n]$  are amplitude weighting factors and  $\phi_i[n]$  are the  
 2574 phase shifts from the path-length differences. The index  $i$  is used to denote the antenna  
 2575 channel number. The amplitude weighting factor is the relative magnitude of the signal  
 2576 received by a particular antenna in the array. This factor properly accounts for antennas  
 2577 that are closer to the radiating source. In general, the beamforming phases can also be  
 2578 functions of time to track the motion of a non-stationary source.

2579 Digital beamforming specifically is the type of beamforming algorithm of interest to  
 2580 Project 8 for CRES. With digital beamforming, the phase shifts are applied to the array  
 2581 signals in software rather than employing fixed beamforming phase shifts in the receiver  
 2582 chain hardware. The advantage of digital beamforming is that for any given series of  
 2583 array data one can specify an arbitrarily large number of beamforming positions and  
 2584 search for electrons using a flexible and easily configurable beamforming grid.

2585 Digital beamforming can be viewed as the spatial filtering, which is a direct conse-  
 2586 quence of the constructive interference condition used to define the beamforming phases.

2587 Digital beamforming causes signals from multiple electrons at different positions in the  
2588 trap to be separated, because the interference condition will cause the signals from  
2589 electrons at other position to cancel out. This spatial filtering effect reduces pile-up that  
2590 could become an issue for large scale CRES experiments using a dense tritium source.

2591 Beamforming positions can be specified with arbitrary densities limited only by  
2592 the available computational resources. This provides a very straight-forward way to  
2593 estimate the position of the electron in the trap by using a dense grid of beamforming  
2594 positions and maximizing the output power of the beamforming summation over this  
2595 grid. This approach to position reconstruction is attractive due the requirements of an  
2596 event-by-event signal reconstruction, which needs an accurate estimation of the exact  
2597 magnetic field experienced by the electron in order to correctly estimate its kinetic  
2598 energy. Combined with an accurate map of the magnetic field inhomogeneities of the  
2599 trap obtained from calibrations, beamforming allows one to apply this magnetic field  
2600 correction with a spatial resolution that is a fraction of the cyclotron wavelength.

2601 **Laboratory Beamforming Demonstrations**

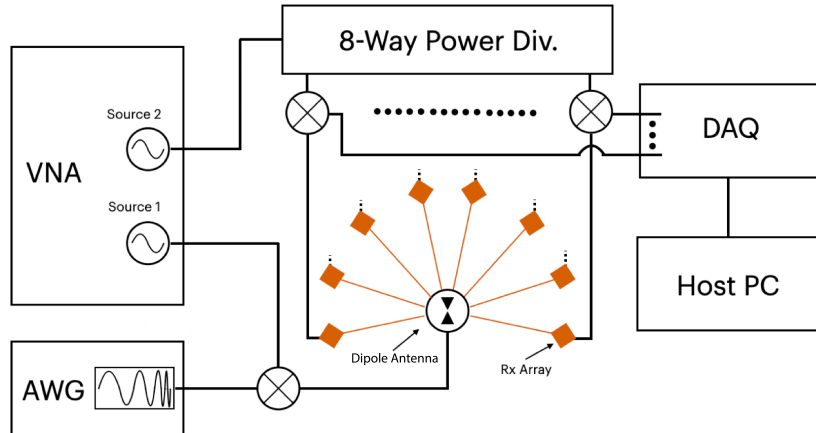


**Figure 4.8.** A system level diagram of the laboratory setup used for beamforming demonstrations at Penn State. For more information on this system see Chapter 5. Signals near 26 GHz are fed to a dipole antenna using an arbitrary waveform generator (AWG) and vector network analyzer (VNA), which drive a mixer. The dipole radiation is collected by an array of antennas connected to the digitizer data acquisition (DAQ) system.

2602 An antenna measurement setup was constructed at Penn State to serve as a testbed  
2603 for antenna prototypes and to perform laboratory validations of array simulations for  
2604 the FSCD. This system is discussed in more detail in Chapter 5. Early versions of

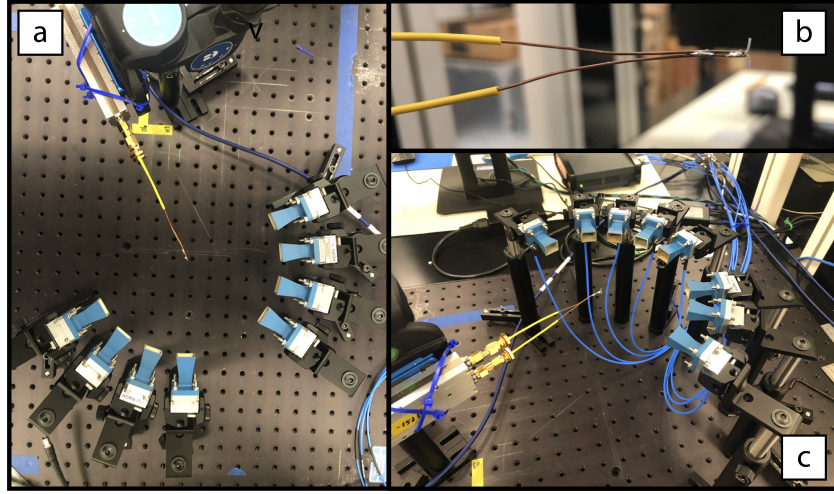


**Figure 4.9.** Photographs of the beamforming demonstration setup. In (a) I show a top-down view of the dipole antenna and the array of eight horn antennas. Manual repositioning of the horn antennas allows one to synthesize a full-circular antenna array. The dipole antenna is mounted on a camera tripod mount that allows for manual position tuning. (b) is a close up image of the dipole, which is manufactured from two segments of semi-rigid coaxial cable. (c) is another image of the dipole and array.

2605 the antenna measurement system (see Figure 4.8 and Figure 4.9) were used to perform  
 2606 beamforming reconstruction studies of a simple probe antenna.

2607 Signals from an arbitrary waveform generator were up-converted to 26 GHz using a  
 2608 mixer and a high-frequency source from a vector network analyzer and fed to a dipole  
 2609 antenna through a balun. The radiation from the dipole antenna was received by an  
 2610 array of horn antennas. The signals from the horn antennas were down-converted to  
 2611 baseband using a collection of mixers and an 8-way power divider. The signals were then  
 2612 digitized and saved to a host computer for analysis.

2613 The data collected using the dipole and horn antenna array is reconstructed using the  
 2614 beamforming reconstruction approach specified in Section 4.3.1. A two-dimensional grid  
 2615 of xy-positions is defined and the beamforming phase shifts for each of these positions  
 2616 is calculated. The phased summation can be visualized by plotting the time-averaged  
 2617 power for each of the summations as a pixel in the resulting beamforming image (see  
 2618 Figure 4.10). White Gaussian noise (WGN) can be added to the data at this stage  
 2619 to simulate more realistic SNR if desired. The beamforming peak maxima is expected  
 2620 to have a Bessel function shape due to the circular symmetry of the array, and by  
 2621 analyzing the size of the beamforming maxima one can confirm that the beamforming  
 2622 reconstruction measurement has similar position resolution as expected from Locust  
 2623 simulations. Additionally, signal detection rates can be estimated from the data by

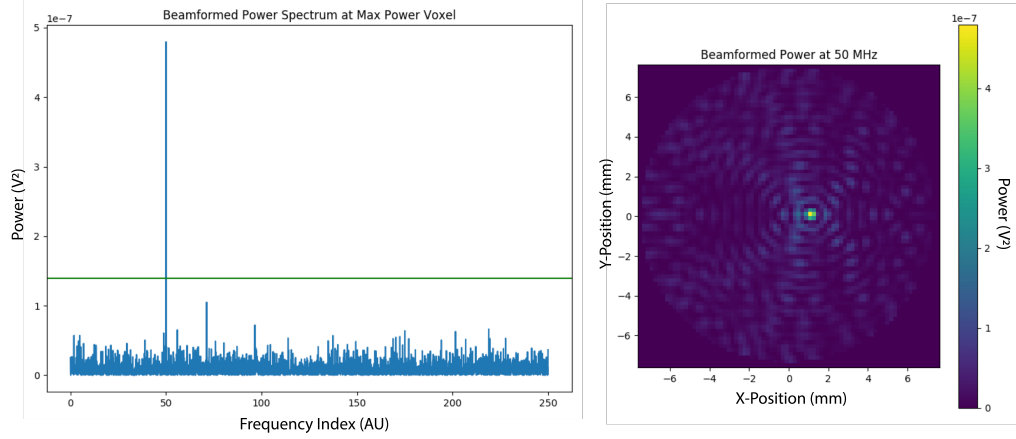


**Figure 4.10.** An example of digital beamforming reconstruction of a dipole antenna using a synthetic array of horn antennas. The beamforming image on the right is constructed by computing the time-averaged power of the summed signals for a two-dimensional grid of beamforming positions. In the image, one can see a clear maximum that corresponds to the position of the dipole antenna. On the left I show the frequency spectrum of the time-series at the maximum power pixel. White Gaussian noise is added to the signal to mimic a more realistic signal-to-noise-ratio. The signal emitted by the dipole is clearly visible as the high power peak in the frequency spectrum.

2624 comparing the magnitude of the beamforming signal peak in the frequency spectra to  
 2625 simulation.

## 2626 FSCD Beamforming Simulations

2627 Locust simulations of the FSCD are used to generate simulated CRES signal data to  
 2628 perform beamforming reconstruction studies. As mentioned in the previous section,  
 2629 the beamforming procedure beings by specifying a set of beamforming positions and  
 2630 corresponding beamforming shifts. The beamforming positions form a grid that covers  
 2631 the region of interest. There are effectively an infinite number of ways to specify the  
 2632 grid positions, however, uniform square grids are the most commonly used due to their  
 2633 simplicity. In the actual experiment the number and pattern of beamforming positions  
 2634 would be optimized to cover the most important regions of the trap volume, which  
 2635 maximizes detection efficiency and minimizes superfluous calculations.

2636 The beamforming grids used for signal reconstruction with the FSCD consist of a set  
 2637 of points that cover the two-dimensional plane formed by the perimeter of the antenna  
 2638 array. The axial dimension is left out because electrons are treated as if they occupy only  
 2639 their average axial position, which corresponds to the center of the magnetic trap. This  
 2640 treatment is valid since it is impossible to resolve the axial position of the electron as a

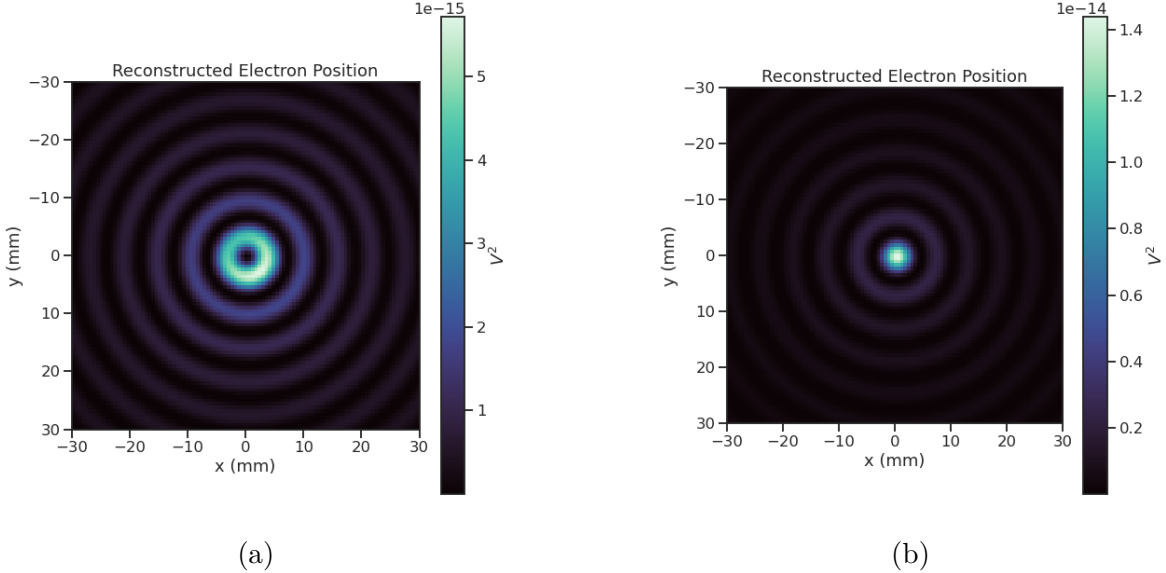


**Figure 4.11.** Beamforming images visualizing the reconstruction of an electron without (a) and with (b) the cyclotron phase correction. The images were generated using data from Locust simulations. The cyclotron phase refers to a phase offset equal to the relative azimuthal position of an antenna in the array. This phase offset is caused by the circular electron orbit and must be corrected for during reconstruction.

function of time due to the rapid oscillation frequencies of trapped electrons.

After beamforming, a summed time-series is obtained for each beamforming position that can be checked for a signal using a detection algorithm. A beamforming image is a visualization method that is equivalent to arranging the beamforming grid points according to their physical locations. Each pixel in the image corresponds to a summed time-series obtained for a digital beamforming position, and the image is obtained taking the time-averaged power at every pixel(see Figure 4.11).

If only the spatial beamforming phase component from Equation 4.20 is used, then the resulting image contains a ring-shaped feature centered on the position of the electron (see Figure 4.11a). The origin of this shape is an additional phase offset particular to a cyclotron radiation source. The circular cyclotron orbit introduces a relative phase offset to the electric fields equal to the azimuthal position of the field measurement point [77, 78]. Therefore, two antennas, one located at an azimuthal position of  $0^\circ$  and another located at an azimuthal position of  $90^\circ$ , will receive CRES signals out of phase by  $90^\circ$ , which is the difference in their azimuthal positions. This phase offset can be corrected by adding an additional term to the beamforming phase equation that is equal

2657 to the azimuthal position of the antenna relative to the electron,

$$\phi_i[n] = \frac{2\pi d_i[n]}{\lambda} + \Delta\varphi_i[n], \quad (4.23)$$

2658 where  $\Delta\varphi_i$  is difference between the azimuthal position of the electron and the  $i$ -th  
 2659 antenna channel. Using the updated beamforming phases changes the ring feature into  
 2660 the expected Bessel peak whose maximum corresponds to the position of the electron.  
 2661 Including this cyclotron phase correction significantly improves the signal detection and  
 2662 reconstruction capabilities of beamforming by more than doubling the summed signal  
 2663 power and shrinking the beamforming maxima feature size.

2664 The beamforming image examples in Figure 4.11 were produced using an electron  
 2665 located on the central axis of the magnetic trap, which do not experience  $\nabla B$ -drifts.  
 2666 However, electrons produced at non-zero radial position the beamforming phases must  
 2667 be made time-dependent to track the position of the electron's guiding center over  
 2668 time. Without this correction the  $\nabla B$ -drift causes the electron to move away from the  
 2669 beamforming position, which effectively spreads the cyclotron radiation power over a  
 wider area in the beamforming image (see Figure 4.12). This effect significantly reduces

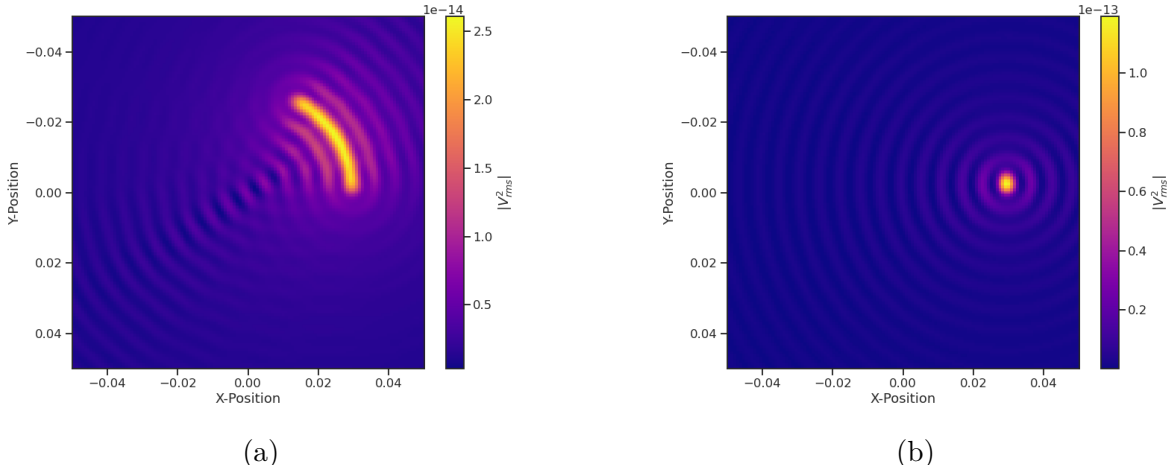


**Figure 4.12.** Beamforming images visualizing the reconstruction of an electron located off the central axis of the FSCD trap. In (a) beamforming is being performed without the  $\nabla B$ -drift correction, and in (b) it is included.

2670 the power of the beamforming maxima and increases the size of the beamforming features,  
 2671 simultaneously harming detection efficiency and position reconstruction.

2673 The  $\nabla B$ -drift correction simply adds a circular time-dependence to the beamforming

2674 positions as a function of time,

$$r[n] = r_0 \quad (4.24)$$

$$\varphi[n] = \varphi_0 + \omega_{\nabla B} t[n], \quad (4.25)$$

2675 where  $\omega_{\nabla B}$  is the drift frequency and  $t[n]$  is the time vector. In the ideal case the  $\nabla B$ -drift  
2676 frequencies from Figure 4.2 for the correct pitch angle and radial position would be used,  
2677 however, it is not possible to know the electron's pitch angle a priori. In principle, one  
2678 could perform multiple beamforming summations for a given beamforming position using  
2679 different drift frequencies and choose the one that maximizes the summed power, but  
2680 this approach leads to a huge computational burden that would be impractical for a  
2681 real FSCD experiment. A compromise is to use an average value of  $\omega_{\nabla B}$  obtained by  
2682 averaging over the drift frequencies for electrons of different pitch angle at a particular  
2683 radius. This approach keeps the computational cost of time-dependent beamforming to a  
2684 minimum while still providing a significant increase in the detection efficiency of digital  
2685 beamforming.

## 2686 **Signal Detection with Beamforming and a Power Threshold**

2687 Up to this point I have neglected a specific discussion of how digital beamforming is used  
2688 for signal detection and reconstruction. Because, strictly speaking, digital beamforming  
2689 consists only of the phased summation of the array signals and cannot be used alone for  
2690 signal detection. The example beamforming images shown in Figure 4.11 and Figure 4.12  
2691 were produced using simulated data that contained no noise, which significantly degrades  
2692 the utility of analyzing the beamforming images for signal detection and reconstruction.

2693 In Project 8, digital beamforming as a detection algorithm is understood to mean  
2694 digital beamforming plus a power or amplitude threshold placed on the frequency  
2695 spectrum obtained by applying a fast Fourier transform (FFT) to the summed time-series  
2696 (see Figure 4.13). This approach is similar to the time-frequency spectrogram analysis  
2697 employed in Phase I and II. However, it is possible to use any signal detection algorithm  
2698 after beamforming. In Section 4.4 I analyze the signal detection performance of the  
2699 power threshold approach in detail.

2700 Without a reconstruction technique that coherently combines the signals from the  
2701 full antenna, the ability to detect CRES signals is drastically reduced (see Figure 4.13).  
2702 Because the CRES signals are in-phase at the correct beamforming position, the summed  
2703 power increases as a function of  $N^2$  compared to a single antenna channel, where  $N$  is

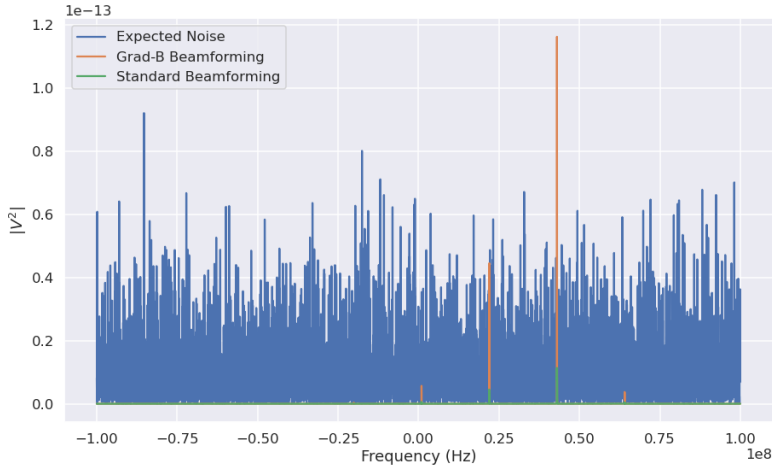


**Figure 4.13.** A plot of a typical frequency spectrum obtained by applying a Fourier transform to the time-series obtained from beamforming. The frequency spectra are plotted without noise on top of an example of a typical noise spectrum to visualize a realistic signal-to-noise ratio. In the example, without beamforming it would not be possible to detect anything since the signal amplitudes would be reduced by a factor of sixty relative to the noise. Additionally, it is clear the  $\nabla B$ -drift correction is needed to detect this electron in the presence of noise.

2704 the number of antennas. It is true that the noise power is also increased by beamforming,  
 2705 but, because the noise is incoherent, its power only increases linearly. Consequently, the  
 2706 SNR of the CRES signal increases linearly with the number of antennas, which greatly  
 2707 improves detection efficiency compared to using only the information in a single antenna.

2708 The power threshold detection algorithm searches for high-power frequency bins that  
 2709 should correspond to a frequency component of the CRES signal. In order to prevent  
 2710 random noise fluctuations from being mistaken as CRES signals the power threshold  
 2711 must be set high enough so that it is unlikely that random noise could be responsible. A  
 2712 consequence of this is that many electrons that can be trapped will go undetected because  
 2713 the modulation caused by axial oscillations leads to the cyclotron carrier power to falling  
 2714 below the decision threshold. The time-dependent beamforming used to correct for the  
 2715  $\nabla B$ -drift increases the volume of the magnetic trap where electrons can be detected,  
 2716 but it is ineffective at increasing the range of detectable pitch angles (see Figure 4.14).  
 2717 Fundamentally, this is because the power threshold only uses a fraction of the signal  
 2718 power to detect electrons and ignores the power present in the frequency sidebands. In  
 2719 the subsequent sections I examine two other signal detection algorithms that seek to  
 2720 improve the detection efficiency of the FSCD by utilizing the more of the signal shape to  
 2721 compute the detection test statistics.

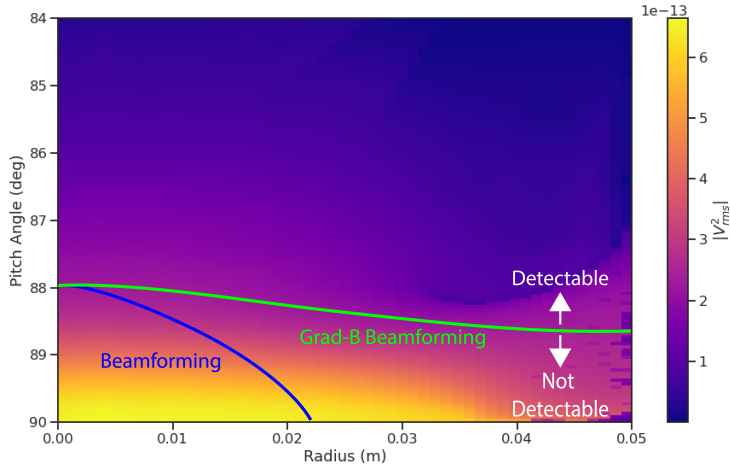


**Figure 4.14.** A plot of the total signal power received by the FSCD array from trapped electrons with different radial positions and pitch angles generated using Locust simulations. The lines on the plot indicate a 10 dB detection threshold above the mean value of the noise in the frequency spectrum. With static beamforming electrons with radial positions larger than about two centimeters are undetectable due to the change in the electron's position over time causing losses from beamforming phase mismatch. This is corrected by including  $\nabla B$ -drift frequencies in the beamforming phases. Both beamforming techniques fail to detect electrons below  $\approx 88.0^\circ$ , since these signal are composed of several relatively weak sidebands that are comparable to the noise.

### 2722 4.3.2 Matched Filtering

#### 2723 Introduction to Matched Filtering

2724 The problem of CRES signal detection is the problem of detecting a signal buried in  
 2725 WGN, which has been examined at great depth in the signal processing literature [74].  
 2726 For a fully known signal in WGN the optimal detector is the matched filter, which means  
 2727 that it achieves the highest true positive rate for a fixed rate of false positives.

2728 The matched filter test statistic is calculated by taking the inner product of the data  
 2729 with the matched filter template

$$\mathcal{T} = \left| \sum_n h^\dagger[n] y[n] \right|, \quad (4.26)$$

2730 where  $h[n]$  is the matched filter template and  $y[n]$  is the data. The matched filter test  
 2731 statistic defines a binary hypothesis test in which the data vector is assumed to be an  
 2732 instance of two possible data classes. By setting a decision threshold on the value of  $\mathcal{T}$ ,  
 2733 one can classify a given data vector as belonging to two distinct hypotheses. Under the

2734 first hypothesis the data is composed of pure WGN, and under the second hypothesis  
 2735 the data is composed of the known signal with additive WGN.

2736 The matched filter template is obtained by rescaling the known signal in the following  
 2737 way

$$h[n] = \frac{x[n]}{\sqrt{\tau \sum_n x^\dagger[n]x[n]}}, \quad (4.27)$$

2738 where  $\tau$  is the variance of the WGN and  $x[n]$  is the known signal. Strictly speaking,  
 2739 Equation 4.27 is only true for noise with a diagonal covariance matrix, which is assumed  
 2740 to be true for the FSCD. Defining the matched filter templates in this way guarantees  
 2741 that the expectation value of  $\mathcal{T}$  is equal to one when the data contains only noise, which  
 2742 is the standard matched filter normalization.

2743 Although matched filters are canonically formulated in terms of a perfectly known  
 2744 signal, it is possible to apply the matched filter technique with imperfect information  
 2745 provided the signal is deterministic. From the discussion of CRES simulation tools (see  
 2746 Section 4.2) it was shown that the shape of CRES signals are completely determined  
 2747 by the initial parameters of the electron. The random collisions with background gas  
 2748 molecules, which cause the formation of signal tracks, are the only stochastic component  
 2749 of the CRES event after the initial beta-decay. Therefore, a matched filter can be used  
 2750 for the detection of deterministic CRES signal tracks between scattering events.

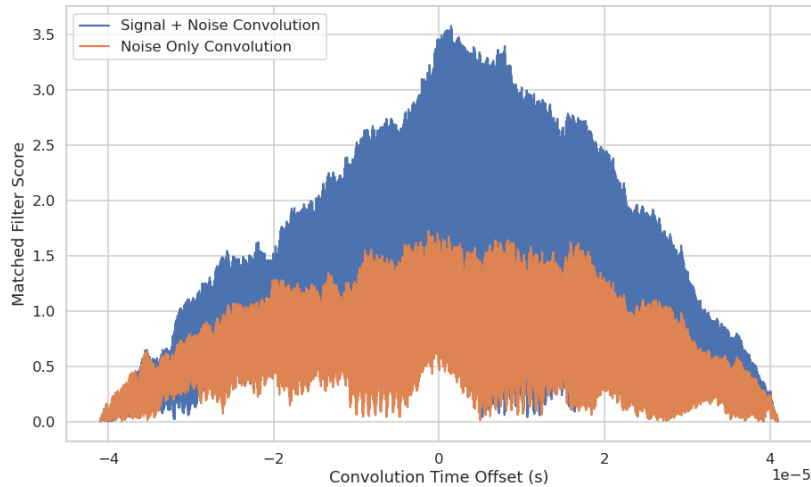


**Figure 4.15.** Example of a convolution of a CRES signal template with a segment of noisy data. A simulated CRES signal was simulated using Locust and normalized to create a matched filter template. When this template is convolved with noisy data the contains the matching signal the convolution output increases dramatically compared to data with only noise. The decreasing convolution output as the time offset of the convolution increases is caused by zero-padding of the data and template.

2751        The matched filter test statistic for CRES signals is a modified version of Equation  
2752        4.26

$$\mathcal{T} = \max_{h,m} |\mathbf{h} * \mathbf{y}| = \max_{h,m} \left| \sum_k h^\dagger[k] x[m-k] \right|, \quad (4.28)$$

2753        where the matched filter inner product has been replaced with a convolution operation  
2754        and a maximization over the template and convolution delay ( $m$ ). Replacing the inner  
2755        product with a convolution accounts for the fact that the start time of the CRES signal is  
2756        now an unknown parameter. In addition, a maximization of the matched filter convolution  
2757        is performed over a number of different templates. Because the shape of the signal is  
2758        unknown, a range of different signal shapes, called a template bank, must be checked  
2759        using an exhaustive search.

## 2760        Matched Filtering in the Frequency Domain

2761        The template bank approach, while powerful, can become computationally intractable.  
2762        Specifically, the time-domain convolution specified by Equation 4.28 is particularly  
2763        computationally intensive and is a major barrier towards the implementation of a  
2764        matched filter for signal detection in an experiment like the FSCD. This can be avoided  
2765        by using the convolution theorem to replace the time-domain convolution with an inner  
2766        product in the frequency domain.

2767        The convolution theorem states that

$$\mathbf{f} * \mathbf{g} = \mathcal{F}^{-1}(\mathbf{F} \cdot \mathbf{G}) \quad (4.29)$$

2768        where  $\mathbf{f}$  and  $\mathbf{g}$  are discretely sampled time-series,  $\mathbf{F}$  and  $\mathbf{G}$  are the respective discrete  
2769        Fourier transforms, and  $\mathcal{F}^{-1}$  is the inverse discrete Fourier transform operator. The  
2770        convolution theorem allows us to perform the matched filter convolution by first com-  
2771        puting the Fourier transform of the template and data, then performing a point-wise  
2772        multiplication of the two frequency series, and finally performing the inverse Fourier  
2773        transform to obtain the convolution output. Because discrete Fourier transforms can be  
2774        performed extremely efficiently, the convolution theorem is almost always used in lieu of  
2775        directly computing the convolution.

2776        One thing to note here is that the convolution theorem for discrete sequences shown  
2777        here, is technically valid only for circular convolutions, which is not directly specified  
2778        in Equation 4.28. However, because typical CRES track lengths are much longer than  
2779        the Fourier analysis window and the frequency chirp rates are small compared to the

2780 time-slice duration, it is safe to use circular convolutions to evaluate matched filter scores  
2781 for CRES signals, which allows one to apply the convolution theorem to compute matched  
2782 filter scores for the FSCD.

2783 **Matched Filter Analysis of the FSCD**

2784 Since the matched filter is the optimal signal detection approach, it provides the ultimate  
2785 upper bounds on signal detection. This makes it a useful algorithm for assessing the  
2786 upper bounds on neutrino mass sensitivity for the FSCD, since it indicates the best  
2787 possible detection efficiency achievable for that experiment configuration. The standard  
2788 approach to performing these studies involves generating numerous simulated electron  
2789 signals that span the kinematic parameter space of electrons.

2790 To limit the number of simulations required to evaluate the detection efficiency,  
2791 the standard approach is to fix the starting axial position, starting azimuthal position,  
2792 starting direction of the perpendicular component of the electron’s momentum, and event  
2793 start time. This reduces the dimensionality of the simulated parameter space to three  
2794 parameters — the starting radial position, starting kinetic energy, and starting pitch  
2795 angle. The fixed variables are nuisance parameters, which do not affect the detection  
2796 efficiency estimates for the FSCD design, because they simply introduce overall phase  
2797 offsets that can be marginalized during the calculation of the matched filter score. Across  
2798 radial position, kinetic energy, and pitch angle one defines a regular grid of parameters  
2799 and uses Locust to simulate the corresponding signals (see Figure 4.16). This grid of  
2800 simulated signals is used to estimate detection efficiency by calculating the detection  
2801 probability of a randomly parameterized signal using the grid as a set of matched filter  
2802 templates (see Section 4.4).

2803 The matched filter approach can also be used to estimate the achievable energy  
2804 resolution of the experiment by using a dense grid of templates generated with parameters  
2805 close to the unknown signal (see figure 4.17). Because matched filter templates with similar  
2806 parameters have closely matching signal shapes, templates with incorrect parameters can  
2807 have nearly identical matched filter scores as the correct template. Since only one sample  
2808 of noise is included in a sample of real data, one cannot guarantee that the template  
2809 with the maximum score corresponds to the ground truth parameters of the signal. This  
2810 introduces uncertainty into the signal parameter estimation that manifests as an energy  
2811 broadening. Dense grids of matched filter templates allow one to quantify this broadening  
2812 by analyzing the parameter space of templates with matched filter scores close to the  
2813 ground truth. This approach is analogous to maximum likelihood estimation and is one

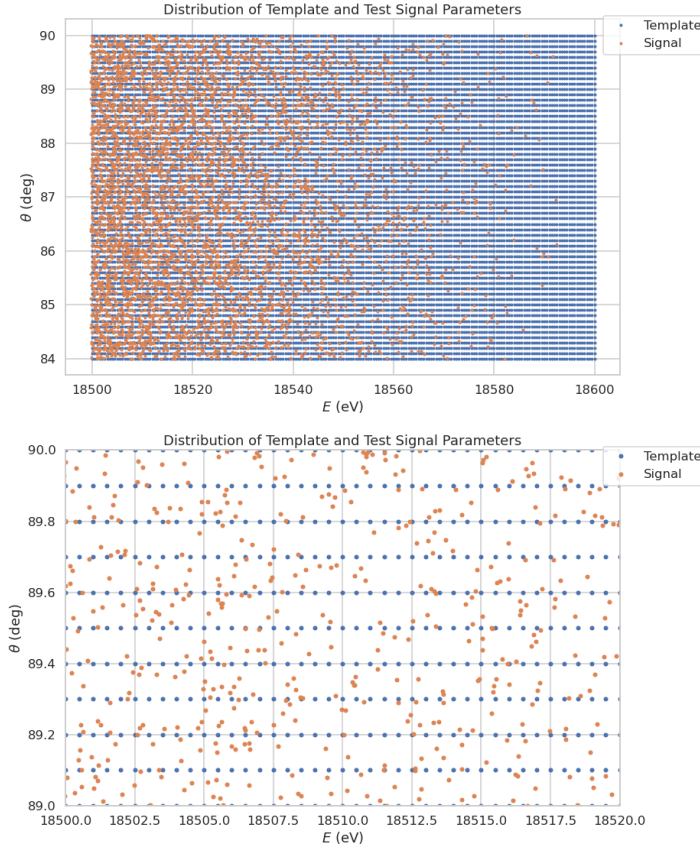


**Figure 4.16.** An example two-dimensional parameter distribution of a matched filter template bank and random test signals.  $\theta$  refers to the pitch angle of the electron and  $E$  is the kinetic energy. The template bank forms a regular grid of in pitch angle and energy; whereas, the test signals are uniformly distributed in pitch angle and follow the tritium beta-decay kinetic energy distribution. This is why there are fewer test signals at higher energies. The need for high match across the full parameter space prevents one from reducing the density of templates in this low activity region. A zoomed in version of the template bank illustrates the relative density of templates and signals needed for match  $> 90\%$ .

2814 key component of a complete sensitivity analysis for an antenna array CRES experiment.

2815 A figure of merit that summarizes the performance of a matched filter template  
 2816 bank at signal detection is "mean match", which is defined as the average ratio of the  
 2817 highest matched filter score for a random signal to the matched filter score for a perfectly  
 2818 matching template. In equation form the match ratio for a single template is given by

$$\text{Match} \equiv \Gamma = \frac{\mathcal{T}_{\text{best}}}{\mathcal{T}_{\text{ideal}}}, \quad (4.30)$$

2819 where  $\mathcal{T}_{\text{best}}$  is the matched filter score of the best fitting template in the bank and  $\mathcal{T}_{\text{ideal}}$

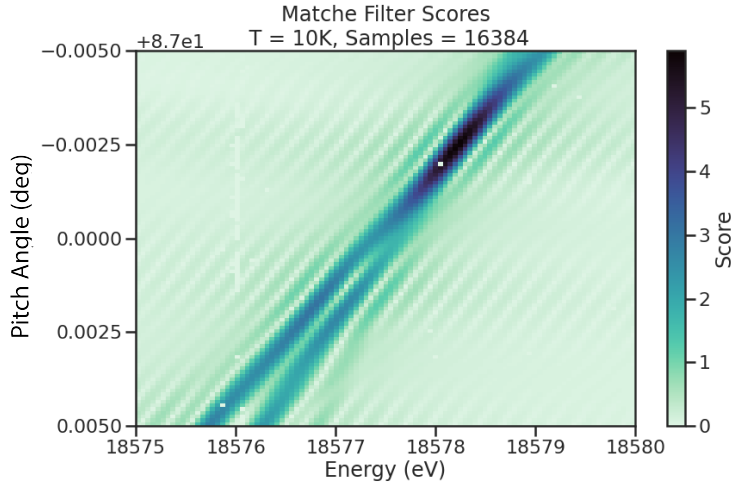


**Figure 4.17.** The matched filter scores of a dense grid of templates in pitch angle energy space. Dense template grids allow one to estimate the kinetic energy of the electron by identifying the best matching template. The uncertainty on this value is proportional to the space of templates that also match the test signal well. In the worst case matched filter templates can be completely degenerate where templates with different parameters match a signal with equal likelihood.

is the hypothetical score one would measure if the signal perfectly matched the template. The mean match is the average value of match for a typical signal inside the parameter range covered by the matched filter template bank. Generally, one desires a mean match as close to unity as possible, which is typically an exponential function of the number of templates in the template bank (see Figure 4.18).

The exponential relationship between match and template bank size manifests for dense and sparse template grids. Sparse template grids are used for signal detection when no prior information on the signal is available; whereas, dense templates grids are more useful for parameter estimation. The mean match value directly influences the detection efficiency of the template bank, but due to the exponential scaling, achieving a high average match at the detection stage can easily overwhelm the available computational resources.

The effect of match on the detection efficiency of the matched filter template bank can be summarized using the ROC curve (see Figure 4.19). The average performance of the template bank can be described by a single ROC curve obtained by averaging over the PDFs that describe the detection probabilities of each template in the bank.

The distribution that describes the matched filter score under the signal hypothesis is a Rician distribution, which has a mean value equal to the matched filter score multiplied by the match ratio (see Section 4.4). Alternatively, the distribution of the matched

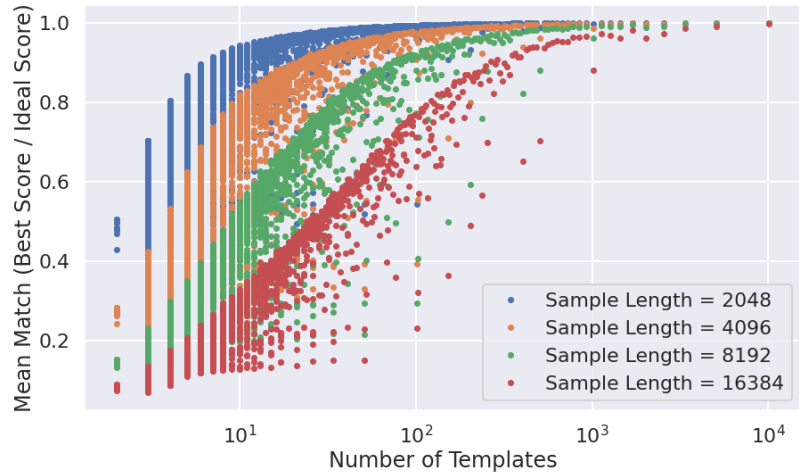


**Figure 4.18.** The mean match of the dense template grid shown in Figure 4.17 for different numbers of templates. Grids of different sizes were obtained by decimating a dense grid of templates and the average match for each grid was computed using the same set of randomly distributed test signals. Plotting the mean match against the size of the grid allows one to visualize the exponential relationship between match and template bank size. The noise in each curve is caused by sampling effects from the decimation algorithm. In general, longer templates are harder to match than shorter templates.

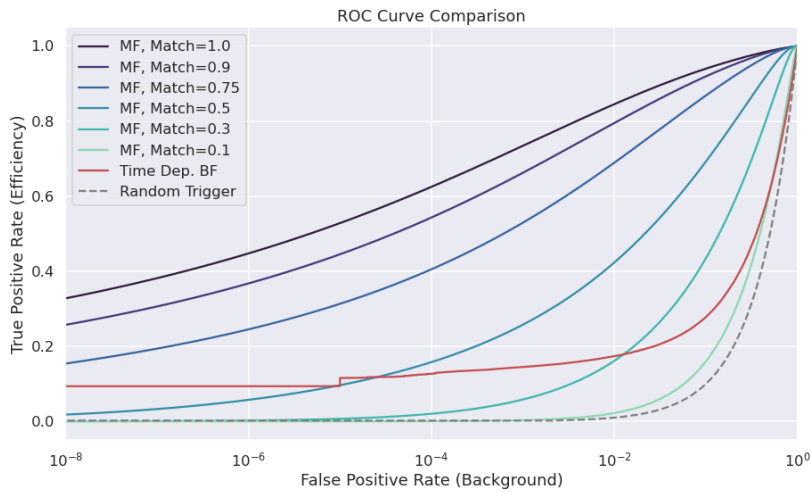


**Figure 4.19.** Matched filter template bank ROC curves as a function of mean match. One can see that for low match a matched filter is on average worse than the more straight forward beamforming detection approach.

filter score when there is no signal in the data follows a Rayleigh distribution, which is equivalent to a Rician distribution with zero mean. The matched filter score for each template in the template bank is described by a separate Rician distribution. Therefore, one way to model detection probability for a given signal is to average across all matched filter distributions in the template bank to obtain a single distribution that describes the statistical behavior of the matched filter score.

A different way to visualize the detection performance for each algorithm is to specify a minimum acceptable false positive rate at the trigger level. This is equivalent to specifying a minimum threshold on the value of the matched filter score or the size of a frequency peak for a beamforming power threshold trigger. One can then draw regions of detectable signals as a function of the electron's pitch angle and radial position (see Figure 4.20). A kinetic energy shift is equivalent to an overall frequency shift of the

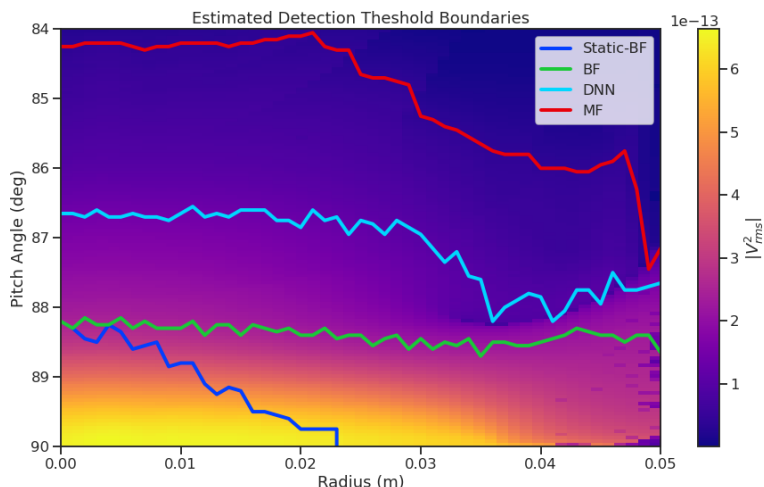


**Figure 4.20.** Boundaries of detectable electrons in pitch angle kinetic energy space for a series of different signal detection algorithms. A detectable signal is defined as a signal that is above a consistent decision with at least 50% probability. This non-rigorous treatment of detection probability is primarily useful for the visualization the relative increases in detection performance provided by the different algorithms. The static beamforming (Static-BF) algorithm is the digital beamforming algorithm introduced above without the  $\nabla B$ -drift correction. The DNN algorithm refers to a convolutional neural network classifier trained to detect CRES signals (see Section 4.3.3).

signal and should have no effect on the detection probability assuming sufficient density of matched filter templates in the energy dimension. A electron is declared "detectable" for the regions in Figure 4.20 if the signal has at least 50% probability of falling above the decision threshold of the respective classifier. One can see that the parameter space of detectable signals is greatly expanded beyond the beamforming power threshold trigger

2856 with a matched filter (MF) or deep neural network (DNN) (see Section 4.3.3). Plots such  
2857 as Figure 4.20 are useful for visualization, but, since the handling of detection likelihood  
2858 is not sufficiently rigorous, the detection probability boundaries are not well-suited to  
2859 sensitivity estimates.

## 2860 Optimized Matched Filtering Implementation for the FSCD

2861 The biggest practical obstacle to the implementation of a matched filter template bank is  
2862 the computational cost associated with exhaustively calculating the matched filter scores;  
2863 therefore, one must employ several optimizations in a practical setting.

2864 Computing a matched filter score requires the convolution of two vectors, which can  
2865 be performed very efficiently by computers if the convolution theorem and fast Fourier  
2866 transforms (FFT) are utilized. Furthermore, one can apply digital beamforming as a  
2867 pre-processing step to reduce the dimensionality of the data before the matched filter.  
2868 In order to understand the relative gain in computational efficiency offered by these  
2869 optimizations I analyze the total number of floating-point operations (FLOP) of several  
2870 matched filter implementations in big  $O$  notation that utilize different combinations of  
2871 optimizations.

2872 A direct implementation of a matched filter as specified by Equation 4.28 involves  
2873 the convolution of  $N_{\text{ch}}$  signals of length  $N_s$  with template signals of length  $N_t$ . The  
2874 FLOPs of the various matched filter implementations on a per-template basis will be  
2875 used as a consistent metric, since each implementation scales linearly with the number of  
2876 templates. The direct convolution approach to matched filtering costs

$$O(N_{\text{ch}}) \times O(N_s \times N_t) \quad (4.31)$$

2877 FLOP per-template, whose cost is dominated by the  $O(M \times N)$  convolution operation.

2878 The computational cost of the direct matched filter approach can be significantly  
2879 reduced by exploiting the convolution theorem and FFT algorithms. By restricting oneself  
2880 to signals and templates that contain equal numbers of samples, the convolution can be  
2881 calculated by Fourier transforming both vectors, performing the point-wise multiplication,  
2882 and taking the inverse Fourier transform to obtain the convolution result. The FFT  
2883 algorithm is able to compute the Fourier transform utilizing only  $O(N \log N)$  operations.  
2884 This optimization results in a computational cost per-template of

$$O(N_{\text{ch}}) \times O(N_s \log N_s) \quad (4.32)$$

2885 A typical signal vector in the FSCD contains  $O(10^4)$  samples in which case the FFT  
 2886 reduces the computational cost of the matched filter by a factor of  $O(10^3)$ . In practice,  
 2887 due to the large reduction in computational cost with a frequency-domain matched filter,  
 2888 direct implementations of the matched filter using a time-domain convolution are almost  
 2889 never attempted in practice. Particularly, a time-domain matched filter is completely  
 2890 computationally infeasible for the the FSCD due to resource constraints.

2891 Rather than relying solely on the matched filter it is tempting to consider using  
 2892 digital beamforming as an initial step in the signal reconstruction for the purposes of  
 2893 data reduction. The primary motivation is to reduce the dimensionality of the data by  
 2894 a factor of  $N_{\text{ch}}$  by combining the array outputs coherently into a single channel. One  
 2895 can view the beamforming operation as a partial matched filter, in the sense that the  
 2896 matched filter convolution contains the beamforming phased summation along with a  
 2897 prediction of the signal shape. By separating beamforming from the signal shape one  
 2898 hopes to reduce the overall computational cost by effectively shrinking the number of  
 2899 templates and reducing the number of operations required to check each one.

2900 The nature of this optimization requires that one account for the number of templates  
 2901 used for pure matched filtering versus the hybrid approach. To first order, the total  
 2902 number of templates at the trigger stage is a product of the number of guesses for each  
 2903 of the electron's parameters

$$N_T = N_E \times N_\theta \times N_r \times N_\varphi, \quad (4.33)$$

2904 where  $N_E$  is the number of kinetic energies,  $N_\theta$  is the number of pitch angles,  $N_r$  is the  
 2905 number of starting radial positions, and  $N_\varphi$  is the number of starting azimuthal positions.  
 2906 The starting axial position and cyclotron motion phase are not necessary to include in  
 2907 the template bank, since these parameters manifest themselves as the starting phase of  
 2908 the signal, which is effectively marginalized when using a FFT to compute the matched  
 2909 filter convolution. Therefore, the total number of operations required by a matched filter  
 2910 to detect a signal in a segment of array data is on the order of

$$O(N_T) \times O(N_{\text{ch}}) \times O(N_s \log N_s) \quad (4.34)$$

2911 With the hybrid approach one removes spatial parameters from the template bank  
 2912 by using beamforming to combine the array signals into a single channel. Beamforming  
 2913 explicitly assumes a starting position, which allows one to use matched filter templates  
 2914 that span the two-dimensional space of kinetic energy and pitch angle. The total

computational cost of the hybrid method is directly proportional to the number of beamforming positions. For the time-dependent beamforming defined in Section 4.3.1, the number of beamforming positions is given by

$$N_{\text{BF}} = N_r \times N_\varphi \times N_{\omega_{\nabla B}}, \quad (4.35)$$

where  $N_r$  and  $N_\varphi$  are the same spatial parameters encountered in the pure matched filter template bank and  $N_{\omega_{\nabla B}}$  is the number of  $\nabla B$ -drift frequency assumptions. If a unique drift frequency is used for each pitch angle then the hybrid approach is effectively equivalent to a pure matched filter in the number of operations. The key efficiency gain of the hybrid approach is to exploit the relatively small differences in  $\omega_{\nabla B}$  for electrons of different pitch angles by using only a few average drift frequencies.

The total number of operations for the hybrid approach can be expressed as a sum of the operations required by the beamforming and matched filtering steps,

$$O(N_{\text{BF}}) \times O(N_{\text{ch}}N_s) + O(N_{\text{BF}}) \times O(N_E N_\theta) \times O(N_s \log N_s). \quad (4.36)$$

The first product in the sum is the number of operations required by beamforming, which is simply the number of beamforming points times the computational cost of the beamforming matrix multiplication, and the second product is the computational cost of matched filtering the summed signal generated by each beamforming position. To compare this to pure matched filtering, one takes the ratio of Equations 4.34 and 4.36 to obtain

$$\Gamma_{\text{BFMF}} = \frac{O(N_{\omega_{\nabla B}})}{O(N_E N_\theta) \times O(\log N_s)} + \frac{O(N_{\omega_{\nabla B}})}{O(N_{\text{ch}})}. \quad (4.37)$$

This expression can be simplified by observing that  $O(N_E N_\theta) \times O(\log N_s) \gg O(N_{\text{ch}})$ , which means that the ratio of computational cost for the two methods can be reduced to

$$\Gamma_{\text{BFMF}} \approx \frac{O(N_{\omega_{\nabla B}})}{O(N_{\text{ch}})}. \quad (4.38)$$

Limiting oneself to a number of estimated drift frequencies of  $O(1)$ , then it can be seen that the estimated computational cost reduction of the hybrid approach is of  $O(N_{\text{ch}})$ . This is a large reduction considering that the FSCD antenna array contains sixty antennas in the baseline design.

The main drawback of the hybrid approach is that the limited number of allowed drift frequency guesses can lead to detection efficiency loss due to phase mismatch. The

2940 degree of phase error from an incorrect drift frequency is proportional to the length of  
 2941 the array data vector used by the signal detection algorithm. For signals with lengths  
 2942 equal to the baseline FSCD Fourier analysis window of 8192 samples, typical phase errors  
 2943 from using an average versus the exact  $\nabla B$ -drift frequency are on the order of a few  
 2944 percent in terms of the signal energy. This has a relatively small impact on the overall  
 2945 detection efficiency, however, future experiments with antenna array CRES will want to  
 2946 balance optimizations such as these during the design phase to keep experiment costs to  
 2947 a minimum while still achieving scientific goals.

## 2948 **Kinetic Energy and Pitch Angle Degeneracy**

2949 Accurate modeling of a matched filter requires one to consider the effects of mismatched  
 2950 signals and template, since this more accurately reflects the real-world usage of a matched  
 2951 filter. One way to study this is to use a signal grid to compute the matched filter scores  
 2952 between mismatched signals and templates and evaluate the matched filter scores under  
 2953 this scenario. What one finds when performing this analysis is that templates for signals  
 2954 with incorrect parameters can have matched filter scores that are indistinguishable from  
 the matched filter score of the correct template (see Figure 4.21 and Figure 4.21).

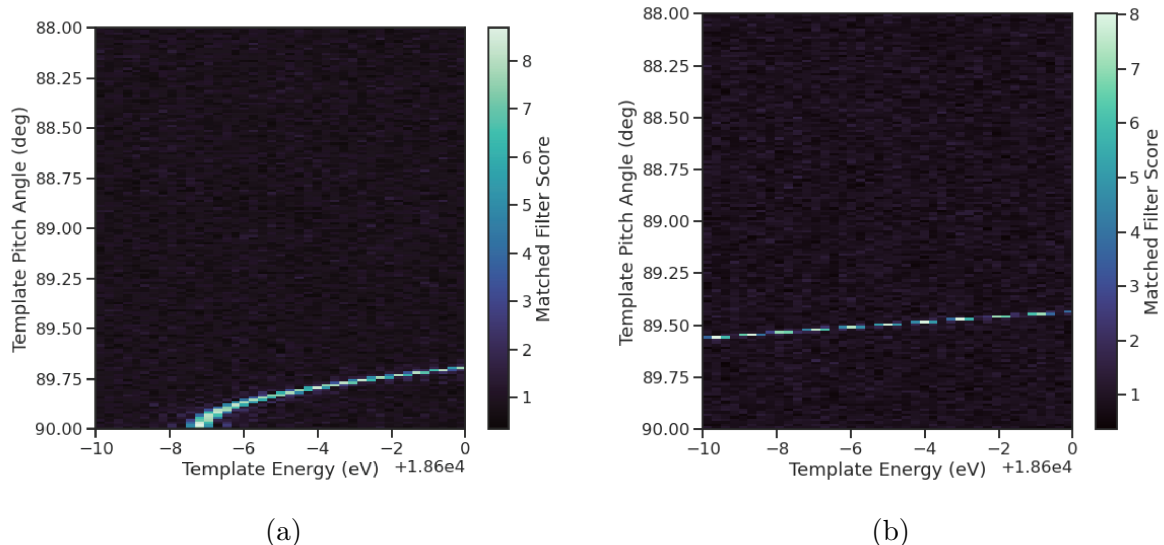


**Figure 4.21.** Two example illustrations of the correlation between kinetic energy and pitch angle imparted by the shape of the FSCD magnetic trap. The correlations manifest themselves as degeneracies in the matched filter score where multiple matched filter templates have the same matched filter for a particular signal. These degeneracies are a sign that the magnetic trap must be redesigned in order to break the correlation between pitch angle and kinetic energy.

2955

2956 This degeneracy in matched filter score is the result of correlations between the kinetic  
 2957 energy and pitch angle of the electron caused by the magnetic trap. These correlations  
 2958 are unacceptable since they greatly reduce the energy resolution of the experiment by  
 2959 causing electrons with specific kinetic energy to match templates across a wide range of  
 energies.

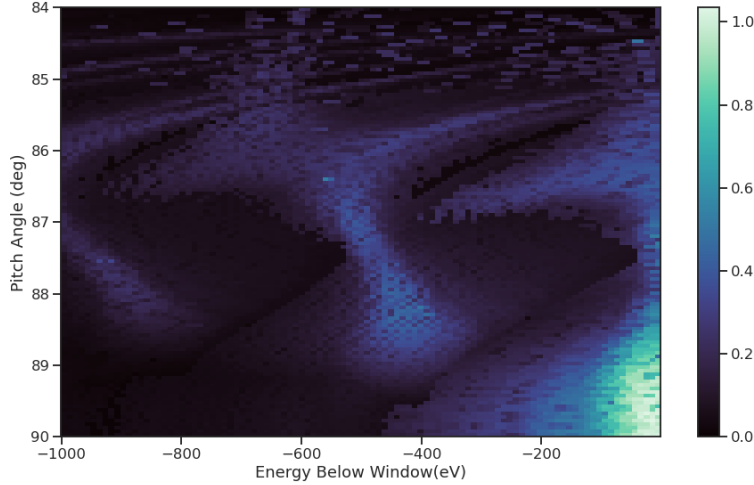


**Figure 4.22.** A visualization of the correlation between energy and pitch angle in the FSCD magnetic trap. The image is formed by computing the match of the best template from a grid consisting of pitch angles from 84 to 90 degrees in steps of 0.05 degrees, kinetic energies from 17574 to 18574 eV, located at 2 cm from the central axis, and simulated for a length of three FSCD time-slices. The signals used to compute the best matching template consisted of a grid from 84 to 90 degrees in steps of 0.05 degrees, kinetic energies from 18550 to 18575 eV in steps of 0.25 eV, located 2 cm from the central axis, and simulated for three FSCD time-slices. The colored regions of the plot show how well signals with lower energy can match those of higher energy for the FSCD magnetic trap, which is proportional to the achievable energy resolution of the FSCD design.

2960  
 2961 This degeneracy cannot be fixed by implementing a different signal reconstruction  
 2962 algorithm. As revealed by the matched filter scores the shapes of the signals for different  
 2963 parameters are identical. Resolving this degeneracy between pitch angle and energy  
 2964 requires the design of a new magnetic trap with steeper walls so that the average magnetic  
 2965 field experienced by an electron is less dependent on pitch angle.

### 2966 4.3.3 Machine Learning

2967 Machine learning is a broad field of research [79] that has been particularly transformative  
 2968 in the recent past. In this Section I provide a brief introduction to some concepts and

2969 techniques of machine learning that were applied to CRES signal detection in my  
2970 dissertation.

## 2971 **Introduction to Machine Learning**

2972 Digitization of the FSCD antenna array generates large amounts of data that must  
2973 be rapidly processed for real-time signal detection and reconstruction. While digital  
2974 beamforming combined with a power threshold is relatively computationally inexpensive,  
2975 it is ineffective at detecting CRES signal with small pitch angles, since it relies on a  
2976 visible frequency peak above the noise. On the other hand, a matched filter is able to  
2977 detect signals with a significantly larger range of parameters, however, the exhaustive  
2978 search of matched filter templates can be computationally expensive. Machine learning  
2979 based triggering algorithms have been used successfully in many high-energy physics  
2980 experiments [80], and recently have shown success in the detection of gravitational wave  
2981 signals [81, 82] in place of more traditional matched filtering methods. The success of  
2982 machine learning in these domains motivates the exploration of machine learning as a  
2983 potential CRES signal detection algorithm.

2984 Various approaches to machine learning are possible, but the one most important  
2985 to the discussion here is the supervised learning approach. In supervised learning, one  
2986 uses a differentiable model or function that is designed to map the input data to the  
2987 appropriate label [79]. The data is represented as a multidimensional matrix of floating  
2988 point values such as an image or a time-series, and the label is typically a class name such  
2989 as signal or noise for classification problems, or a continuous value like kinetic energy for  
2990 regression problems.

2991 In supervised learning the model is trained to map from the data to the correct label  
2992 by evaluating the output of the model using a training dataset consisting of a set of  
2993 paired data and labels. To evaluate the difference between the model output and the  
2994 correct label a loss function is used to quantify the error between the model prediction  
2995 and the ground truth. For example, a common loss function in regression problems is the  
2996 squared error loss function, which quantifies error using the squared difference between  
2997 the model output and label.

2998 Using the outputs of the loss function the next step in supervised learning is to  
2999 compute the gradient of error with respect to the model parameters in a process called  
3000 backpropagation. The gradients are used to update the model parameter values in  
3001 order to minimize errors in the model predictions across the whole dataset. This loop is  
3002 performed many times while randomly shuffling the dataset until the error converges to a

3003 minimum value at which point the training procedure has finished. It is standard practice  
3004 to monitor the training procedure by evaluating the performance of the model using a  
3005 separate validation dataset that matches the statistical distribution of the training data  
3006 and to check the performance of the model after training using yet another dataset called  
3007 the test dataset. These practices help to guard against overtraining which is a concern  
3008 for models with many parameters.

3009 **Convolutional Neural Networks**

3010 A popular class of machine learning models are neural networks. A neural network is  
3011 a function composed of a series of linear operations called layers, which take a piece of  
3012 data typically represented as a matrix, multiply the elements of the data by a weight,  
3013 and then sums these products to produce an output matrix. Neural networks composed  
3014 of purely linear operations are unable to model complex non-linear behavior. Therefore,  
3015 non-linear activation functions are applied to the outputs of each of the layers to increase  
3016 the ability of the neural network to model complex relationships between the data.

3017 Neural networks are typically composed of at least three layers, but with the present  
3018 capabilities of computer hardware they typically contain much more than this. The first  
3019 layer in a neural network is called the input layer, because it takes the data objects  
3020 as input, and the last layer in a neural network is known as the output layer. The  
3021 output layer is trained by machine learning to map the data to an output label using  
3022 the supervised learning procedure described in Section 4.3.3. Between the input and the  
3023 output layers are typically several hidden layers that receive inputs from and transmit  
3024 outputs to other layers in the neural network model. The term deep neural network  
3025 (DNN) refers to those neural networks that have at least one hidden layer, which have  
3026 proven to be extremely powerful tools for pattern recognition and function approximation.

3027 An important type of DNN are convolutional neural networks (CNN) that typically  
3028 contain several layers which perform a convolution of the input with a set of filters. These  
3029 convolution operations are typically accompanied by layers that attempt to down-sample  
3030 the data along with the standard neural network activation functions. A standard CNN  
3031 is composed of several convolutional layers at the beginning of the network and ends  
3032 with a series of fully-connected neural network layers at the output. Intuitively, one  
3033 can imagine that the convolutional layers are extracting features from the data that  
3034 fully-connected layers use to perform the classification or regression task.

3035 **Deep Filtering for Signal Detection in the FSCD**

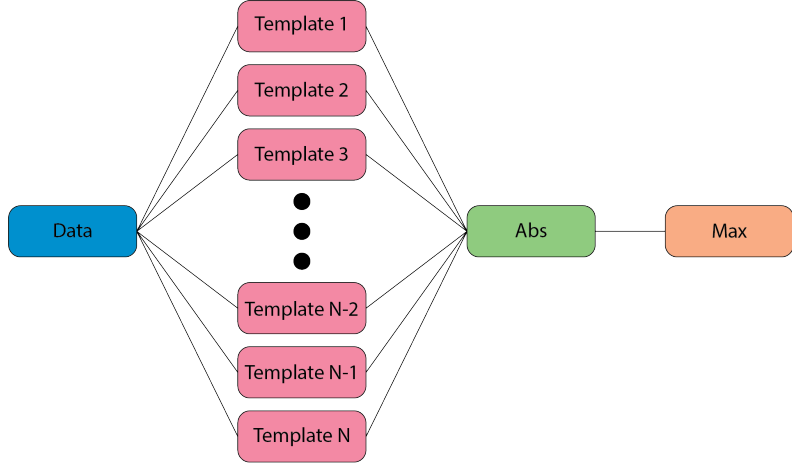


**Figure 4.23.** A representation of a matched filter template bank as a convolutional neural network. The network has a single layer composed of the templates, which act as convolutional filters. The activation of the neural network is an absolute value followed by a max operator.

3036     CNNs have been extremely influential in the field of computer vision, particularly tasks  
 3037     such as image segmentation and classification, but have also been applied in numerous  
 3038     experimental physics contexts. Given the particular challenge posed by signal detection  
 3039     and reconstruction in the FSCD, CNNs are an interesting choice for real-time signal  
 3040     detection, since this application requires both high efficiency and fast evaluation.

3041     In the machine learning paradigm, signal detection is a binary classification problem  
 3042     between the signal and noise data classes. My investigation focuses specifically on the  
 3043     application of CNNs to signal detection in the FSCD, which is motivated by relatively  
 3044     recent demonstrations of CNNs achieving classification accuracies for gravitational wave  
 3045     time-series signals comparable to a matched filter template bank. In this framework  
 3046     it is possible to interpret the matched filter as a type of CNN composed of a single  
 3047     convolutional layer with the templates making up the layer filters (see Figure 4.23).  
 3048     Since this neural network has no hidden layers, it is not a DNN, but one can attempt to  
 3049     construct a proper CNN that attempts to reproduce the classification performance of the  
 3050     matched filter network, which can be referred to as "deep filtering".

3051     The reason why deep filtering can be effective is that it may be possible to exploit  
 3052     redundancies and correlations between templates, which allows one to perform signal  
 3053     detection with similar accuracy but with fewer computations. This is relevant to real-time  
 3054     detection scenarios like the FSCD experiment. In Section 4.4 I perform a detailed  
 3055     comparison of the signal detection performance of a CNN to beamforming and a matched

3056 filter template bank.

3057 Deep filtering is conceptually a simple technique. Similar to a matched filter template  
3058 bank, many simulated CRES signals are generated and used to train a model to distinguish  
3059 between signal and noise data (see Figure 4.24). To reduce the dimensionality of the  
3060 input FSCD data, a digital beamforming summation is applied to the raw time-series  
3061 data generated by Locust to compress the 60-channel data to a single time-series. CRES  
3062 signals have a sparse frequency representation and experiments training CNN's on time-  
3063 series and frequency-series data found that models trained on frequency spectrum data  
3064 performed significantly better. Therefore, an FFT is applied to the summed time-series  
3065 before being normalized and fed to the classification model.

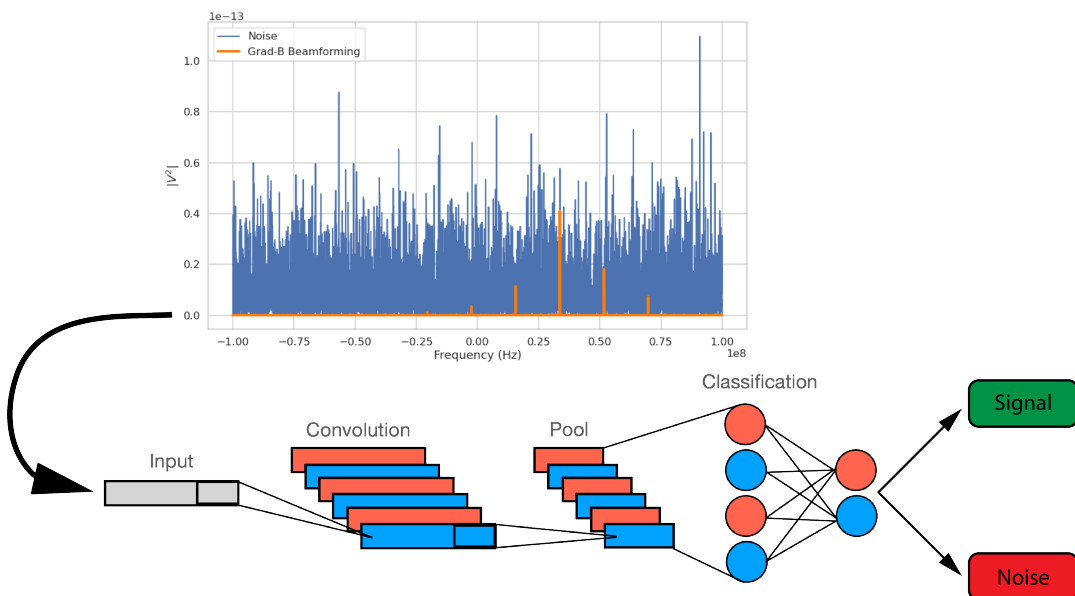


**Figure 4.24.** A graphical depiction of CRES signal detection using a CNN. A noisy segment of data is converted to a frequency series using digital beamforming and a FFT. The complex-valued frequency series is input into a trained CNN model that classifies the data as signal or noise using a decision threshold on the CNN output.

3066 The data used to train the model consists of an equal proportion of signal and noise  
3067 frequency spectra. Unique samples of WGN are generated and added to the signals during  
3068 training time to avoid having to pre-generate and store large samples of noise data. The  
3069 binary cross-entropy loss function combined with the ADAM optimizer proved effective  
3070 at training the models to classify CRES data. A simple hyperparameter optimization  
3071 was performed by manually tuning model, loss function, and optimizer parameters. The  
3072 model and training loops was implemented in python using the PyTorch deep learning  
3073 framework. Standard machine learning practices were followed when training the models,

such as overtraining monitoring using a validation dataset. Models were trained until the training loss and accuracy converged and then evaluated using a separate test data set.

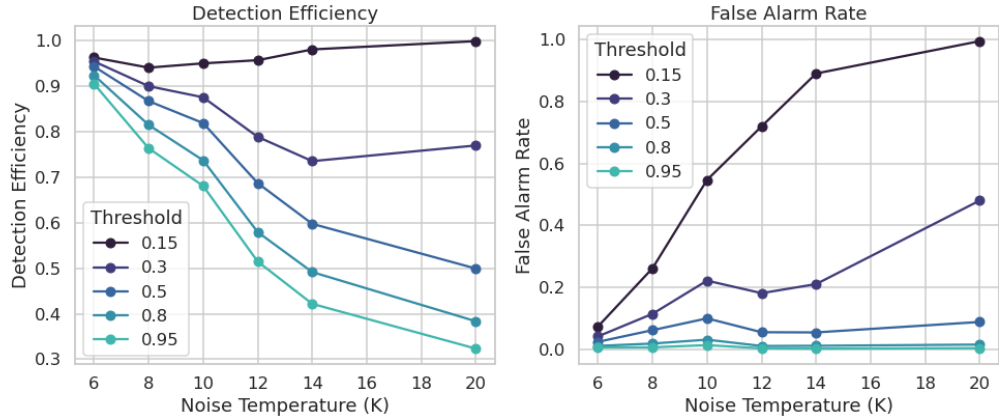


**Figure 4.25.** The detection efficiency and false alarm rate (false positive rate) as a function of the decision threshold for different values of the noise temperature. The model is trained to output a value close to one for data that contains a signal and outputs a value near zero when the data contains only noise. One sees that a lower decision threshold will have a high detection efficiency at the cost of a high rate of false alarms.

The classification results of the test dataset are used to quantify the relationship between the true positive rate and the false positive rate for the model. The true positive rate is analogous to detection efficiency and the false positive rate is a potential source of background in the detector. One can limit the rate of false positives using a sufficiently high threshold on the model output at the cost of a lower detection efficiency (see Figure 4.25 and Figure 4.26). As expected, the performance of the model at signal classification is negatively effected by the noise power, which is quantified by the noise temperature.

## 4.4 Analysis of Signal Detection Algorithms for the FSCD

This section consists of a modified manuscript for an antenna-based CRES signal detection paper prepared for publication in JINST. The contents of this paper were still undergoing collaboration review at the time of writing. In it I present a detailed analysis of the signal detection performance of the three signal detection approaches discussed so far using a population of simulated CRES signals generated with Locust. The focus of the paper is on the performance of the signal detection algorithms for pitch angles below  $88.5^\circ$  where the beamforming power threshold is least effective.

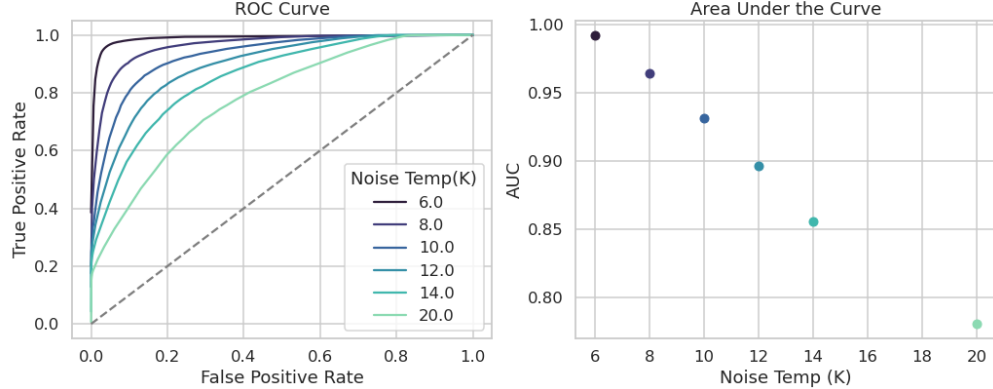


**Figure 4.26.** ROC curves for a CNN model classifying CRES signals. One can see that the area under the curve, which is a figure of merit that describes the performance of the classifier, is roughly linearly dependent with the noise temperature.

### 3091 4.4.1 Introduction

3092 One approach to large volume CRES is to surround a large volume with an array of  
 3093 antennas that together collect a portion of the cyclotron radiation emitted by trapped  
 3094 electrons [41, 83]. A promising design is an inward-facing uniform cylindrical array that  
 3095 surrounds the tritium containment volume. Increasing the size of the antenna array,  
 3096 by adding additional rings of antennas along the vertical axis, allows one to grow the  
 3097 experiment volume until a sufficient amount of tritium gas can be observed by the array.  
 3098 A challenging aspect of this approach is that the total radiated power emitted by an  
 3099 electron near the tritium spectrum endpoint is on the order of 1 fW or less in a 1 T  
 3100 magnetic field, which is then distributed among all antennas in the array. Because the  
 3101 CRES signal information is spread across the antenna array, detecting the presence of  
 3102 a CRES signal and determining the electron's kinetic energy requires reconstructing  
 3103 the entire array output over the course of the CRES event, posing a significant data  
 3104 acquisition and signal reconstruction challenge.

3105 Previous measurements with the CRES technique (see Section 3.3) have utilized  
 3106 a threshold on the frequency spectrum formed from a segment of CRES time-series  
 3107 data. This algorithm relies on the detection of a frequency peak above the thermal  
 3108 noise background, which limits the kinematic parameter space of detectable electrons  
 3109 (see Section 4.4.2.2). Although a power threshold based classification was adequate for  
 3110 smaller detectors, improvements in detection efficiency are needed for better sensitivity  
 3111 to the neutrino mass. Better detection efficiency is possible by taking advantage of the  
 3112 deterministic CRES signal structure with a matched filter or machine learning based

3113 classifier [84]. In order to evaluate the relative gains in detection efficiency that come  
3114 from utilizing these algorithms for antennas, analytical models that describe the detection  
3115 performance a power threshold and matched filter classifier are developed. In addition,  
3116 a basic convolutional neural network (CNN) is implemented and tested as a first step  
3117 towards the development of neural-network based classifiers for antenna array based  
3118 CRES measurements. These results allow for a comparison between the estimated  
3119 detection efficiencies of each of these methods, which are weighed against the associated  
3120 computational costs for real-time applications.

3121 The outline of the remainder of this chapter is as follows. Section 4.4.2 is an overview  
3122 of a prototypical antenna array CRES experiment, and describes the approach to real-time  
3123 signal identification. Section 4.4.3 develops models for the power threshold and matched  
3124 filter algorithms and introduces the machine learning approach and CNN architecture.  
3125 Section 4.4.4 describes the process for generating simulated CRES signal data and the  
3126 details of training the CNN. Finally, Section 4.4.5 compares the signal classification  
3127 accuracy for the three approaches and discusses the relevant trade-offs in terms of  
3128 detection efficiency and computational cost.

## 3129 **4.4.2 Signal Detection with Antenna Array CRES**

### 3130 **4.4.2.1 Antenna Array and Data Rate Estimates**

3131 In order to explore the potential of antenna array CRES for neutrino mass measurement,  
3132 the Project 8 Collaboration has developed a conceptual design for a prototype antenna  
3133 array CRES experiment [41,83], called the Free-space CRES Demonstrator or FSCD (see  
3134 Figure 4.27). The FSCD utilizes a single ring of antennas, which is the simplest form of a  
3135 uniform cylindrical array configuration, to surround a radio-frequency (RF) transparent  
3136 tritium gas vessel. A prototype version of this antenna array has been built and tested  
3137 by the Project 8 collaboration [44] to validate simulations of the array radiation pattern  
3138 and beamforming algorithms [85]. In the FSCD the antenna array is positioned at the  
3139 center of the magnetic trap formed by a set of electromagnetic coils, which create a local  
3140 minimum in the magnetic field with flat central region and steep walls in the radial and  
3141 axial directions.

3142 When an electron is trapped its motion consists of three primary components. The  
3143 component with the highest frequency is the cyclotron orbit whose frequency is determined  
3144 by the size of the background magnetic field. The FSCD design assumes a background  
3145 magnetic field value of approximately 0.96 T, which results in cyclotron frequencies

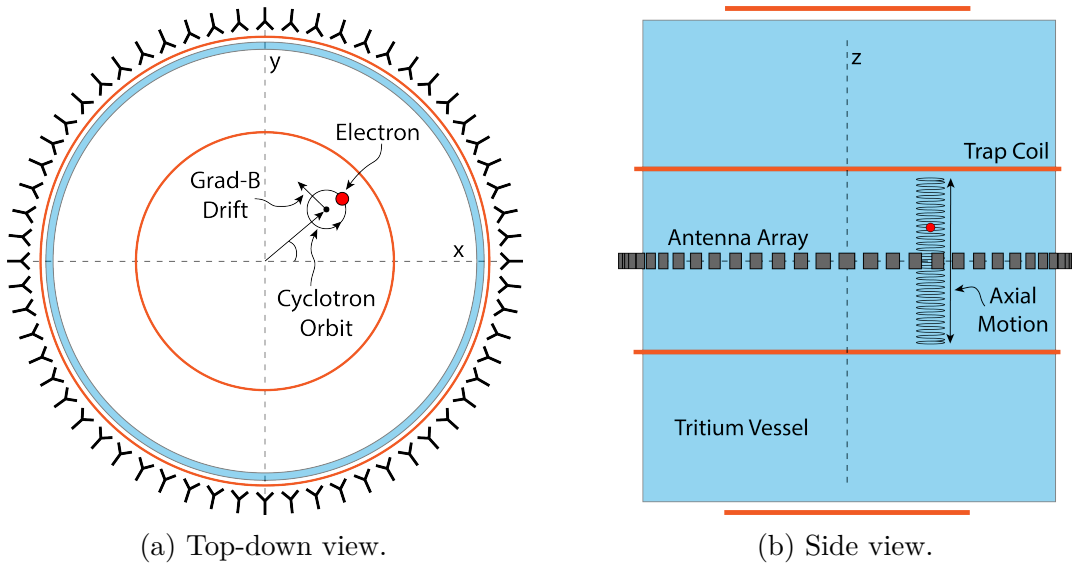


**Figure 4.27.** An illustration of the conceptual design for an antenna array CRES tritium beta-decay spectrum measurement. The antenna array geometry consists of a 20 cm interior diameter with 60 independent antenna channels arranged evenly around the circumference. The nominal antenna design is sensitive to radiation in the frequency range of 25-26 GHz, which corresponds to the cyclotron frequency of electrons emitted near the tritium beta-spectrum endpoint in a 0.96 T magnetic field. The array is located at the center of the magnetic trap produced by a set of current-carrying coils. The nominal magnetic trap design is capable of trapping electrons up to 5 cm away from the central axis of the array and traps electrons within an approximately 6 cm long axial region centered on the antenna array.

for electrons with kinetic energies near the tritium beta-spectrum endpoint of 26 GHz.  
 The component with the next highest frequency is the axial oscillation experienced by electrons with pitch angles<sup>5</sup> of less than 90° [64]. The flat region of the FSCD magnetic trap extends approximately 3 cm above and below the antenna array plane causing electrons to move back and forth as they are reflected from the trap walls. Typical oscillation frequencies are on the order of 10's of MHz, which results in an oscillation period that is  $O(10^3)$  smaller than the duration of a typical CRES event. Therefore, the axial extent of the electron's motion is generally ignored for the purposes of reconstruction, since the electron can be treated as if it is located in the average axial position at the bottom of the magnetic trap. The component of motion with the smallest frequency is the  $\nabla B$ -drift caused by radial field gradients in the trap, producing an orbit of the electron around the central axis of the trap with a frequency on the order of a few kHz, dependent on the pitch angle and the radial position of the electron.

<sup>5</sup>Pitch angle is defined as the angle of the particle's total momentum with respect to the local magnetic field.

3159        Each component of motion influences the shape of the cyclotron radiation signals  
 3160      received by the antenna array; therefore, the data acquisition (DAQ) system must be  
 3161      properly designed in order to resolve the effects of the cyclotron motion, pitch angle, and  
 3162       $\nabla$ -B drift on the signal shape. Frequency down-conversion allows for intentional under-  
 3163      sampling of the CRES signals at a nominal bandwidth of 200 MHz. The bandwidth is  
 3164      required to be large enough to contain all sidebands produced by pitch angle modulation,  
 3165      but must be limited to reduce the Nyquist-Johnson noise power for adequate signal-to-  
 3166      noise ratio. The estimated noise temperature for the FSCD is  $\approx 10$  K, achievable with  
 3167      low-noise HEMT amplifiers and cryogenic temperatures.

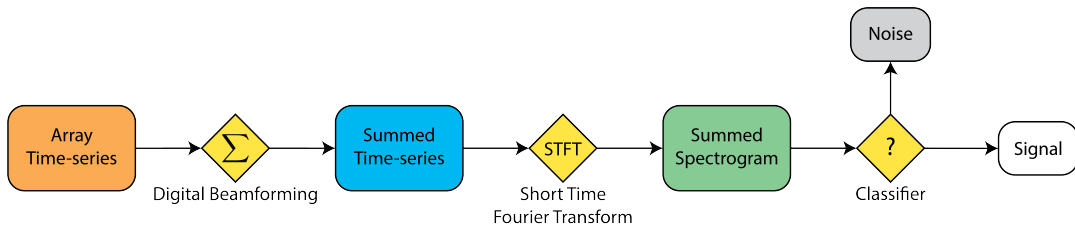


**Figure 4.28.** A block diagram illustration of the real-time triggering algorithm proposed for antenna array CRES reconstruction.

3168        A design goal for the FSCD DAQ system is to enable a significant portion of the  
 3169      CRES event reconstruction to occur in real-time. The estimated data volume generated  
 3170      by the FSCD is 1 exabyte of raw data per year of operation, with the nominal array size  
 3171      of 60 antennas sampled at 200 MHz, which would be too expensive to store for offline  
 3172      processing. Therefore, it is ideal to perform some CRES event reconstruction in real-time  
 3173      so that it is possible to save a reduced form of the data for offline analysis. The first step  
 3174      of the real-time reconstruction would be a real-time signal detection algorithm, which is  
 3175      the focus of this paper. The basic approach consists of three operations performed on the  
 3176      time-series data blocks including digital beamforming, a short time Fourier transform  
 3177      (STFT), and a binary classification algorithm to distinguish between signal and noise  
 3178      data (see Figure 4.28).

#### 3179      4.4.2.2 Real-time Signal Detection

3180      The first step in the real-time detection algorithm is digital beamforming, which is a  
 3181      phased summation of the signals received by the array (see Figure 4.29). The phase shifts  
 3182      correspond to the path length differences between a spatial position and the antennas  
 3183      such that, when there is an electron located at the beamforming position, all the signals  
 3184      received by the array constructively interfere. Since one does not know a priori where an

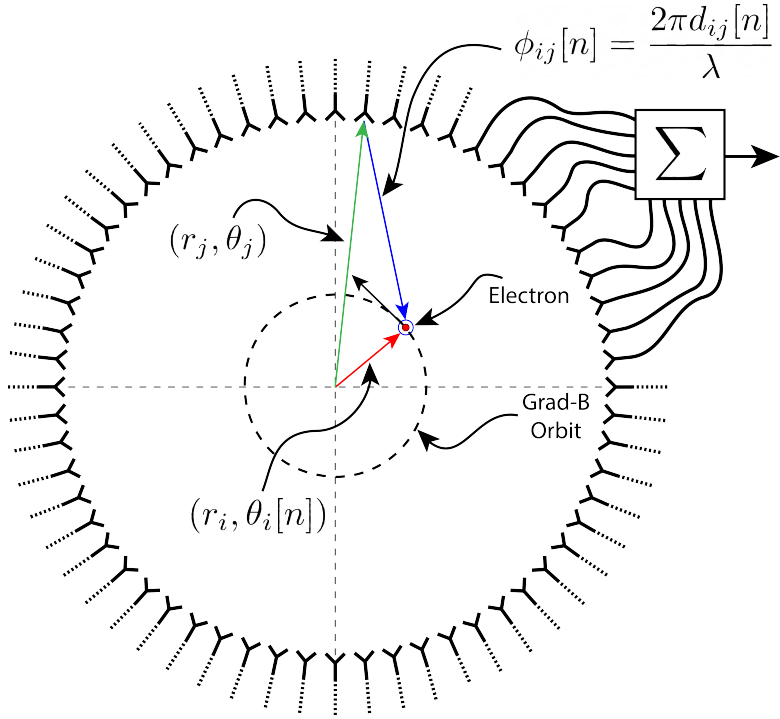


**Figure 4.29.** An illustration of the digital beamforming procedure. The blue lines indicate the distances from the beamforming position to each antenna. In the situation depicted the actual position of the electron matches the beamforming position; therefore, one expects constructive interference when the phase shifted signals are summed. To prevent the electron's  $\nabla B$ -motion from moving the electron off of the beamforming position, the beamforming phases include time-dependence to follow the trajectory of the electron in the magnetic trap.

3185 electron will be produced in the detector, a grid of beamforming positions is designed to  
 3186 cover the entire azimuthal plane where electrons can be trapped. A beamforming phased  
 3187 summation is performed for all points in the grid at each time-step. As shown in Section  
 3188 4.4.2.1, the axial oscillation of the electrons prevents one from resolving its position along  
 3189 the z-axis; therefore, the beamforming grid need only cover the possible positions of the  
 3190 electron in the two-dimensional plane defined by the antenna array.

3191 Digital beamforming can be expressed as

$$\mathbf{y}[n] = \Phi^T[n]\mathbf{x}[n], \quad (4.39)$$

3192 where  $\mathbf{x}[n]$  is the array snapshot vector at the sampled time  $n$ ,  $\Phi[n]$  is the matrix of  
 3193 beamforming phase shifts, and  $\mathbf{y}[n]$  is the summed output vector that contains the  
 3194 voltages for each of the summed channels corresponding to a particular beamforming  
 3195 position. The elements of the beamforming phase shift matrix can be expressed as a

3196 weighted complex exponential

$$\Phi_{ij}[n] = A_{ij}[n] \exp(2\pi i \phi_{ij}[n]), \quad (4.40)$$

3197 where the indices  $i$  and  $j$  label the beamforming and antenna positions respectively. The  
3198 weight  $A_{ij}$  accounts for the relative power increase for antennas that are closer to the  
3199 position of the electron, and  $\phi_{ij}$  is the total beamforming phase shift for the  $j$ -th antenna  
3200 at the  $i$ -th beamforming position.

3201 The beamforming phase shift is a sum of two terms described by Equation 4.23, which  
3202 in the notation of Figure 4.29 is

$$\phi_{ij}[n] = \frac{2\pi d_{ij}[n]}{\lambda} + \theta_{ij}[n]. \quad (4.41)$$

3203 The  $\nabla B$ -drift in the trap is accounted for using time-dependent beamforming phases as  
3204 in Equation 4.25. In the coordinate system of Figure 4.29 the time-dependent azimuthal  
3205 position of the electron is

$$\theta_i[n] = \omega_{\nabla B} t[n] + \theta_{i,0}. \quad (4.42)$$

3206 Predicting accurate values of  $\omega_{\nabla B}$  for a specific trap and set of kinematic parameters can  
3207 be done with simulations, which are performed using the Locust software package [65]  
3208 developed by Project 8.

3209 After digital beamforming, a short-time Fourier transform (STFT) is applied to the  
3210 summed time-series to obtain the signal frequency spectrum (see Figure 4.30). From the  
3211 detection perspective, the frequency representation of the CRES data is advantageous  
3212 compared to the time domain, due to the sparseness of CRES signals in the frequency  
3213 domain. The frequency spectra of CRES signals are well-approximated by a frequency and  
3214 amplitude modulated sinusoidal whose carrier frequency increases as a linear chirp [64].  
3215 The modulation is caused by the axial oscillation of the electron in the magnetic trap,  
3216 and the linear chirp is caused by the energy loss due to cyclotron radiation, which results  
3217 in a relatively slow increase in the frequency components of the CRES signal over time.  
3218 A typical CRES signal increases in frequency by approximately 15 kHz during the  
3219 standard Fourier analysis window of 40.96  $\mu$ sec, which is smaller than the frequency  
3220 bin width for a 200 MHz sample rate. Therefore, when considering a single frequency  
3221 spectrum it is justifiable to neglect the effects of the linear frequency chirp.

3222 The majority of the CRES signal power for electrons in the FSCD trap is contained in  
3223 a single frequency component when the electron has a pitch angle  $\gtrsim 88.5^\circ$ . The remain-

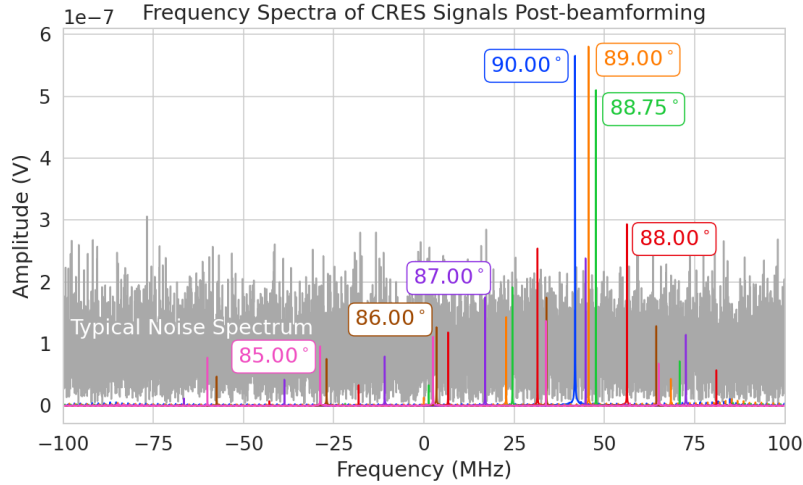


**Figure 4.30.** Frequency spectra of simulated CRES events in the FSCD magnetic trap after beamforming. The signal of a  $90^\circ$  electron consists of a single frequency component that is clearly detectable using a power threshold on the frequency spectrum. This power threshold remains effective for signals with relatively large pitch angles such as  $89.0^\circ$  and  $88.75^\circ$ , which are composed of a main carrier and a few small sidebands. Signals with smaller pitch angles, below about  $88.5^\circ$ , are dominated by sidebands such that no single frequency component can be reliably distinguished from the noise with a power threshold.

ing signal power is distributed between a small number of sidebands with amplitudes proportional to the electron's axial modulation (see Figure 4.30). Signal detection for these pitch angles is straightforward using a simple power threshold on the STFT, since the amplitude of the main signal peak is well above the thermal noise spectrum. However, as the pitch angle of the electron is decreased below  $88.5^\circ$ , the maximum amplitude of the frequency spectrum becomes comparable to typical noise fluctuations. At this point, the power threshold trigger is no longer able to distinguish between signal and noise leading to a reduction in detection efficiency, which is directly linked to the neutrino mass sensitivity of the FSCD. Because the distribution of electron pitch angles is effectively uniform, utilizing a signal detection algorithm that can improve efficiency for pitch angles less than  $88.5^\circ$  will lead to improvements in the neutrino mass sensitivity of the FSCD.

#### 4.4.3 Signal Detection Algorithms

Modeling detection performance requires one to pose the signal detection problem in a consistent manner. The approach studied here uses the frequency spectra obtained from a STFT applied to the beamformed time-series from the FSCD to perform a binary hypothesis test. The basic mathematics of this hypothesis test approach was described

3240 above (Section 4.3), where the noise and signal hypotheses represent the following samples  
 3241 of data,

$$\mathcal{H}_0 : y[n] = \nu[n] \quad (4.43)$$

$$\mathcal{H}_1 : y[n] = x[n] + \nu[n]. \quad (4.44)$$

3242 Under hypothesis  $\mathcal{H}_0$  the vector representing the frequency spectrum ( $y[n]$ ) is composed of  
 3243 complex white Gaussian noise (cWGN,  $\nu[n]$ ) with total variance  $\tau$ , and under hypothesis  
 3244  $\mathcal{H}_1$  the frequency spectrum is composed of a CRES signal ( $x[n]$ ) with added cWGN.  
 3245 The dominant noise source for the FSCD is expected to be thermal Nyquist-Johnson  
 3246 noise, which is well approximated by a cWGN distribution. The hypothesis test is  
 3247 performed by calculating the ratio between the log-likelihood probability distributions  
 3248 for the classifier under  $\mathcal{H}_1$  and  $\mathcal{H}_0$ , which is the standard Neyman-Pearson approach  
 3249 to hypothesis testing [74]. The output of the log-likelihood ratio test is called the test  
 3250 statistic, which is used to assign the data as belonging to the noise or signal classes using  
 3251 a decision threshold.

3252 In practice, the decision threshold is selected by finding the value of the test statistic  
 3253 that guarantees a tolerable rate of false positives. Given this false positive rate (FPR),  
 3254 one attempts to find a classifier that maximizes the true positive rate (TPR), which is  
 3255 the probability of correctly identifying if a piece of data contains signal or noise. Because  
 3256 FSCD signal classifiers will be used to evaluate the spectra of  $O(10^2)$  beamforming  
 3257 positions every  $40.96 \mu\text{sec}$ , there is a requirement that the signal classifiers with FPR  
 3258 significantly smaller than 1% to reduce the burden placed on later stages of the CRES  
 3259 reconstruction chain.

#### 3260 4.4.3.1 Power Threshold

3261 The power threshold detection algorithm uses the maximum amplitude of the frequency  
 3262 spectrum as the detection test statistic. Consider the  $\mathcal{H}_0$  hypothesis where the signal is  
 3263 pure cWGN. The performance of the power threshold can be modeled by first analyzing  
 3264 a single bin in the frequency spectrum. The probability that the amplitude of a single  
 3265 frequency bin falls below the decision threshold is given by the Rayleigh cumulative  
 3266 distribution function (CDF),

$$\text{Ray}(x; \tau) = 1 - \exp(-|x|^2/\tau), \quad (4.45)$$

3267 where the complex value of the frequency bin is  $x$ , and  $\tau$  is the cWGN variance. Because  
 3268 the noise samples are independent and identically distributed (IID), the probability that  
 3269 all bins in the frequency spectrum fall below the threshold is the joint CDF formed by  
 3270 the product of each individual frequency bin CDF,

$$F_0(x; \tau, N_{\text{bin}}) = \text{Ray}(x; \tau)^{N_{\text{bin}}}. \quad (4.46)$$

3271 Finally, the PDF for the power threshold classifier can be obtained by differentiating  
 3272 Equation 4.46.

3273 The noise variance of a beamformed frequency spectrum can be obtained directly  
 3274 from the estimated noise power in a single antenna channel. The Nyquist-Johnson noise  
 3275 power is given by  $k_B T \Delta f$ , where  $k_B$  is Boltzmann's constant,  $T$  is the system noise  
 3276 temperature, and  $\Delta f$  is the sample rate. The beamformed noise variance is increased  
 3277 by a factor of  $N_{\text{ch}}$ , where  $N_{\text{ch}}$  is the number of antennas, caused by the summation of  
 3278 incoherent noise samples, however, the noise variance per frequency bin is decreased by a  
 3279 factor equal to the number of samples in the STFT ( $N_{\text{FFT}}$ ). The final expression for the  
 3280 noise variance of the beamformed frequency spectrum is given by

$$\tau = k_B T \Delta f N_{\text{ch}} R / N_{\text{FFT}}, \quad (4.47)$$

3281 where the system impedance ( $R$ ) has been used to convert from power to voltage-squared.

3282 The probability distribution for the power threshold classifier under  $\mathcal{H}_1$  is calculated  
 3283 in a similar way, but the frequency bins that contain signal must be treated separately.  
 3284 The probability that the amplitude of a frequency bin containing both signal and noise  
 3285 bin falls below the decision threshold is described by a Rician CDF,

$$\text{Rice}(x; \tau, \alpha) = 1 - \int_x^\infty d|\tilde{x}| \frac{2|\tilde{x}|}{\tau} \exp\left(-\frac{|\tilde{x}|^2 + |\alpha|^2}{\tau}\right) \mathcal{I}_0\left(\frac{2|\tilde{x}||\alpha|}{\tau}\right), \quad (4.48)$$

3286 where the parameter  $|\alpha|$  defines the noise-free amplitude of the signal. The CDF that  
 3287 describes the probability that the entire spectrum falls below the decision threshold is  
 3288 the product of both signal and noise CDFs,

$$F_1(x; \tau, \alpha, N_{\text{bin}}, N_s) = \text{Ray}(x; \tau)^{N_{\text{bin}} - N_s} \prod_{k=0}^{N_s} \text{Rice}(x; \tau, \alpha_k). \quad (4.49)$$

3289 The first half of Equation 4.49 is the contribution from the bins in the frequency spectrum

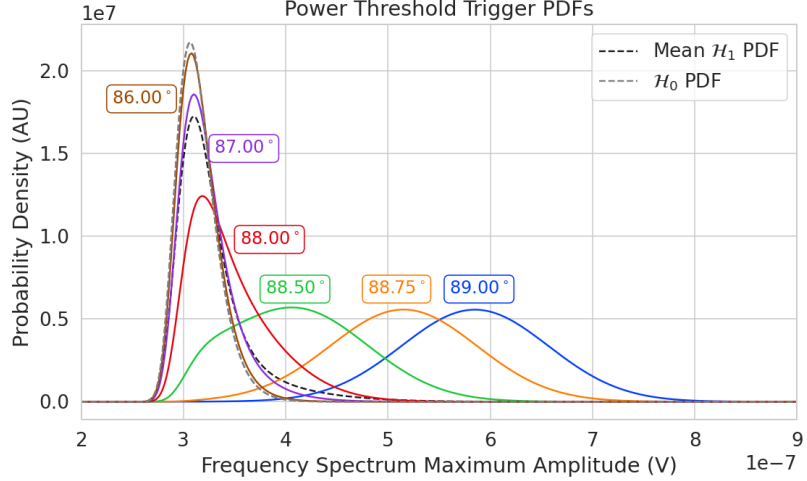


**Figure 4.31.** PDFs of the power threshold test statistic for CRES signals with various pitch angles as well as the PDF for the noise-only signal case. The average PDF computed for pitch angles ranging from 85.5 to 88.5° is also shown. As the pitch angle is decreased the signal PDF converges towards the noise PDF which indicates that the power threshold trigger is unable to distinguish between small pitch angle signals and noise.

3290 that contain only noise, and the second half is the product of the Rician CDFs for the  
 3291 frequency bins that contain signal peaks with a noise-free amplitude of  $|\alpha_k|$ . Figure 4.31  
 3292 shows plots of example PDFs under  $\mathcal{H}_1$  and  $\mathcal{H}_0$ .

#### 3293 4.4.3.2 Matched Filtering

3294 The shape of a CRES signal in-between random scattering events with the background  
 3295 gas is completely determined by the initial conditions of the electron, which implies that  
 3296 it is possible to apply matched filtering as a signal detection algorithm. A matched filter  
 3297 uses the shape of the known signal, which is called a template, to filter the incoming  
 3298 data by computing the convolution between the signal and the data [74]. The matched  
 3299 filter is the optimal detector, which means it achieves the maximum TPR for a particular  
 3300 FPR, under the assumption that the signal is perfectly known and the noise is Gaussian  
 3301 distributed. Since CRES signals have an unknown shape but are deterministic, the  
 3302 matched filter can be applied by using simulations to generate a large number of signal  
 3303 templates, called a "template bank", which spans the parameter space of possible signals.  
 3304 Then at detection time, the template bank is used to identify signals by performing the  
 3305 matched filter convolution for each template in an exhaustive search.

3306 CRES signals are highly periodic in nature. In such cases, it is advantageous to utilize  
 3307 the convolution theorem to replace the matched filter convolution with an inner product

3308 in the frequency-domain. Utilizing the matched filter formalism described above (Section  
 3309 4.3.2) the matched filter test statistic can be written as

$$\mathcal{T} = \max_h \left| \sum_{n=0}^{N_{\text{bin}}} h^\dagger[n] y[n] \right|, \quad (4.50)$$

3310 where  $h^\dagger[n]$  is the complex conjugate of the signal template.

3311 The approach to deriving PDFs that describe the matched filter template bank will  
 3312 be to first derive PDFs for  $\mathcal{H}_0$  and  $\mathcal{H}_1$  in the case of a single template and use these  
 3313 solutions to create PDFs that describe the multi-template case. In the case when the  
 3314 template bank consists of only a single template it is possible to derive an exact analytical  
 3315 form for the PDF. Consider the  $\mathcal{H}_1$  case, where the equation describing the matched  
 3316 filter test statistic, also known as the matched filter score, becomes

$$\mathcal{T} = \left| \sum_{n=0}^{N_{\text{bin}}} h^\dagger[n] y[n] \right|. \quad (4.51)$$

3317 Each noisy frequency bin is a sum of signal and cWGN, which means  $y[n]$  is also a  
 3318 Gaussian distributed variable. Therefore, the value of the inner product between the  
 3319 template and the data is also a complex Gaussian variable; and, since the matched filter  
 3320 score is the magnitude of this inner product, it must follow a Rician distribution.

3321 The distribution that describes the matched filter score under  $\mathcal{H}_1$  can be derived  
 3322 starting with the matched filter template equation. The matched filter template  $\mathbf{h}$  is a  
 3323 simulated signal ( $\mathbf{x}_h$ ) with a normalization factor

$$\mathbf{h} = \frac{\mathbf{x}_h}{\sqrt{\tau |\mathbf{x}_h|^2}}, \quad (4.52)$$

3324 where  $\tau$  is the noise variance. Inserting this into Equation 4.50 and expressing the data  
 3325 as a sum between a signal and a WGN vector yields,

$$\mathcal{T} = \frac{1}{\sqrt{\tau |\mathbf{x}_h|^2}} \left| \sum_{n=1}^{N_{\text{bin}}} x_h^\dagger[n] x[n] + \sum_{n=1}^{N_{\text{bin}}} x_h^\dagger[n] \nu[n] \right|. \quad (4.53)$$

3326 The first term is a scalar product between the signal and template vectors and the  
 3327 second term is a complex Gaussian distributed variable with variance one. For the  
 3328 purposes of identifying the statistical distribution, it is useful to rewrite the summation

<sup>3329</sup> describing an inner product

$$\sum_{n=1}^{N_{\text{bin}}} x_h^\dagger[n]x[n] = \mathbf{x}_h \cdot \mathbf{x} = |\mathbf{x}_h \cdot \mathbf{x}|e^{i\vartheta} \leq |\mathbf{x}_h||\mathbf{x}|e^{i\vartheta}, \quad (4.54)$$

<sup>3330</sup> the last step utilizes the Cauchy-Schawrz inequality, where equality is guaranteed when  
<sup>3331</sup>  $\mathbf{x} = \mathbf{x}_h$ . Instead of the inequality it is useful to define a quantity called "match" such that

$$|\mathbf{x}_h \cdot \mathbf{x}|e^{i\vartheta} = |\mathbf{x}_h||\mathbf{x}|\Gamma e^{i\vartheta}, \quad (4.55)$$

<sup>3332</sup> where the match factor  $\Gamma \in [0, 1]$ . The match factor quantifies how well the template  
<sup>3333</sup> matches the signal.

<sup>3334</sup> The fact that the second term is a random complex Gaussian variable with unity  
<sup>3335</sup> variance can be seen by noting that each of the noise samples are drawn from the complex  
<sup>3336</sup> Gaussian distribution,  $\mathcal{N}(0, \tau)$ . Therefore,

$$\frac{x_h^\dagger[n]}{\sqrt{\tau|\mathbf{x}_h|^2}}\nu[n] \sim \mathcal{N}\left(0, \frac{x_h^\dagger[n]x_h[n]}{|\mathbf{x}_h|^2}\right), \quad (4.56)$$

$$n = \sum_{n=1}^{N_{\text{bin}}} \frac{x_h[n]}{\sqrt{\tau|\mathbf{x}_h|^2}}\nu[n] \sim \mathcal{N}\left(0, \frac{\sum_{n=1}^{N_{\text{bin}}} x_h^\dagger[n]x_h[n]}{|\mathbf{x}_h|^2}\right) = \mathcal{N}(0, 1). \quad (4.57)$$

<sup>3337</sup> Equation 4.53 can now be simplified

$$\mathcal{T} = ||\mathbf{h}||\mathbf{x}|\Gamma e^{i\vartheta} + n|, \quad (4.58)$$

<sup>3338</sup> where Equation 4.52 has been used to redefine the inner product term. The quantity  
<sup>3339</sup>  $||\mathbf{h}||\mathbf{x}|\Gamma$  is a real number, which is the matched filter score that one would expect if the  
<sup>3340</sup> data contained no noise. The final simplification is to define  $\mathcal{T}_{\text{ideal}} = ||\mathbf{h}||\mathbf{x}|\Gamma$ , from which  
<sup>3341</sup> one obtains

$$\mathcal{T} = |\mathcal{T}_{\text{ideal}}e^{i\vartheta} + n|. \quad (4.59)$$

<sup>3342</sup> From Equation 4.59 on can see that  $\mathcal{T}$  is simply the magnitude of a complex number  
<sup>3343</sup> with added cWGN of variance 1, which follows the Rician distribution; therefore the  
<sup>3344</sup> distribution that describes the matched filter score for a single template under  $\mathcal{H}_1$  is

$$P_1(x; \mathcal{T}_{\text{ideal}}) = 2x \exp(- (x^2 + \mathcal{T}_{\text{ideal}}^2)) I_0(2x\mathcal{T}_{\text{ideal}}). \quad (4.60)$$

<sup>3345</sup> The shape of the matched filter score distribution is controlled by the parameter  $\mathcal{T}_{\text{ideal}}$ ,

3346 which is effectively the value of the matched filter score if the data contained no noise.  
 3347 Without noise, the data vector reduces to the signal,  $\mathbf{x}$ , in which case Equation 4.51  
 3348 becomes the magnitude of an inner product between two vectors. The magnitude of an  
 3349 inner product can be expressed in terms of the magnitudes of the vectors and a constant  
 3350 that describes the degree of orthogonality between them. Applying this to Equation 4.51,  
 3351 one obtains

$$\mathcal{T}_{\text{ideal}} = |\mathbf{h}^\dagger \cdot \mathbf{x}| = |\mathbf{h}| |\mathbf{x}| \Gamma \quad (4.61)$$

3352 where  $\Gamma$  describes the orthogonality between  $\mathbf{h}$  and  $\mathbf{x}$ .  $\Gamma$  effectively quantifies how well  
 3353 the template matches the unknown signal in the data.

3354 The matched filter score PDF under  $\mathcal{H}_0$  is readily obtained from Equation 4.60 by  
 3355 setting the value of  $\mathcal{T}_{\text{ideal}}$  to zero, since the data contains no signal in the noise case.  
 3356 Doing this, one obtains a Rayleigh distribution,

$$P_0(x) = 2x \exp(-x^2). \quad (4.62)$$

3357 Equations 4.60 and 4.62 describe the behavior of the matched filter test statistic  
 3358 under  $\mathcal{H}_0$  and  $\mathcal{H}_1$  for a single template. However, defining a PDF that describes the  
 3359 matched filter test statistic in the case of multiple templates is in general a mathematically  
 3360 intractable problem, since there is no guarantee of orthogonality between matched filter  
 3361 templates. This leads to correlations between the matched filter scores of different  
 3362 templates, because only one sample of noise is used to compute the matched filter scores  
 3363 of the template bank. In order to proceed, it is assumed that the matched filter scores for  
 3364 all templates are IID variables, which allows one to ignore correlations between templates.  
 3365 The overall effect of this will be an underestimate of the performance of the matched  
 3366 filter by over-estimating the required number of templates and; therefore, the magnitude  
 3367 of the statistical trials penalty.

3368 The probability that the matched filter score falls below the decision threshold under  
 3369  $\mathcal{H}_0$  is again given by the CDF. Because of the assumption that matched filter scores from  
 3370 different templates are independent, the probability that the matched filter score for all  
 3371 templates falls below the threshold value is simply the joint CDF, which is

$$F_0(x) = \left(1 - e^{-x^2}\right)^{N_t}, \quad (4.63)$$

3372 where  $x$  is the matched filter score threshold and  $N_t$  is the number of templates. One  
 3373 should expect that the distribution describing the maximum score of the matched filter

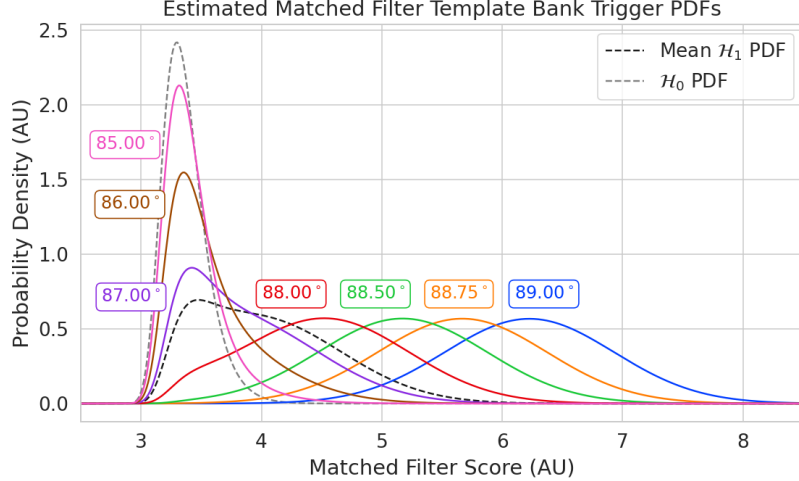


**Figure 4.32.** Plots of PDFs that describe the matched filter template bank test statistic for CRES signals with various pitch angles, as well as the estimated PDF for the noise only case.  $10^5$  matched filter templates are used and perfect match between signal and template i.e.  $\Gamma_{\text{best}} = 1$  is assumed. The mean PDF includes signals ranging from  $85.5 - 88.5^\circ$  in pitch angle. There is a larger distinction between the signal PDFs at small pitch angles compared to the power threshold, which indicates a higher detection efficiency for these signals.

3374 template bank depends on  $N_t$ , because with more templates there is a greater chance of  
 3375 a random match between the template and data.

3376 The CDF that describes  $\mathcal{H}_1$  is derived by starting with the CDF of the best matching  
 3377 template,  $F_{\text{best}}(x; \mathcal{T}_{\text{best}})$ . Because of the orthogonality assumption, the matched filter  
 3378 scores for all other templates are negligible ( $\mathcal{T}_{\text{ideal}} \approx 0$ ). The joint CDF that describes  
 3379 the total template bank is obtained by combining the distributions for all templates used  
 3380 during detection. Therefore, the estimated CDF under  $\mathcal{H}_1$  is

$$F_1(x; \mathcal{T}_{\text{best}}) = F_{\text{best}}(x; \mathcal{T}_{\text{best}}) \left(1 - e^{-x^2}\right)^{N_t}. \quad (4.64)$$

3381 Figure 4.32 shows plots of the matched filter template bank PDFs under  $\mathcal{H}_0$  and  $\mathcal{H}_1$ .

#### 3382 4.4.3.3 Machine Learning

3383 The focus in this paper is on the potential of Convolutional Neural Networks (CNN)  
 3384 as a machine learning based signal classifier at the trigger level. CNNs are constructed  
 3385 using a series of convolutional layers, each composed of a set of filters that are convolved  
 3386 with the input data. The individual convolutional filters can be viewed heuristically  
 3387 as matched filter templates [86] that are learned from a set of simulated data rather

than being directly generated. This opens the possibility of finding a more efficient representation of the matched filter templates during the training process that can potentially reduce computational cost at inference time while retaining good classification performance.

The machine learning approach is distinct from the power threshold and matched filtering in that there is no attempt to manually engineer a test statistic that can be computed from the input data. Instead, a test statistic is calculated by constructing a differentiable function that maps the complex frequency series to a binary classification as signal or noise. The differentiable function is trained using supervised learning to correctly perform this mapping. The test statistic for the machine learning classifier is expressed mathematically as

$$\mathcal{T} = G(\mathbf{y}; \boldsymbol{\Omega}) \quad (4.65)$$

where  $\mathbf{y}$  is the noisy data vector and  $G(\mathbf{y}; \boldsymbol{\Omega})$  is the machine learning model parameterized by the weights  $\boldsymbol{\Omega}$ .

**Table 4.1.** A summary of the CNN model layers and parameters. The output of each 1D-Convolution and Fully Connected layer is passed through a LeakyReLU activation function and re-normalized using batch normalization before being passed to the next layer in the model. The output of the final Fully Connected layer in the model is left without activation so that the model outputs can be directly passed to the Binary Cross-entropy loss function used during training. The first layer in the network has two input channels for the real and imaginary components of the spectrum.

Layer	Type	Input Channels	Output Channels	Parameters
1	1D-Convolution	2	15	( $N_{\text{kernel}} = 4$ , $N_{\text{stride}} = 1$ )
2	Maximum Pooling	15	15	( $N_{\text{kernel}} = 4$ , $N_{\text{stride}} = 4$ )
3	1D-Convolution	15	20	( $N_{\text{kernel}} = 4$ , $N_{\text{stride}} = 1$ )
4	Maximum Pooling	20	20	( $N_{\text{kernel}} = 4$ , $N_{\text{stride}} = 4$ )
5	1D-Convolution	20	25	( $N_{\text{kernel}} = 4$ , $N_{\text{stride}} = 1$ )
6	Maximum Pooling	25	25	( $N_{\text{kernel}} = 4$ , $N_{\text{stride}} = 4$ )
7	Fully Connected	3200	512	NA
8	Fully Connected	512	64	NA
9	Fully Connected	64	2	NA

The CNN architecture used for this work is summarized by Table 4.1. No strategic hyper-parameter optimization approach was implemented beyond the manual testing of different CNN architecture variations, so this particular model is best viewed as a proof-of-concept rather than a rigorously optimized design. Numerous model variations were tested, some with significantly more layers and convolutions filters per layer, as well as others that were even smaller than the architecture in Table 4.1. Ultimately, the

3407 model architecture choice was driven by the motivation to find the minimal model whose  
3408 classification performance was still comparable to the larger CNN's tested, because of  
3409 the importance of minimizing computational cost in real-time applications. It is possible  
3410 that more sophisticated machine learning models could improve upon the classification  
3411 results achieved here, but this investigation is left for future work.

#### 3412 4.4.4 Methods

##### 3413 4.4.4.1 Data Generation

3414 Simulated CRES signals were generated using the Locust simulations package [65, 77].  
3415 Locust uses the separately developed Kassiopeia package [63] to calculate the magnetic  
3416 fields produced by a user defined set of current carrying coils along with any specified  
3417 background magnetic fields, resulting in a magnetic trap. Next, Kassiopeia calculates the  
3418 trajectory of an electron in this magnetic field starting from a set of user specified initial  
3419 conditions. The Locust software then uses the electron trajectories from Kassiopeia  
3420 to calculate the resulting electromagnetic fields using the Liénard-Wiechert equations,  
3421 and determines the voltages generated in the antenna array with the antenna transfer  
3422 function. Locust then simulates the down-conversion, filtering, and digitization steps  
3423 resulting in the simulated CRES signals for an electron.

3424 The shape of the received CRES signal is determined by the initial kinematic param-  
3425 eters, including the starting position of the electron, the starting kinetic energy of the  
3426 electron, and the pitch angle. The studies performed here are constrained to a single  
3427 initial electron position located at  $(x, y, z) = (5, 0, 0)$  mm. Two datasets are generated  
3428 using this starting position by varying the initial kinetic energy and pitch angle. The  
3429 first dataset consists of a two-dimensional square grid spanning an energy range from  
3430 18575-18580 eV with a spacing of 0.1 eV, and pitch angles from 85.5-88.5° with a spacing  
3431 of 0.001°, resulting in 153051 signals with a unique energy-pitch angle combination. This  
3432 dataset is intended to represent a matched filter template bank. The upper range of pitch  
3433 angles is limited because of the greater relative detection efficiency of the matched filter  
3434 and neural network classifiers in this pitch angle range. The second dataset was generated  
3435 by randomly sampling uniform probability distributions covering the same parameter  
3436 space to produce approximately 50000 signals randomly parameterized in energy and  
3437 pitch angle. This dataset provides the training and test data for the machine learning  
3438 approach, and acts as a representative sample of signals to evaluate the performance of  
3439 the matched filter template bank.

3440     Each signal was simulated for a duration of  $40.96 \mu\text{s}$  or 8192 samples starting at  
 3441    time  $t = 0$  s for all simulations. This duration represents a single frequency spectrum  
 3442    generated by the STFT. The FSCD antenna array has sixty channels, and the output of  
 3443    the Locust simulations are a matrix of array snapshots with a size given by the number  
 3444    of channels times the event length ( $N_{\text{ch}} \times N_{\text{sample}}$ ). The raw data from Locust is first  
 3445    summed using digital beamforming and converted to frequency spectra using a Fourier  
 3446    transform. The beamforming procedure uses the exact position and  $\nabla B$ -drift correction  
 3447    to simplify the comparison between trigger algorithms. Many beamforming positions  
 3448    would be used in practice and potentially several estimates of a typical  $\omega_{\nabla B}$  depending  
 3449    on the variation of the  $\nabla B$ -drift frequency with pitch angle.

#### 3450    **4.4.4.2 Template Number and Match Estimation**

3451    The estimated PDF for the matched filter template bank on the number of templates and  
 3452    the mean match ( $\Gamma_{\text{best}}$ ). A given signal with random parameters will have a template in  
 3453    the filter bank that gives the highest matched filter score; therefore, the mean match  
 3454    ratio is obtained by averaging over the best matching templates for a representative  
 3455    population of test signals.  $\Gamma_{\text{best}}$  is a figure of merit that characterizes the performance of  
 3456    a template bank at signal detection. One expects that with more templates the value  
 3457    of  $\Gamma_{\text{best}}$  will increase, however, there is a point of diminishing returns at which more  
 3458    templates will not significantly increase match, but will still increase the likelihood of  
 3459    false positives. Therefore, it is desirable to use the minimum number of templates that  
 provide an acceptable mean value of  $\Gamma_{\text{best}}$ .

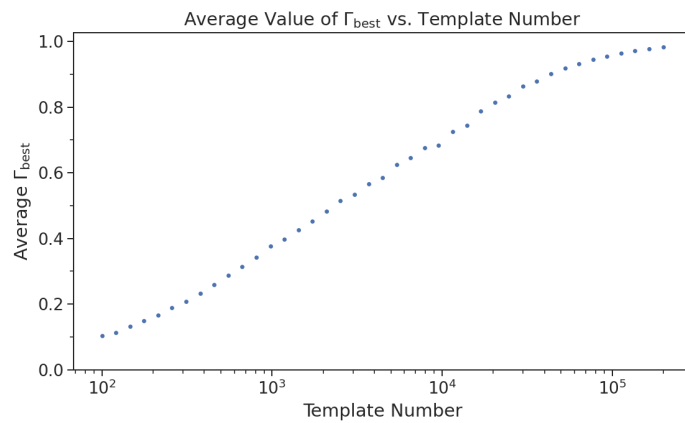


**Figure 4.33.** The mean match of the matched filter template bank to a test set of randomly parameterized signals as a function of the number or density of templates. The parameter space includes pitch angles from  $85.5 - 88.5^\circ$  and energies from 18575 – 18580 eV.

3460 To quantify the relationship between match and template number, the mean match  
3461 of the random dataset to a selection of templates from the regularly spaced dataset was  
3462 calculated using a subset of the mean match values from Figure 4.18 with a sample  
3463 length of 8192. Again, one sees that the average value of  $\Gamma_{\text{best}}$  is an exponential function  
3464 of the number of templates (see Figure 4.33). Using this plot one can infer the required  
3465 number of templates for the desired value of mean match.

#### 3466 4.4.4.3 CNN Training and Data Augmentation

3467 The random dataset is split in half to create distinct training and test datasets for  
3468 training the model. A randomly selected 20% of the training data is isolated for use as  
3469 a validation set during the training loop. The size of the training, validation, and test  
3470 datasets are tripled by appending two additional copies of the data to increase the sample  
3471 size of the dataset after data augmentation. A different sample of noise is added to the  
3472 simulation data during the training loop, which prevents the model from overtraining on  
3473 noise features. The training and test datasets contain an equal split between signal and  
3474 noise data, which are randomly shuffled after each training epoch.

3475 The Locust simulation data was augmented to make the datasets more representative  
3476 of actual experiment data. As the signals are loaded for training a unique random phase  
3477 shift is applied. Since the simulations are generated using the same initial axial position  
3478 and cyclotron orbit phase, the randomization is an attempt to prevent overtraining on  
3479 these features. During each training epoch the data is randomly shuffled and split into  
3480 batches of 2500 signals. Each batch of signals is then circularly shifted by a random  
3481 number of frequency bins to simulate a kinetic energy shift from  $-75$  to  $20$  eV, which  
3482 imitates a dataset with a larger energy range. Next, a sample of cWGN, consistent  
3483 with  $10$  K Nyquist-Johnson noise, is generated and added to the signal, which prevents  
3484 overtraining on noise features. As a final step, the data is renormalized by the standard  
3485 deviation of the noise so that the range of values in the data is close to  $[-1, 1]$ , which  
3486 ensures well-behaved back-propagation.

3487 The Binary Cross-entropy loss function is used to compute the loss for each batch of  
3488 data, and the model weights are updated using the ADAM optimizer with a learning  
3489 rate of  $5 \times 10^{-3}$ . After each training epoch, the loss and classification accuracy of the  
3490 validation dataset are computed to monitor for overtraining. It was noticed that because  
3491 of the relatively high noise power and the fact that a new sample of noise was used for  
3492 each batch, it was nearly impossible to over-train the model. Typically, the loss and

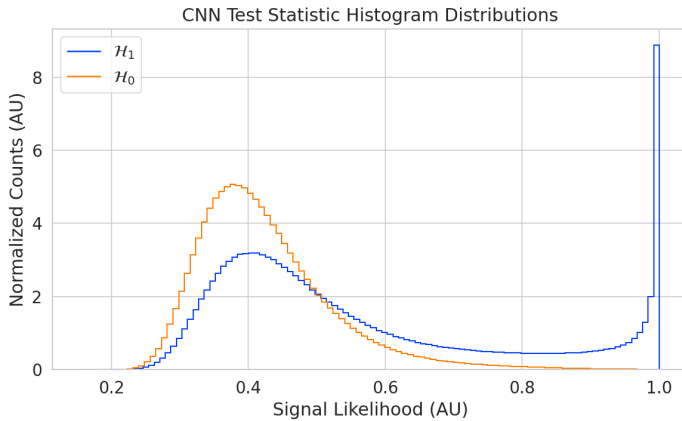


**Figure 4.34.** Histograms of the trained CNN model output from the test dataset. The blue histogram shows the model outputs for signal data. The oddly shaped peak near the end is the result of the softmax function mapping the long tail of the raw output distribution to the range  $[0, 1]$ .

classification accuracy of the model converged after a few hundred training epochs, but the training loop was extended to 3000 epochs to attempt to achieve the best possible performance. The training procedure generally took about 24 hrs using a single NVIDIA V100 GPU [87].

After training the model, it was used to classify the test dataset and generate histograms of the model outputs for both classes of data. The data augmentation procedure for the evaluation of the test data mirrors the training procedure without the validation split. Since a random circular shift and a new sample of WGN is added to each batch, the testing evaluation loop is run for 100 epochs to get a representative sample of noise and circular shifts. The model outputs are passed through a softmax activation and then combined into histograms (see Figure 4.34).

## 4.4.5 Results and Discussion

### 4.4.5.1 Trigger Classification Performance

The detection performance of the signal classifiers can be compared by computing the receiver operating characteristic (ROC) curves (see Figure 4.35). A single ROC curve is obtained for the matched filter and power threshold classifiers by averaging over analytical ROC curves obtained from the distributions in Section 4.4.3. Two ROC curves are calculated for the matched filter with different numbers of templates and mean match. The ROC curve describing the CNN is obtained numerically from the histograms of the

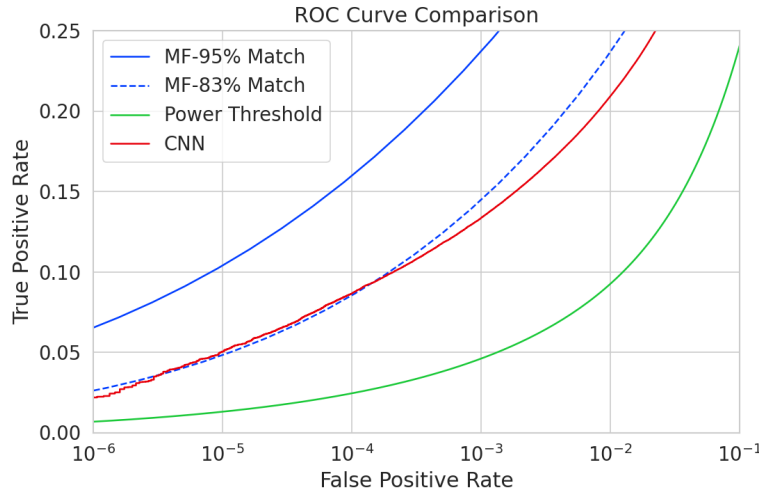


**Figure 4.35.** ROC curves describing the detection efficiency or true positive rates for the three signal classification algorithms examined in this paper. The matched filter (MF) and Power Threshold curves are computed analytically using the distribution functions introduced in Section 4.4.3, and the CNN curve is computed numerically using the classification results on the test dataset. The percent match indicated in the legend refers to the mean match of the classifier.

3512 model outputs for each signal class.

3513 The TPR of a signal classifier is equivalent to its detection efficiency, and one sees  
 3514 that for the population of signals with pitch angles  $< 88.5^\circ$  the power threshold has  
 3515 a consistently lower detection efficiency than the CNN and the matched filter. This  
 3516 result might have been predicted from the visualization of signal spectra in Figure 4.30,  
 3517 where it can be seen that a noise peak and a signal peak cannot be distinguished with  
 3518 high-confidence at small pitch angles. The CNN offers a significant and consistent increase  
 3519 in detection efficiency over the power threshold approach, with the relative improvement  
 3520 in detection efficiency increasing as the false positive rate decreases.

3521 If one compares the CNN to the matched filter, it can be seen that the performance of  
 3522 the tested network is roughly equivalent to a matched filter detector with a mean match  
 3523 of about 83%, which uses approximately  $2 \times 10^4$  matched filter templates. The overall  
 3524 best detection efficiency is achieved by the matched filter classifier if a large enough  
 3525 template bank is used. The plot displays the ROC curve for a matched filter template  
 3526 bank with 95% mean match, which is achieved with approximately  $10^5$  templates. Since  
 3527 the matched filter is known to be statistically optimal for detecting a known signal in  
 3528 WGN, it is unsurprising that this algorithm has the highest detection efficiency.

3529 An important difference between the matched filter and CNN algorithms is that the

3530 CNN relies upon convolutions as its fundamental calculation mechanism; whereas our  
3531 implementation of a matched filter utilizes an inner product. Since convolution is a  
3532 translation invariant operation, the detection performance of CNN can be extended to  
3533 a wider range of CRES event kinetic energies with less cost than the matched filter, a  
3534 feature that is exploited during the CNN training by including circular translations of  
3535 the CRES frequency spectra in the training loop. Increasing the range of detectable  
3536 kinetic energies with a matched filter requires a proportional increase in the number of  
3537 templates, which directly translates into increased computational and hardware costs.  
3538 From a practical perspective, the detection algorithm is always limited by the available  
3539 computational hardware, so estimating the relative costs is a key factor in determining  
3540 their feasibility. A more detailed analysis of the relative costs of each of the detection  
3541 algorithms is performed below.

#### 3542 4.4.5.2 Computational Cost and Hardware Requirements

3543 The trade-off between better detection efficiency and computational cost is common  
3544 to many signal detection problems and the FSCD is no exception. Computational  
3545 costs can be related to actual hardware costs by calculating the theoretical amount of  
3546 computer hardware required to implement the signal classifiers for real-time detection.  
3547 The approach taken here utilizes order of magnitude estimates of the theoretical peak  
3548 performance values for currently available Graphics Processing Units (GPUs) as a metric.  
3549 This approach underestimates the amount of required hardware, since it is unlikely that  
3550 any CRES detection algorithm could reach the theoretical peak performance of the  
3551 hardware.

3552 Since the signal detection algorithms are designed to work using beamformed frequency  
3553 spectra, the computational cost of beamforming combined with a fast Fourier transform  
3554 (FFT) is constant for all classifiers. The beamforming grid is assumed to contain  $N_{\text{bf}}$   
3555 beamforming positions, each of which will produce a frequency spectrum containing  $N_{\text{bin}}$   
3556 after the FFT.

3557 Considering the power threshold classifier, this results in  $N_{\text{bin}}N_{\text{b}}$  frequency bins  
3558 that must be checked every  $N_{\text{bin}}/f_s$  seconds. The 20 cm diameter FSCD array requires  
3559  $N_{\text{bf}} \approx O(10^2)$  for sufficient coverage and has a sampling frequency  $f_s = 200$  MHz with a  
3560 Fourier analysis window of  $N_{\text{bin}} = 8192$  samples. Therefore the power threshold requires  
3561 approximately  $O(10^{10})$  FLOPS to check in real-time with these parameters

3562 Current generations of GPUs have peak theoretical performances in the range of  
3563  $O(10^{13}) - O(10^{14})$  FLOPS [88], dependent on the required floating-point precision of

3564 the computation. Therefore, the entire computational needs of a real-time triggering  
3565 system using a power threshold classifier, including digital beamforming and generation  
3566 of the STFT, could be met by a single high-end GPU or a small number of less powerful  
3567 GPUs. Since triggering is only one step of the full real-time signal reconstruction  
3568 approach, limiting the computational cost of this stage is ideal. However, the power  
3569 threshold classifier does not provided sufficient detection efficiency across the entire  
3570 range of possible signals, which is the primary motivation for exploring more complicated  
3571 triggering solutions.

3572 As discussed, the computational cost of the matched filter approach requires counting  
3573 the number of templates that must be checked for each frequency spectra produced by  
3574 the STFT. Computing the matched filter scores requires  $O(N_{\text{bf}}N_t N_{\text{bin}})$  operations, since  
3575 for each of the beamforming positions one must multiply  $N_t$  templates with a data vector  
3576 that has length  $N_{\text{bin}}$ . The computation must be performed in a time less-than or equal  
3577 to  $N_{\text{bin}}/f_s$  to keep up with the data generation rate. A 5 eV range of kinetic energies  
3578 required  $10^4$  to  $10^5$  templates in order for the matched filter to exceed the performance  
3579 of the CNN. The number of templates is expected to scale linearly with the total kinetic  
3580 energy range of interest; therefore,  $10^5$  to  $10^6$  matched filter templates would be expected  
3581 for the nominal 50 eV analysis window of the FSCD. Considering this, the estimated  
3582 computational cost of the matched filter is between  $O(10^{15})$  to  $O(10^{16})$  FLOPS, which is  
3583  $O(10^2)$  to  $O(10^3)$  high-end GPUs.

3584 The computational cost of the CNN can be estimated by simply summing the compu-  
3585 tational costs of the convolutions and matrix multiplications specified by the network  
3586 architecture shown in Table 4.1. Each convolutional layer consists of  $N_{\text{in}}N_{\text{out}}N_{\text{kernel}}L_{\text{input}}$   
3587 floating-point operations, where  $N_{\text{in}}$  is the number of input channels,  $N_{\text{out}}$  is the number  
3588 of output channels,  $N_{\text{kernel}}$  is the size of the convolutional kernel, and  $L_{\text{input}}$  is the length  
3589 of the input vector, and the fully connected layers each contribute  $N_{\text{in}}N_{\text{out}}$  operations.  
3590 Summing all the neural network layers it is estimated that the CNN requires  $O(10^6)$   
3591 floating point operations to evaluate each frequency spectra; therefore, the total com-  
3592 putational cost of the CNN trigger is value multiplied by the number of beamforming  
3593 positions per the data acquisition time, which is  $O(10^{13})$  FLOPS or  $O(10^0)$  GPUs.

3594 Compared with the matched filter approach the CNN requires  $O(100)$  to  $O(1000)$   
3595 fewer GPUs to implement, dependent on the exact number of templates used in the  
3596 template bank. The 50 eV kinetic energy range is motivated by the application of these  
3597 detection algorithms to an FSCD-like neutrino mass measurement experiment. However,  
3598 if a significantly larger range of kinetic energies is required, a CNN may be the preferred

3599 detection approach despite the lower mean detection efficiency due to computational cost  
3600 considerations.

3601 Additional experiments with larger CNNs, generated by increasing the depth and  
3602 width of the neural network, were performed. It was observed that these changes  
3603 provided minimal ( $\lesssim 1\%$ ) improvement in the classification accuracy of the model. A  
3604 potential reason for this could be the sparse nature of the signals in the frequency  
3605 domain and the low SNR, which makes for a challenging dataset to learn from. Future  
3606 work might investigate modifications to the neural network architecture such as sparse  
3607 convolutions, which may improve the classification accuracy of the model or further  
3608 reduce the computational costs of this approach. Alternatively, more complicated CNN  
3609 architectures such as a ResNet [89] or VGG model [90] may provide improved classification  
3610 performance over a basic CNN. An additional promising area of investigation are recurrent  
3611 neural networks, which may be able to exploit the time-ordered features of the STFT for  
3612 more accurate signal detection if the electron signals last for multiple Fourier transform  
3613 windows.

3614 The estimate of the computational costs of the matched filter is somewhat naive if one  
3615 notices that the majority of the values that make up a CRES frequency spectrum are zero  
3616 (see Figure 4.30). Therefore, the majority of operations in the matched filter inner product  
3617 are unnecessary, and one could instead evaluate the matched filter inner product using  
3618 only the  $\lesssim 10$  frequency peaks that make up the CRES signal. This optimization reduces  
3619 the number of operations required to check each template by a factor of  $O(100)$  to  $O(1000)$ ,  
3620 which brings the estimated computational cost of the matched filter in line with the  
3621 CNN. Although this level of sparsity results in a multiplication with very low arithmetic  
3622 complexity, the resulting sparse matched filter algorithm is still likely to be constrained  
3623 by memory access speed rather than compute speed. Ultimately, the comparison of  
3624 the relative computational and hardware costs between the matched filter and CNN  
3625 will depend on the efficiency of the software implementation and hardware support for  
3626 neural network and sparse matrix calculations, which will need to be determined using  
3627 real-world benchmarks.

#### 3628 **4.4.6 Conclusion**

3629 Increasing the detection efficiency and overall event rate of the CRES technique represents  
3630 a key developmental path towards new scientific results and broader applications of the  
3631 CRES technique. It is what motivates both the antenna array detection approach and  
3632 the development of real-time signal reconstruction algorithms. The work presented here

3633 demonstrates that significant gains in the detection efficiency of the CRES technique  
3634 are achievable by utilizing triggering algorithms that account for the specific shape of  
3635 CRES signals in the detector. These algorithms emphasize the need for accurate and fast  
3636 methods for CRES simulation, since they directly contribute to the success of matched  
3637 filter methods by providing a way to generate expected signal templates and also serve  
3638 as a source of training data for machine learning approaches.

3639 The down-side of these more advanced approaches to signal detection is the increase  
3640 in computational resources required to implement them. However, it was shown that a  
3641 CNN of minimal size was able to significantly improve detection performance above the  
3642 baseline power threshold trigger algorithm with a theoretical computational cost of only  
3643  $O(1)$  high-end GPU. This algorithm improves on detection performance while requiring  
3644 at least a factor  $O(10^2)$  less in computer relative to a matched filter template bank,  
3645 which would be the classical approach to signal detection in Gaussian noise. Future work  
3646 obtaining real-life benchmarks of the CNN and matched filter algorithms are required to  
3647 support these conclusions, but this study has indicated that a real-time signal detection  
3648 algorithm for an antenna array CRES experiment is computationally feasible without  
3649 extraordinary compute power.

3650 While this work has focused on the real-time detection of CRES signals from antenna  
3651 arrays, these same signal classifiers could be used in CRES experiments utilizing different  
3652 detector technologies, since the same principles of signal detection will apply. For example,  
3653 previous CRES measurements by the Project 8 collaboration that utilized a waveguide  
3654 gas cell, could have improved their detection efficiency by employing a matched filter  
3655 or neural network classifier to identify trapped electrons with pitch angles that are too  
3656 small to be detected by the power threshold approach. Furthermore, alternative CRES  
3657 detector technologies such as resonant cavities [41] could also see similar improvements  
3658 in detection efficiency, which is of crucial importance to future efforts by the Project 8  
3659 collaboration to utilize CRES to measure the neutrino mass.

3660    **Chapter 5** |

3661    **Antenna and Antenna Measurement Sys-**

3662    **tem Development for the Project 8 Ex-**

3663    **periment**

3664    **5.1 Introduction**

3665    The FSCD (free space CRES demonstrator) and antenna array CRES (cyclotron radiation  
3666    emission spectroscopy) represent an innovative approach to beta-decay spectroscopy.  
3667    While much can be learned from simulations about the systematics of CRES with antenna  
3668    arrays, laboratory measurements and demonstrations provide critical inputs to sensitivity  
3669    and simulation models, and provide a means for calibration and commissioning of the  
3670    experiment. Therefore, a robust program of antenna and antenna measurement hardware  
3671    development is key to the success of the FSCD and the development of antenna array  
3672    CRES more broadly.

3673    In this chapter I summarize the development of an antenna measurement system at  
3674    Penn State to implement and test the techniques of antenna array CRES on the bench-top.  
3675    In Section 5.2 I provide an introduction to some fundamental parameters and concepts  
3676    related to antenna measurements as well as an overview of the Penn State antenna  
3677    measurement system hardware. In Section 5.3 I include the manuscript of a paper [78]  
3678    which details the design and characterization of a specialized antenna developed to mimic  
3679    the electric fields emitted by an electron in a CRES experiment. This antenna, called  
3680    the Synthetic Cyclotron Antenna (SYNCA), is intended as a calibration tool for antenna  
3681    arrays developed for CRES measurements. Lastly, in Section 5.4 I summarize a set of  
3682    prototype FSCD antenna array measurements with the SYNCA [44], which I use to  
3683    validate the simulated performance of the antenna array and estimate systematic errors  
3684    associated with the antenna array.

## 3685 5.2 Antenna Measurements for CRES experiments

### 3686 5.2.1 Antenna Parameters

3687 Antenna characterization measurements are intended to validate simulations of the  
3688 antenna array performance, which ultimately informs the neutrino mass sensitivity of  
3689 the experiment. In this section, I shall summarize a few fundamental concepts relating  
3690 to antennas and antenna measurement, before introducing how Project 8 uses antenna  
3691 measurements for the development of antenna array CRES.

#### 3692 5.2.1.1 Radiation Patterns

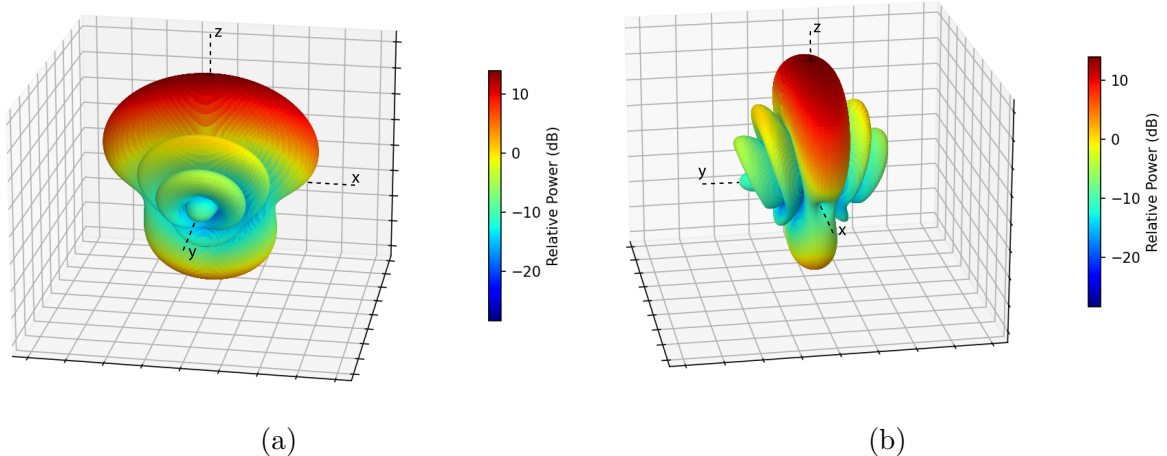


**Figure 5.1.** An example radiation pattern generated using HFSS simulations. The color and radial distance of the surface from the origin indicate the relative magnitude of radiation power emitted by the antenna in that direction. The primary goal of most antenna measurements is typically to measure the antenna pattern, which is used to derive many useful antenna performance parameters.

3693 Antennas are conductive structures designed to carry alternating electric currents  
3694 to transmit energy in the form of EM (electro-magnetic) waves [68]. Perhaps the most  
3695 fundamental way to characterize an antenna, is to map out the radiated power density  
3696 as a function of position, which is called the radiation pattern (see Figure 5.1). The  
3697 radiation power density is obtained by calculating the time-averaged Poynting vector for  
3698 all positions surrounding the antenna, which in equation form is

$$\mathbf{W}(x, y, z) = \langle \mathbf{E}(x, y, z, t) \times \mathbf{H}^*(x, y, z, t) \rangle_t, \quad (5.1)$$

3699 where  $\mathbf{E}(x, y, z, t)$  and  $\mathbf{H}(x, y, z, t)$  are the time-dependent electric and magnetic fields  
 3700 produced by the antenna [49]. The radiation power density has units of  $\text{W/m}^2$  and is  
 3701 more typically called the energy flux density in physics applications, since it is a measure  
 3702 of the amount of energy passing through a unit area over time.

3703 Because the radiation power density is a measure of power per unit area, its value  
 3704 in a particular direction will depend on the distance from the antenna at which one is  
 3705 measuring. This is undesirable for practical applications. A related quantity, which is  
 3706 distance independent, is the energy flux per unit solid angle or radiation intensity, which  
 3707 is computed directly from the radiation power density by multiplying by the squared  
 3708 distance from the antenna. Specifically,

$$U = r^2 W(x, y, z), \quad (5.2)$$

3709 where  $r$  is the distance from the antenna to the field measurement point. The radiation  
 3710 intensity is typically defined in regions where the Poynting vector consists only of a radial  
 3711 component where it is safe to treat as a scalar quantity.

### 3712 5.2.1.2 Directivity and Gain

3713 Since the radiation intensity is a measure of average power per unit solid angle, it is  
 3714 independent of distance and more useful as feature for antenna measurement. The  
 3715 radiation intensity is directly related to antenna directivity and gain, which are common  
 3716 antenna engineering figures-of-merit. Directivity is defined as the ratio between the  
 3717 radiation intensity at particular point on the radiation pattern to the average radiation  
 3718 intensity computed over all solid angles [68]. The equation that relates the radiation  
 3719 intensity to directivity is

$$D = \frac{U}{U_0} = \frac{4\pi U}{P_{\text{rad}}}, \quad (5.3)$$

3720 where  $U_0$  is the average radiation intensity over all solid angles, which simply the total  
 3721 radiated power ( $P_{\text{rad}}$ ) divided by  $4\pi$ . Closely related to directivity is antenna gain, which  
 3722 accounts for energy losses that occur inside then antenna when attempting to transmit  
 3723 or receive a signal. The antenna gain is given by

$$G = \frac{4\pi U}{P_{\text{in}}}, \quad (5.4)$$

3724 where  $P_{\text{in}}$  is the total power delivered to the antenna. Gain can be thought of as the ratio  
 3725 of the antenna's radiation intensity to that of a hypothetical isotropic, lossless radiator.

3726 The maximum values of gain and directivity exhibited by the main lobe of the antenna  
 3727 pattern as well as the ratio between the gain of the main lobe and any side-lobes are  
 3728 important figures-of-merit to evaluate antenna design performance.

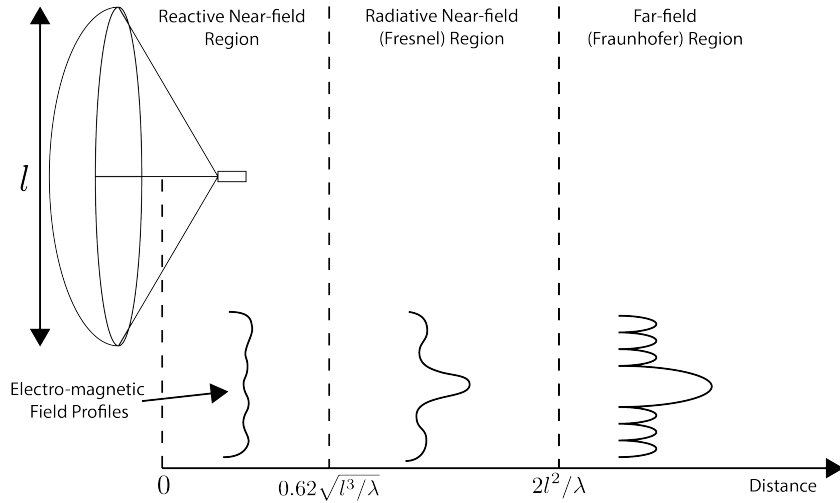


**Figure 5.2.** An illustration of the three field regions important for the analysis of an antenna system. Very close to the antenna the electric fields are primarily reactive so there is no radiation. If a receiving antenna were placed in this region most of the energy would be reflected back to the transmitter. Outside of the reactive near-field is the radiative near field. At these distances the antenna does radiate, but the radiation pattern is not well-defined since it changes based on the distance of the receiving antenna. It is only in the far-field region where the radiation pattern becomes constant as a function of distance, which is where the majority of antenna engineering is assumed to take place. The antenna arrays developed by Project 8 for CRES measurements operate in the radiative near-field due to the importance of limiting power loss from free-space propagation, which complicates the design of the antenna system.

### 3729 5.2.1.3 Far-field and Near-field

3730 Radiation patterns are well-defined only in regions where the shape of the radiation  
 3731 pattern is independent of distance. The region where this approximation is valid is called  
 3732 the "far-field", and in this region the EM fields from the antenna can be approximated as  
 3733 spherical plane waves. A rule of thumb for antennas is that the far-field approximation  
 3734 applies when the condition

$$R > \frac{2l^2}{\lambda} \quad (5.5)$$

3735 is true. In this expression,  $R$  is the distance from the antenna,  $l$  is the largest characteristic  
 3736 dimension of the antenna, and  $\lambda$  is the wavelength of the radiation (see Figure 5.2).

3737 The region very close to the antenna is called the reactive near-field, because in this  
 3738 region the reactive component of the EM field is dominant. Unlike radiative electric

3739 fields, the reactive electric and magnetic fields are out of phase from each other by  $90^\circ$ ,  
 3740 since they are caused by electrostatic and magnetostatic effects from the self-capacitance  
 3741 and self-inductance of the antenna. The reactive fields are unable to transfer energy a  
 3742 significant distance from the antenna and are thus completely negligible for most antenna  
 3743 applications. The limit of the reactive near-field for an electrically-large antenna is  
 3744 typically taken to be

$$R < 0.62\sqrt{l^3/\lambda}. \quad (5.6)$$

3745 The unique application of antennas by Project 8 is limited by reactive near-field effects,  
 3746 since it defines an absolute minimum distance for detectable electrons inside the uniform  
 3747 cylindrical antenna array. If electrons are too close to the edge of the array than reactive  
 3748 near-field effects leads to a large reduction in the received power and detection efficiency.  
 3749 This leads to a significant volume inside the antenna array that is unsuitable for CRES  
 3750 lowering the volumetric efficiency of the antenna array CRES technique.

3751 Between the reactive near-field and the far-field is the radiative near-field region. In  
 3752 this region the fields are primarily radiative, however, it is too close to the antenna for  
 3753 the spherical plane wave approximation to apply. Therefore, interference effects between  
 3754 EM waves emitted from different points on the antenna occur causing the shape of the  
 3755 radiation pattern to change as a function of distance from the antenna. Evaluating the  
 3756 far-field distance limit for the FSCD antennas one finds an estimated far-field distance  
 3757 of 43 cm, which is a factor of four larger than the radius of the antenna array designed  
 3758 for the experiment. Consequently, it is expected that near-field effects will influence  
 3759 the performance of the antenna array highlighting the importance of calibration and  
 3760 characterization measurements to mitigate these effects.

#### 3761 **5.2.1.4 Polarization**

3762 The polarization of an EM wave defines the spatial orientation of the electric field  
 3763 oscillations. Conventionally, polarization vectors a defined in the plane perpendicular  
 3764 to the direction of propagation for the EM wave. For radiation moving in the radial ( $\hat{r}$ )  
 3765 direction the electric field can be decomposed into the orthogonal basis

$$\mathbf{E}_{\text{tot}} = E_\theta \hat{\theta} + E_\phi \hat{\phi}, \quad (5.7)$$

3766 assuming a spherical coordinate system.

3767 In general, one defines partial radiation patterns, directivities, and gains so that the  
 3768 performance of the antenna can be analyzed for the desired polarization. The radiation

<sup>3769</sup> pattern defined in terms of partial patterns is

$$U_{\text{tot}} = U_\phi + U_\theta, \quad (5.8)$$

<sup>3770</sup> where  $U_\phi$  and  $U_\theta$  are the radiation intensities in a particular direction for the respective  
<sup>3771</sup> polarization components. Similarly, a quantity such as gain can be written in terms of  
<sup>3772</sup> partial gains,

$$G_{\text{tot}} = G_\phi + G_\theta = \frac{2\pi U_\phi}{P_{\text{in}}} + \frac{2\pi U_\theta}{P_{\text{in}}}. \quad (5.9)$$

<sup>3773</sup> An electron performing a circular orbit in the XY-plane from the side, viewed along  
<sup>3774</sup> the X or Y axes, would be seen as performing a linear oscillation perpendicular to the  
<sup>3775</sup> viewing axis. From this picture, one would predict that the primary polarization of  
<sup>3776</sup> electric fields from CRES events is linearly polarization in the  $\hat{\phi}$  direction in the XY-plane.

### <sup>3777</sup> 5.2.1.5 Antenna Factor and Effective Aperture

<sup>3778</sup> A useful way to characterize the performance of an antenna is to measure the electric  
<sup>3779</sup> field magnitude required to produce a signal with an amplitude of one volt in the antenna  
<sup>3780</sup> terminals. This ratio between the magnitude of the incoming electric field and the  
<sup>3781</sup> magnitude of the signal produced by the antenna is called the antenna factor, which is  
<sup>3782</sup> written as

$$A_F = \frac{|\mathbf{E}_{\text{in}}|}{V_{\text{ant}}}, \quad (5.10)$$

<sup>3783</sup> where  $A_F$  is the antenna factor,  $E_{\text{in}}$  is the incoming electric field, and  $V_{\text{ant}}$  is the magnitude  
<sup>3784</sup> of the voltage produced by the antenna.

<sup>3785</sup> The antenna factor can be expressed in terms of the antenna's gain through a related  
<sup>3786</sup> quantity called the effective aperture. The effective aperture defines for a given incident  
<sup>3787</sup> radiation power density ( $\text{W/m}^2$ ) the power that is received by the antenna. Therefore,  
<sup>3788</sup> the effective aperture gives the equivalent area of the antenna,

$$A_{\text{eff}} = \frac{P_{\text{rec}}}{P_{\text{in}}} = \frac{\lambda^2}{4\pi} G, \quad (5.11)$$

<sup>3789</sup> where the received power is  $P_r$  and the total incoming power is  $P_{\text{in}}$ .

<sup>3790</sup> The magnitude of the Poynting vector can be written as

$$|\mathbf{S}_{\text{in}}| = |\mathbf{E}_{\text{in}}|^2 / \eta_0, \quad (5.12)$$

3791 where  $\eta_0$  is the impedance of free-space, which relates the magnitudes of the electric and  
3792 magnetic fields in a vacuum, and is defined by

$$\eta_0 = \frac{|\mathbf{E}|}{|\mathbf{H}|} = \sqrt{\frac{\epsilon_0}{\mu_0}}. \quad (5.13)$$

3793 Therefore, the total received power by the antenna is

$$P_{\text{rec}} = |\mathbf{S}_{\text{in}}| A_{\text{eff}} = |\mathbf{S}_{\text{in}}| \frac{\lambda^2}{4\pi} G = \frac{|\mathbf{E}_{\text{in}}|^2 \lambda^2 G}{4\pi \eta_0}. \quad (5.14)$$

3794 To relate this to the antenna factor recall that the voltage produced by the antenna  
3795 is related to the received power by

$$P_{\text{rec}} = \frac{V_{\text{ant}}^2}{Z} = \frac{|\mathbf{E}_{\text{in}}|^2}{A_{\text{F}}^2 Z}, \quad (5.15)$$

3796 where  $Z$  is the system impedance. Setting Equations 5.14 and 5.15 equal to each other,  
3797 one obtains the following expression for antenna factor in terms of gain

$$A_{\text{F}} = \sqrt{\frac{4\pi\eta_0}{ZG\lambda^2}} = \frac{9.73}{\lambda\sqrt{G}}. \quad (5.16)$$

3798 The second expression in Equation 5.16 is obtained by evaluating the constant terms  
3799 assuming a system impedance of  $50 \Omega$ .

3800 This exercise highlights that the majority of antenna parameters that one cares  
3801 to measure about an antenna can be obtained from the radiation or gain pattern of  
3802 the antenna. The antenna factor is a particularly important parameter for CRES  
3803 measurements due to it's relevance to antenna array simulations with the Locust software  
3804 [65, 77].

3805 To compute the response of the antenna to the electric field, Locust relies upon  
3806 linear time-invariant system theory, which computes the response of the antenna (i.e. the  
3807 voltage time series generated by the antenna) using a convolution between the electric field  
3808 time-series and the antenna impulse response. This approach is necessary for correctly  
3809 modeling the antenna response to the electric field due to the broadband and non-  
3810 stationary nature of the electric fields from CRES events. Since antenna measurements  
3811 take place under steady-state conditions, parameters such as the radiation pattern, gain,  
3812 and antenna factor are defined in the frequency domain. However, by performing an  
3813 inverse Fourier transform on the antenna factor one obtains the antenna impulse response,

3814 which is used to calculate CRES signal voltages in Locust.

## 3815 5.2.2 Antenna Measurement Fundamentals

### 3816 5.2.2.1 Friis Transmission Equation

3817 The antenna factor or antenna transfer function is used to model how the antenna  
3818 responds to electric fields emitted from a CRES event. Therefore, directly measuring the  
3819 antenna transfer functions of the array is a key step in the commissioning and calibrating  
3820 the FSCD experiment. A common approach to antenna characterization is to perform a  
3821 two antenna transmit-receive measurement where an antenna with a known gain is used  
to characterize the unknown gain of the antenna under test (see Figure 5.3).

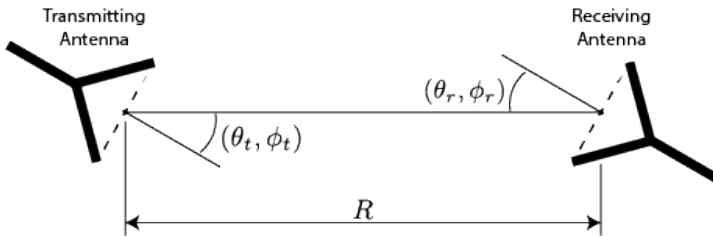


**Figure 5.3.** An illustration of the Friis measurement technique commonly used for antenna characterization measurements.

3822  
3823 Analyzing this two antenna setup involves calculating the power received from the  
3824 transmitting antenna. The received power density is expressed as a function of the  
3825 antenna gain in a direction  $(\theta_t, \phi_t)$  at frequency  $f$  and distance  $R$

$$w_t = \frac{P_t}{4\pi R^2} G_t(\theta_t, \phi_t, f), \quad (5.17)$$

3826 where the subscript  $t$  denotes the transmitting antenna, and  $P_t$  is the total power delivered  
3827 to the transmitting antenna. The power density is power per unit area, so the total  
3828 power delivered to the receiving antenna is the transmitted power density multiplied by  
3829 the effective area of the receiving antenna

$$P_r = w_t A_{\text{eff},r} = P_t \frac{G_t(\theta_t, \phi_t, f) G_r(\theta_r, \phi_r, f) c^2}{(4\pi R f)^2}, \quad (5.18)$$

3830 where  $G_r(\theta_r, \phi_r, f)$  is the gain of the receiving antenna. Equation 5.18 is called the Friis  
3831 transmission equation [91], which is of fundamental importance for antenna measurements,  
3832 since it allows one to measure the gain of an unknown antenna by measuring the power

3833 received from an antenna with a known gain pattern. Alternatively, if an antenna with a  
 3834 known gain pattern is unavailable, two identical antennas with unknown gain patterns  
 3835 can be used.

3836 **5.2.2.2 S-Parameters and Network Analyzers**

3837 It is more common to measure the ratio of the received power to the transmitted power  
 3838 instead of the absolute received power

$$\frac{P_r}{P_t} = \frac{G_t(\theta_t, \phi_t, f) G_r(\theta_r, \phi_r, f) c^2}{(4\pi R f)^2}. \quad (5.19)$$

3839 This power ratio can be easily measured using a vector network analyzer (VNA), which  
 3840 automates a significant fraction of the measurement process. Network analyzers are used  
 3841 to measure the scattering or S-parameters of a multi-port RF device [92], which describes  
 3842 how waves are scattered between the device ports. Friis antenna measurements can be  
 3843 modeled as a two-port microwave device that is characterized by measuring how incident  
 voltage waves are transmitted or reflected (see Figure 5.4). The scattered waves ( $V_1^-$

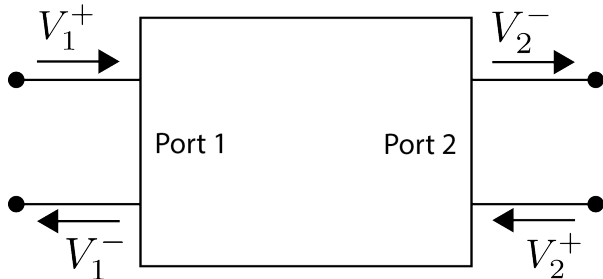


**Figure 5.4.** Illustration of a two-port S-parameter measurement setup. S-parameters characterize how incoming waves of voltage or power scatter off of the RF device under test. This allows you to measure important properties of the device. In particular, this framework can be used to model a two antenna radiation pattern measurement, which can be automated using a VNA.

3844  
 3845 and  $V_2^-$ ) can be written in terms of the incident ( $V_1^+$  and  $V_2^+$ ) waves using the scattering  
 3846 matrix

$$\begin{pmatrix} V_1^- \\ V_2^- \end{pmatrix} = \begin{pmatrix} S_{11} & S_{12} \\ S_{21} & S_{22} \end{pmatrix} \begin{pmatrix} V_1^+ \\ V_2^+ \end{pmatrix}, \quad (5.20)$$

3847 where the elements of the matrix are the device S-parameters. It is assumed that,  
 3848 when exciting the device from a particular port, that all other ports in the network are  
 3849 terminated at the system impedance. This ensures that the incident waves from other  
 3850 ports in the network are zero. Therefore, the S-parameters are the ratios between the

3851 scattered and incident waves,

$$S_{ij} = \frac{V_i^-}{V_j^+}. \quad (5.21)$$

3852 Alternatively, S-parameters can be defined as the ratio of the scattered and incident  
3853 power, which is proportional to the ratio of the squared voltage waves.

3854 Returning to the antenna measurement setup, it is clear that measuring the ratio of  
3855 the received to the transmitted power is equivalent to measuring the ratio of power being  
3856 scattered from port 1 to port 2 in a RF (radio-frequency) network. Therefore, measuring  
3857 an antenna's gain can be accomplished quite easily using a VNA to perform a two port  
3858  $S_{21}$  measurement.

3859 **5.2.2.3 Antenna Array Commissioning and Calibration Measurements**

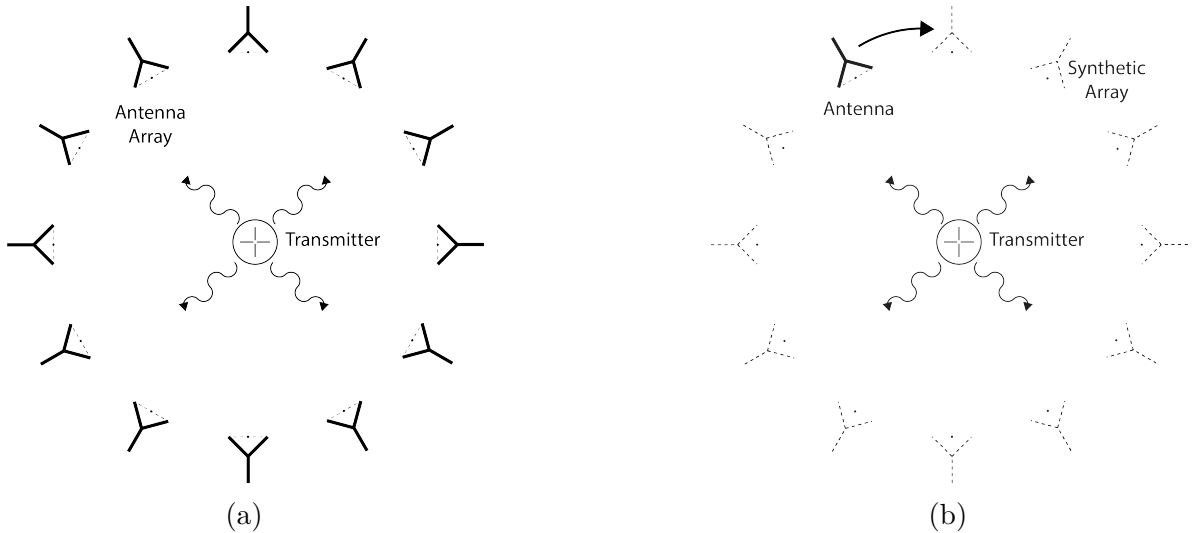


**Figure 5.5.** Two measurement approaches to characterizing an antenna array for CRES measurements. The full-array approach (a) requires a complete antenna array with all the associated hardware. The synthetic array approach (b) utilizes a single antenna and a set of rotation/translation stages to reposition the transmitter or the receiving antenna to synthesize the signals that would be received by the full-array. This approach reduces the cost and complexity of array measurements. A down-side of the synthetic array approach is that multi-channel effects such as reflections cannot be measured. Utilizing both the full-array and the synthetic array is a powerful way to quantify the impact of errors from the multi-channel array.

3860 Measuring the gain of each individual array element allows to predict the features of  
3861 the signals received during a CRES event (see Section 5.2.1.5). However, unpredictable  
3862 changes to the antenna performance can be introduced by the incorporation of the

3863 antennas into the circular array geometry, therefore, both individual antenna and full-  
3864 array characterization measurements are performed as part of the commissioning of the  
3865 FSCD.

3866 There are two main approaches to array measurements that could be used for  
3867 characterization and calibration (see Figure 5.5). One approach is to construct the  
3868 complete array and use a omni-directional transmitting antenna to measure the power  
3869 received by each channel in the antenna array. In Section 5.3 I describe the development  
3870 of an omni-directional transmitter that also mimics the radiation phase characteristics of a  
3871 CRES event, which is useful because the entire array can be tested without repositioning.  
3872 Alternatively, a full antenna array can be synthesized by repeatedly moving and measuring  
3873 a single array element. This approach is ideal for identifying if different channels in the  
3874 antenna array are affecting each other through multi-path interference by comparing the  
3875 measurement results of the synthetic array to the real array.

### 3876 **5.2.3 The Penn State Antenna Measurement System**

3877 The development of antenna array based CRES requires the capability to test and  
3878 calibrate different antenna array designs to validate the performance of the as-built  
3879 antenna array before and during the experiment. With these aims in mind an antenna  
3880 measurement system was developed at Penn State specifically designed to mimic the  
3881 characteristics of the FSCD experiment.

3882 The Penn State antenna measurement system utilizes a two antenna measurement  
3883 configuration with a stationary reference antenna and a test antenna mounted on a set  
3884 of motorized translation and rotation stages (see Figure 5.6). The antenna measurement  
3885 system can be operated in two distinct modes, one focused on the characterization of  
3886 the radiation patterns of prototype antennas, and the other focused on the validation of  
3887 data-acquisition (DAQ) and CRES signal reconstruction techniques to bridge the gap  
3888 between real measurements and simulation. In both measurement configurations, it is  
3889 critical to isolate the antennas from the environment so that multi-path reflections do not  
3890 negatively influence the measurement results. For this reason the measurement volume  
3891 is surrounded with microwave absorber foam (AEMI AEC-1.5) specifically designed to  
3892 attenuate microwave radiation near the 26 GHz measurement range of the system.

3893 In the first measurement configuration, the reference antenna is a well-characterized  
3894 horn antenna as pictured, since horn antennas have well-known and stable radiation  
3895 patterns making them ideal as standard references. For characterization measurements,  
3896 the test antenna represents the antenna-under-test whose pattern is being characterized.

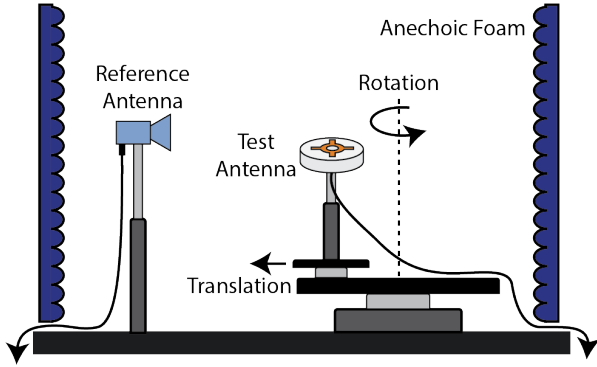


**Figure 5.6.** Illustration of the antenna measurement system developed for the Project 8 Collaboration. The reference and test antennas can be connected to different data acquisition configurations depending on the measurement goals. The reference antenna is typically a standard horn antenna and the test antenna is mounted on a set of translation stages for positioning. Automated translation stages allows for relatively painless data-taking enabling synthetic antenna array measurements using only a single receiving antenna. Anechoic form designed to mitigate RF reflections surrounds the setup.

3897 Mounting the test antenna on motorized rotation and translation stages allows for  
 3898 automation, which significantly speeds up the radiation pattern measurement process.

3899 The second measurement configuration mimics the conditions of the FSCD as it  
 3900 concerns the antenna array and DAQ system. In this configuration, the reference antenna  
 3901 is a prototype FSCD antenna, and the test antenna is a specially designed synthetic  
 3902 cyclotron antenna (SYNCA) as picture in Figure 5.6. The SYNCA is designed such that  
 3903 the radiation pattern mimics that of a CRES electron so that the signals received by the  
 3904 prototype CRES array antenna mimic what is expected for a real CRES experiment.

3905 Figure 5.7 shows two high-level system diagrams of the Penn State antenna measure-  
 3906 ment system that depict the important system components and the connections between  
 3907 them. The two configurations of the measurement system utilize different hardware. For  
 3908 characterization and radiation pattern measurements, the configuration shown in Figure  
 3909 5.7a is used. In this case a vector network analyzer (VNA) is used as the transmission  
 3910 source and data acquisition system, which is easy to calibrate over a wide range of  
 3911 frequencies. The configuration in 5.7b is used to mimic the FSCD experiment, since this  
 3912 system includes a more realistic receiver chain.

3913 The characterization configuration utilizes a network analyzer (Keysight N5222A)  
 3914 with two independent sources and four measurement ports as the primary measurement  
 3915 tool. A standard reference antenna is connected to one measurement port, and the test  
 3916 antenna is connected to a second port. The typical reference antenna used for these  
 3917 studies is a Pasternack PF9851 horn antenna. In the measurement shown, the test

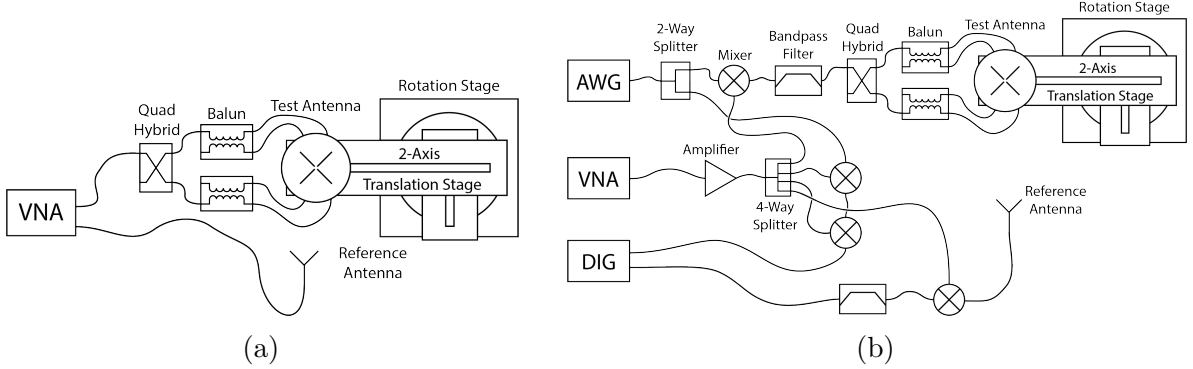


**Figure 5.7.** Diagrams of two measurement system configurations. Configuration (a) utilizes a VNA and is more suited to antenna characterization. Configuration (b) utilizes an AWG (arbitrary waveform generator) and VNA as a signal generation system and digitizer to collect measurement data, which is more suited to simulating CRES measurements. The transmission chain utilizes a quadrature hybrid and a pair of baluns to drive the cross-dipole variant test antenna developed for synthetic CRES measurements.

3918 antenna represents a SYNCA antenna, which requires a transmission chain consisting of  
 3919 quadrature hybrid coupler (Marki QH-0226) connected to two baluns (Marki BAL-0026)  
 3920 to generate feed signals with the appropriate phases. The VNA measures the radiation  
 3921 pattern by performing a transmission S-parameter measurement, which can be used with  
 3922 the knowledge of the reference antenna's radiation pattern to determine the radiation  
 3923 pattern of the test antenna (see Section 5.2.1).

3924 The second configuration incorporates more hardware components to mimic the DAQ  
 3925 system envisioned for the FSCD experiment. The basic approach is to produce CRES-like  
 3926 radiation and use an antenna combined with a realistic RF receiver chain to acquire the  
 3927 signals. On the transmit side, an arbitrary waveform generator (AWG, RIGOL DG5252)  
 3928 is used to generate a waveform that mimics a CRES signal at a baseband frequency up  
 3929 to 250 MHz. This frequency is then up-converted to the CRES signal frequency band  
 3930 of 25.8 to 26.0 GHz using a mixer (Marki MM1-0832L) and a bandpass filter (K&L  
 3931 Microwave 3C62-25900/T200-K/K) to reject unwanted mixing components outside out  
 3932 of the 200 MHz CRES signal band. The local oscillator signal for mixing is provided by  
 3933 one of the VNA sources configured to run in a continuous wave setting. On the receive  
 3934 side, a prototype antenna is used to detect the radiation emitted by the test antenna,  
 3935 which is down-converted and filtered using the same mixer and bandpass filter as the  
 3936 transmission chain. Lastly, data acquisition is performed using a 14-bit ADC sampling  
 3937 at 500 MSa/s (CAEN DT530) to digitize the down-converted signals.

3938 In order to distribute the LO to all mixers a 4-way power splitter (MiniCircuits

3939 ZC4PD-18263-S+) along with an amplifier (Marki APM-6848) is used to drive the four  
3940 mixers used in the measurement system. A limitation of using the VNA as an LO source  
3941 is that there is no control of the LO phase when a measurement is triggered by the  
3942 control script, which leads to a random phase offset between acquisitions. This makes it  
3943 impossible to perform synthetic array measurements, which require strict control over  
3944 the starting phase of the transmitted signal. In order to monitor the random phase of the  
3945 LO, a 2-way power splitter (MiniCircuits Z99SC-62-S+) is used to split the signal from  
3946 the AWG between the transmission path and a LO monitoring path. The LO monitoring  
3947 path consists of an up-conversion and down conversion using two mixers connected by a  
3948 coaxial cable, and monitors the relative phase of the LO using a channel on the digitizer  
3949 to sample this path. A phase shift in the LO will lead to a proportional phase shift in  
3950 the mixed signal, which is measured and removed from the received signals.

3951 The test antenna is mounted on a set of motorized stages, which are identical for  
3952 both measurement configurations. A rotational stage (ThorLabs PRMTZ8) is used as  
3953 the base layer with additional translation stages mounted on top. The rotational stage is  
3954 ideal for measuring a complete azimuthal scan of the test antenna's radiation pattern  
3955 as well as for moving a SYNCA antenna in circular motion to recreate the symmetry  
3956 of the FSCD antenna array. On top of the rotational stage, are mounted two linear  
3957 translation stages (ThorLabs MTS50-Z8 and MTS25-Z8) in a cross-wise manner so that  
3958 the test antenna can be moved along two perpendicular axes. Using the linear stages in  
3959 combination with the rotational stage allows one to fine-tune the positioning of the test  
3960 antenna so that it can be perfectly aligned with the central axis of the array. A LabView  
3961 script was developed to automate the measurement of a full 360° radiation pattern and  
3962 control the measurement electronics. Data from these acquisitions is stored on university  
3963 provided cloud storage.

### 3964 **5.3 Development of a Synthetic Cyclotron Antenna (SYNCA)** 3965 **for Antenna Array Calibration**

3966 This section is the manuscript of the publication [78] detailing the development of a  
3967 Synthetic Cyclotron Antenna (SYNCA) for antenna array characterization measurements  
3968 by the Project 8 collaboration.

### 3969 5.3.1 Introduction

3970 Neutrinos are the most abundant standard model fermions in our universe, but due to  
3971 weak interaction cross-sections with other particles, neutrinos are particularly difficult  
3972 to study. Consequently, many fundamental properties of neutrinos are still unknown  
3973 including the absolute scale of the neutrino mass [24]. Direct, kinematic measurements of  
3974 the neutrino mass are particularly valuable due to their model independent nature [37].  
3975 To date the most sensitive direct neutrino mass measurements have been performed by  
3976 the KATRIN collaboration [93], which measures the molecular tritium  $\beta$ -decay spectrum  
3977 to infer the neutrino mass. Current data from neutrino oscillation measurements [24]  
3978 allow for neutrino masses significantly smaller than the design sensitivity of the KATRIN  
3979 experiment; therefore, there is a need for new technologies for performing direct neutrino  
3980 mass measurements to probe lower neutrino masses.

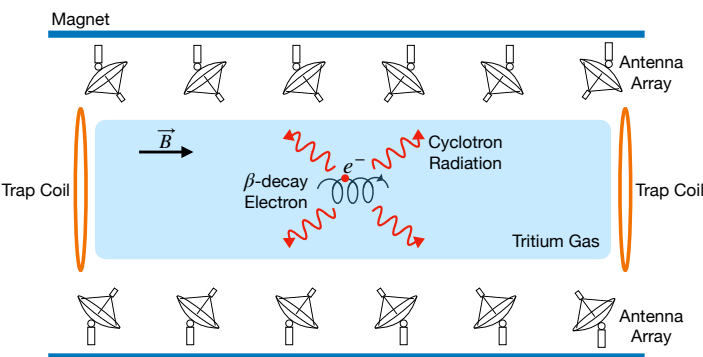


**Figure 5.8.** A sketch of an antenna array large-volume CRES experiment. Electrons from  $\beta$ -decays are confined in a magnetic field using a set of trap coils. The cyclotron radiation produced by the motion of the trapped electrons can be detected by a surrounding antenna array to determine the electron energies. Measuring the energies of many electrons produces a  $\beta$ -decay spectrum.

3981 The Project 8 collaboration is developing new methods for neutrino mass measurement  
3982 based on Cyclotron Radiation Emission Spectroscopy (CRES) [56, 94–96], with the goal  
3983 of measuring the absolute scale of the neutrino mass with a 40 meV/c<sup>2</sup> sensitivity [37, 73].  
3984 This sensitivity goal will require the development of two separate technical capabilities.  
3985 First is the development of an atomic tritium source, which avoids significant spectral  
3986 broadening due to molecular final states [55]. Second is the technology for performing  
3987 CRES in a multi-cubic-meter experimental volume with high combined detection and  
3988 reconstruction efficiency, which is required in order to obtain sufficient event statistics  
3989 near the tritium spectrum endpoint.

One approach for a large-volume CRES experiment is to use an array of antennas, which surrounds a volume of tritium gas, to detect the cyclotron radiation produced by the  $\beta$ -decay electrons when they are trapped in a background magnetic field using a set of magnetic trapping coils (see Figure 5.8). Project 8 has developed a conceptual experiment design to study the feasibility of this approach. The design consists of a single circular array of antennas with a radius of 10 cm and 60 independent channels positioned around the center of the magnetic trap. The motivation behind this antenna array design is to first develop an understanding of the antenna array approach to CRES with a small scale experiment before attempting to scale the technique to large volumes by using multiple antenna rings to construct the full cylindrical array. The development of the antenna array approach to CRES has largely proceeded through simulations using the Locust software package [77, 97], which is used to model the fields emitted by CRES events and predict the signals received by the surrounding antenna array. To validate these simulations, a dedicated test stand is being constructed to perform characterization measurements of the prototype antenna array developed by Project 8 (see Figure 5.9) and benchmark signal reconstruction methods using a specially designed transmitting calibration probe antenna.

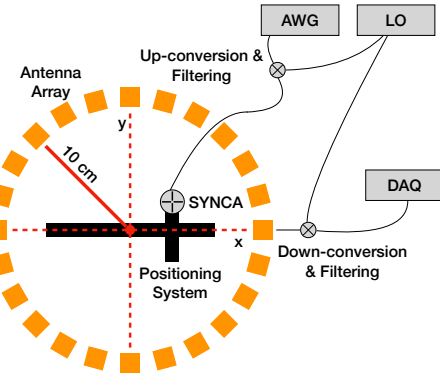


**Figure 5.9.** A schematic of the antenna array test stand. The circular antenna array has a radius of 10 cm with 60 independent channels (limited number shown for clarity). The test stand includes an arbitrary waveform generator (AWG), local oscillator (LO), and data acquisition (DAQ) hardware. Finally, a specialized Synthetic Cyclotron Antenna (SYNCA) is used to inject signals to test the antenna array.

We call this probe antenna the Synthetic Cyclotron Antenna or SYNCA. The SYNCA is a novel antenna design that mimics the cyclotron radiation generated by individual charged particles trapped in a magnetic field, which will be used in the antenna test stand to perform characterization measurements, simulation validation, and reconstruction benchmarking. This paper provides an overview of the design, construction, and

characterization measurements of the SYNCA performed in preparation for its usage as a transmitting calibration probe.

In Section 5.3.2 we provide a description of the cyclotron radiation field characteristics that we recreate with the SYNCA. In Section 5.3.3 we give an overview of the simulations performed to develop an antenna design that mimics the characteristics of cyclotron radiation. In Section 5.3.4 we outline characterization measurements to validate that the fields generated by the SYNCA match simulation, and finally in Section 5.3.5 we demonstrate an application of the SYNCA to test phased array reconstruction techniques on the bench-top.

### 5.3.2 Cyclotron Radiation Phenomenology

To understand the cyclotron radiation phenomenology that the SYNCA should mimic, we consider a charged particle moving at relativistic speed in the presence of an external magnetic field (see Figure 5.10). In the special case we shall examine, the entirety of the electron's momentum is directed perpendicular to the magnetic field; therefore, the trajectory of the electron is confined to the cyclotron orbit plane. Because the momentum vector is oriented perpendicular to the magnetic field, electrons with these trajectories are said to have pitch angles of 90°.

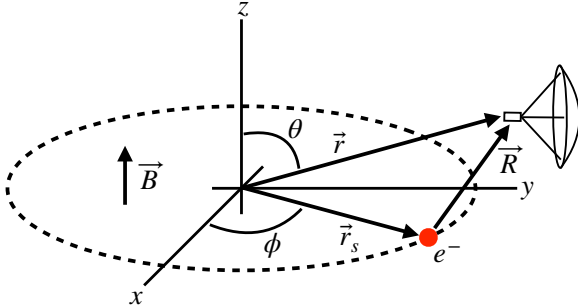


**Figure 5.10.** An electron (red dot) performing cyclotron motion in the x-y plane. The resulting cyclotron radiation is observed by an antenna located at the field point of interest.

The cyclotron radiation fields generated by this circular trajectory are those which we aim to reproduce with the SYNCA. We can describe the electromagnetic (EM) fields using the Liénard-Wiechert equations [49, 77], which in non-covariant form express the electric field as

$$\vec{E} = e \left[ \frac{\hat{n} - \vec{\beta}}{\gamma^2(1 - \vec{\beta} \cdot \hat{n})^3 |\vec{R}|^2} \right]_{tr} + \frac{e}{c} \left[ \frac{\hat{n} \times [(\hat{n} - \vec{\beta}) \times \dot{\vec{\beta}}]}{(1 - \vec{\beta} \cdot \hat{n})^3 |\vec{R}|} \right]_{tr}, \quad (5.22)$$

4033 where  $e$  is the particle's charge,  $\hat{n} = (\vec{r} - \vec{r}_s)/|\vec{r} - \vec{r}_s|$  is the unit vector pointing from the  
 4034 electron to the field measurement point,  $\vec{\beta} = \dot{\vec{r}}_s/c$  is the velocity of the particle divided  
 4035 by the speed of light, and  $\gamma$  is the relativistic Lorentz factor. The equation is meant to  
 4036 be evaluated at the retarded time as indicated by  $t_r = t - |\vec{R}|/c$ , which accounts for the  
 4037 time delay due to the finite speed of light between the point where the field was emitted  
 4038 and the point where the field is detected.

4039 We would like to simplify Equation 5.22 it at all possible. As a first step we analyze  
 4040 the relative magnitudes of the electric field polarization components. Consider an electron  
 4041 following a circular cyclotron orbit in a uniform magnetic field whose guiding center  
 4042 is positioned at the origin of the coordinate system. The equation of motion can be  
 4043 expressed as

$$\vec{r}_s = (r_c \cos \omega_c t_r) \hat{x} + (r_c \sin \omega_c t_r) \hat{y}. \quad (5.23)$$

4044 For single antenna located along the  $y$ -axis at position  $\vec{r} = r_a \hat{y}$  we are interested in the  
 4045 incident electric fields from the electron. The electric field is given by Equation 5.22,  
 4046 which we evaluate in the regime where  $r_a \gg r_c$ . This limit can be justified by comparing  
 4047 the radius of the cyclotron orbit for an electron with the tritium beta-spectrum endpoint  
 4048 energy of 18.6 keV in a 1 T magnetic field to the typical ( $r_a \simeq 100$  mm) radial position  
 4049 of the receiving antenna. We find that the cyclotron orbit has a radius of 0.46 mm which  
 4050 is approximately a factor of 200 smaller than the typical antenna radial position. In this  
 4051 regime we can make the approximation  $\vec{R} \simeq r_a \hat{y}$  and the expression for the electric field  
 4052 at the antenna's position becomes

$$\vec{E} = \frac{e}{\gamma^2 r_a^2} \frac{\hat{x} \left( \frac{r_c \omega_c}{c} \sin \omega_c t_r \right) + \hat{y} \left( 1 - \frac{r_c \omega_c}{c} \cos \omega_c t_r \right)}{(1 - \frac{r_c \omega_c}{c} \cos \omega_c t_r)^3} - \frac{e}{c r_a} \frac{\hat{x} \left( \frac{r_c^2 \omega_c^3}{c^2} - \frac{r_c \omega_c^2}{c} \cos \omega_c t_r \right)}{(1 - \frac{r_c \omega_c}{c} \cos \omega_c t_r)^3}. \quad (5.24)$$

4053 Since the receiving antenna is part of a circular array of antennas, it is useful to rewrite  
 4054 Equation 5.24 in terms of the azimuthal ( $\hat{\phi}$ ) and radial ( $\hat{r}$ ) polarizations. Making use of  
 4055 the fact that for an antenna located at  $R = r_a \hat{y}$  that  $\hat{\phi} = -\hat{x}$  and  $\hat{r} = \hat{y}$  we find

$$\vec{E} = \hat{\phi} E_\phi + \hat{r} E_r \quad (5.25)$$

$$E_\phi = \frac{e}{(1 - \frac{r_c \omega_c}{c} \cos \omega_c t_r)^3} \left[ -\frac{\frac{r_c \omega_c}{c} \sin \omega_c t_r}{\gamma^2 r_a^2} + \frac{\omega_c \left( \frac{r_c^2 \omega_c^2}{c^2} - \frac{r_c \omega_c}{c} \cos \omega_c t_r \right)}{c r_a} \right] \quad (5.26)$$

$$E_r = \frac{e \left( 1 - \frac{r_c \omega_c}{c} \sin \omega_c t_r \right)}{\gamma^2 r_a^2 (1 - \frac{r_c \omega_c}{c} \cos \omega_c t_r)^3}. \quad (5.27)$$

For the purposes of designing a synthetic cyclotron radiation antenna we are interested in the dominant electric field polarization emitted by the electron. The antenna is being designed to mimic the cyclotron radiation produced by electrons with kinetic energies of approximately 18.6 keV in a 1 T magnetic field [55]. Since the relativistic beta factor for an electron with this kinetic energy is  $|\vec{\beta}| \simeq \frac{1}{4}$ , the approximations  $\gamma \simeq 1$  and  $\frac{r_c \omega_c}{c} \simeq \frac{1}{4}$  are justified. Inserting these expressions into the equations for the electric field components above simplifies the comparison of the magnitudes of the two components. Additionally, we compare the time-averaged magnitudes to evaluate the root mean squared electric field ratio. The time-averaged ratio of the radial and azimuthally polarized electric fields with the above simplifications is given by

$$\frac{\langle |E_r| \rangle}{\langle |E_\phi| \rangle} = \frac{8 - \sqrt{2}}{\left| 1 - \frac{r_a}{r_c} \frac{1-2\sqrt{2}}{8} \right|} \simeq \frac{r_c}{r_a} \frac{8(8 - \sqrt{2})}{2\sqrt{2} - 1} = 0.13, \quad (5.28)$$

where we have made use of the fact that for these magnetic fields and kinetic energies the cyclotron radius is much smaller than the radius of the antenna array.

From Equation 5.28 we see that the time-averaged azimuthal polarization is larger than the radial polarization by about a factor of 8, which makes it the dominant contribution to the electric fields at the position of the antenna. We must also consider the directivity of the receiving antenna which can have a gain that is disproportionately large for a specific polarization component. Because the  $E_\phi$  component is dominant, the receiving antenna array is designed with an azimuthal polarization, which negates the voltages induced in the antenna from the radially polarized fields. Therefore, we conclude that for the purpose of designing the SYNCA antenna it is acceptable to approximate the electric fields from Equation 5.22 as purely azimuthally or  $\phi$ -polarized. The simplified expression for the electric field received by an antenna becomes

$$\vec{E} = E_\phi \hat{\phi} = \frac{e^{\frac{r_c \omega_c}{c}}}{4r_a r_c} \left[ \frac{\frac{r_c \omega_c}{c} - \cos \omega_c t - \frac{4r_c}{r_a} \sin \omega_c t}{(1 - \frac{r_c \omega_c}{c} \cos \omega_c t)^3} \right]_{t_r} \hat{\phi}, \quad (5.29)$$

where the radius of the cyclotron orbit is called  $r_c$ , the cyclotron frequency is called  $\omega_c$ , and the radial position of the receiving antenna is called  $r_a$ . Equation 5.29 has been evaluated in the non-relativistic limit where  $\gamma \simeq 1$ , which is justified by the fact that  $|\vec{\beta}| \simeq \frac{c}{4}$  for an electron with an 18.6 keV kinetic energy in a 1 T magnetic field.

This rather complicated expression can be simplified using Fourier analysis. Assuming a background magnetic field of 1 T and a kinetic energy of 18.6 keV we calculate

4084 numerically the electric field using Equation 5.29 and apply a discrete Fourier Transform  
to visualize the frequency spectrum (see Figure 5.11).

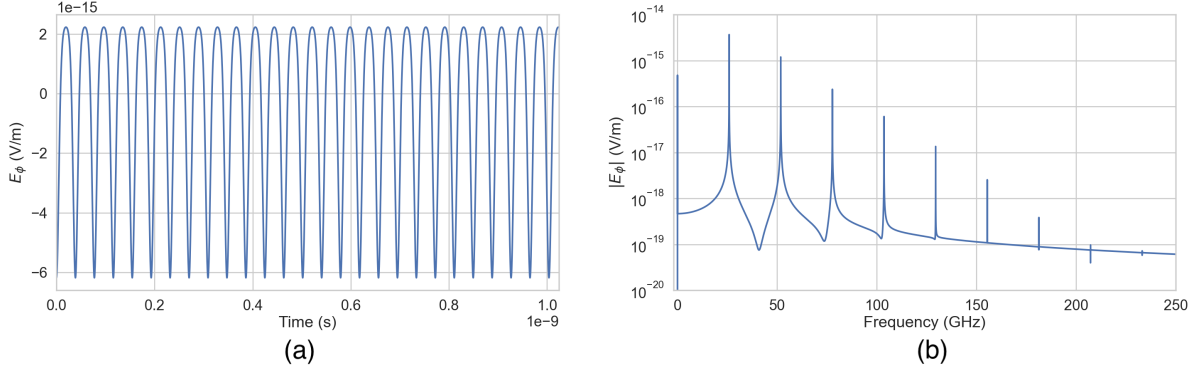


**Figure 5.11.** A plot of the numeric solution to Equation 5.30. The time-domain representation of the signal (a) is composed of a zero frequency term and a series of harmonics separated by the main cyclotron frequency as shown in the plot of the frequency spectrum (b). We can see that the relative amplitude of the harmonics beyond  $k = 7$  are smaller than the main carrier by a factor of about  $10^{-5}$  and are completely negligible.

4085  
4086 We observe that the azimuthally polarized electric field is periodic with a base cyclotron  
4087 frequency of 25.898 GHz corresponding to the highest power frequency component in  
4088 Figure 5.11. The frequency spectrum reveals that the signal is composed of a constant  
4089 term with zero frequency and a series of harmonics separated by 25.898 GHz. Therefore,  
4090 we can represent the azimuthal electric fields from the electron as a linear combination  
4091 of pure sinusoids with frequencies given by  $\omega_k = k\omega_c$  ( $k \in 0, 1, 2, \dots$ ) and amplitudes  
4092 extracted from the Fourier representation. Using this representation we can transform  
4093 the equation for the azimuthally polarized electric fields in Equation 5.29 into

$$E_\phi = \frac{e^{\frac{r_c \omega_c}{c}}}{4r_a r_c} \sum_{k=0}^7 A_k e^{i\omega_k t_r}, \quad (5.30)$$

4094 where we have truncated the sum over harmonics at the 7th order for completeness. The  
4095 amplitudes  $A_k$  are dimensionless complex numbers, which encode the relative powers of  
4096 the harmonics as well as the starting overall phase of the cyclotron radiation. Because  
4097 magnitude of the relative amplitudes exponentially decreases for higher harmonics, it is  
4098 usually sufficient to consider only the terms up to  $k = 4$  where the relative amplitude  
4099 of the harmonics has decreased from the main carrier by a factor of approximately 100.  
4100 However, for completeness we include harmonics up to 7th order in Equation 5.30. The  
4101 range of frequencies to which the receiving antenna array in the antenna test stand is  
4102 sensitive is defined by the antenna's transfer function. The receptive bandwidth for

4103 the antennas used in the test stand is a range of frequencies with a bandwidth on the  
 4104 order of a few GHz centered around the main cyclotron carrier frequency of 25.898 GHz.  
 4105 Therefore, the higher order harmonics as well as the zero frequency term can be ignored  
 4106 when considering only the signals that will be received by the antenna array.

4107 Considering only the 1st order harmonic term from Equation 5.30, which represents  
 4108 the portion of the electric field that will be detected by the array, and evaluating this at  
 4109 the retarded time we obtain the following for the  $\phi$ -polarized electric fields

$$E_\phi \propto \cos \left( \omega_c \left( t - |\vec{R}|/c \right) - \Delta \right), \quad (5.31)$$

4110 where the arbitrary phase  $\Delta$  is defined by  $A_k = |A_k|e^{i\Delta}$ . We are interested in the  
 4111 characteristics of the amplitude of the electric field as a function of the radial distance  
 4112 component ( $|\vec{R}|$ ) of the retarded time. In particular, the maximum of  $E_\phi$  occurs when  
 4113 the argument of the cosine function is equal  $n\pi$  where  $n \in \{0, \pm 2, \pm 4, \dots\}$ ; however, the  
 4114 solutions where  $n$  is negative can be discarded since they represent unphysical negative  
 4115 overall phases. Applying this condition to Equation 5.31 gives a condition on the radial  
 4116 position of the maximum of  $E_\phi$

$$\omega_c(t - |\vec{R}|/c) - \Delta = n\pi, \quad (5.32a)$$

$$|\vec{R}| = \frac{c}{\omega_c} ((\omega_c t - \Delta) - n\pi), \quad (5.32b)$$

4117 which is a function of time in the frame of the moving electron ( $t$ ). Equation 5.32 can  
 4118 be further simplified by noticing that the azimuthal position of the electron ( $\phi_e(t)$ ) as a  
 4119 function of time is defined by  $\phi_e(t) = \omega_c t - \Delta$  which reduces Equation 5.32 to

$$|\vec{R}| = \frac{c}{\omega_c} (\phi_e(t) - n\pi). \quad (5.33)$$

4120 Equation 5.33 represents an archimedian spiral which is formed when plotting the  
 4121 amplitude of  $E_\phi$  in the x-y plane. The solution where  $n = 0$  represents the leading edge  
 4122 of the radiation spiral which propagates outward from the electron at the speed of light.  
 4123 The additional solutions for  $n > 0$  represent the persistent spiral at radii inside the  
 4124 leading edge of the radiated fields that have not yet been detected by the receiver at the  
 4125 current time. In Figure 5.12a we show the expected spiral pattern for the maxima of the  
 4126 cyclotron radiation.

4127 In particular, we note that for the circular array geometry of the test stand, depicted  
 4128 as the series of circles in Figure 5.12a, each antenna receives a linearly polarized wave

4129 with a phase offset that corresponds to the azimuthal angle for that antenna element.  
 4130 Therefore, as we show in Figure 5.12b, when the relative phase of the received signal is  
 4131 plotted as a function of the receiving antenna's azimuthal position the result is also an  
 4132 Archimedean spiral.

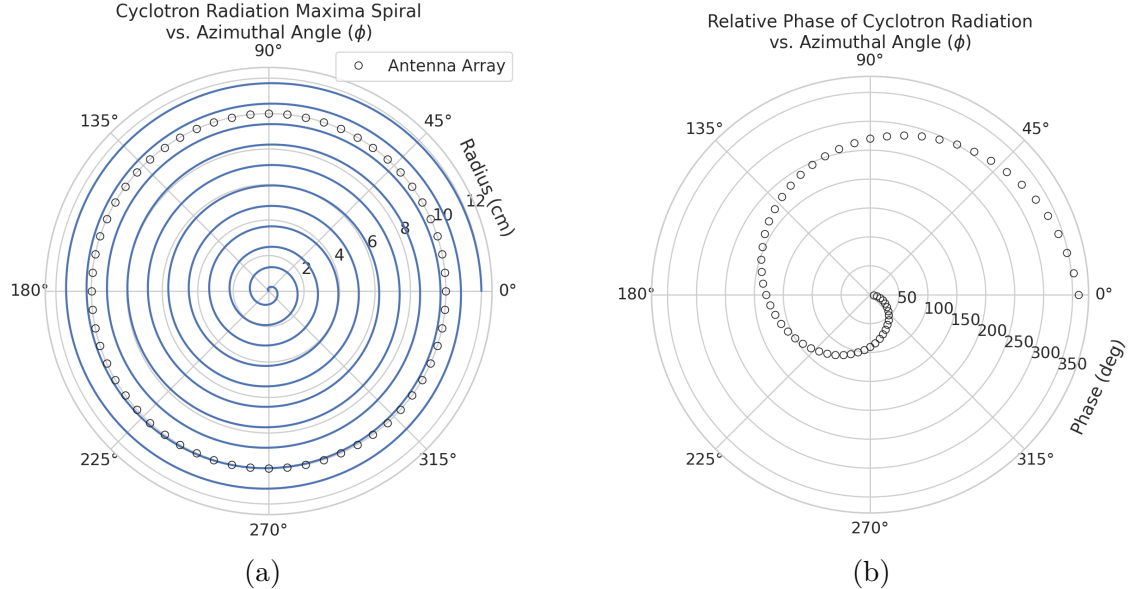


**Figure 5.12.** The amplitude maxima of the cyclotron radiation form an Archimedean spiral as the radiation propagates outward from the cyclotron orbit center (a). A circular antenna array located at a fixed radius from the orbit center will receive electric fields with equal magnitude in each of its channels, but the phase of the electric field incident on each array channel will be linearly out of phase from its neighbor antennas by an amount equal to the angular separation of the two channels (b).

4133 Based on these analytical calculations we can characterize the magnitude, polarization,  
 4134 and phase of the signals received by the antenna array using three criteria. These criteria  
 4135 are the basis of comparison for the radiation produced by the SYNCA and cyclotron  
 4136 radiation emitted by electrons and will be used to evaluate the performance of antenna  
 4137 designs. The criteria are:

- 4138 1. Electric fields that are  $\phi$ -polarized near  $\theta = 90^\circ$
- 4139 2. Uniform time-averaged electric field magnitudes around the circumference of a  
4140 circle centered on the antenna
- 4141 3. Electric fields whose phase is equal to the azimuthal angle at the point of measure-  
4142 ment plus a constant

4143        The Locust simulation package [97] can be used to directly simulate the EM fields  
4144        generated by electrons performing cyclotron motion to validate the analytical calculations.  
4145        Locust simulates the EM fields by first calculating the trajectory of the electrons in  
4146        the magnetic trap using the Kassiopeia software package [98]. The trajectory can then  
4147        be used to solve for the EM fields using the Liénard-Wiechert equations directly with  
4148        no approximations. The resulting electric field solutions drive a receiving antenna by  
4149        convolving the time-domain fields with the finite-impulse response filter of the antenna  
4150        or they can be examined directly to study the field characteristics that the SYNCA must  
4151        reproduce. In the next section we compare the radiation field patterns for electrons  
4152        simulated with Locust to patterns from a SYNCA antenna design.

### 4153        **5.3.3 SYNCA Simulations and Design**

#### 4154        **Early SYNCA Design Development**

4155        A crossed-dipole antenna [99] (see Figure 5.13) was identified early on as a candidate  
4156        SYNCA design. The crossed-dipole is a circularly polarized antenna, consequently, the  
4157        electric fields measured in the plane of the dipole antenna exhibit the same relative phase  
4158        offsets as a 90° electron in a magnetic trap. These phase offsets were measured with the  
4159        first rudimentary crossed-dipole prototype manufactured from coaxial cables with the  
4160        insulation and shield stripped away.

4161        Because the SYNCA is ultimately a calibration tool, it is desireable that the antenna  
4162        have a well-characterized and robust antenna pattern. Therefore, manufacturing a  
4163        SYNCA using the stripped wire method shown in Figure 5.13 is infeasible. Studies of  
4164        crossed-dipole antennas manufactured out of printed circuit boards were performed using  
4165        HFSS to identify an antenna design that imitated an electron, while being more robust  
4166        and simpler to manufacture (see Figure 5.14).

4167        Identifying a design that was robust, manufacturable, and matched the electric fields  
4168        of a trapped electron proved to be a non-trivial task. The primary factor driving the  
4169        difficulty was the high operating frequency of the antenna (26 GHz) combined with  
4170        the requirement that the antenna be electrically-small. An antenna that is electrically-  
4171        small at 26 GHz has a largest dimension on the order of 1 mm, which poses significant  
4172        manufacturability challenges given the limited available budget for SYCNA fabrication.

4173        One of the key limitations with the small size requirements is the diameter of the  
4174        coaxial cables needed to feed the crossed-dipole antenna. The smallest commonly available  
4175        rigid coaxial cables available on the market have diameters of approximately 0.5 mm,

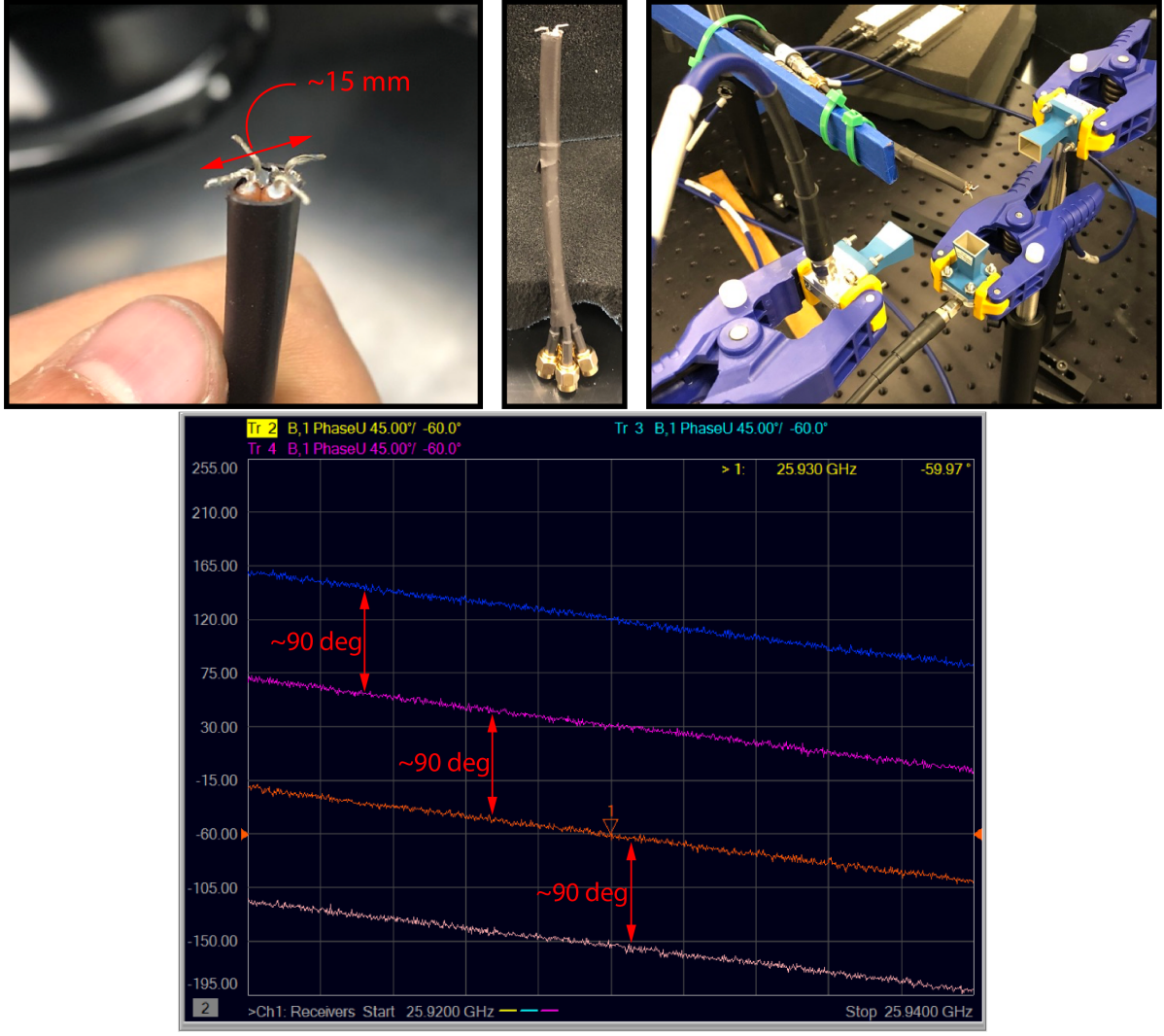


**Figure 5.13.** Images of an early prototype crossed-dipole antenna manufactured by hand and the first measurement setup. The antenna was constructed by hand using four stripped coaxial cables. The antenna was connected to one port of the VNA, and the remaining three ports on the VNA were connected to horn antenna arranged with 90 deg offsets around the crossed-dipole. The measured unwrapped S-parameter phases exhibit the desired relative phase behavior for a SYNCA. These early measurements were the first laboratory proof-of-principle for the crossed-dipole SYNCA.

4176 which limited the spacing between dipole arms to a minimum of about 1 mm. The  
 4177 crossed-dipole antenna performs better as a SYNCA if the dipole arm separation is  
 4178 significantly less than the operating wavelength. Therefore, the high operating frequency  
 4179 ultimately limited how well the SYNCA could mimic an electron. If the desired cyclotron  
 4180 frequency was lowered by an order of magnitude to approximately 3 GHz a significantly  
 4181 higher quality SYNCA could be manufactured at lower cost.

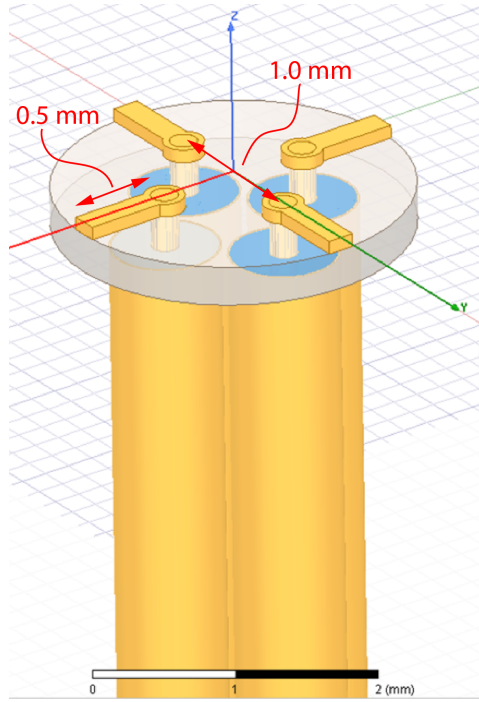


**Figure 5.14.** An early iteration of a crossed-dipole SYNCA antenna simulated in HFSS. The antenna is electrically small at 26 GHz, which requires dipole arms on the order of 1 mm long. This design is limited by the minimum achievable distance between the dipole arms caused by the available diameters of coaxial cables. The assumed termination scheme for the coaxial cables to the antenna is hand-soldering, which introduces random variation in the antenna pattern from the inevitable blobs of solder left on the surface of the PCB.

4182 The decision to use coaxial transmission lines terminated on the antenna PCB with a  
 4183 hand-soldered connection was driven primarily to limit the costs of SYNCA development  
 4184 and contributed to the observable variations in the SYNCA's gain and phase patterns.  
 4185 A second iteration of the SYNCA design that minimized hand-soldering by using surface-  
 4186 mount components could significantly reduce variations in the antenna pattern. The  
 4187 major drawback in the development of a surface-mount SYNCA is the cost, and given the  
 4188 transition to a cavity based design for Phase IV, such a design was never investigated.

#### 4189 **Finalized SYNCA Simulations and Design**

4190 One of the main drawbacks of a standard crossed-dipole design is that they do not radiate  
 4191 uniform electric fields near the  $\theta = \pi/2$  plane. Typical crossed-dipole antennas use dipole  
 4192 arm lengths equal to  $\lambda/4$  or larger [99], where  $\lambda$  is the wavelength at the desired operating  
 4193 frequency. Such large arm lengths cause the electric field magnitude to vary significantly  
 4194 around the circumference of the antenna. However, making the antenna electrically small

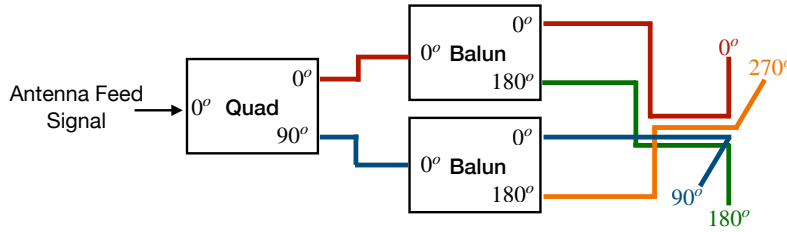


**Figure 5.15.** An idealized crossed-dipole antenna consists of two electric dipole antennas oriented perpendicular to each other and is fed with four signals with a quadrature phase relationship. An example antenna feed circuit is shown which is composed of a chained combination of a quadrature hybrid-coupler (Quad) and two baluns.

4195 by shrinking the arm length can improve the antenna pattern uniformity.

4196 In general, the criterion for an electrically small antenna is that the largest dimension  
 4197 of the antenna ( $D$ ) obey  $D \lesssim \lambda/10$  [68]. In our application, we are attempting to mimic  
 4198 the cyclotron radiation emitted by electrons produced from tritium  $\beta$ -decay with energies  
 4199 near the spectrum endpoint. For a background magnetic field of 1 T, the corresponding  
 4200 cyclotron frequency of tritium endpoint electrons is approximately 26 GHz. Therefore, the  
 4201 electrically small condition would require that the largest dimension of the crossed-dipole  
 4202 antenna be smaller than 1.2 mm.

4203 A crossed-dipole antenna with an overall size of 1.2 mm is challenging to fabricate due  
 4204 to the small dimensions of the dipole arms that, in practice, are fragile and unsuitable  
 4205 for use as a calibration probe. To mitigate some of the challenges with the fabrication  
 4206 of such a small antenna, a variant crossed-dipole antenna design using printed circuit  
 4207 board (PCB) technology (see Figure 5.16) was developed in partnership with an antenna  
 4208 prototyping company, Field Theory Consulting <sup>1</sup>.

4209 The PCB crossed-dipole design uses four rectangular pads to represent the dipole arms,  
 4210 which are connected by a thin circular trace. The circular trace both adds mechanical  
 4211 stability to the antenna and improves the azimuthal uniformity of the electric fields  
 4212 compared to a more standard crossed-dipole geometry. Furthermore, the circular trace  
 4213 allows for a greater separation between dipole arms than standard crossed-dipoles, which  
 4214 is required to accommodate the coaxial connections to each pad. The pads each contain  
 4215 a through-hole solder joint to connect coaxial transmission lines using hand soldering.  
 4216 The antenna PCB has no ground plane on the bottom layer as this was observed in

---

<sup>1</sup><https://fieldtheoryinc.com/>

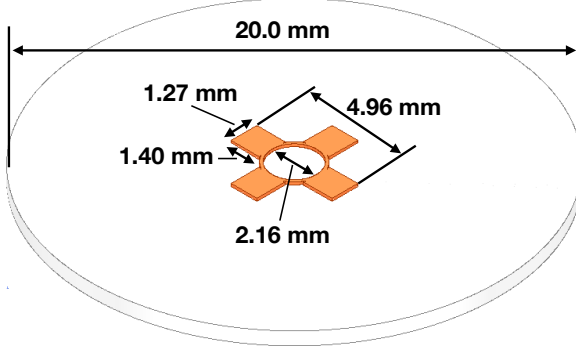


**Figure 5.16.** A model of the PCB crossed-dipole antenna with dimensions. The design has an inside diameter of 2.16 mm for the central circular trace, which is 0.13 mm wide. The dipole arms each have a width of 1.27 mm and protrude beyond the circular trace by 1.40 mm, which gives an overall width of 4.96 mm for the length of the antenna PCB trace from end-to-end. The overall size of the antenna is 20.0 mm the majority of which is the PCB dielectric material. This design was observed in simulation to maintain the field characteristics of the idealized crossed-dipole while being simpler to fabricate due to the increased size of the antenna.

4217 simulation to significantly distort the radiation pattern in the plane of the PCB. The  
 4218 only ground planes present in the model are the outer conductors of the four coaxial  
 4219 transmission lines which feed the antenna. These are left unterminated on the bottom of  
 4220 the PCB dielectric material.

4221 The antenna design development utilized a combination of Locust electron simula-  
 4222 tions and antenna simulations using ANSYS HFSS [69], a commercial finite-element  
 4223 electromagnetic simulation software. Two antenna designs were simulated: an idealized  
 4224 electrically small crossed-dipole antenna with an arm length of 0.40 mm and an arm  
 4225 separation of 0.05 mm, as well as a PCB crossed-dipole antenna with the dimensions  
 4226 shown in Figure 5.16. Plotting the magnitude of the electric fields generated by the  
 4227 antennas across a 10 cm square located in the same plane as the respective antennas  
 4228 reveals the expected cyclotron spiral pattern (see Figure 5.17) which closely matches  
 4229 the prediction for simulated electrons. The spiral pattern demonstrates that the electric  
 4230 fields have the appropriate phases to mimic cyclotron radiation, which fulfills SYNCA  
 4231 criterion 3 identified in Section 5.3.2.

4232 As we can see from Figure 5.18, the crossed-dipole antenna, which uses an idealized  
 4233 geometry, exhibits good agreement with simulation. The antenna has a maximum  
 4234 deviation from a simulated electron of approximately 0.5 dB in the total electric field, 1  
 4235 dB for the  $\phi$ -polarized electric field and 1 dB for the  $\theta$ -polarized electric field.

4236 In comparison, the pattern of the PCB crossed-dipole antenna, because the simulation  
 4237 incorporates the geometry of the coax transmission lines, exhibits some distortion from

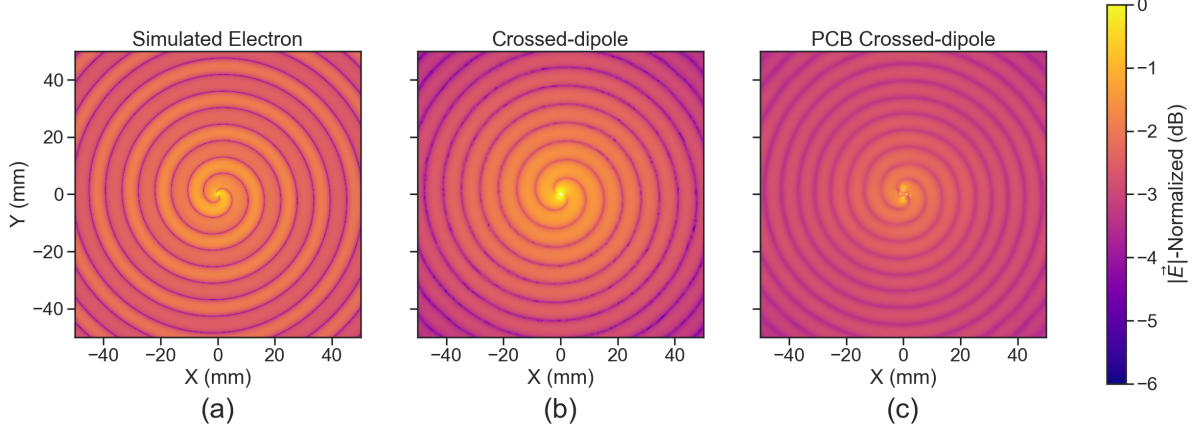


**Figure 5.17.** A comparison of the electric field magnitudes, normalized by the maximum value of the electric field in each simulation, plotted on a 10 cm square to visualize the Archimedean spirals formed by the electron (a), the crossed-dipole antenna (b), and a PCB crossed-dipole antenna (c). The matching patterns indicate that the electric fields have similar phase characteristics. These images were generated using Locust simulations for the electron and ANSYS HFSS for both antennas.

the idealized cross-dipole simulations. The vertically oriented ground planes of the coax lines introduce more  $\theta$ -polarized electric fields than are observed for simulated electrons near  $\theta = 90^\circ$ . The significant  $\theta$ -polarized field minimum is still present but shifted to approximately  $\theta = 65^\circ$ . The  $\theta$ -polarized field deviations of the PCB crossed-dipole antenna should not greatly impact the performance of the antenna because the receiving antenna array is primarily  $\phi$ -polarized. Therefore deviations in the  $\theta$ -polarized fields will be suppressed due to the polarization mismatch. More importantly, the  $\phi$ -polarized electric field pattern generated by the PCB crossed-dipole closely matches simulated electrons across the polar angle range of  $50^\circ < \theta < 150^\circ$ . In this region the PCB crossed-dipole differs by less than 0.5 dB from simulated electrons. This range greatly exceeds the beamwidth of the receiving antenna array which is designed to be most sensitive to fields produced near  $\theta = 90^\circ$ . Therefore, we conclude that the PCB crossed-dipole antenna generates a  $\phi$ -polarized radiation pattern that fulfills SYNCA criterion 1 from Section 5.3.2.

The final SYNCA criterion is related to the uniformity of the electric fields when measured azimuthally around the antenna. As we saw for real electrons in Section 5.3.2 it is expected that the magnitude of the electric field be completely uniform as a function of the azimuthal angle due to the symmetry of the cyclotron orbit. In Figure 5.19 we plot the total electric field as a function of azimuthal angle for an electron, the crossed-dipole antenna, and the PCB crossed-dipole antenna. The crossed-dipole antenna exhibits

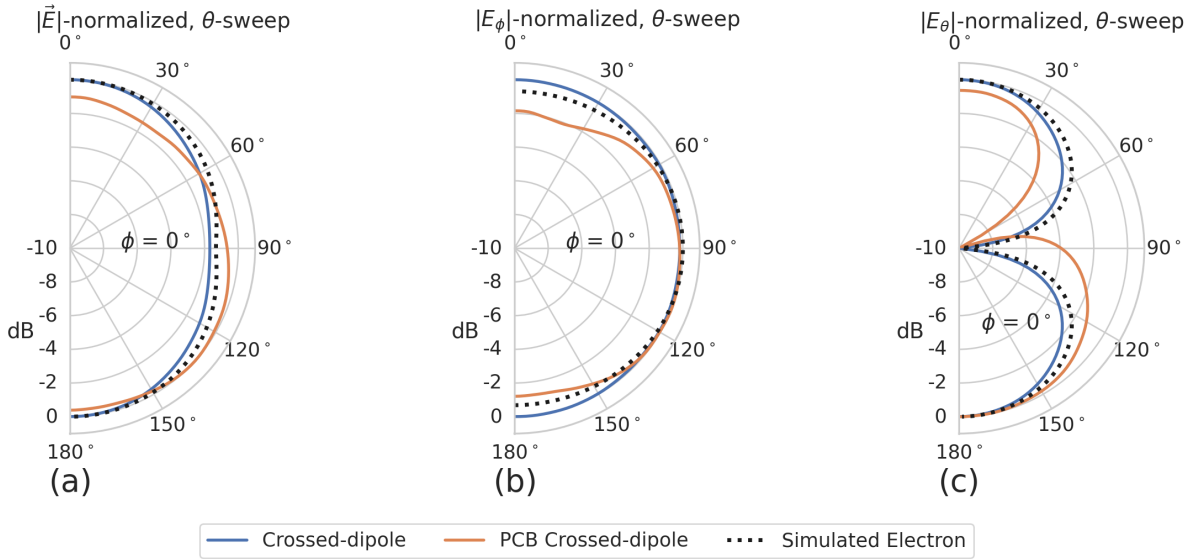


**Figure 5.18.** A comparison of the normalized electric field magnitudes for the ideal crossed-dipole, PCB crossed-dipole, and a simulated electron as a function of the polar angle ( $\theta$ ). (a) Shows the total electric field, (b) shows the  $\phi$ -polarized electric field component, and (c) shows the  $\theta$ -polarized electric field component. These images were generated using Locust simulations for the electron and ANSYS HFSS for both antennas.

perfect uniformity around the azimuthal angle, whereas the PCB crossed-dipole has a small periodic deviation with a maximum difference of 0.3 dB caused by the coaxial transmission lines below the PCB. Such a small deviation from uniformity is acceptable since it is smaller than the expected variation in uniformity caused by imperfections in the antenna fabrication process, which modifies the antenna shape in an uncontrolled manner by introducing solder blobs with a typical size of a few tenths of a millimeter on the dipole arms (see Figure 5.20). Additionally, the SYNCA will be separately calibrated to account for azimuthal differences in the electric field magnitude. Therefore we see from the simulated performance of the PCB crossed-dipole antenna that this antenna design meets all three of the SYNCA criteria.

#### 5.3.4 Characterization of the SYNCA

Two SYNCAs were manufactured using the PCB crossed-dipole design (see Figure 5.20). The antenna PCB (Matrix Circuit Board Materials, MEGTRON 6) is connected to four 2.92 mm coaxial connectors (Fairview Microwave, SC5843) using semi-rigid coax (Fairview Microwave, FMBC002), which also physically support the antenna PCB. The antenna PCB consists only of two layers which correspond to the copper antenna trace

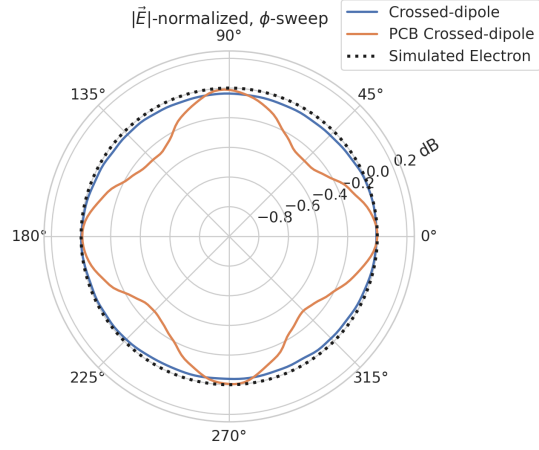


**Figure 5.19.** A comparison of the normalized electric field magnitudes for the crossed-dipole, PCB crossed-dipole, and a simulated electron as a function of the azimuthal angle ( $\phi$ ) evaluated at  $\theta = 90^\circ$ . This image was generated using Locust simulations for the electron and ANSYS HFSS for both antennas.

and the PCB dielectric. Each coax line is connected to the associated dipole arm using through-hole soldering and phase matched to ensure that the electrical length of each of the transmission lines is identical at the operating frequency. The antenna PCB is further reinforced using custom cut polystyrene foam blocks, which have an electrical permittivity nearly identical to air. A custom 3D printed mount is included at the base of the antenna to support the coax connectors and to provide a sturdy mounting base.

Characterization measurements were performed using a Vector Network Analyzer (VNA) to measure the electric field magnitude and phase radiated by the SYNCA to verify the radiation pattern (see Figure 5.21). The VNA is connected to the SYNCA at one port through a hybrid-coupler whose outputs are connected to two baluns to generate the signals with the appropriate phases to feed the SYNCA (see Figure 5.15). The other port of the VNA is connected to a single reference horn antenna that serves as a field probe. To position the SYNCA, a combination of translation and rotation stages are used to characterize the antenna's fields across the entire radiation pattern circumference. This measurement scheme is equivalent to measuring the fields generated by the SYNCA using a full circular array of probe antennas.

The antenna measurement space is surrounded by RF anti-reflective foam to isolate the measurements from the lab environment (see Figure 5.21b) and remaining reflections are removed using the VNA's time-gating feature. The SYNCA is affixed to the stages by a custom RF transparent mount made of polystyrene foam. The coaxial cables deliver the antenna feed signals generated by the VNA to the SYNCA while still allowing

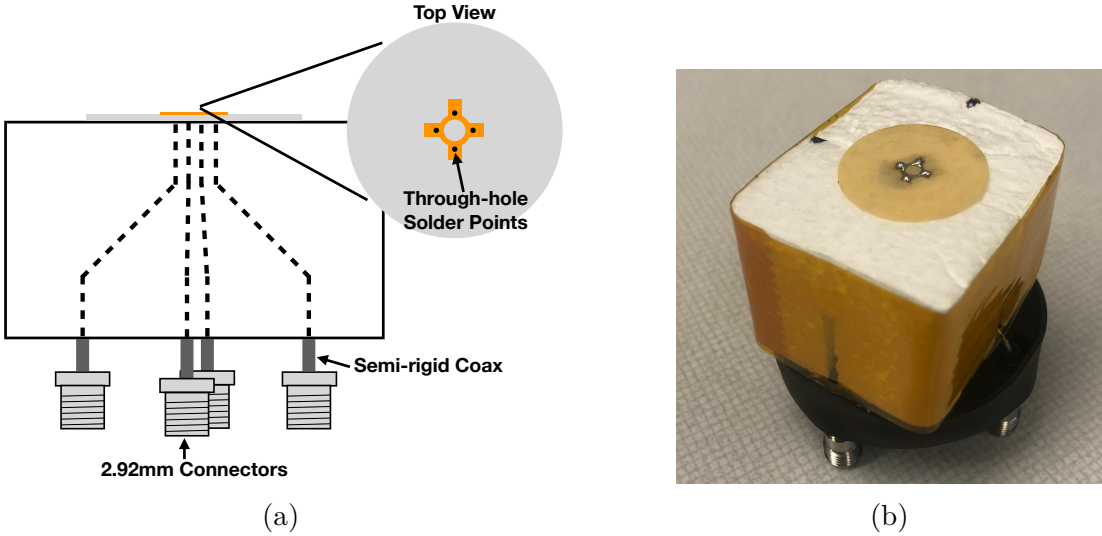


**Figure 5.20.** (a) A cartoon schematic which highlights the routing of the semi-rigid coax transmission lines. (b) A photograph of a SYNCA constructed using the modified crossed-dipole PCB antenna design. Visible in the photograph of the SYNCA are four blobs of solder which are an artifact of the SYNCA’s hand-soldered construction. These solder blobs are the most significant deviation from the SYNCA design shown in Figure 5.16 and are responsible for a significant fraction of the irregularities seen in the antenna pattern.

unrestricted rotation. The horn antenna probe is nominally positioned in the plane formed by the antenna PCB ( $\theta = 90^\circ$  or  $z = 0$  mm) at a distance of 10 cm from the SYNCA, to match the expected position of the antenna array relative to the SYNCA in the antenna array test stand. The horn antenna can be manually raised or lowered to different relative vertical positions to characterize the radiation pattern at different polar angles.

Several  $360^\circ$  scans were performed with probe vertical offsets of -10.0 mm, -5.0 mm, 0.0 mm, 5.0 mm, and 10.0 mm relative to the antenna PCB plane. These probe offsets cover a 2 cm wide vertical region centered on the SYNCA PCB, approximately equal to  $\pm 6$  degrees of polar angle. The measurements show that the SYNCA is generating fields with nearly isotropic magnitude across the probed region. The standard deviation of the electric field magnitude measured around the antenna circumference is approximately 2.9 dB for a typical rotational scan. The presence of a significant pattern null is noted near  $45^\circ$  (see Figure 5.22), which we attribute to small imperfections in the antenna PCB that could be introduced from the hand soldered terminations connecting the coax cables to the antenna. There is no significant difference in the radiation pattern when measured across the 2 cm vertical range. The measured relative phases closely follow



**Figure 5.21.** A schematic of the VNA characterization measurements (a). This setup allows for antenna gain and phase measurements across a full  $360^\circ$  of azimuthal angles using a motorized rotation stage and control of the radial position of the SYNCA using a translation stage. A photo of the setup in the lab is shown in (b).

4312 the expectation for an electron, being linear with the measurement rotation angle and  
 4313 forming the expected spiral pattern. Other than the small phase imperfections there is  
 4314 a slight sinusoidal bias to the phase data, which we determined is the result of a small  
 4315 ( $\lesssim 1$  mm) offset of the antenna's phase center from the rotation axis of the automated  
 4316 stages.

4317 The characterization measurements confirm the simulated performance of the SYNCA.  
 4318 As expected the fields generated by the antenna are nearly isotropic in magnitude,  $\phi$ -  
 4319 polarized, and are linearly out of phase around the circumference of the antenna as  
 4320 predicted for cyclotron radiation in Section 5.3.2. Small imperfections in the magnitude  
 4321 and phase of the antenna are expected, particularly at the antenna's high operating  
 4322 frequency of 26 GHz where small geometric changes can have significant impacts on  
 4323 electrical properties. However, calibration through careful characterization measurements  
 4324 can be used to remove the majority of these pattern imperfections, including the relatively  
 4325 large pattern null near  $45^\circ$ , which will allow for the usage of the SYNCA as a test source  
 4326 for free-space CRES experiments utilizing antenna arrays. In the next section we use the  
 4327 VNA measurements obtained here as a calibration for signal reconstruction using digital  
 4328 beamforming.

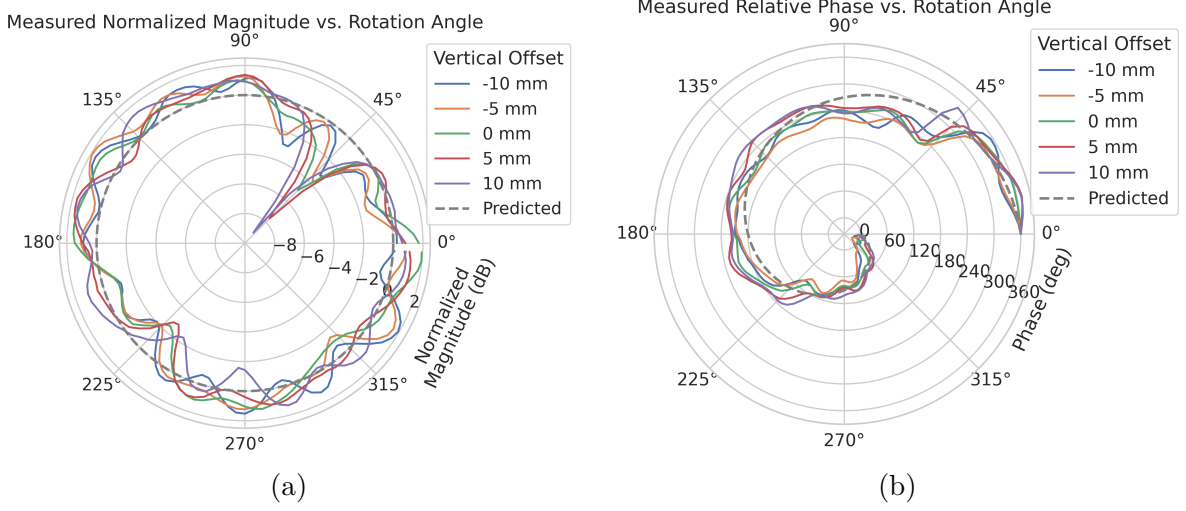


**Figure 5.22.** Linear interpolations of the measured electric field magnitude (a) and phase (b). The data was acquired using a VNA at 120 points spaced by 3 degrees from 0 to 357 degrees of azimuthal angle. The different color lines indicate the vertical offset of the horn antenna relative to the SYNCA PCB and the dashed line shows the expected shape from electron simulations. No significant difference in the antenna pattern is observed for the measured vertical offsets.

### 4329 5.3.5 Beamforming Measurements with the SYNCA

4330 Digital beamforming is a standard technique for signal reconstruction using a phased  
 4331 array [100]. The SYNCA, since it exhibits the same cyclotron phases as a trapped  
 4332 electron, can be used to perform simulated CRES digital beamforming reconstruction  
 4333 experiments on the bench-top without the need for the magnet, cryogenics, and vacuum  
 4334 systems required by a full CRES experiment. The fields received by the individual  
 4335 elements of the antenna array will have phases dependent on the spatial position of the  
 4336 source relative to the antennas. Therefore, a simple summation of the received signals  
 4337 will fail to reconstruct the signal due to destructive interference between the individual  
 4338 channels in the array. However, applying a phase shift associated with the source's  
 4339 spatial position removes phase differences and results in a constructive summation of the  
 4340 channel signals (see Figure 5.23). We can summarize the digital beamforming operation  
 4341 succinctly using the following equation

$$y[t_n] = \sum_{m=0}^{N-1} x_m[t_n] A_m e^{i\phi_m}, \quad (5.34)$$

4342 where  $y[t_n]$  represents the summed array signal at time  $t_n$ ,  $x_m[t_n]$  is the signal received  
 4343 by channel  $m$  at time  $t_n$ ,  $\phi_m$  is the phase shift applied to the signal received at channel  
 4344  $m$ , and  $A_m$  is an amplitude weighting factor that accounts for the different signal power  
 4345 received by individual channels. By changing the digital beamforming phases, the point  
 4346 of constructive interference can be scanned across the sensitive region of the array to  
 4347 search for the location of a radiating source, which is identified as the point of maximum  
 4348 summed signal power above a specified threshold. The digital beamforming phases consist  
 4349 of two components,

$$\phi_m = 2\pi d_m / \lambda + \theta_m, \quad (5.35)$$

4350 where  $d_m$  is the distance from the  $m$ -th array element to the source, and  $\theta_m$  is the  
 4351 relative angle between the source position and the  $m$ -th antenna. The first component is  
 4352 the standard digital beamforming phase that corresponds to the spatial position of the  
 4353 source, and the second component is the cyclotron phase that corresponds to the relative  
 4354 azimuthal phase offset.

4355 With a small modification to the hardware used to characterize the SYNCA (see  
 4356 Figure 5.21), we can perform a digital beamforming reconstruction of a synthetic CRES  
 4357 event. By replacing the VNA with an arbitrary waveform generator (AWG), the SYNCA  
 4358 can be used to generate cyclotron radiation with an arbitrary signal structure, which  
 4359 can then be detected by digitizing the signals received by the horn antenna. Rotational  
 4360 symmetry allows us to use the rotational stage of the positioning system to rotate the  
 4361 SYNCA to recreate the signals that would have been received by a complete circular

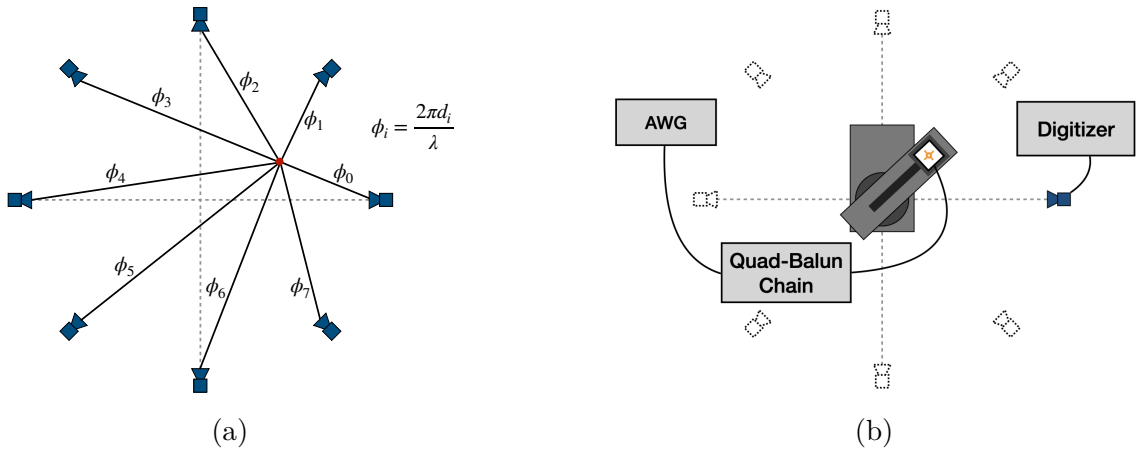


**Figure 5.23.** (a) A depiction of the relative phase differences for signals received by a circular antenna array from an isotropic source. The phases correspond to a unique spatial position.  
 (b) A schematic of the setup used to perform digital beamforming.

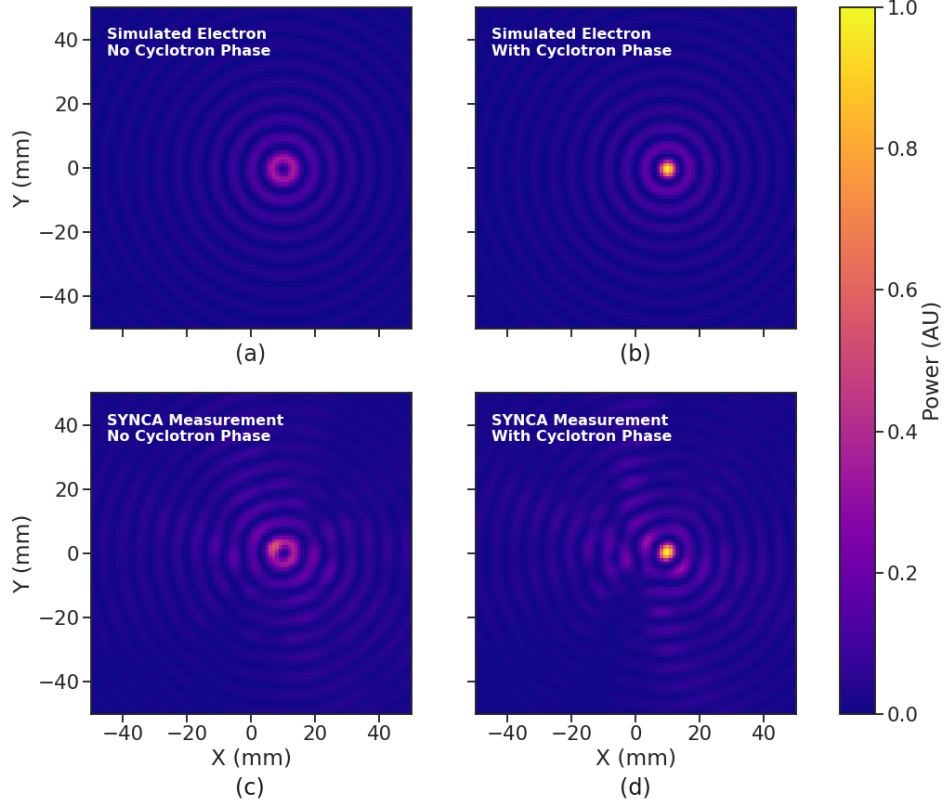


**Figure 5.24.** Digital beamforming maps generated using a simulated 60 channel array and electron simulated using the Locust package. (a) and (b) show the beamforming maps for simulated electrons without the cyclotron spiral phases and with the cyclotron spiral phases respectively. (c) and (d) show the beamforming maps produced from SYNCA measurements. We observe good agreement between simulated electrons and the SYNCA measurements.

4362 array of antennas.

4363 Using this setup, signals from a 60 channel circular array of equally spaced horn  
 4364 antennas were generated with the SYNCA positioned 10 mm off the central array axis,  
 4365 reconstructed using digital beamforming, and compared to Locust simulation (see Figure  
 4366 5.24). When the cyclotron spiral phases are not used, which is equivalent to setting  $\theta_m$   
 4367 in Equation 5.35 to zero, the SYNCA's position is reconstructed as a relatively faint ring  
 4368 as predicted by simulation. However, when the appropriate cyclotron phases are used  
 4369 during the beamforming procedure, both the simulated electron and the SYNCA appear  
 4370 as a single peak of high relative power corresponding to the source position. Therefore,  
 4371 we observe good agreement between the simulated and SYNCA reconstructions. While it  
 4372 may seem that for the case with no cyclotron phase corrections the ring reconstructs the  
 4373 position of the electron as effectively as beamforming with the cyclotron phase corrections,

4374 it is important to note that the simulations and measurements were generated without a  
 4375 realistic level of thermal noise. The larger maxima region and lower signal power, which  
 4376 occurs without the cyclotron phase corrections, significantly reduce the probability of  
 detecting an electron in a realistic noise background.

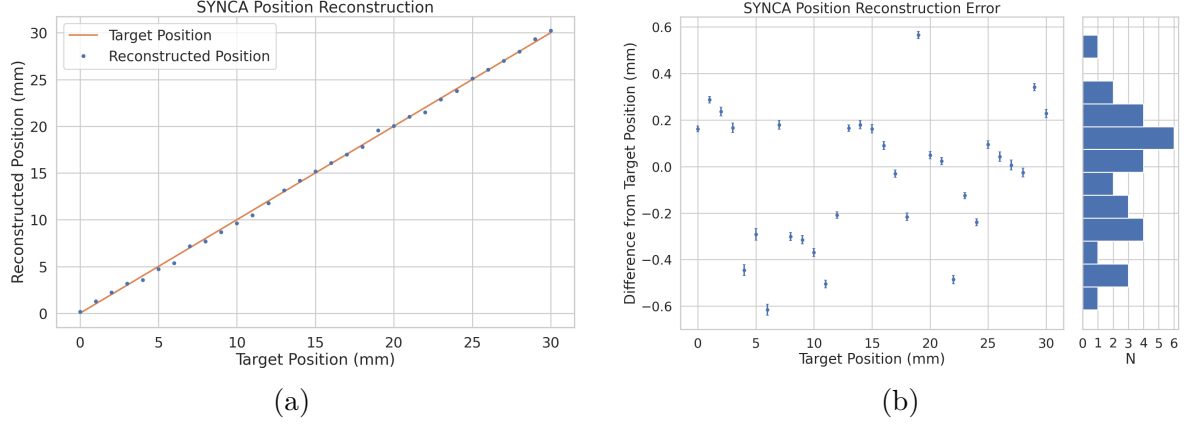


**Figure 5.25.** A plot of the SYNCA’s reconstructed position using the synthesized horn-antenna array and digital beamforming. (a) Shows the reconstructed position of the SYNCA compared with the target position indicated by the positioning system readout. (b) Shows the reconstruction error, which is the difference between the target and reconstructed positions. The error bars in (b) are the uncertainty in the mean position of the 2D Gaussian used to fit the digital beamforming reconstruction peak obtained from the fit covariance matrix. The mean fit position uncertainty of 0.02 mm is an order of magnitude smaller than the typical reconstruction error of 0.3 mm obtained by calculating the standard deviation of the difference between the reconstructed and target position.

4377  
 4378 To bound the beamforming capabilities of the synthetic array of horn antennas, we  
 4379 performed a series of beamforming reconstructions where the SYNCA was progressively  
 4380 moved off the central axis of the array (see Figure 5.25). To extract an estimate of the  
 4381 position of the SYNCA using the digital beamforming image we apply a 2-dimensional  
 4382 (2D) Gaussian fit to the image data and extract the estimated centroid value. We find  
 4383 that the synthetic horn antenna array reconstructs the position of the SYNCA with a  
 4384  $1\sigma$ -error of 0.3 mm with no apparent trend across the 30 mm measurement range. This  
 4385 reconstruction error is an order of magnitude larger than mean fit position uncertainty  
 4386 of 0.02 mm indicating that systematic effects related to the SYNCA positioning system  
 4387 could be contributing additional uncertainty to the measurements. Note that the current  
 4388 mean reconstruction error of 0.3 mm is a factor of 20 smaller than the full width at half  
 4389 maximum of the digital beamforming peak (6 mm), which could be interpreted as a naive  
 4390 estimate of the position reconstruction performance of this technique. Because these  
 4391 measurements are intended as a proof-of-principle demonstration, we do not investigate

4392 potential sources of systematic errors further; however, we expect that a similar and  
4393 more thorough investigation will be performed using the Project 8 antenna array test  
4394 stand, where typical reconstruction errors can be used to estimate the energy resolution  
4395 limits of antenna array designs.

### 4396 5.3.6 Conclusions

4397 In this paper we have introduced the SYNCA, which is a novel antenna design that  
4398 emits radiation that mimics the unique properties of the cyclotron radiation generated by  
4399 charged particles moving in a magnetic field. The characterization measurements of the  
4400 SYNCA validated the simulated performance of the PCB crossed-dipole antenna design.  
4401 Additionally, the SYNCA was used to estimate the position reconstruction capabilities  
4402 of a synthesized array of horn antennas and experimentally reproduced the simulated  
4403 digital beamforming reconstruction of electrons.

4404 While the SYNCA performs well, there exist discrepancies in the phase and magnitude  
4405 of the radiation pattern compared to the simulated SYNCA design that are related to  
4406 the small geometric differences in the soldered connections. Future design iterations that  
4407 replace the soldered connections with a fully surface mount design could improve the  
4408 radiation pattern at the cost of some complexity and expense. Furthermore, improving  
4409 the design of the antenna PCB and mounting system would allow the antenna to be  
4410 inserted into a cryogenic and vacuum environment where in-situ antenna measurement  
4411 calibrations could be performed.

4412 The discrepancies in the radiation pattern and phases exhibited by the as-built  
4413 SYNCA should not greatly impact its performance as a calibration probe. Both magni-  
4414 tude and phase variations can be accounted by applying the SYNCA characterization  
4415 measurements as a calibration to the data collected by the antenna array test stand. The  
4416 separate calibration of the SYNCA radiation does not impact the primary goals for the  
4417 antenna array test stand which are array calibration and signal reconstruction algorithm  
4418 performance characterization, because it can be performed with standard reference horn  
4419 antennas with well understood characteristics.

4420 The SYNCA antenna technology advances the CRES technique by providing a  
4421 mechanism to characterize free-space antenna arrays for CRES measurements without  
4422 the need for a magnet and cryogenics system, which would be required for calibration  
4423 using electron sources. Both the Project 8 collaboration as well as future collaborations  
4424 which are developing antenna array based CRES experiments can make use of SYNCA  
4425 antennas as an important component of their calibration and commissioning phases.

4426 **5.4 FSCD Antenna Array Measurements with the SYNCA**

4427 **5.4.1 Introduction**

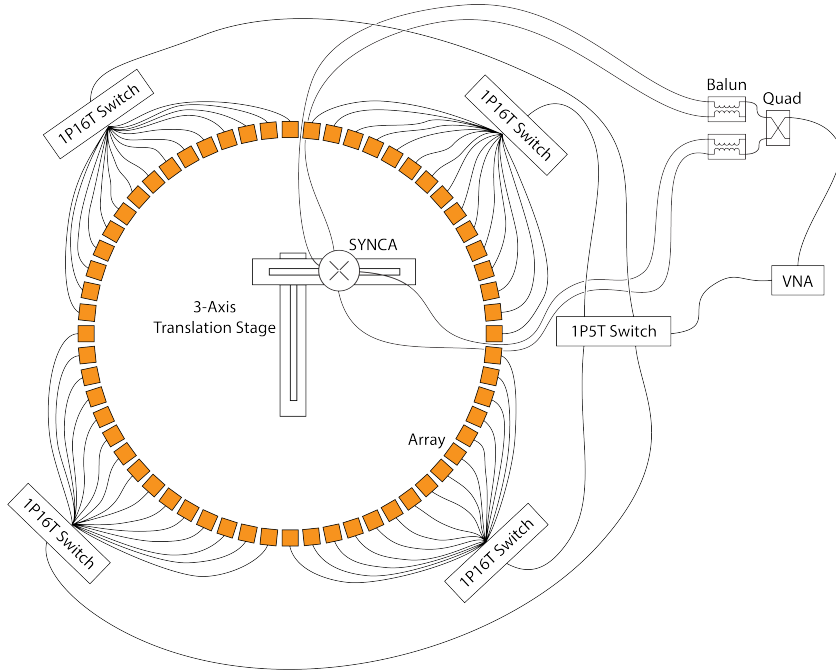


**Figure 5.26.** A diagram of the array measurement system used to test the prototype FSCD antenna array. A VNA is used as the primary measurement tool, which is connected to the array through a series of switches. The other port of the VNA connects to the SYNCA through the quad-balun chain used to provide the SYNCA feed signals. During measurements the SYNCA is positioned inside the center of the antenna array and translated to different radial and axial positions using a 3-axis manual translation stage setup.

4428 Using the SYNCA it is possible perform full-array measurements of prototype versions  
4429 of the FSCD antenna array with a realistic cyclotron radiation source (see Figure 5.26).  
4430 The goal is to compare the measured power received to FSCD simulations as a function  
4431 of the radial and axial position of the SYNCA source. These measurements are intended  
4432 to validate the antenna research and development by Project 8, which has been driven  
4433 primarily by simulations with Locust [65] and CRESana (see Section 4.2.3), and identify  
4434 any discrepancies with these simulations tools. This knowledge will provide confidence  
4435 in the simulations necessary for the analysis of the sensitivity of larger antenna array  
4436 based CRES experiment designs to the neutrino mass.

4437 As shown in Section 5.3, the SYNCA has some radiation pattern imperfections  
4438 that complicate the comparison between measurement and simulation data. One way

4439 to disentangle the effects of these imperfections is to perform an additional set of  
4440 measurements using a synthetic antenna array setup along with the SYNCA antenna.  
4441 Since the synthetic array setup uses only a single array antenna, the data should be  
4442 free of errors associated with individual antenna differences and multi-path interference,  
4443 which are two error sources being tested with the full-array setup. By comparing the  
4444 synthetic array data to the FSCD array data and to simulation data one can evaluate the  
4445 significance of these effects relative to the errors introduced by SYNCA imperfections.

## 4446 **5.4.2 Measurement Setups**

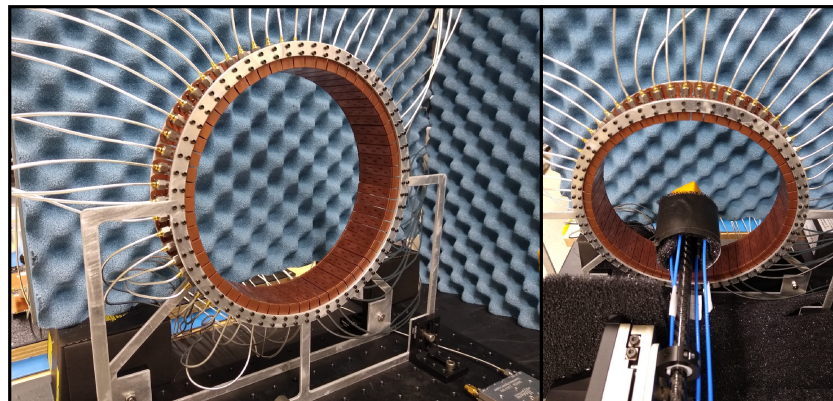
### 4447 **5.4.2.1 FSCD Array Setup**

4448 The antenna design that composes the array is the 5-slot waveguide antenna developed  
4449 for the FSCD experiment (see Figure 5.27a). The antenna is 5 cm long and is constructed  
4450 out of WR-34 waveguide with a 2.92 mm coax connector located at the center of the  
4451 antenna. Copper flanges located on both ends of the antenna are used to mount the  
4452 antenna in the array support structure. The antennas are supported by two circular steel  
4453 brackets that can be bolted to both ends of the waveguide to construct the circular array  
4454 (see Figure 5.27b). The antenna array consists of sixty identical waveguide antennas  
4455 with a radius of 10 cm. The array is mounted perpendicular to an optical breadboard  
4456 surface using a pair of the steel brackets, which provide sufficient space for the coaxial  
4457 cable connections and allows for easy positioning of the SYNCA antenna. The SYNCA is  
4458 mounted on the end of a carbon fiber rod attached to a set of manual translation stages,  
4459 which are used to move the SYNCA antenna to different positions inside the array (see  
4460 Figure 5.27c). The stages allow for independent motion in three different axes and can  
4461 position the SYNCA at radial distances up to 5 cm from the center.

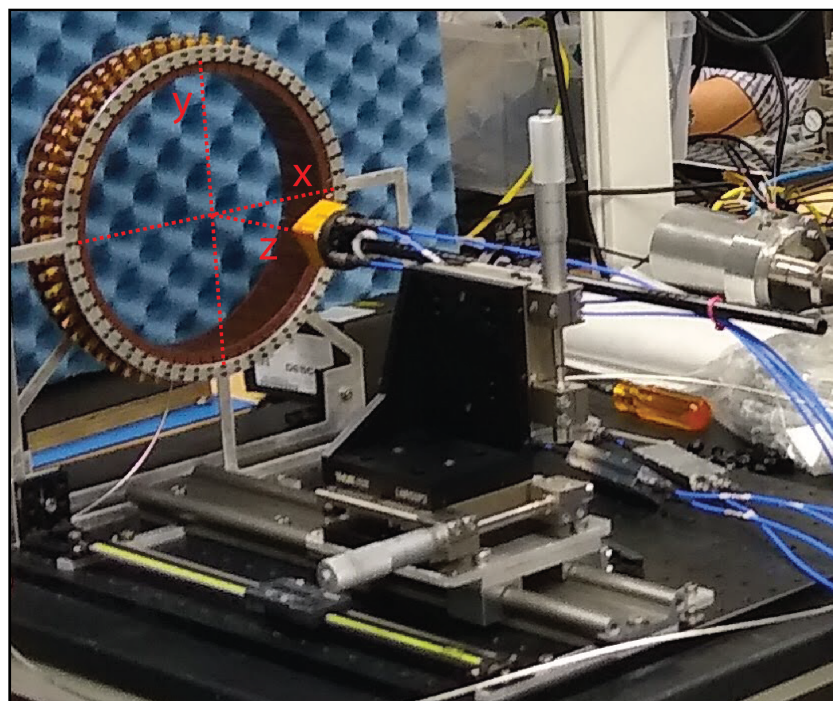
4462 Data acquisition is accomplished using a two-port VNA in combination with a series  
4463 of microwave switches that allow the VNA to connect to each channel in the array . The  
4464 first port of the VNA is connected to the quad-balun chain used to feed the SYNCA (see  
4465 Section 5.3), and the second port of the VNA connects to a 1P5T microwave switch. The  
4466 1P5T switch is connected to four separate 1P16T switch boards that connect directly  
4467 to the array. The data acquisition is controlled by a python script running on a lab  
4468 computer, which is connected to the VNA and an Arduino board programmed to control  
4469 the microwave switches. The script uses the switches to iteratively connect each of the  
4470 antennas in the array to the VNA. The VNA is configured to load a specific calibration  
4471 file for each antenna channel and performs the measurements of all available S-parameters.



(a)



(b)



(c)

**Figure 5.27.** Photos of the prototype FSCD antenna (a), the FSCD array and SYNCA (b), and the translation stages and coordinate system used to position the SYNCA (c).

4472 The separate calibration files is an attempt to remove phase and magnitude errors caused  
4473 by different propagation through the RF switches. Array measurements were performed  
4474 for the set of SYNCA positions consisting of radial (x-axis) positions from 0 to 50 mm  
4475 in 5 mm steps and axial (z-axis) positions from 0 to 50 mm in 5 mm steps resulting in  
4476 121 array measurements. At each SYNCA position the two-port S-parameter matrix  
4477 is measured using a linear frequency sweep from 25.1 to 26.1 GHz with 101 discrete  
4478 frequencies.

4479 **5.4.2.2 Synthetic Array Setup**

4480 A photograph of the setup used to perform the synthetic array measurements is shown  
4481 in Figure 5.28. A difference between this setup and the FSCD array setup is that the  
4482 synthetic array measurements were performed with a waveform generator and digitizer  
4483 instead of a VNA. The electronics configuration is identical to the diagram in Figure  
4484 5.7b. Despite the differences, one is still able to compare the measured phases of the  
4485 synthetic array and the relative magnitude of the power, since the digitized signal power  
4486 is directly proportional to S21.

4487 The arbitrary waveform generator in the setup is configured to produce a 64 MHz  
4488 sine wave signal that is up-converted to 25.864 GHz using a mixer and the VNA source.  
4489 This signal is passed through a bandpass filter and fed to the SYNCA quad-balun chain.  
4490 A single FSCD antenna is positioned 10 cm from the SYNCA and aligned vertically so  
4491 that the center of the 5-slot waveguide is in the plane of the SYNCA PCB (see Figure  
4492 5.28). This position corresponds to  $z = 0$  in Figure 5.27c. The SYNCA is rotated  
4493 in three degree steps to synthesize an antenna array with 120 channels. This channel  
4494 count is more than could physically fit in a 10 cm radius array, but there is no cost to  
4495 over-sampling. The signals from the FSCD antenna are down-converted using the second  
4496 mixer connected to the VNA source before being digitized at 250 MHz and saved to  
4497 disk. Several synthetic array measurement scans were performed by using the linear  
4498 translation stage to change the radial position of the SYNCA. In total eight scans were  
4499 taken from 0 to 35 mm using a radial position step size of 5 mm.

4500 **5.4.3 Simulations, Analysis, and Results**

4501 The Locust and CRESana simulation packages utilize the antenna transfer functions  
4502 to calculate the power that would be received by each antenna from a CRES electron.  
4503 The equivalent quantity in the measurement setup is the S21 matrix element, which

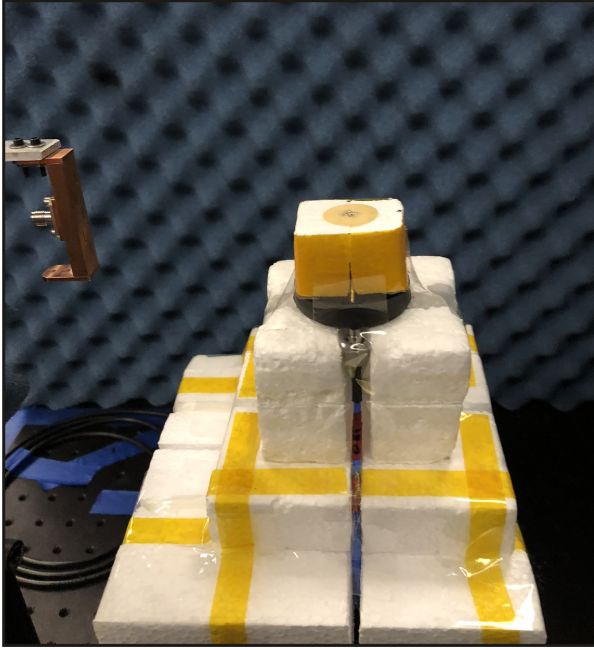


**Figure 5.28.** A photo of the FSCD antenna and the SYNCA in the synthetic array measurement setup at Penn State.

4504 indicates the ratio of the power received by an antenna in the array to the amount of  
4505 power delivered to the SYNCA. Therefore, the analysis focuses on comparing the relative  
4506 magnitudes and phase of the S21 parameters measured by the VNA as a function of the  
4507 array channel and the SYNCA position. Additionally, a beamforming reconstruction  
4508 using the S21 data is done to evaluate how the summed power and beamforming images  
4509 change as a function of the position of the SYNCA.

4510 **5.4.3.1 Simulations**

4511 Simulations for the FSCD array measurements were performed using CREsana, which  
4512 performs analytical calculations of the EM-fields produced by an electron at the position  
4513 of the antennas. At each sampled time CREsana computes the electric field vector at the  
4514 antenna positions, which is projected onto the antenna polarization axis to obtain the  
4515 co-polar electric field. The magnitude of the co-polar electric field is then multiplied by  
4516 a flat antenna transfer function to calculate the corresponding voltage signal. CREsana  
4517 simulations exploit the flat transfer functions of the FSCD antennas, which allows the  
4518 electric field to be multiplied by the antenna transfer function rather than performing  
4519 the full FIR calculation. These calculations produce a voltage time-series for each of the  
4520 antennas in the array that can be compared to the laboratory measurements.

CRESana was configured to simulate a  $90^\circ$  electron in a constant background magnetic field of  $\approx 0.958$  T with a kinetic energy of 18.6 keV. These parameters were chosen in order to mimic a CRES event near the tritium beta-decay spectrum endpoint in the FSCD experiment. The constant background magnetic field guarantees that the guiding center of the electron is stationary across the duration of the simulation which is consistent with the SYNCA in the laboratory measurements. Simulations were performed with the electron's guiding center at radial positions from 0 to 45 mm in steps of 1 mm and axial positions from 0 to 30 mm in steps of 1 mm. The simulations generated time series consisting of 8192 samples at 200 MHz for the sixty channel FSCD antenna array geometry.

#### 5.4.3.2 Phase Analysis

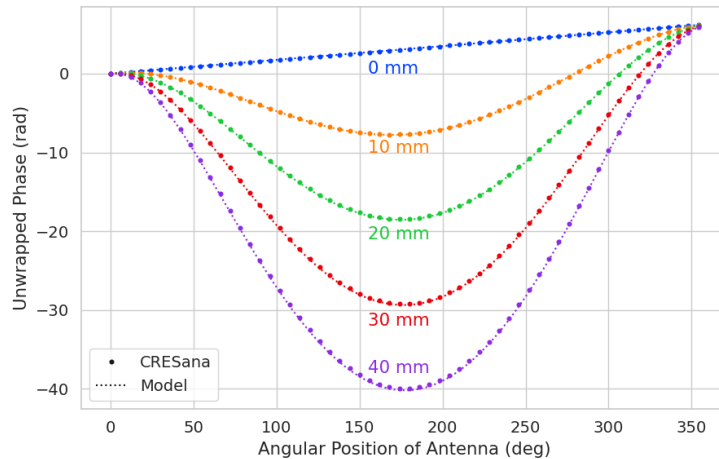


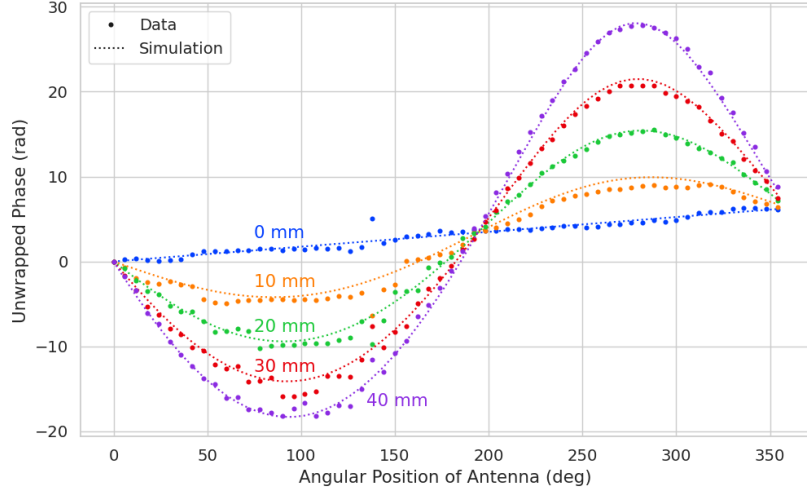
**Figure 5.29.** The unwrapped phases of signals received by the FSCD antenna array from an electron with a  $90^\circ$  pitch angle located in the plane of the antenna array. The data points indicated the phases extracted from simulation and the dashed lines show the model predictions.

Correct modeling of the signal phases is fundamental to reconstruction for both beamforming and matched filter approaches. The beamforming reconstruction relies on a signal phase model developed from Locust simulations, which allows one to predict the relative signal phases for a specific magnetic trap and electron position. The equation for the model is

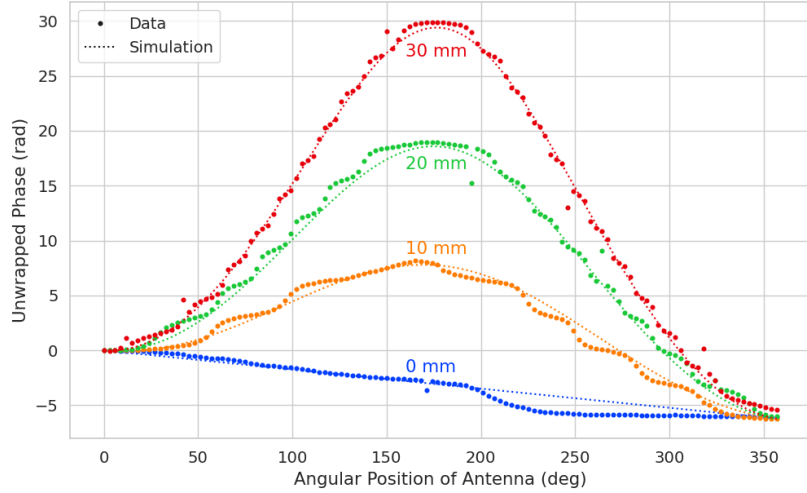
$$\phi_{ij}(t) = \frac{2\pi d_{ij}(t)}{\lambda} + \theta_{ij}(t), \quad (5.36)$$

where  $d_{ij}(t)$  is distance between the assumed electron position and the antenna position, and  $\theta_{ij}(t)$  is the angular separation between the electron and antenna positions. For

4539 details on the components of the phase model see Section 5.3.2. In Figure 5.29 I compare  
 4540 the phases predicted by Equation 5.36 to phases extracted from CRESana simulations of  
 4541 an electron located in the plane of the antenna array at a series of radial positions. One  
 4542 observes excellent agreement between the model and simulation.



(a)



(b)

**Figure 5.30.** Plots of the measured unwrapped phases from the FSCD array (a) and the synthetic array (b) compared to the model predictions for a series of radial positions. The different phases of the sinusoidal phase oscillations in the two plots reflects differences in the coordinate systems of the measurements.

4543 The measured signal phases from the FSCD array and synthetic array are shown  
 4544 in Figures 5.30a and 5.30b compared to the signal phase model. The axial position of

4545 the SYNCA in both plots is  $z = 0$  mm, such that the plane of the PCB is aligned with  
 4546 the center of the FSCD antenna. The data shown in Figure 5.30a corresponds to the  
 4547 S-parameters measured at 25.80 GHz which is the frequency closest to the one used in  
 4548 the synthetic array setup. The different slope and sinusoidal phases exhibited by Figure  
 4549 5.30a and 5.30b reflects differences in the coordinate system for each setup. In general,  
 4550 the phase model predicts the large scale features of the phases well, but there are some  
 4551 small scale deviations or errors from the phase model that do not appear to be present  
 4552 in simulation.

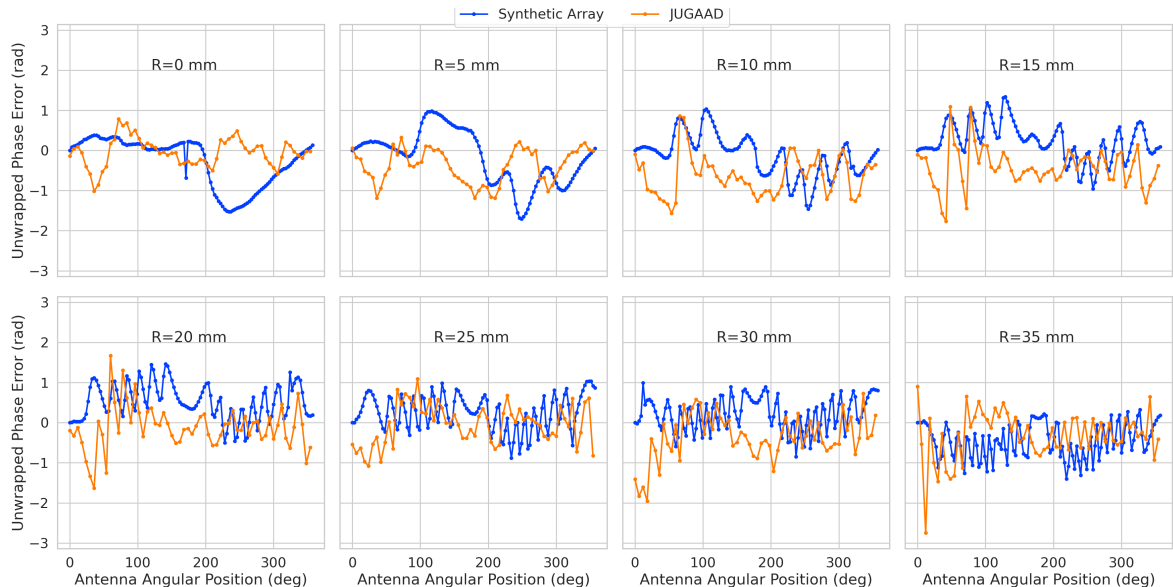


**Figure 5.31.** The phase errors between the measurement and model for the synthetic array (blue) and the FSCD array (orange) for a series of radial positions. The label JUGAAD refers to an alternative name for the FSCD array setup. As the SYNCA is translated off-axis phase errors with progressively higher oscillation frequency enter into the measurements.

4553 A comparison of the phase errors, which are the difference between measurement and  
 4554 model is shown in Figure 5.31. The FSCD array data is referred to as the JUGAAD  
 4555 data in the plot legend, which is an alternative name for the FSCD array setup.

4556 The phase error at  $R = 0$  in Figure 5.31 forms a smooth curve, with the exception of  
 4557 an outlier data point caused by a bug in the data acquisition script. One can attribute  
 4558 the observed phase error at this position to imperfections in the antenna pattern of the  
 4559 SYNCA. As the SYNCA is moved away from  $R = 0$  mm one observes that the phase  
 4560 error exhibits oscillations whose frequency increases as a function of the radial position  
 4561 of the SYNCA. These oscillations have the appearance of a diffraction pattern, which  
 4562 is particularly clear for the radii  $\geq 15$  mm, due to the bilateral symmetry of the phase

4563 error peaks around  $180^\circ$ .

4564 One can observe a higher average variance in the phase errors measured for the FSCD  
4565 array compared to the synthetic array. This is best seen by comparing the curves at  
4566  $R \leq 15$  mm where the smooth synthetic array curves are distinct from the relatively  
4567 noisy FSCD array errors. The extra noise in the FSCD array is most likely caused by  
4568 differences in the radiation patterns of the antennas that make up the array as well as  
4569 differences in the transmission lines through the switch network that introduce additional  
4570 phase errors into the measurement. Since the synthetic array measurements use only  
4571 a single antenna, these extra error terms are not present, which explains the relatively  
4572 smoother phase error curves. Despite the extra phase errors in the FSCD array, it is still  
4573 possible to observe a similar phase error oscillation effect as the SYNCA is moved away  
4574 from  $R = 0$  mm.

4575 The diffraction pattern exhibited by the phase error oscillations is more easily observed  
4576 by plotting the phase errors in a two-dimensional map, which is done in Figures 5.32a and  
4577 5.32b. For the synthetic array data ones observes a relatively clear diffraction pattern  
4578 that emerges as the SYNCA is moved radially. The bilateral symmetry of the diffraction  
4579 patterns is due to the bilateral symmetry of the circular synthetic array around the  
4580 translation axis of the SYNCA. A similar pattern is also visible in the FSCD array data,  
4581 although, it is obscured by the additional phase error that results from the multi-channel  
4582 array.

4583 The physical origin of the phase error diffraction pattern is attributed to interference  
4584 effects arising from path-length differences between the individual slots in the FSCD  
4585 antenna and the SYNCA transmitter. Since measurements are being performed in the  
4586 radiative near-field of the FSCD antenna, the path length differences between the slots  
4587 introduces a significant change in the summation of the signals that occurs inside the  
4588 waveguide, which causes the radiation pattern of the antenna to change as a function of  
4589 distance. Therefore, when the SYNCA is positioned off-axis the different path-lengths  
4590 from the SYNCA to each antenna results in different radiation patterns leading to the  
4591 observed diffraction pattern.

4592 This near-field effect is not present in simulations, because in order to simplify the  
4593 calculations it is assumed that the far-field approximation can be applied to the FSCD  
4594 antennas. This means that the radiation pattern and antenna transfer functions are  
4595 independent of the distance between the transmitter and the receiving antenna. In  
4596 principle, the near-field effects can be accounted for with a more detailed simulation of  
4597 the FSCD antennas either in CRESana or Locust, which would result in an additional

4598 term in the beamforming phase model. However, this would increase the computational  
4599 intensity of the simulation software. In the next section I briefly discuss the impact of  
4600 these near-field effects on the measured magnitude of the signals.

4601 **5.4.3.3 Magnitude Analysis**

4602 Exactly as for the signal phase, one can use simulations to construct a model that  
4603 describes the magnitude of the signals received by each channel in the antenna array.  
4604 By examining the results of simulations or by analyzing the Liénard-Wiechert equation  
4605 one can show that radiation pattern from a 90° pitch angle electron in a magnetic field  
4606 is omni-directional. Therefore the relative magnitudes of the signals received by each  
4607 channel will be determined by the free-space power loss, which is proportional to the  
4608 inverse distance between the assumed electron position and the antenna.

4609 A consequence of this is that the signals produced in the array for electrons off the  
4610 central axis will have larger amplitudes for the antennas closer to the electron compared  
4611 to those which are further away. The amplitudes of the signals received by the array  
4612 from an electron located at a series of radial positions are shown in Figure 5.33.

4613 One expects to see a similar trend in the signal magnitudes in both the FSCD and  
4614 synthetic arrays. The normalized signal magnitudes extracted from the full and synthetic  
4615 array setups for a series of radial SYNCA positions are shown in Figure 5.34. The data  
4616 corresponds to a SYNCA axial position of  $z = 0$  mm and at a frequency 25.86 GHz. One  
4617 complication is that the radiation pattern of the SYNCA is not perfectly omni-directional,  
4618 which causes the measured magnitudes at  $R = 0$  mm to diverge from the perfectly flat  
4619 behavior exhibited by electrons.

4620 As the SYNCA is moved off-axis one observes a similar increase in the number of  
4621 magnitude peaks in the synthetic array data that one would expect from a diffraction  
4622 pattern, although this trend is not as stark compared to the phase data. Noticeably,  
4623 there does not appear to be a set of channels with disproportionately larger amplitude at  
4624 large  $R$ , which would be expected based on the trends from CREsana.

4625 Comparing the magnitudes of the synthetic array to the FSCD array in Figure 5.34,  
4626 one observes a similar amount of variability in the magnitudes at  $R = 0$  mm, although  
4627 there is potentially more small scale error in the magnitude curve caused by channel  
4628 differences in the FSCD array. A similar trend is seen in the number of magnitude error  
4629 peaks in the FSCD array data to the synthetic array data, which mirrors the diffraction  
4630 effect observed in the phase data. The diffraction effect can be visualized more clearly  
4631 by plotting a similar two-dimensional map of the magnitudes (see Figure 5.35).

4632        The fact that one observes a similar diffraction pattern in the signal magnitudes  
4633      as a function the SYNCA position reinforces the conclusions from the phase analysis  
4634      that near-field effects are having a significant impact on the radiation pattern of the  
4635      FSCD array. These near-field effects lead to changes in the magnitude and phase of the  
4636      radiation pattern of the FSCD antenna as a function of distance. If left uncorrected these  
4637      errors reduce detection efficiency by causing power loss in the beamforming or matched  
4638      filter reconstruction due to phase mismatch. I explore the impact of these phase and  
4639      magnitude errors on beamforming in the next section.

4640      **5.4.3.4 Beamforming Characterization**

4641      Errors in the signal magnitudes and phases lead to errors in signal reconstruction. For  
4642      example, a matched filter reconstruction requires accurate knowledge of the signals in  
4643      each channel to achieve optimal performance. Uncorrected errors leads to mismatches  
4644      between the template and signal, which reduces detection efficiency and introduces  
4645      uncertainty in the parameter estimation. In this section, I analyze the beamformed signal  
4646      amplitude as a function of the position of the SYNCA to quantify the impact of the  
4647      phase and magnitude errors on signal reconstruction. Because of the imperfections in  
4648      the SYNCA source, it is inappropriate to directly compare the measured beamformed  
4649      signal amplitudes of the FSCD array or synthetic array to simulations. Because such a  
4650      comparison, would not allow one to disentangle losses that occur because of the antenna  
4651      array from those that occur because of the source. Therefore, I focus on comparing  
4652      the measured beamforming results of the FSCD array to the synthetic array, since the  
4653      SYNCA imperfections are common to both setups.

4654      The first method of comparison is to analyze the images generated by applying the  
4655      beamforming reconstruction specified in Section 4.3.1 to the FSCD and synthetic array  
4656      data (see Figure 5.36). The beamforming grid consisting of a square  $121 \times 121$  grid  
4657      spanning a range of -60-mm to 60 mm in the x and y dimensions. The beamforming  
4658      images formed from the synthetic array produces a three-dimensional matrix where each  
4659      grid position contains a summed time series. A single beamforming image is formed from  
4660      this data matrix by taking the mean over the time dimension. In the case of the FSCD  
4661      array, the VNA generates frequency domain data such that each grid position contains a  
4662      summed frequency series produced by the VNA sweep. For this data a single image is  
4663      formed by averaging in the frequency domain.

4664      There is a clear difference between the synthetic and FSCD array beamforming images,  
4665      which is the additional faint beamforming maxima located directly opposite the maxima

4666 corresponding to the SYNCA position. The images in Figure 5.36 were generated with  
4667 data collected at a SYNCA radial position of 15 mm, which agrees well with the observed  
4668 beamforming maximum in both images. The faint beamforming peak is located directly  
4669 opposite of the true beamforming maximum similar to a mirror image. Therefore, the  
4670 origin of this additional feature appears to be reflections between the two sides of the  
4671 circular antenna array that are not present for the synthetic array since only a single  
4672 physical antenna is used.

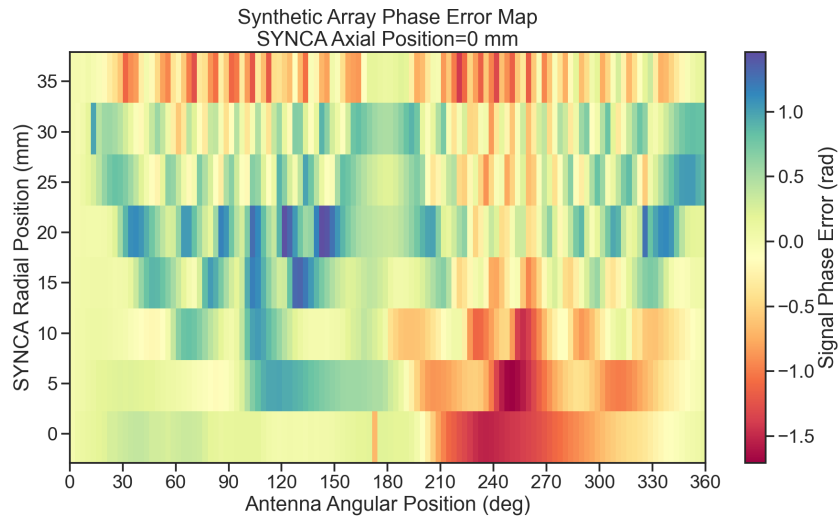
4673 From the beamforming images the maximum amplitude is extracted, which can be  
4674 plotted as a function of the radial position of the SYNCA (see Figure 5.37). The phase  
4675 errors observed in the FSCD and synthetic arrays leads to power loss at the beamforming  
4676 stage due to phase mismatches between the signals at different channels. This power loss  
4677 can be quantified by comparing the signal amplitude obtained from beamforming to the  
4678 amplitude which would be obtained from an ideal summation. The ideal summation is  
4679 performed by phase shifting each array channel to an identical phase and then summing.  
4680 The comparison between the beamforming and ideal sums is shown in Figure 5.37,  
4681 where it is seen that the synthetic and FSCD arrays experience power losses from the  
4682 beamforming summation.

4683 The beamforming power loss can be quantified using the ratio of the beamforming to  
4684 ideal signal amplitudes. Computing this ratio as a function of SYNCA radial position  
4685 radius for the FSCD and synthetic arrays, it is found that the FSCD array has a uniformly  
4686 smaller beamforming amplitude ratio, which means that the FSCD array has a larger  
4687 beamforming power loss (see Figure 5.38). The primary contributions to the beamforming  
4688 power loss in the synthetic array are phase errors from the SYNCA and phase errors  
4689 from the FSCD antenna near-field. Both of these phase errors contribute to beamforming  
4690 losses in the FSCD array, but there are clearly additional phase errors in the FSCD array  
4691 measurements contributing to the smaller ratio. Two potential error sources include phase  
4692 differences in the different antenna channels that could not be corrected by calibration as  
4693 well as reflections between antennas in the array. The total effect of these additional phase  
4694 errors is to reduce the beamforming amplitude ratio by about 5% from the beamforming  
4695 ratio of the synthetic array. Therefore, it is estimated that if no effort is made to correct  
4696 these phase errors in an FSCD-like experiment, then one would expect approximately a  
4697 10% total signal amplitude loss from a beamforming signal reconstruction.

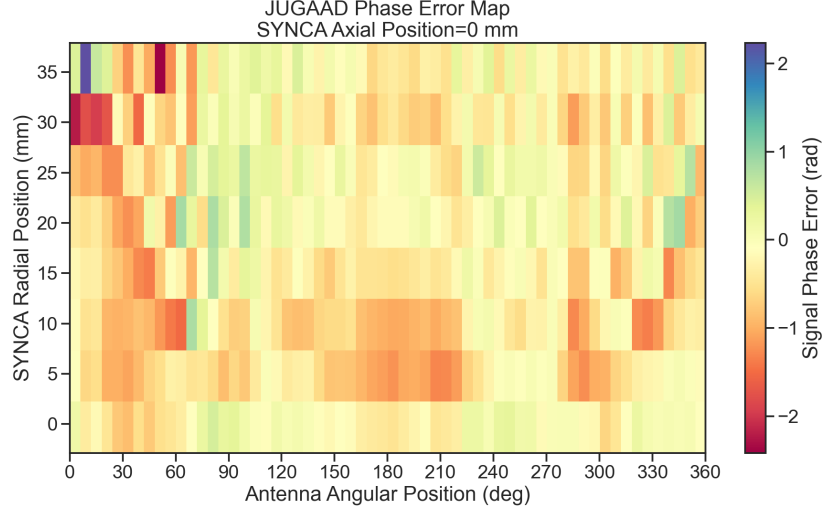
#### **4698 5.4.4 Conclusions**

4699 The estimated power loss of a beamforming reconstruction obtained from this analysis  
4700 provides valuable inputs to sensitivity calculations of a FSCD-like antenna array exper-  
4701 iment to measure the neutrino mass, since it helps to bound systematic uncertainties  
4702 from the antenna array and reconstruction pipeline. This power loss lowers the estimated  
4703 detection efficiency of the experiment since some of the signal power is lost due to  
4704 improper combining between channels and also increases the uncertainty in the electron's  
4705 kinetic energy by contributing to errors in the estimation of the electron's cyclotron  
4706 frequency.

4707 If these reconstruction losses prove unacceptable there are steps that can be taken  
4708 to mitigate their effects. Some examples include the development of a more accurate  
4709 antenna simulation approach that can reproduce the observed near-field interference  
4710 patterns of the FSCD antennas and the implementation of a calibration approach that  
4711 allows for the relative phase delays of the array to be measured without changing or  
4712 disconnecting the antenna array configuration.



(a)



(b)

**Figure 5.32.** Two dimensional plots of the phase errors for the synthetic array (a) and the FSCD (JUGAAD) array (b). In both plots there is evidence of a similar diffraction pattern with bilateral symmetry, but the FSCD array measurements have an additional phase error contribution from the different antennas and paths through the switch network.

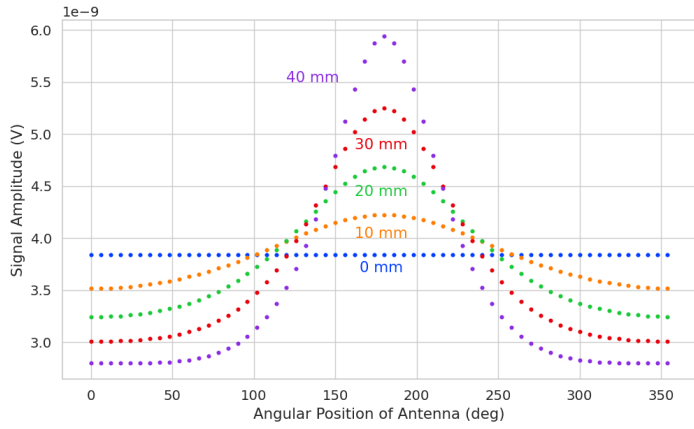


**Figure 5.33.** The amplitude of the signals from CREsana for the FSCD array from a 90° electron. As the electron is moved from  $R = 0$  the signals begin to have unequal amplitudes depending on the distance from the electron to the antenna.

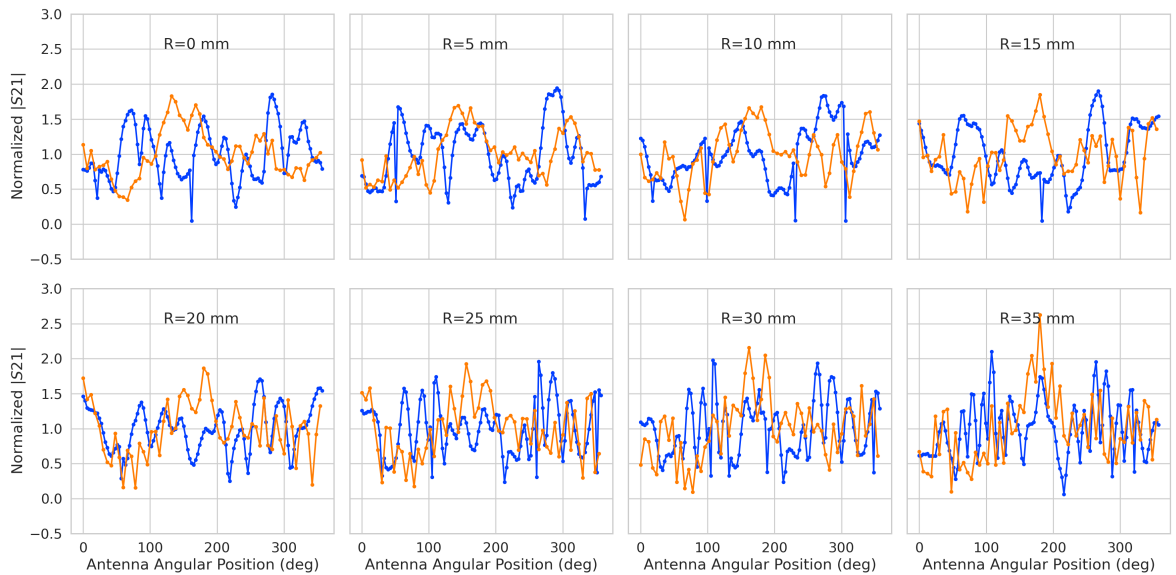
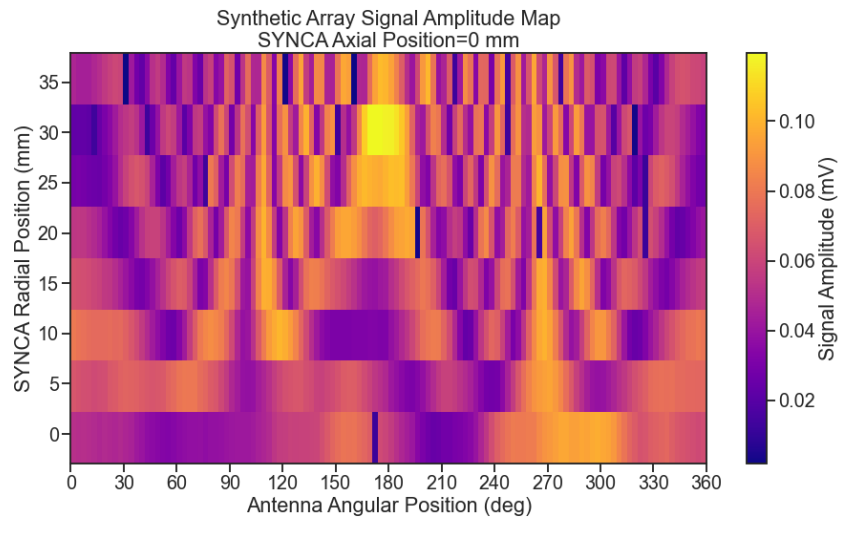
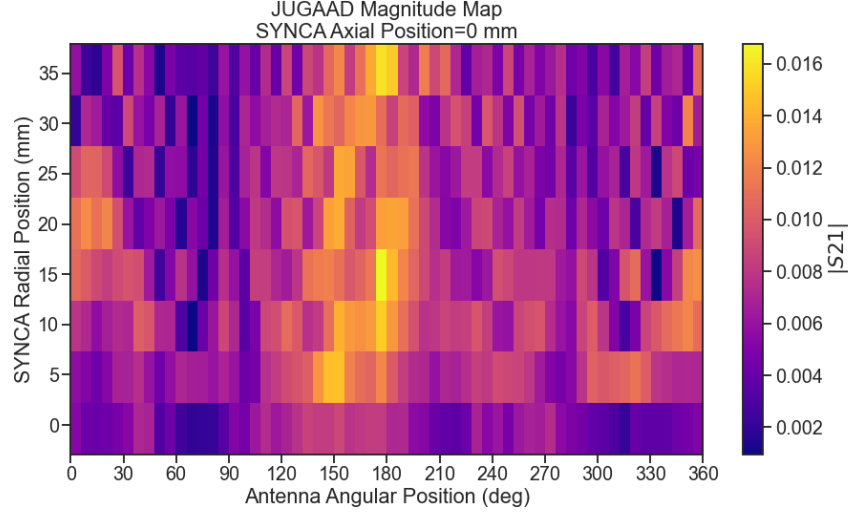


**Figure 5.34.** The normalized magnitudes of the S21 parameters measured in the FSCD (orange) and synthetic array (blue) setups. The dominant observed behavior as a function of radius is the increase in the number of magnitude peaks, which was noted in the phase error curves. There does not appear to be a strong change in the relative amplitude of a group of antennas as predicted by CREsana.



(a)



(b) The two-dimensional maps showing the diffractive pattern exhibited by the FSCD and synthetic array signal magnitudes.

**Figure 5.35.**

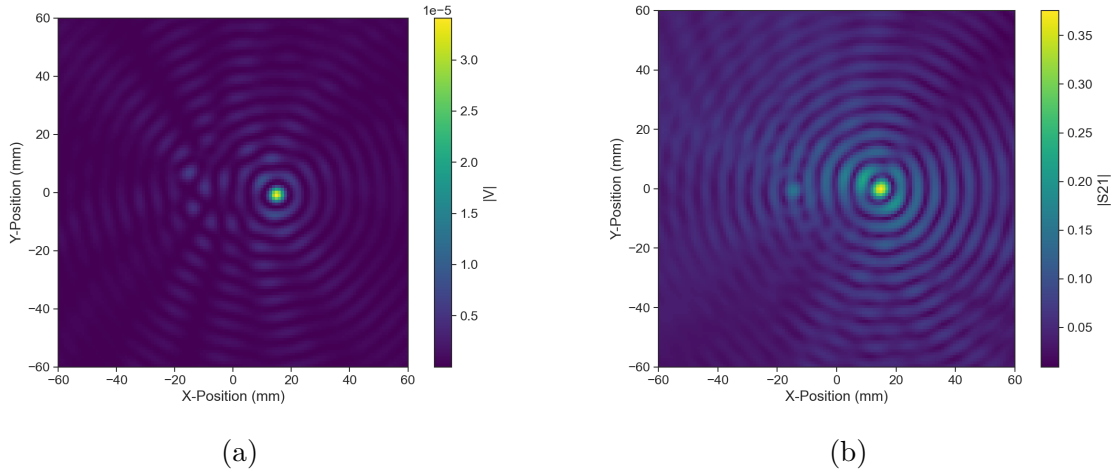


**Figure 5.36.** Beamforming images from the synthetic array (a) and FSCD array (b) setups with the SYNCA positioned 15 mm off the central axis. In both images, there is a clear maxima that corresponds to the true SYNCA position. However, in the FSCD array there is an additional faint peak located at the opposite position of the beamforming maximum. This additional peak is the mirror of the true peak and is the result of reflections between antennas in the FSCD array.

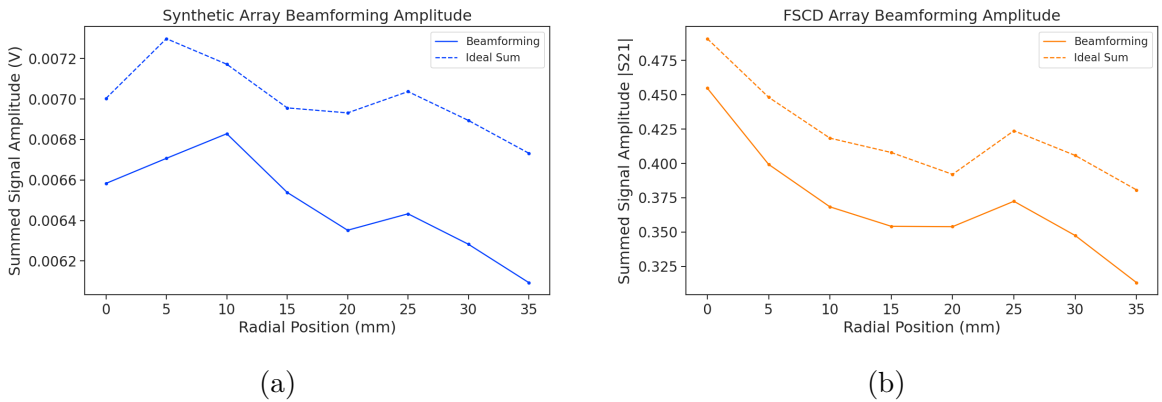


**Figure 5.37.** A comparison of the maximum signal amplitude obtained by beamforming to the signal amplitude obtained with an ideal summation as a function of the radial position of the SYNCA. The amplitudes for the synthetic array are shown in (a) and the FSCD array are shown in (b). In both setups, the signal amplitudes obtained from beamforming are smaller than the signal amplitude that could be attained with the ideal summation without phase mismatch.

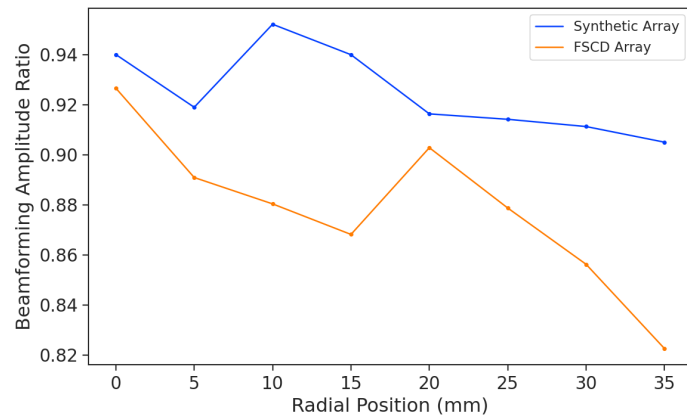


**Figure 5.38.** The ratio of the beamforming signal amplitude to the ideal signal amplitude for the FSCD and synthetic arrays. The FSCD array has a larger power loss from phase error compared to the synthetic array which indicates that calibration errors associated with the multiple channels as well as reflections are impacting the signal reconstruction.

## **Chapter 6**

# **Development of Resonant Cavities for Large Volume CRES Measurements**

### **6.1 Introduction**

The cavity approach was originally an alternative CRES measurement technology under consideration by the Project 8 collaboration for the Phase IV experiment. After pursuing an antenna array based CRES demonstrator design for several years, the increasing costs and complexity of the antenna arrays led to a reconsideration of the baseline technology for the ultimate CRES experiment planned by Project 8. Currently, a cavity based CRES experiment is the preferred technology choice for future experiments by the Project 8 collaboration including the Phase IV experiment.

In this chapter I provide a brief summary of resonant cavities and sketch out the key features of a cavity based CRES experiment. In Section 6.2 I provide a brief introduction to cylindrical resonant cavities and the solutions for the electromagnetic fields in the cavity volume.

In Section 6.3 I describe the main components of a cavity based CRES experiment, including the background and trap magnets, cavity geometry and design, and cavity coupling considerations. I also discuss some relevant trade-offs between an antenna array and cavity CRES experiment, and highlight some reasons for the transition of Project 8 to the development of a cavity based experiment.

Finally, in Sections 6.4 and 6.5, I present the design and development of an open mode-filtered cavity that could be used in a cavity based CRES experiment with atomic tritium. The results of the cavity simulations are confirmed by laboratory measurements of a proof-of-principle prototype that demonstrates key features of the design.

## 6.2 Cylindrical Resonant Cavities

Resonant cavities are sealed conductive containers, which allows one to describe the electromagnetic (EM) fields contained in the cavity volume as a superposition of resonant modes [92]. The field shapes of the resonant modes are determined by Maxwell's equations and the boundary conditions enforced by the cavity geometry. Of interest to Project 8 for CRES measurements are cylindrical cavities due to their ease of construction and integration with atom and electron trapping magnets.

### 6.2.1 General Field Solutions

Consider a long segment of conducting material with a cylindrical cross-section (see Figure 6.1). A geometry such as this can be used as a waveguide transmission line to transfer EM energy from point to point, or, if conducting shorts are inserted on both ends of the cylinder, the waveguide becomes a resonant cavity.

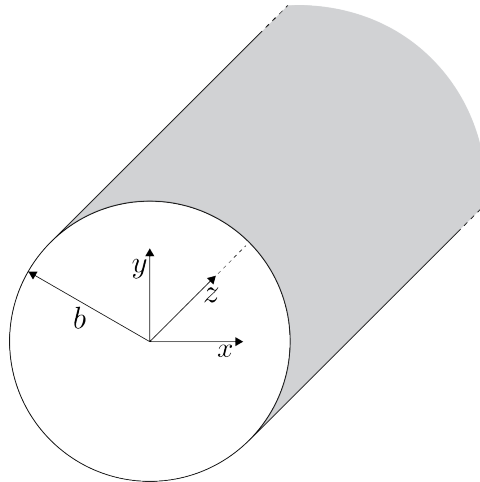


**Figure 6.1.** Geometry of a cylindrical waveguide with radius  $b$ .

The fields allowed inside a cylindrical cavity are determined by the boundary conditions of the cylindrical geometry. The general approach to solving the fields begins by assuming solutions to Maxwell's equations of the form

$$\mathbf{E}(x, y, z) = (\mathbf{e}(x, y) + \hat{z}e_z(x, y))e^{-i\beta z}, \quad (6.1)$$

$$\mathbf{H}(x, y, z) = (\mathbf{h}(x, y) + \hat{z}h_z(x, y))e^{-i\beta z}. \quad (6.2)$$

The solutions assume a harmonic time dependence of the form  $e^{i\omega t}$  and propagation

4753 along the positive z-axis. The functions  $\mathbf{e}(x, y)$  and  $\mathbf{h}(x, y)$  represent the transverse  
 4754  $(\hat{x}, \hat{y})$  components of the electric and magnetic fields respectively, and  $e_z(x, y)$ ,  $h_z(x, y)$   
 4755 represent the longitudinal components. The version of Maxwell's equations in the case  
 4756 where there are no source terms can be written as a pair of coupled differential equations,

$$\nabla \times \mathbf{E} = -i\omega\mu\mathbf{H}, \quad (6.3)$$

$$\nabla \times \mathbf{H} = i\omega\epsilon\mathbf{E}, \quad (6.4)$$

4757 where  $\epsilon$  and  $\mu$  are the permittivity and permeability of the material inside the waveguide  
 4758 or cavity. Using the field solutions from Equations 6.1 and 6.2 one can solve for the  
 4759 transverse components of the fields in terms of the longitudinal fields. Because cylindrical  
 4760 cavities are of interest, it is advantageous to write the field solutions in cylindrical  
 4761 coordinates. After performing this transformation, the set of four equations for the  
 4762 transverse field components are

$$H_\rho = \frac{i}{k_c^2} \left( \frac{\omega\epsilon}{\rho} \frac{\partial E_z}{\partial\phi} - \beta \frac{\partial H_z}{\partial\rho} \right), \quad (6.5)$$

$$H_\phi = \frac{-i}{k_c^2} \left( \omega\epsilon \frac{\partial E_z}{\partial\rho} + \frac{\beta}{\rho} \frac{\partial H_z}{\partial\phi} \right), \quad (6.6)$$

$$E_\rho = \frac{-i}{k_c^2} \left( \beta \frac{\partial E_z}{\partial\rho} + \frac{\omega\mu}{\rho} \frac{\partial H_z}{\partial\phi} \right), \quad (6.7)$$

$$E_\phi = \frac{i}{k_c^2} \left( -\beta \frac{\partial E_z}{\partial\phi} + \omega\mu \frac{\partial H_z}{\partial\rho} \right), \quad (6.8)$$

4763 where  $k_c$  is the cutoff wavenumber defined by  $k_c^2 = k^2 - \beta^2$  with  $k = \omega\sqrt{\mu\epsilon}$  being the  
 4764 wavenumber of the EM radiation.

4765 This set of equations can be used to solve for a variety of different modes, which can  
 4766 be obtained by setting conditions on  $E_z$  and  $H_z$ . For cylindrical cavities two types of  
 4767 modes are allowed, which correspond to solutions where  $E_z = 0$  and  $H_z = 0$  respectively.

### 4768 6.2.2 TE and TM Modes

4769 The TE family of modes corresponds to the case where  $E_z = 0$ . This implies that  $H_z$  is  
 4770 a solution to the Helmholtz wave equation

$$(\nabla^2 + k^2)H_z = 0. \quad (6.9)$$

4771 For solutions of the form  $H_z(\rho, \phi, z) = h_z(\rho, \phi)e^{-i\beta z}$ , Equation 6.9 can be solved using  
 4772 the standard technique of separation of variables. Rather than reproduce the derivation  
 4773 here I shall simply quote the solutions for the transverse fields [92], which are

$$H_\rho = \frac{-i\beta}{k_{c_{nm}}} (A \sin n\phi + B \cos n\phi) J'_n(k_{c_{nm}}\rho) e^{-i\beta_{nm}z}, \quad (6.10)$$

$$H_\phi = \frac{-i\beta n}{k_{c_{nm}}^2 \rho} (A \cos n\phi - B \sin n\phi) J_n(k_{c_{nm}}\rho) e^{-i\beta_{nm}z}, \quad (6.11)$$

$$E_\rho = \frac{-i\omega\mu n}{k_{c_{nm}}^2 \rho} (A \cos n\phi - B \sin n\phi) J_n(k_{c_{nm}}\rho) e^{-i\beta_{nm}z}, \quad (6.12)$$

$$E_\phi = \frac{i\omega\mu}{k_{c_{nm}}} (A \sin n\phi + B \cos n\phi) J'_n(k_{c_{nm}}\rho) e^{-i\beta_{nm}z}. \quad (6.13)$$

4774 One observes that the solutions have a periodic dependence on  $\phi$ , and radial profiles  
 4775 given by the Bessel functions of the first kind. The integer indices  $n$  and  $m$  arise from  
 4776 continuity conditions on the EM fields in the azimuthal and radial directions. For the  
 4777 TE modes, the indices range from  $n \geq 0$  and  $m \geq 1$ .  $k_{c_{nm}}$  is the cutoff wavenumber for  
 4778 the TE<sub>nm</sub> mode given by

$$k_{c_{nm}} = \frac{p'_{nm}}{b}, \quad (6.14)$$

4779 where  $b$  is the radius of the cavity or waveguide and  $p'_{nm}$  is the  $m$ -th root of the derivative  
 4780 of the  $n$ -th order Bessel function (see Table 6.1).

**Table 6.1.** A table of the values of  $p'_{nm}$ .

$n$	$p'_{n1}$	$p'_{n2}$	$p'_{n3}$
0	3.832	7.016	10.174
1	1.841	5.331	8.536
2	3.054	6.706	9.970

4781 The TM mode family corresponds to the case where  $H_z = 0$ , and  $(\nabla^2 + k^2)E_z = 0$ .  
 4782 Again, solutions are assumed of the form  $E_z(\rho, \phi, z) = e_z(\rho, \phi)e^{-i\beta z}$ , for which the general  
 4783 form of the solutions is the same as for the TE modes. However, the different boundary  
 4784 conditions for the TM modes results in particular solutions with a different form, which I  
 4785 shall quote here without derivation. The transverse fields of the TM modes are given by

$$H_\rho = \frac{-i\omega\epsilon n}{k_{c_{nm}}^2 \rho} (A \cos n\phi - B \sin n\phi) J_n(k_{c_{nm}}\rho) e^{-i\beta_{nm}z}, \quad (6.15)$$

$$H_\phi = \frac{-i\omega\epsilon}{k_{c_{nm}}} (A \sin n\phi + B \cos n\phi) J'_n(k_{c_{nm}}\rho) e^{-i\beta_{nm}z} \quad (6.16)$$

$$E_\rho = \frac{-i\beta}{k_{c_{nm}}} (A \sin n\phi + B \cos n\phi) J'_n(k_{c_{nm}}\rho) e^{-i\beta_{nm}z}, \quad (6.17)$$

$$E_\phi = \frac{-i\beta n}{k_{c_{nm}}^2 \rho} (A \cos n\phi - B \sin n\phi) J_n(k_{c_{nm}}\rho) e^{-i\beta_{nm}z}, \quad (6.18)$$

<sup>4786</sup> which one may notice are the same solutions as the TE modes with  $H$  and  $E$  flipped.

<sup>4787</sup> The cutoff wavenumber for the TM modes is given by,  $k_{c_{nm}} = p_{nm}/b$ , where the values of

<sup>4788</sup>  $p_{nm}$  correspond to the  $m$ -th zero of the  $n$ -th order Bessel function (see Table 6.2).

**Table 6.2.** A table of the values of  $p_{nm}$ .

$n$	$p_{n1}$	$p_{n2}$	$p_{n3}$
0	2.405	5.520	8.654
1	3.832	7.016	10.174
2	5.135	8.417	11.620

### <sup>4789</sup> 6.2.3 Resonant Frequencies of a Cylindrical Cavity

<sup>4790</sup> A cylindrical cavity is constructed by taking a section of cylindrical waveguide and  
<sup>4791</sup> shorting both ends with conductive material. This means that the electric fields inside a  
<sup>4792</sup> cylindrical cavity are exactly those derived in Section 6.2.2 with the additional condition  
 that the electric fields must go to zero at  $z = 0$  and  $z = L$  (see Figure 6.2).

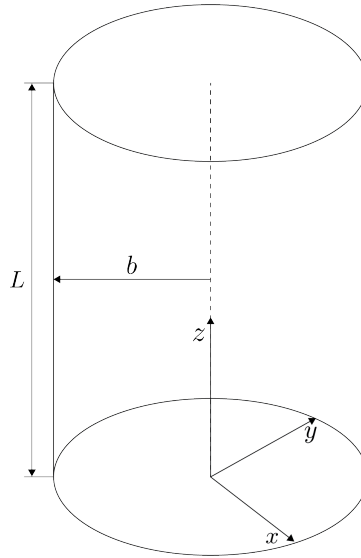


**Figure 6.2.** The geometry of a cylindrical cavity with length  $L$  and radius  $b$ .

<sup>4793</sup>

4794 The transverse electric field solutions for a cylindrical waveguide are of the form

$$\mathbf{E}(\rho, \phi, z) = \mathbf{e}(\rho, \phi) (A_+ e^{-i\beta_{nm}z} + A_- e^{i\beta_{nm}z}), \quad (6.19)$$

4795 where  $A_+$  and  $A_-$  are arbitrary amplitudes of forward and backward propagating waves.

4796 In order to enforce that  $\mathbf{E}$  is zero at both ends of the cavity it is required that

$$\beta_{nm}L = 2\pi\ell, \quad (6.20)$$

4797 where  $\ell = 0, 1, 2, 3, \dots$ . Using this constraint on the propagation constant one can solve

4798 for the resonant frequencies of the  $\text{TE}_{nml}$  and the  $\text{TM}_{nml}$  modes in a cylindrical cavity.

4799 For the TE modes the resonant frequencies are

$$f_{nml} = \frac{c}{2\pi\sqrt{\mu_r\epsilon_r}} \sqrt{\left(\frac{p'_{nm}}{b}\right)^2 + \left(\frac{\ell\pi}{L}\right)^2}, \quad (6.21)$$

4800 and the frequencies of the TM modes are

$$f_{nml} = \frac{c}{2\pi\sqrt{\mu_r\epsilon_r}} \sqrt{\left(\frac{p_{nm}}{b}\right)^2 + \left(\frac{\ell\pi}{L}\right)^2}. \quad (6.22)$$

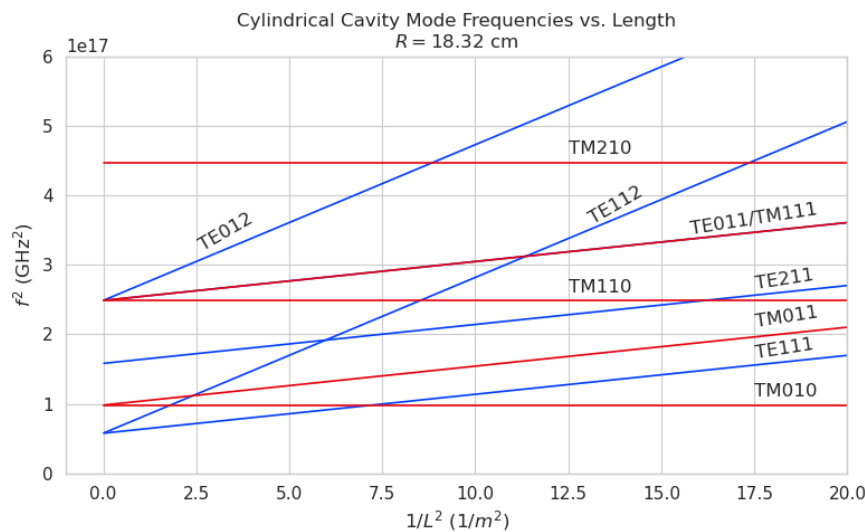


**Figure 6.3.** Relation of mode frequency to cavity length for a cylindrical cavity with a radius of 18.32 cm.

## 4801 6.2.4 Cavity Q-factors

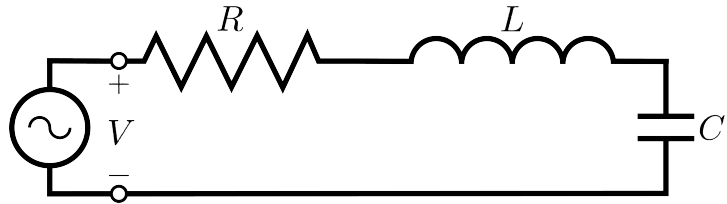


Figure 6.4. A series RLC circuit.

4802 The resonant behavior of cylindrical cavities can be modeled as a series RLC circuit  
 4803 (see figure 6.4). The input impedance of the circuit can be obtained by applying  
 4804 Kirchhoff's laws to calculate the impedance of the equivalent circuit. For a series RLC  
 4805 circuit the input impedance is

$$Z_{\text{in}} = \left( \frac{1}{R} + \frac{1}{i\omega L} + i\omega C \right). \quad (6.23)$$

4806 The resistance in the circuit represents all sources of loss in the cavity, which is primarily  
 4807 caused by the finite conductivity of the cavity walls. The inductor and capacitor represent  
 4808 the energy stored in the cavity in the form of electric and magnetic fields. If the circuit  
 4809 is being driven by an external power source the input power can be written in terms of  
 4810 the circuit input impedance and the source voltage

$$P_{\text{in}} = \frac{1}{2} Z_{\text{in}} |I|^2 = \frac{1}{2} |I|^2 \left( \frac{1}{R} + \frac{1}{i\omega L} + i\omega C \right). \quad (6.24)$$

4811 The resistor introduces a loss into the system with a power given by

$$P_{\text{loss}} = \frac{1}{2} |I|^2 R, \quad (6.25)$$

4812 and the capacitor and inductor store energies given by

$$W_e = \frac{1}{4} \frac{|I|^2}{\omega^2 C}, \quad (6.26)$$

$$W_m = \frac{1}{4} |I|^2 L, \quad (6.27)$$

4813 respectively. Using these expressions the input power and input impedance can be written

4814 in terms of the lost power and stored energy

$$P_{\text{in}} = P_{\text{loss}} + 2i\omega(W_m - W_e), \quad (6.28)$$

$$Z_{\text{in}} = \frac{P_{\text{loss}} + 2i\omega(W_m - W_e)}{\frac{1}{2}|I|^2}. \quad (6.29)$$

4815 The condition for resonance in the RLC circuit is that the stored magnetic energy  
4816 is equal to the stored electric energy ( $W_e = W_m$ ). When this occurs  $Z_{\text{in}} = R$ , which is a  
4817 purely real impedance, and  $P_{\text{in}} = P_{\text{loss}}$ . The resonant frequency of the circuit can be  
4818 determined from the condition  $W_e = W_m$  from which one finds that

$$\omega_0 = \frac{1}{\sqrt{LC}}. \quad (6.30)$$

4819 An important performance parameter for any resonant system is the Q-factor, which  
4820 quantifies the quality of the resonator as the ratio of the stored energy multiplied by the  
4821 resonant frequency to the average energy lost per second. For the series RLC circuit, the  
4822 Q-factor is given by the expression

$$Q_0 = \omega \frac{W_e + W_m}{P_{\text{loss}}} = \frac{1}{\omega_0 RC}, \quad (6.31)$$

4823 from which one observes that as the resistance of the RLC circuit is decreased the quality  
4824 factor of the resonator increases. From the perspective of cylindrical cavities this implies  
4825 that as one decreases the resistance of the cavity walls it is expected that the Q-factor of  
4826 the cavity should increase, which is indeed the case. In certain applications where a high  
4827 Q is desireable it is possible to manufacture a cavity out of superconducting materials in  
4828 order to minimize the power losses of the system.

4829 The Q-factor of the resonator also determines with bandwidth (BW) of the system. A  
4830 cavity with a high Q-factor will resonant with a smaller range of frequencies than a cavity  
4831 with a low Q-factor. To see this examine the behavior of the RLC circuit when driven by  
4832 frequencies near the resonance. For a frequency  $\omega = \omega_0 + \Delta\omega$ , where  $\Delta\omega = \omega - \omega_0 \ll \omega_0$ ,  
4833 the input impedance can be written as

$$Z_{\text{in}} = R + i\omega L \left( \frac{\omega^2 - \omega_0^2}{\omega^2} \right), \quad (6.32)$$

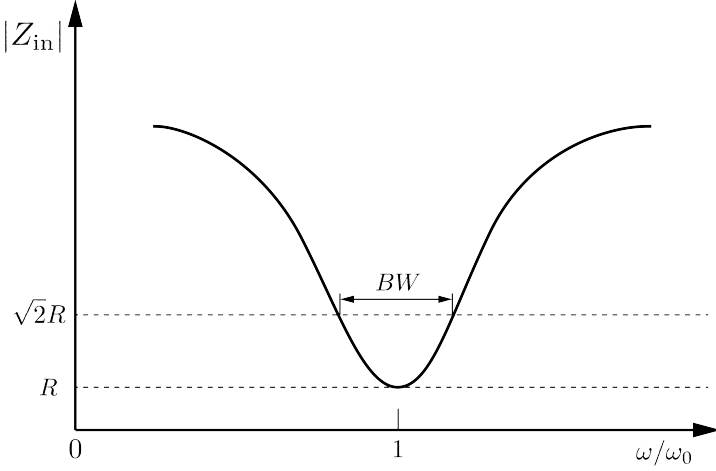


**Figure 6.5.** Illustration of the behavior of the input impedance of the series RLC circuit as a function of the driving frequency. The BW is proportion to the width of the resonance, which is inversely proportional to Q.

4834 and by expanding  $(\omega^2 - \omega_0^2)/\omega^2$  to first order in  $\Delta\omega$ , one obtains

$$Z_{\text{in}} \approx R + i \frac{2RQ_0\Delta\omega}{\omega_0}. \quad (6.33)$$

4835 Therefore, the magnitude of the input impedance near the resonance is given by

$$|Z_{\text{in}}| = R \sqrt{1 + 4Q_0^2 \frac{\Delta\omega^2}{\omega^2}}, \quad (6.34)$$

4836 from which it is seen that for the series RLC circuit the input impedance is minimized  
 4837 at the resonant frequency, which corresponds to the maximum input power (see Figure  
 4838 6.5). The half-power BW is the range of frequencies over which the input power drops to  
 4839 half the input power on resonance. This occurs when  $|Z_{\text{in}}| = \sqrt{2}R$ , which corresponds to  
 4840  $\Delta\omega/\omega = \text{BW}/2$ . Using Equation 6.34 one can find that

$$2R^2 = R^2(1 + Q_0^2\text{BW}^2), \quad (6.35)$$

4841 which implies

$$\text{BW} = \frac{1}{Q_0} \quad (6.36)$$

4842 It is important to emphasize that the Q-factor defined here,  $Q_0$ , is technically the  
 4843 unloaded Q. It reflects the quality of the cavity or resonant circuit without the influence  
 4844 of any external circuitry. In practice, however, a cavity is invariably coupled to an

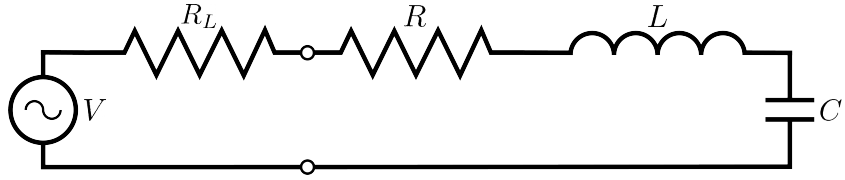


**Figure 6.6.** A series RLC circuit coupled to an external circuit with input impedance  $R_L$ .

4845 external circuit to drive a cavity resonance or to measure the energy of a resonant mode.  
 4846 Coupling a cavity to an external circuit changes the Q by loading the equivalent cavity  
 4847 RLC circuit (see Figure 6.6). The Q-factor of the cavity when it is loaded by an external  
 4848 circuit is called the loaded Q, which is the quantity that one actually measures when  
 4849 exciting a resonance in the cavity. Using the series RLC circuit model one can see that  
 4850 the load resistor in Figure 6.6 will add in series with the resistor in the circuit for a total  
 4851 equivalent resistance of  $R + R_L$ . Therefore, the loaded Q is given by

$$Q_L = \frac{1}{\omega_0(R + R_L)C}, \quad (6.37)$$

4852 from which one observes that the loaded Q is always less than the intrinsic Q of the  
 4853 cavity.

4854 The amount of coupling that is desireable depends on the specific application of  
 4855 the resonator. If one wants a resonator that is particular frequency selective then it  
 4856 makes sense to limit the amount of coupling to the cavity to maintain a small BW,  
 4857 alternatively, if a larger BW is need one can increase the cavity coupling by tuning the  
 4858 input impedance of the external circuit. The critical point, where maximum power is  
 4859 transferred between the cavity and the external circuit, occurs when the input impedance  
 4860 of the cavity matches the input impedance of the external transmission line. For the  
 4861 series RLC circuit on resonance, this matching condition corresponds to

$$Z_0 = Z_{in} = R, \quad (6.38)$$

4862 where  $Z_0$  is the impedance of the transmission line. The loaded Q at this critical point  
 4863 is, therefore,

$$Q_L = \frac{1}{2\omega_0 Z_0 C} = \frac{Q_0}{2}. \quad (6.39)$$

4864 One can described the degree of coupling between the cavity and an external circuit by

4865 defining a coupling factor,  $g$ , such that,

$$g = \frac{Q_0}{Q_L} - 1. \quad (6.40)$$

4866 When  $g = 1$  then  $Q_L = Q_0/2$ , and the cavity is said to be critically coupled. If  
4867  $Q_L < Q_0/2$ , then the cavity is undercoupled to the transmission line, corresponding to  
4868  $g < 1$ . Alternatively, if  $Q_L > Q_0/2$ , then  $g > 1$ , and the cavity is overcoupled to the  
4869 transmission line. Various specialized circuits can be used to tune the input impedance  
4870 of the external circuit as seen by the cavity to achieve a wide range of different coupling  
4871 factors based on the desired application of the cavity.

## 4872 6.3 The Cavity Approach to CRES

### 4873 6.3.1 A Sketch of a Molecular Tritium Cavity CRES Experiment

4874 Resonant cavities can be used to perform CRES measurements, and they represent the  
4875 current preferred technology by the Project 8 collaboration. The basic approach to a  
4876 neutrino mass measurement using a resonant cavity and molecular tritium beta-decay  
source is illustrated by Figure 6.7.

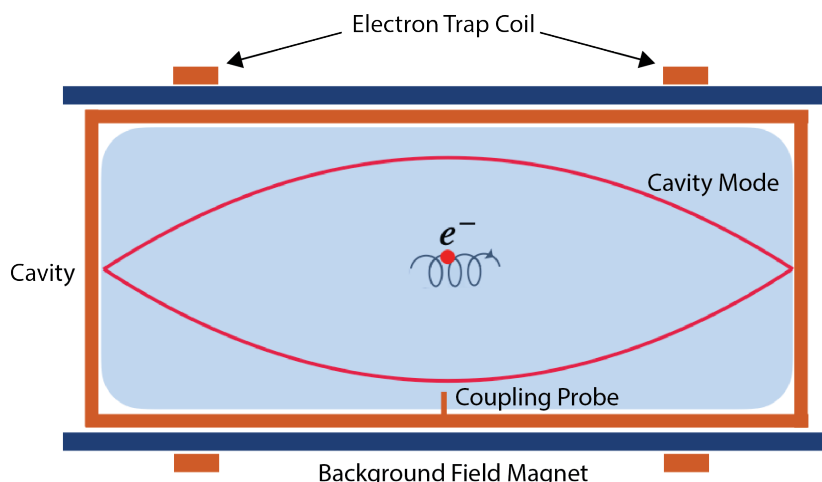


**Figure 6.7.** A cartoon depiction of a cavity CRES experiment. A metallic cavity filled with tritium gas is inserted into a uniform background magnetic field to perform CRES measurements. Electrons from beta-decays inside the cavity can be trapped and used to excite a resonant mode(s). By coupling to the cavity mode with a suitable probe one can measure the cyclotron frequency of the electron and perform CRES.

4877

4878 At the core of the experiment is a large resonant cavity filled with tritium gas. The  
4879 filled cavity is then placed in a uniform magnetic field provided by a primary magnet,  
4880 which provides the background magnetic field. The value of the background magnetic field  
4881 sets the range of cyclotron frequencies for electrons emitted near the tritium spectrum  
4882 endpoint. When a beta-decay electron is produced in the cavity it is trapped using a set  
4883 of magnetic pinch coils that keep electrons inside the cavity volume.

4884 Electrons trapped inside the cavity do not radiate in the same way as electrons  
4885 in free-space. Effectively, the same boundary conditions that were used to derive the  
4886 resonant modes of a cylindrical cavity in Section 6.2 apply to the radiation of the electron  
4887 as well. The coupling of an electron performing cyclotron motion in a cavity has been  
4888 studied in detail for measurements of the electron’s magnetic moment [101–103]. If an  
4889 electron is emitted with a kinetic energy that corresponds to a cyclotron frequency that  
4890 matches a resonant frequency of the cavity, then energy radiated by the electron excites  
4891 a corresponding resonance in the cavity. The strength of the electron’s coupling to the  
4892 cavity is given to first order by the dot product between the electrons trajectory and  
4893 the electric field vector of the resonant mode. Additional effects, such as the Purcell  
4894 enhancement [104], alter the emitted power from the free-space Larmor equation [50]. If  
4895 an electron is moving with a cyclotron frequency that is far from any resonant modes  
4896 in the cavity, then radiation from the electron is suppressed. One can interpret this  
4897 somewhat surprising effect as the metallic walls of the cavity reflecting the radiated  
4898 energy back to the electron.

4899 Detecting an electron in the cavity is accomplished by coupling the cavity to an  
4900 external transmission line that leads to an amplifier and RF receiver chain [105]. The  
4901 coupling of the cavity resonance to the amplifier occurs through a coupling probe or  
4902 aperture designed to read-out the excitation of the mode(s) excited by the electron. For  
4903 CRES measurements, the placement of a wire antenna coupling probe inside the cavity  
4904 volume leads to unacceptable losses of tritium atoms due to recombination to molecular  
4905 tritium on the antenna surface, therefore, apertures are the preferred coupling method  
4906 for cavity CRES experiments.

4907 One of the attractive features of the CRES technique for neutrino mass measurement  
4908 is the gain in statistics that comes from the differential nature of the tritium spectrum  
4909 measurement. Initially, this seems incompatible with cavities, due to the narrow reso-  
4910 nances of cavity modes giving relatively small bandwidth. However, by intentionally  
4911 over-coupling to a single cavity mode one can achieve bandwidths of a few 10’s of MHz  
4912 (see Section 6.2), which is sufficient for a measurement of the tritium spectrum endpoint

4913 region.

### 4914 **6.3.2 Magnetic Field, Cavity Geometry, and Resonant Modes**

#### 4915 **Magnetic Field and Volume Scaling**

4916 For a CRES experiment, cylindrical cavities are a natural choice since they match  
4917 the geometry of standard solenoid magnets, which are needed in order to produce the  
4918 background magnetic field for CRES measurements. Furthermore, the cylindrical shape is  
4919 compatible with a Halbach array, which is the leading choice of atom trapping technology  
4920 for future atomic tritium experiments by the Project 8 collaboration. Cylindrical cavities  
4921 also benefit from well-established machining practices that are able to achieve high  
4922 geometric precision at large lengths. More exotic cavity designs are under-consideration  
4923 and there are ongoing efforts to investigate the potential advantages these may have over  
4924 the standard cylindrical geometry.

4925 As shown in Section 6.2, the physical dimensions of the cavity are directly coupled to  
4926 the resonant frequencies of the cavity. This dependency links the size of the cavity to  
4927 the magnitude of the background magnetic field, because the magnetic field determines  
4928 the cyclotron frequencies of trapped electrons. Specifically, as the size of the cavity is  
4929 increased to accommodate larger volumes of tritium gas, the frequencies of the resonant  
4930 modes decrease proportionally. This requires that the magnetic field also decrease in  
4931 order to maintain coupling between electrons and the desired cavity mode.

4932 The required cavity size is ultimately determined by the required statistics in the  
4933 tritium spectrum endpoint region. Because the gas density must be kept below a certain  
4934 level to ensure that electrons have sufficient time to radiate before scattering, larger  
4935 volumes become the only way to achieve higher event statistics. To achieve the sensitivity  
4936 goals of Phase III and IV cavity volumes on the order of several cubic-meters are required,  
4937 which pushes one towards frequencies in the range of 100's of MHz.

#### 4938 **Single-mode Cavity CRES**

4939 It is tempting to consider maintaining a high magnetic field, while still increasing the size  
4940 of the cavity, in order to increase the radiated power from trapped electrons for better  
4941 SNR. However, if one were to maintain the same magnetic field while increasing the  
4942 size of the cavity, the electrons would begin to couple to higher order modes with more  
4943 complicated transverse geometries. The danger with this approach is that a complicated  
4944 mode structure could introduce systematic errors into the CRES signals. Example

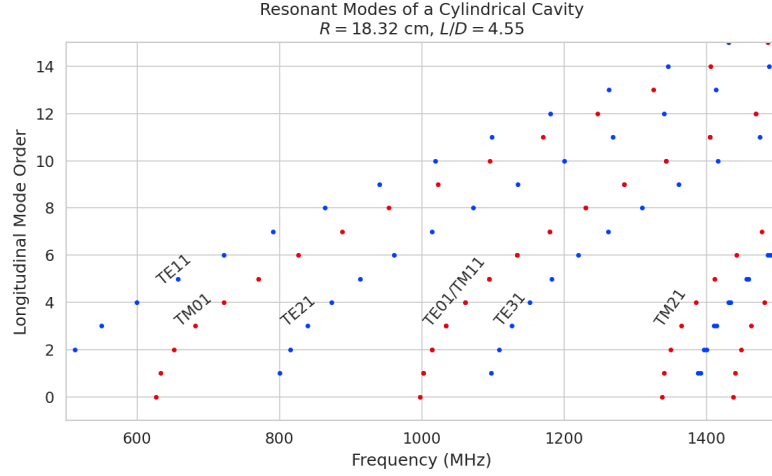
4945 systematics include unpredicted mode hybridization or changes in the mode shapes from  
4946 imperfections in the cavity construction, which would prevent reconstruction of the  
4947 electron's starting kinetic energies with adequate resolution. For this reason, it is ideal  
4948 to operate with magnetic fields that give cyclotron frequencies near the fundamental  
4949 frequency of the cavity, where the mode structure is relatively simple (see Figure 6.8).  
4950 In this frequency region it is possible to perform CRES by coupling to only a single  
4951 resonant mode; however, it is currently an open question if a single mode measurement  
4952 will provide enough information about an individual electron's position to reconstruct  
4953 the full event. Regardless, developing a solid understanding of the CRES phenomenology  
4954 when an electron is coupling to a single mode will be a necessary step towards a future  
4955 multi-mode cavity experiment.

#### 4956 Considerations for Resonant Mode Selection

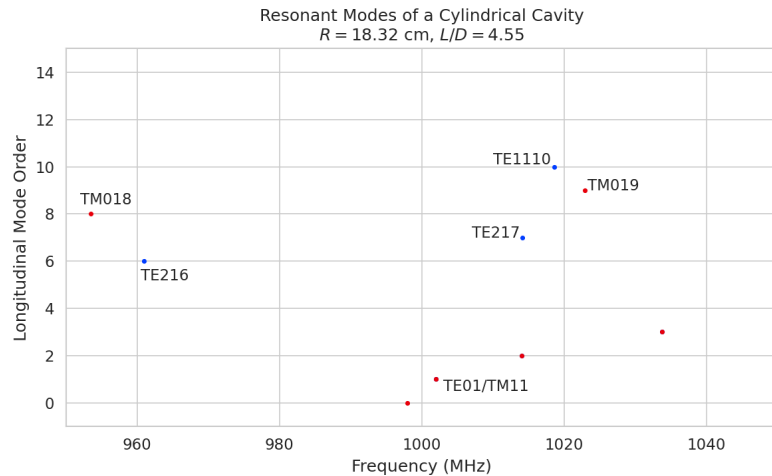
4957 A single-mode cavity experiment begs the question, which resonant mode is best for  
4958 CRES measurements? There is an immediate bias towards low order  $TE_{nm}$  and  $TM_{nm}$   
4959 modes due to the multi-mode considerations discussed above. Additionally, there is a  
4960 preference towards modes with longitudinal index  $\ell = 1$  with a single antinode along the  
4961 vertical axis of the cylindrical cavity. The reason for this is that there is a phase change  
4962 in the electric fields between antinodes that leads to modulation effects that destroy the  
4963 carrier frequency signal information.

4964 A second consideration for mode selection is the volumetric efficiency of the mode.  
4965 Volumetric efficiency can be thought of as an integral over the volume of the cavity  
4966 weighted by the relative amplitude of the mode. From the perspective of simply maximiz-  
4967 ing the volume useable for CRES measurements, this integral would be as close to unity  
4968 as possible. However, there is a requirement to reconstruct the position of the electrons  
4969 inside the cavity volume so that the local magnetic fields can be used to convert the  
4970 measured cyclotron frequency to a kinetic energy. With a single mode this necessarily  
4971 requires a variable transverse mode amplitude, which lowers the volumetric efficiency, so  
4972 that position of the electron in the cavity can be estimated from the average amplitude  
4973 of the CRES signal. Longitudinal indices of  $\ell = 1$  have an advantage in volumetric  
4974 efficiency over higher order  $\ell$  modes, since there are only two longitudinal nodes, one at  
4975 each end of the cavity. Therefore, the average coupling strength of trapped electrons as  
4976 they oscillate axially is higher for  $\ell = 1$  modes.

4977 An additional factor for mode selection is the intrinsic or unloaded Q of the mode.  
4978 In terms of SNR it is advantageous to use a mode with a very high  $Q_0$ , which is then



(a)



(b)

**Figure 6.8.** Examples of the resonant mode frequencies of a cylindrical cavity. This cavity has a radius of 18.32 cm and a length to diameter ratio of 4.55. Several families of resonant modes are relevant in the  $\approx 800$  MHz bandwidth of (a); however, after zooming in to a  $\sim 80$  MHz bandwidth centered on TE011 one sees that only a handful of resonant modes have frequencies close to TE011. Since the bandwidth required for a cavity CRES experiment is  $O(10)$ 's MHz, a significant number of resonant modes can be safely ignored since their resonant frequencies are far from the CRES bandwidth.

4979 highly overcoupled to achieve the necessary bandwidth to cover the tritium endpoint  
4980 spectrum. A high intrinsic Q ( $Q_0$ ) combined with a small loaded Q ( $Q_L$ ) requires a  
4981 large cavity coupling factor ( $g$ , see Equation 6.40). Because of the impedance mismatch  
4982 associated with large coupling factors, the noise power contributed by the physical cavity  
4983 temperature is reduced by a factor proportional to  $1/g$ , which allows one to achieve

4984 adequate SNR without the requirement of cooling the entire cavity to single Kelvin  
4985 temperatures.

4986 An example of a resonant mode that exhibits these traits is the TE<sub>011</sub> mode. At present  
4987 the TE<sub>011</sub> mode is the preferred resonance for a single-mode cavity CRES experiment  
4988 by the Project 8 collaboration. TE<sub>011</sub> is a low order mode located in a region relatively  
4989 far from other cavity modes. Furthermore, the separation of the TE<sub>011</sub> mode can be  
4990 improved by various mode-filtering techniques discussed in Section 6.4.2 below. TE<sub>011</sub>  
4991 consists of a single longitudinal antinode that can provide pitch angle information in the  
4992 form of amplitude modulation, and has an electric field with a radial profile given by the  
4993  $J'_0$  Bessel function allowing for radial position estimation. Lastly, the TE<sub>011</sub> mode has a  
4994 relatively high intrinsic Q compared to nearby modes, which helps with SNR. Unloaded  
4995 Q's greater than 80000 are achievable for a 1 GHz TE<sub>011</sub> resonance using a copper walled  
4996 cavity.

### 4997 6.3.3 Trade-offs Between the Antenna and Cavity Approaches

4998 The choice between cavities and antennas for large-scale CRES measurements is not  
4999 without trade-offs. Both the antenna array and cavity approaches are relatively immature  
5000 techniques, and at present there are no known obstacles that would prevent either  
5001 approach from being used for a large scale neutrino mass experiment. The preference for  
5002 cavities is largely driven by important practical considerations that could make a cavity  
5003 based experiment significantly cheaper than an antenna experiment of similar size and  
5004 scope. However, the switch to cavities also introduces new challenges less relevant to the  
5005 antenna array, which must be solved in order for Project 8 to achieve its neutrino mass  
5006 measurement goals.

5007 One of the major relative drawbacks of the antenna array approach is the size and  
5008 complexity of the data-acquisition system. A large-scale antenna array experiment  
5009 requires  $O(100)$  antennas independently digitized at rates of  $O(10)$  to  $O(100)$  MHz. Since  
5010 there is insufficient information in a single antenna channel to detect or reconstruct the  
5011 CRES signal, the entire array output must be processed during the signal reconstruction.  
5012 Because data storage becomes an issue with these data volumes, there is a real-time  
5013 signal reconstruction requirement that allows one to detect CRES signals buried in the  
5014 thermal noise. As discussed in Section 4.4, the computational cost of these real-time  
5015 detection algorithms are potentially quite large for even a small scale antenna array  
5016 experiment. However, the operating principle of a cavity experiment allows the CRES  
5017 signal to be detected using only a single read-out channel digitized at rates of  $O(10)$  MHz,

5018 which reduces the cost of the data acquisition system by many orders of magnitude.

5019 From an engineering perspective, the simple geometry and thin-walls of a cylindrical  
5020 cavity are simpler to interface with the cryogenic and magnetic subsystems needed  
5021 for a CRES experiment. Conversely, the antenna array requires careful design and  
5022 engineering to accommodate the antenna array and receiver electronics in proximity to  
5023 the trapping magnets. Additionally, due to near-field interference effects, the antenna  
5024 array is unable to reconstruct CRES events within the reactive near-field distance of the  
5025 antennas. Because atom trapping requirements require magnetic fields which correspond  
5026 to cyclotron frequencies for endpoint electrons less than 1 GHz, the required stand-off  
5027 distance leads to a significant loss in useable experiment volume, necessitating larger and  
5028 more expensive magnets.

5029 Another advantage to the cavity approach is the relatively compact sideband structure,  
5030 which is a result of the low modulation index for cavity CRES signals. The axial motion  
5031 in an antenna array experiment leads to frequency modulation and sidebands. The shape  
5032 of the sideband structure is determined by the modulation index,  $h = \frac{\Delta f}{f_a}$ , where  $\Delta f$   
5033 is the size of the frequency deviation and  $f_a$  is the axial frequency. The large electron  
5034 traps required for a cubic-meter-scale experiment leads to high modulation indices, which  
5035 causes the signal spectrum to be made up of numerous low power sidebands that make  
5036 reconstruction and detection challenging. This behavior was observed in simulations  
5037 of the FSCD in which carrier power decreased with pitch angle due to the increase in  
5038 modulation index (see Figure 4.30). For cavities, however, the modulation index remains  
5039 near  $h = 1$  even for very long magnetic traps due to the high phase velocity in cavities  
5040 relative to the axial velocity of the electron. This results in an almost ideal spectrum  
5041 shape that has a strong carrier frequency with a few sidebands whose relative amplitudes  
5042 encode pitch angle information.

5043 A downside of the cavity approach is the apparent difficulty of estimating the position  
5044 of the electron using only the coupling of the electron to a single mode. The amplitude of  
5045 the TE<sub>011</sub> mode is completely independent of the azimuthal coordinate, and thus position  
5046 reconstruction using the TE<sub>011</sub> mode is only able to estimate the radial position of the  
5047 electron. This position degeneracy may lead to magnetic field uniformity requirements  
5048 that are too challenging to meet due to mechanical uncertainties in cavity and magnet  
5049 construction, as well as uncertainties caused by nuisance external magnetic fields such  
5050 as the Earth's field and magnetic fields from building materials. A multi-mode cavity  
5051 experiment may provide a way to extract more precise information on the position of  
5052 the electron by analyzing the coupling of the electron to several modes that overlap in

5053 different ways.

## 5054 **6.4 Single-mode Resonant Cavity Design and Simulations**

5055 The single-mode cylindrical cavities envisioned for the Phase III and IV experiments must  
5056 be carefully engineered in order to measure the neutrino mass with the desired sensitivity.  
5057 In this section I summarize some simulation studies performed to analyze early design  
5058 concepts for a single-mode cavity. The primary tool for these investigations was Ansys  
5059 HFSS, which was also used for the development of the SYNCA antenna described in  
5060 Section 5.3.

### 5061 **6.4.1 Open Cylindrical Cavities with Coaxial Terminations**

#### 5062 **Design Concept**

5063 A basic cavity design question relevant to Project 8's ultimate goal of an atomic tritium  
5064 CRES experiment is how to build a cavity that can be efficiently filled with atomic  
5065 tritium. To keep the rate of atom loss from recombination on surfaces low, it is ideal if  
5066 the ends of the cylindrical cavity are as open as possible so that tritium atoms can flow  
5067 inside unimpeded. Additionally, one of the primary calibration techniques planned for  
5068 future CRES experiments involves CRES measurements using electrons injected from  
5069 an electron gun source, which also requires an opening at the cavity end. Cylindrical  
5070 cavities with open ends can be manufactured, however, the intrinsic Q-factors of these  
5071 cavities are orders of magnitude less than their sealed counterparts, which reduces the  
5072 signal-to-noise ratio when that cavity is used for CRES measurement.

5073 Cylindrical cavities with mostly open ends that also exhibit Q values for the  $TE_{01\ell}$   
5074 modes similar to sealed cavities can be built by using coaxial endcaps to terminate the  
5075 cavity. Cavities of this type have been manufactured for specialized applications related  
5076 to the measurements of the dielectric constants of liquefied gasses (see Figure 6.9) [3, 4].  
5077 This cavity design leaves the ends of the cavity wide open, but retains high Q-values for  
5078 the  $TE_{01\ell}$  modes due to the coaxial endcap, which are designed to perfectly reflect the  
5079 electric fields of  $TE_{01\ell}$  modes. Coupling to the  $TE_{01\ell}$  mode is achieved via an aperture  
5080 located at the center of the cavity wall.

5081 A cavity similar to Figure 6.9 is a candidate design for the future CRES experiments  
5082 by Project 8, since it appears to elegantly solve many practical issues that arise when  
5083 combining cavity CRES and atomic tritium. The coaxial endcaps leave significant regions

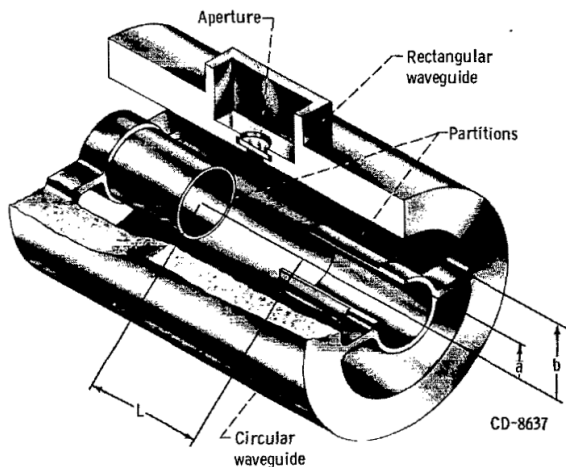


**Figure 6.9.** An image of an open cavity with coaxial terminations used for dielectric constant measurements. Figure from [3].

of the cavity ends completely open, which allows for the entrance of atomic tritium as well as the pumping away of molecular tritium that has recombined on the cavity walls. These open ends are achieved while preserving the high Q-values of the  $TE_{01\ell}$  modes, which is important for extracting as much signal power from the electron as possible. In subsequent sections this cavity design will be analyzed in more detail, primarily by using HFSS simulations to analyze the resonant mode structure of this cavity geometry.

#### Coaxial Terminator Constraints

The reason that coaxial endcaps can be used to achieve high Q-values for the  $TE_{01\ell}$  modes is that the electric fields for these modes are purely azimuthally polarized (see Equations 6.12 and 6.13). Therefore, the boundary conditions that require the electric field to go to zero at the cavity ends can be supplied using a coaxial partition of the correct radius (see Figure 6.10). Because the cylindrical shape enforced by the partition does not match the boundary conditions of other cavity modes, these terminations also significantly suppress the Q-factors of non- $TE_{01\ell}$  modes, which is potentially beneficial for a single-mode cavity CRES experiment.

The correct radius of the cylindrical partition is derived by setting up the boundary value problem in Figure 6.10, and analyzing the reflection and transmission coefficients for waves incident on the coaxial terminators. The basic problem is to identify the radius  $a$  where the reflection coefficient for the  $TE_{01\ell}$  modes becomes equal to 1. One can show that if the coaxial partitions are made sufficiently long relative to the wavelength of the

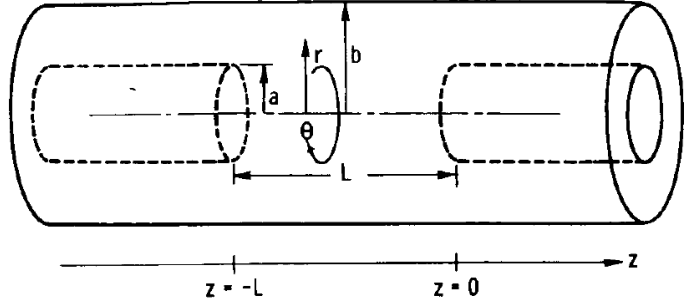


**Figure 6.10.** The simplified geometry of an open cavity with coaxial terminations. Figure from [4].

5104 TE<sub>01</sub> modes then perfect reflection can be achieved. This derivation is quite lengthy  
 5105 and complex and is presented in full in [4]. Here, I shall simply explain the resulting  
 5106 conditions on the partition radius for perfect reflection.

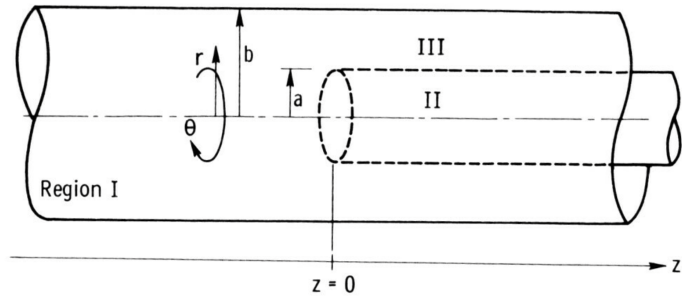


**Figure 6.11.** Electric field regions for the open cavity boundary value problem. Figure from [4].

5107 The open cavity boundary value problem is solved by expressing the forms of the  
 5108 electric fields in the different regions of the cavity and requiring that the electric fields are  
 5109 continuous. There are effectively three distinct regions in the open cavity corresponding  
 5110 to the central cavity volume, the inner coaxial volume, and the outer coaxial volume (see  
 5111 Figure 6.11).

5112 In Region I, the boundary conditions are those of a cylindrical waveguide, and it  
 5113 is required that  $E_\phi$  for the TE<sub>0m</sub> modes go to zero at the cavity wall ( $r = b$ ). This  
 5114 necessitates  $J'_{0m}(k_{c0m}b) = 0$ . A solution for the radius  $a$  is desired such that the TE<sub>01</sub>  
 5115 mode propagates, but other TE<sub>0m</sub> modes are below the cutoff frequency for the circular  
 5116 waveguide. This is equivalent to requiring

$$3.832 < k_{c0m}b < 7.016, \quad (6.41)$$

5117 where the numbers 3.832 and 7.016 correspond to the first and second zeros of the Bessel  
 5118 function (see Table 6.1).

5119 In Region II the boundary conditions are those of a cylindrical waveguide, but with  
 5120 a smaller radius. The condition that  $E_\phi = 0$  at the cylindrical partition radius is that  
 5121  $J'_{0m}(k_{c0m}a) = 0$ . To ensure perfect reflection, all modes in Region 1 of the cavity must be  
 5122 below the cutoff frequency of the circular waveguide formed by the inner volume of the  
 5123 coaxial terminator. Therefore, solutions where the condition

$$k_{c0m}a < 3.832, \quad (6.42)$$

5124 is true are required.

5125 Finally, in Region III the boundary condition are those of a coaxial waveguide. One  
 5126 needs to guarantee that  $E_\phi = 0$  at both  $r = b$  and  $r = a$ , which involves finding the  
 5127 eigenvalues of the following equation

$$J'_0(k_{c0m}a)Y'_0(k_{c0m}b) - J'_0(k_{c0m}b)Y'_0(k_{c0m}a) = 0, \quad (6.43)$$

5128 where  $Y'_0$  the zeroth-order derivatives of the Bessel function of the second kind. The  
 5129 solutions to this equation depend on the value of the ratio  $b/a$ . The approximate solution  
 5130 is given by

$$\delta_n a \simeq \frac{n\pi}{b/a - 1}, \quad (6.44)$$

5131 where  $\delta_n$  are eigenvalues of Equation 6.43. Similar to Region II, solutions for which  
 5132 the TE<sub>01</sub> modes of Region I are below the cutoff frequency of Region III are needed.  
 5133 Therefore, it is required that

$$k_{c0m} < \delta_1. \quad (6.45)$$

5134 In general, one has some freedom in specifying the value of  $b/a$ . A value typically used  
 5135 in practice is  $b/a = 2.082$ , which corresponds to positioning the radius of the cylindrical  
 5136 partition at the maxima of the TE<sub>01</sub> electrical fields.

5137 Using the constraints from the three field regions one can develop a coaxial terminator  
 5138 that acts as a virtual perfectly conducting surface for the TE<sub>01</sub> modes. The only required  
 5139 inputs are the desired frequency of the TE<sub>011</sub> mode and a choice for the value of  $b/a$ .

## 5140 6.4.2 Mode Filtering

5141 The general case of an electron coupling to a resonant cavity is complicated. This is  
5142 because cavities contain an infinite number of resonant modes, which for higher order  
5143 modes, have couplings to the electron with a complex spatial dependence. The danger is  
5144 that improper modeling of the electron's coupling to the cavity can lead to systematic  
5145 errors in the CRES measurements that prevent a high-resolution measurement of the  
5146 electron's kinetic energy. This in part drives the preference for a single-mode cavity  
5147 experiment that uses only the electron's coupling to the TE<sub>011</sub> mode to perform CRES,  
5148 assuming that sufficient information on the electron's position can be obtained with a  
5149 single mode.

5150 The TE<sub>011</sub> mode is in a region where there are relatively few other modes to which  
5151 the electron could couple(see Figure 6.8). However, one can see that the frequency of  
5152 the TE<sub>011</sub> is perfectly degenerate with the TM<sub>111</sub> mode, which means that electrons will  
5153 inevitably couple to both modes if they have the correct cyclotron frequency.

5154 The magnitude of the impact of the electron coupling to both TE<sub>011</sub> and TM<sub>111</sub> is  
5155 currently unknown. To first order an electron coupling to both modes will lose more  
5156 energy over time, which can be measured by observing the frequency chirp rate of the  
5157 signal. This effect may be small enough to be negligible or simple enough to model, so  
5158 that the cavity can be treated as an effective single-mode cavity. Alternatively, one could  
5159 consider devising a coupling scheme that is sensitive to both the TE<sub>011</sub> and the TM<sub>111</sub>  
5160 modes. By measuring the coupling of the electron to both modes more information on  
5161 the position of the electron could be obtained, which could improve the position and  
5162 energy resolution of the CRES measurements.

5163 A different approach is the mode filtering approach, which seeks to obtain a single  
5164 TE<sub>011</sub> mode cavity using perturbations to the cavity walls that selectively suppress the  
5165 TM modes, while leaving the TE modes mostly unperturbed. The type of perturbations  
5166 required can be determined by visualizing the surface currents induced in the cavity  
5167 walls by each type of mode (see Figure 6.12). By definition, all TM have electric fields  
5168 directed along the vertical axis of the cylindrical cavity, which means that perturbations  
5169 that impede currents in this direction will modify TM resonances. On the other hand,  
5170 the TE<sub>01</sub> modes induce azimuthal currents in the cavity walls; therefore, it is possible  
5171 to break the degeneracy between TE<sub>01</sub> and TM<sub>11</sub> by using a cavity perturbation that  
5172 suppresses axial currents, but does not affect the flow of azimuthal currents.

5173 Figure 6.12 shows two cavity design concepts that achieve this selective current  
5174 perturbation. The resistive approach inserts a series of thin dielectric rings into the walls

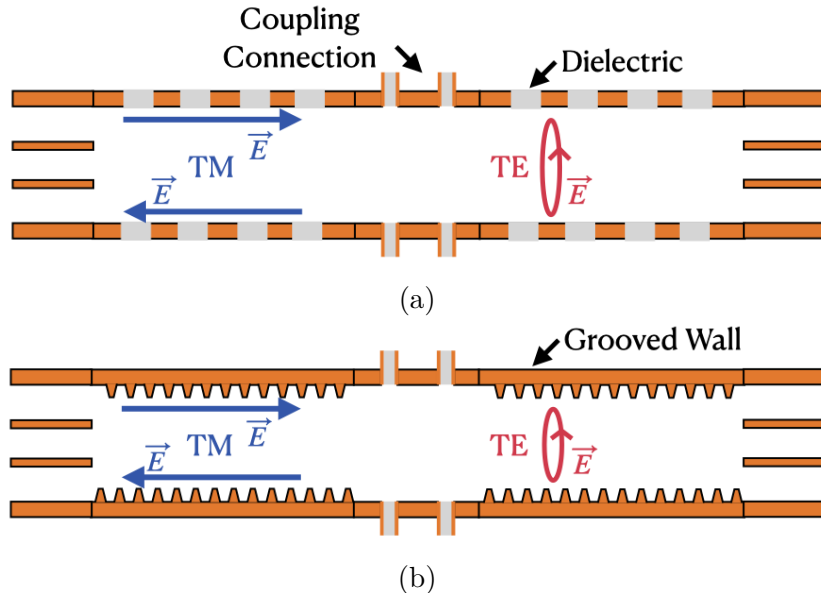


**Figure 6.12.** Two mode filtering concepts to break the degeneracy of  $TE_{01}$  and  $TM_{11}$  modes. The resistive approach uses dielectric materials to impede currents that travel vertically along the cavity while leaving azimuthal currents unperturbed. An alternative approach is to impede the currents using grooves cut into the cavity wall, which achieve the same effect with an inductive impedance.

of the cavity that introduces a resistive and capacitive impedance to the longitudinal currents, while leaving azimuthal current paths intact. Cavities of this type with high  $TE_{01}$  Q's have also been constructed by tightly wrapping a thin, dielectric coated wire around a mold to form the cavity wall. An alternative method is to introduce an inductive impedance by cutting grooves or a thread pattern on the inside wall of the cavity. For reasons of manufacturability and compatibility with tritium the grooved cavity approach is the preferred method for mode-filtered cavity construction by Project 8.

#### 6.4.3 Simulations of Open, Mode-filtered Cavities

A candidate design for a single  $TE_{011}$  mode CRES experiment is a cavity that utilizes the coaxial terminations combined with a mode-filtering wall. The first step towards validating that a cavity that combines these two design features will operate as expected is a thorough simulation effort for which finite element method (FEM) simulation software is invaluable. The primary tool for electromagnetic FEM calculations inside Project 8 is Ansys HFSS, which has a robust and well-established eigenmode solver that can identify the resonant frequencies and associated Q-factors for given structure.

Four variations of a cavity design with a  $\sim 1$  GHz  $TE_{011}$  resonance were implemented

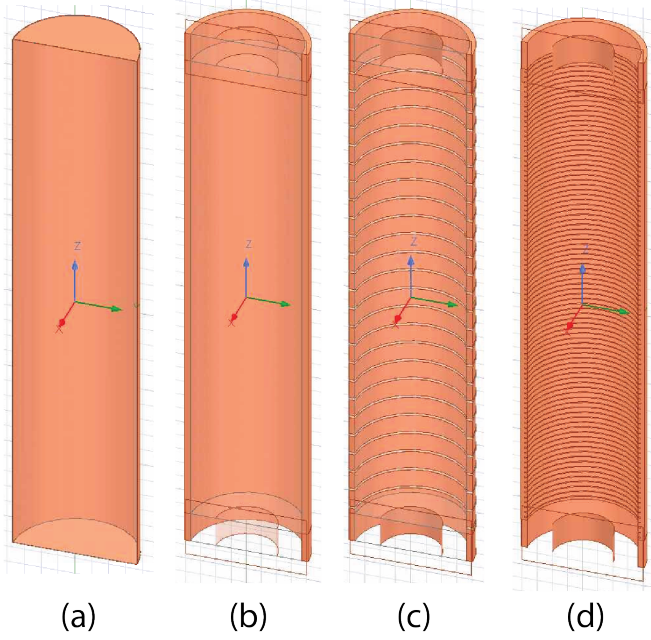


**Figure 6.13.** Four cavity design variations. (a) is a standard sealed cylindrical cavity, (b) is an open cavity with smooth walls, (c) is an open cavity with walls made of alternating conductor and dielectric, and (d) is an open cavity with grooved walls. The main cavity and coaxial terminator parameter are identical for all four cavities.

in HFSS (see Figure 6.13). The four designs include a standard cylindrical cavity, an open cavity with smooth walls, an open cavity with walls made of alternating conductor and dielectric, and an open cavity with grooved walls. The relevant design parameters are summarized in Table 6.3. All cavities were simulated using copper walls and filled with a vacuum dielectric. The identities of the resonant modes found by HFSS were validated by visual inspection of the electric and magnetic field patterns and by comparison to analytical calculations of the mode frequencies.

**Table 6.3.** A table of cavity design parameters used for HFSS simulations.

Name	Qty.	Unit	Description
$D_{\text{cav}}$	326.4	mm	Cavity diameter
$L_{\text{cav}}$	1668.0	mm	Cavity length
$D_{\text{term}}$	200.2	mm	Inner diameter of coaxial terminator
$L_{\text{term}}$	100.0	mm	Terminator length
$l_{\text{die}}$	8.3	mm	Dielectric spacer thickness
$\Delta l_{\text{die}}$	66.7	mm	Distance between dielectric spacers
$l_{\text{groove}}$	3.0	mm	Groove height
$d_{\text{groove}}$	9.0	mm	Groove depth
$\Delta l_{\text{groove}}$	18.3	mm	Distance between grooves

5198 The results of the HFSS simulations validate our predictions of the resonant behavior  
of an open, mode-filtered cavity developed in the preceding sections (see Figure 6.14) One

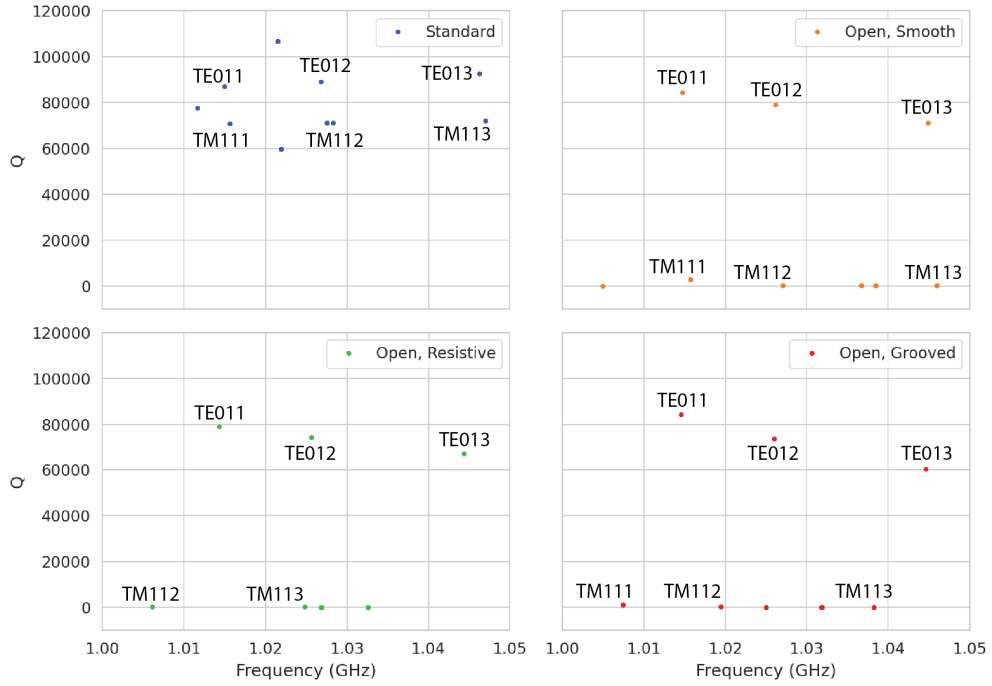


**Figure 6.14.** The frequencies and Q-factors of the resonant modes identified by HFSS for the cavity variations shown in Figure 6.13. The fully-sealed cavity with smooth walls has several high-Q modes near the  $TE_{011}$  resonance. Introducing the open-termination preserves the Q-factors of the  $TE_{01\ell}$  modes and suppresses the Q-factors of the modes whose boundary conditions do not match the cylindrical partition. Both the resistive and grooved wall perturbations shift the resonant frequencies of the TM modes away from the  $TE_{011}$  mode. By properly tuning the geometry of the grooves or the resistive spacers several MHz of frequency separation can be achieved.

5199  
5200 can see that for a standard cavity the  $TE_{01}$  and the  $TM_{11}$  are degenerate in frequency  
5201 with relatively high Q-factors. The open-ended cavity preserves the high Q-factors of  
5202 the  $TE_{01}$  modes, while the other modes, since their boundary conditions do not match  
5203 the coaxial geometry, have their Q-factors suppressed. One can see that the effect of  
5204 the resistive and inductive mode-filtering schemes is to effectively shift the resonant  
5205 frequencies of the  $TM_{11}$  modes below those of the associated  $TE_{01}$  modes, which breaks  
5206 the degeneracy. Optimization of the dielectric spacer or groove parameters can ensure  
5207 that the  $TE_{011}$  mode is isolated from other modes by  $O(10)$  MHz, which provides sufficient  
5208 bandwidth for a measurement of the tritium spectrum endpoint.

5209 Further optimization of the cavity design requires a more detailed cavity simulation  
5210 that includes the cavity coupling mechanism as well as other geometry modifications

5211 required for integration into the magnetic and tritium gas subsystems. Perhaps more  
5212 important is the development of the capability to simulate the interaction of electrons  
5213 with the cavity so that simulated CRES signals can be generated using cavities designed  
5214 for CRES measurements. Simulated CRES signals can then be used to estimate the  
5215 neutrino mass sensitivity of the experiment, which allows for the optimization of the cavity  
5216 design towards the configuration that provides the best measurement of the neutrino  
5217 mass.

## 5218 **6.5 Single-mode Resonant Cavity Measurements**

5219 Measurement test stands play an important role in the research and development process  
5220 that cannot be replaced by simulations. For example, constructing a prototype CRES  
5221 cavity forces one to consider important practical issues such as manufacturability and  
5222 machine tolerances that may require modifications to the design. Furthermore, by  
5223 comparing laboratory measurements of a real cavity to simulations, one can quantify  
5224 the impact of imperfections and real-life measurement systematics, which allows for  
5225 more accurate sensitivity estimates of the experiment. Lastly, the development of these  
5226 prototypes helps to build the necessary experience and expertise within the collaboration  
5227 required for more complicated experiments to succeed.

5228 With these objectives in mind a prototype cavity was constructed to demonstrate the  
5229 open, mode-filtered cavity concept explored in the previous sections. The primary goal  
5230 of the measurements was to validate that an open, mode-filtered cavity suppressed the  
5231 TM<sub>11</sub> modes as predicted by HFSS simulations.

### 5232 **6.5.1 Cavities and Setup**

5233 Two rudimentary cavities were constructed using segments of copper pipe available from  
5234 McMaster-Carr (see Figure 6.15). The design consists of copper pipes of two diameters.  
5235 The larger diameter pipe forms the main cavity wall and the smaller diameter pipe is  
5236 used to create a coaxial termination. The diameter of the outer pipe was chosen to  
5237 produce a TE<sub>011</sub> resonance of approximately 6 GHz, while the diameter of the smaller  
5238 pipe was selected based on the open termination criteria introduced in Section 6.4.1. The  
5239 approximate diameters and lengths of the copper pipe are summarized in Table 6.4.

5240 Coupling to the cavity was achieved using a hand-formable segment of coaxial cable  
5241 stripped at one end to form a loop antenna. This was inserted into a small hole located

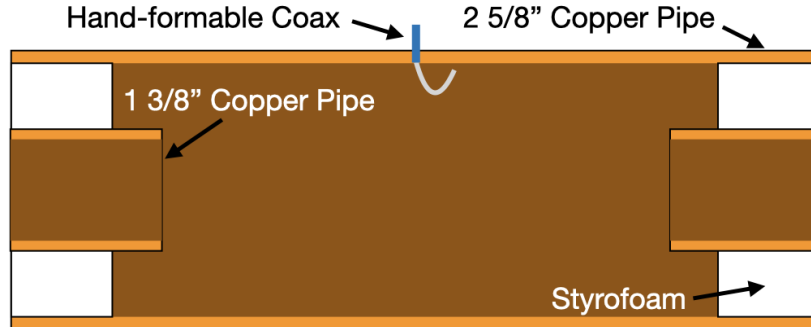


**Figure 6.15.** A cartoon depicting the design of the open-ended cavity prototype designed to operate at approximately 6 GHz. The main cavity wall was composed of a single copper pipe. A mode-filtered version of this cavity was constructed by

5242 at the center of the main cavity wall. The coaxial terminators were supported inside the  
 5243 main cavity by carving a spacer from polystyrene foam (styrofoam) so that they could  
 5244 be easily inserted into the cavity and repositioned. The dielectric constant of styrofoam  
 5245 is quite close to air at microwave frequencies so this is expected to have minimal impact  
 5246 on the resonant properties of the cavity.

**Table 6.4.** A table of parameters describing the cavity prototypes. Certain values such as the cavity length and the distance between dielectric spacers are approximate due to variation in the machining of the copper. In particular, the filtered cavity was constructed from conducting copper segments that varied in size from 1.50" to 1.85".

Name	Qty.	Unit	Description
$D_{\text{cav}}$	2.625	in	Cavity diameter
$L_{\text{cav}}$	$\approx 13$	in	Cavity length
$D_{\text{term}}$	1.375	in	Inner diameter of coaxial terminator
$L_{\text{term}}$	1.575	in	Terminator length
$l_{\text{die}}$	0.75	in	Dielectric spacer thickness
$\Delta l_{\text{die}}$	$\approx 1.50$ to $1.85$	in	Distance between dielectric spacers

5247 The effective length of the cavity is given by the distance between the inner edges of  
 5248 the coaxial terminations. The length of the outer section of pipe that forms the main wall  
 5249 of the cavity is approximately 16" in length which leads to a cavity length of  $\approx 13"$  when  
 5250 both terminators are inserted in the cavity. Because the terminators were not rigidly  
 5251 mounted this distance is only approximate, but the uncertain length of the cavity will  
 5252 not prevent us from validating the open cavity design.

5253 Along with the smooth-walled open cavity, a resistively mode-filtered cavity was  
 5254 constructed by creating dielectric spacers out of segments of clear PVC pipe (see Figure  
 5255 6.16). The spacers were machined such that the conductive segments of the cavity would

5256 be separated by 0.75" when the cavity was fully assembled. Due to variations in the  
 5257 lengths of the copper segments that make up the cavity wall the distance between spacers  
 5258 has significant variation with average value of about 1.7". Eight total spacers were used  
 5259 to build the cavity, which when assembled was approximately 16" in total length similar  
 to the non-filtered cavity.

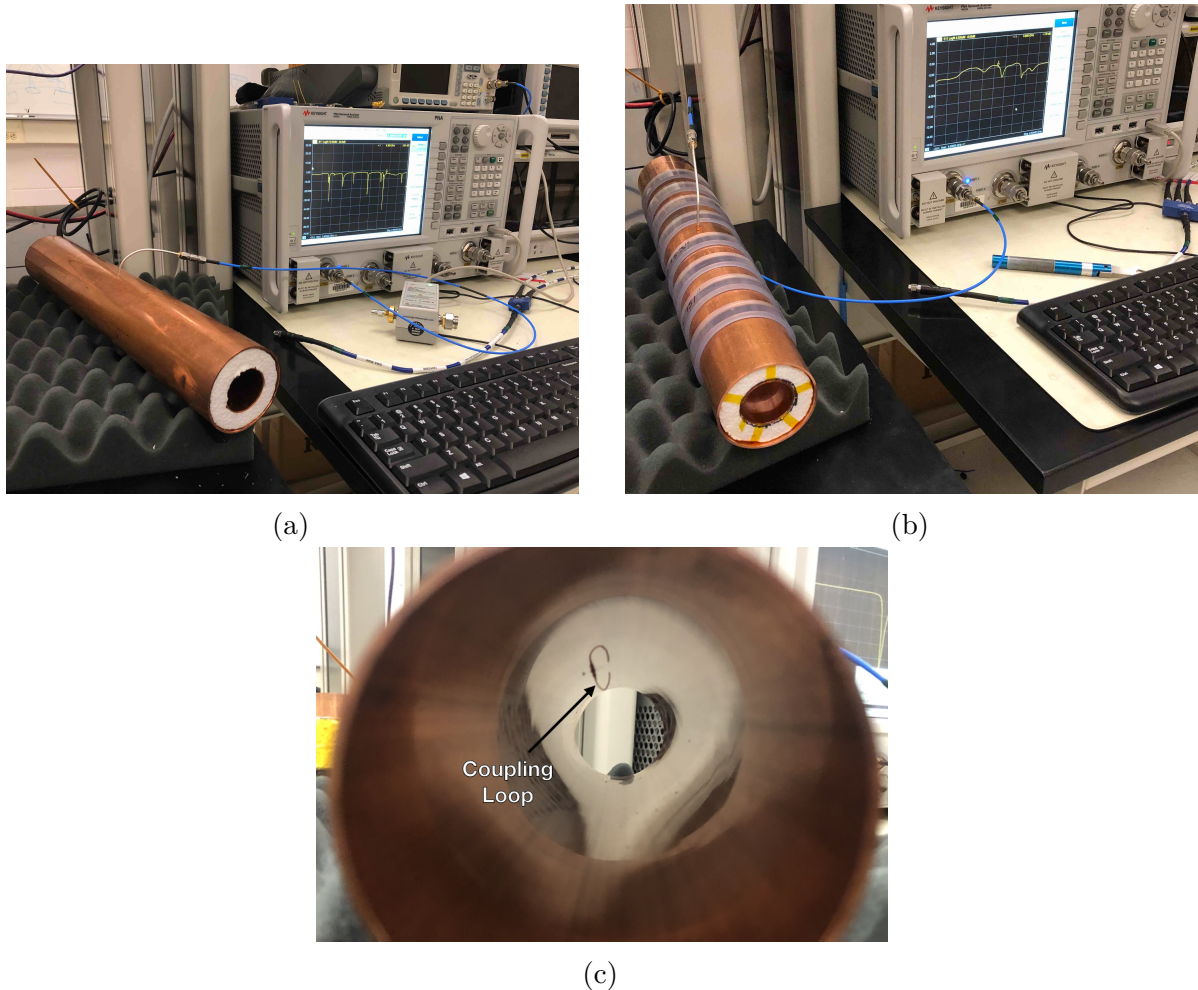


**Figure 6.16.** Images depicting the measurement of the filtered and non-filtered open cavities using the VNA. The coupling loop in the figure is shown in the TE orientation.

5260 Measurements of both cavities were performed using a VNA connected to the cavity  
 5261 coupling probe (see Figure 6.16). By measuring the return loss over a range of frequencies  
 5262 one can measure the frequencies and relative Q-factors of the resonant modes in the  
 5263 cavity. Due to the opposite polarity of the electric fields for the TE and TM modes,  
 5264 the loop coupling probe must be rotated 90° to change the polarity of the loop antenna.  
 5265 When the antenna is oriented such that the loop opening faces the ends of the cavity, it

5267 couples primarily to the TE modes which have magnetic fields directed along the long  
 5268 axis of the cavity (see Figure 6.16). If the coupling loop is turned by  $90^\circ$  from where  
 5269 it is shown in the image then it will couple to the TM modes which have azimuthally  
 5270 directed magnetic fields. In this way both the TE and TM resonances can be measured  
 5271 independently.

## 5272 **6.5.2 Results and Discussion**

5273 The primary analysis for the prototype cavities involved a simple visualization of the return loss as measured by the VNA and a comparison between the filtered and non-  
 5274 filtered variations. Since the resonances measured by the VNA are not labeled, there is an uncertainty about the true identities of the modes measured by the VNA. To resolve  
 5275 this I performed a simulation of the simplest possible cavity that could be created from the prototype components, which is a fully open cavity created by removing the coaxial  
 5276 inserts. The fully-open cavity with the as-built dimensions was simulated in HFSS to get  
 5277 estimates on the positions of the  $\text{TE}_{011}$  and  $\text{TM}_{111}$  modes (see Figure 6.17).

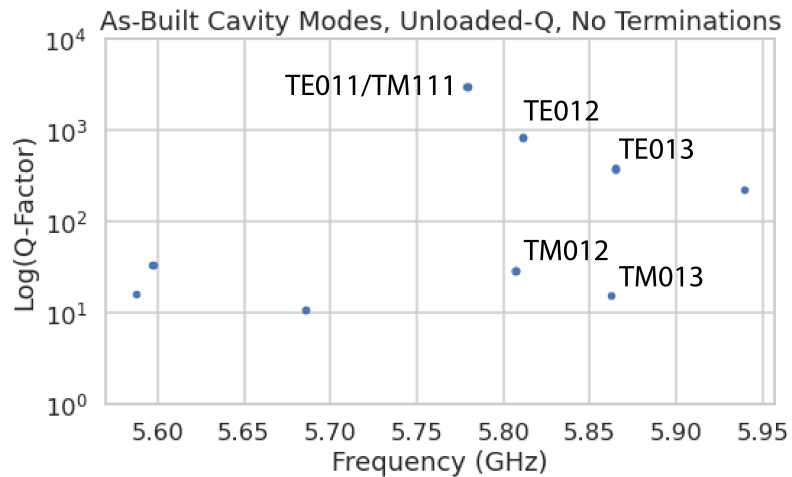


**Figure 6.17.** HFSS simulation results for a the as-built cavity with the coaxial terminators removed. The  $\text{TE}_{011}/\text{TM}_{111}$  frequency is approximately 5.78 GHz.

5281 Simulation of the fully open cavity shows that the  $\text{TE}_{011}/\text{TM}_{111}$  modes have a  
 5282 frequency of approximately 5.78 GHz in the fully open cavity. If the frequency of this  
 5283 mode is compared to the measurements of the filtered and non-filtered cavities with the  
 5284 terminators removed one can easily identify the  $\text{TE}_{011}$  mode at approximately 5.75 GHz  
 5285 (see Figure 6.18).

5286 In both variations of the non-filtered cavities one sees that the  $\text{TE}_{011}$  mode is degen-  
 5287 erate with what appears to be a doublet of TM modes located at the  $\text{TM}_{111}$  frequency  
 5288 position. This doublet is actually the  $\text{TM}_{111}$  mode, which has two polarizations with  
 5289 opposite polarizations. Because any real pipe used to construct a cavity will not be  
 5290 perfectly round due to manufacturing tolerances, it is likely that the frequency degeneracy  
 between the two polarizations is broken, which results in the doublet peaks.

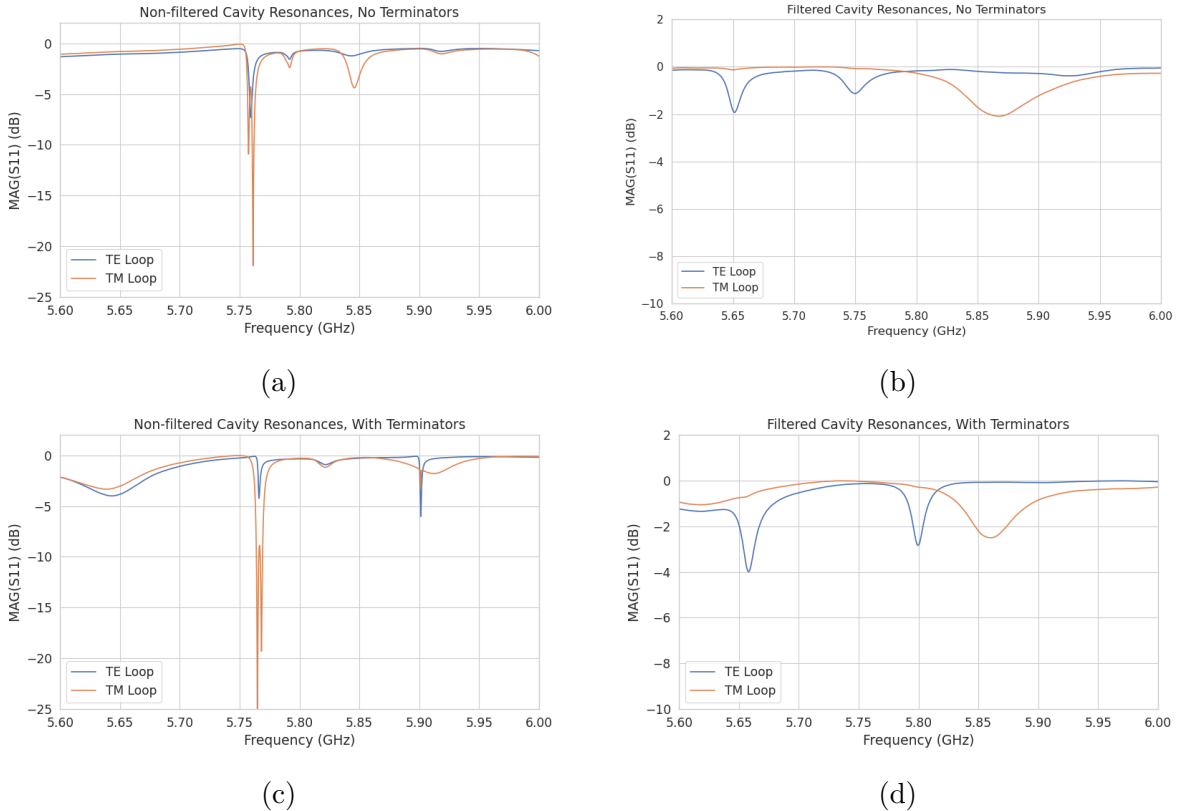


**Figure 6.18.** Measurements of the filtered and non-filtered prototype cavities acquired with the VNA.

5291  
 5292 The S-parameter plot for the filtered cavity without terminators has an isolated TE  
 5293 resonance at 5.65 GHz, associated with the  $\text{TE}_{011}$  mode. The frequency of this mode  
 5294 is lower than the non-filtered cavity due to a difference in the overall lengths of the  
 5295 cavities. An obvious difference between the filtered and non-filtered cavities is that  
 5296 there is no  $\text{TM}_{111}$  doublet at the  $\text{TE}_{011}$  frequency. This is what one would expect if  
 5297 the mode-filtering was suppressing the TM modes. There appears to be a noticeable  
 5298 difference in the Q of the  $\text{TE}_{011}$  resonance between non-filtered and filtered variations as  
 5299 indicated by the increased resonance depth for the filtered cavity. Overall, the Q-factors  
 5300 of the filtered cavity appear significantly smaller than the non-filtered cavity due to the

5301 increase in resonance width. This is likely caused by the relatively large widths of the  
5302 dielectric spacers, which are partially impeding the TE modes.

5303 One can see from these cavity measurements that, in principle, resistive mode-filtering  
5304 can be used to separate the  $TE_{011}$  resonance from the degenerate  $TM_{111}$  modes in  
5305 combination with the open cavity endcaps. This finding agrees with the expectations  
5306 from HFSS, which should provide confidence that the eigenmode solver is correctly  
5307 modeling the behavior of the cavity. Although I did not perform a similar study using  
5308 a cavity with grooved walls, it is expected that the resonant mode structure would be  
5309 similar to the cavity studied here.

5310 While this prototype cavity is a good first step, several deficiencies prevent this setup  
5311 from providing more than qualitative information to the design of cavities for CRES. This  
5312 includes the rudimentary approach to cavity coupling using a stripped coax antenna and  
5313 the inability to map the field density in the cavity volume. Improvements in these areas  
5314 are required so that measurements from a real cavity can provide useful information to  
5315 cavity CRES simulations that will ultimately inform neutrino mass sensitivity estimates.

5316 Future work with prototype cavities must include an improved cavity coupling scheme,  
5317 which is robust and compatible with atomic tritium. Since the cavity will ultimately  
5318 be filled with atomic tritium, a coupling antenna cannot be used due to the losses of  
5319 atomic tritium caused by recombination on the antenna surfaces. Possible non-invasive  
5320 coupling schemes include aperture coupling, where the cavity is coupled to an external  
5321 waveguide structure through an aperture, or a split-ring coupling approach, where the  
5322 center segment of the cylindrical cavity wall is replaced an isolated conductive ring with  
5323 a small vertical slit. The aperture coupling approach is a standard coupling scheme [92]  
5324 used in a wide range of applications, but at low frequencies the size of the external  
5325 waveguide conflicts with design of the atom trapping magnet and cryogenics system.  
5326 The split-ring approach could potentially be coupled to a small coaxial transmission line  
5327 which is more compatible with the rest of the experiment design. A challenge with this  
5328 coupling scheme is achieving a large enough coupling factor by correctly engineering  
5329 the geometry of the split-ring and the connection to the coax transmission line. The  
5330 design and optimization of this coupling scheme is an area of current research in the  
5331 collaboration.

5332 The robustness of the coupling mechanism is relevant due to the difficulty in modeling  
5333 its effect on the cavity modes. Small changes in geometry can have a large influence on  
5334 the coupling and hence the performance of the cavity, therefore, correctly modeling the  
5335 cavity coupling is critical for accurate CRES simulations. Coupling schemes that rely

5336 on connections to coaxial lines are potentially at a disadvantage in this regard due to  
5337 the affect of soldering imperfections or unintended bends in the coax on the coupling.  
5338 Future work will identify a coupling scheme for the cavity compatible with the neutrino  
5339 mass goals of Project 8.

5340 Imperfections in the geometry of a real cavity will necessarily distort the resonant  
5341 modes away from simulation predictions. This will change the coupling of an electron  
5342 to the cavity and thus change the expected signal structure. Ultimately, this effect will  
5343 limit the achievable energy resolution of the experiment unless the differences between  
5344 simulation and a real cavity can be sufficiently characterized and calibrated. One possible  
5345 approach to this is to utilize a "bead puller" system [106] to strategically perturb the  
5346 cavity by moving a conductive bead through the cavity volume. The small perturbation  
5347 caused by the bead affects the phase of the cavity resonances proportional to the total  
5348 magnitude of the electric field at that position, so by moving the bead through the  
5349 cavity volume the total electric field can be mapped and compared to simulation. This  
5350 information can provide bounds on the relative perturbations to the cavity mode structure  
5351 from real-life imperfections compared to the idealized cavity in HFSS.

5352    **Chapter 7 |**

5353    **Conclusion and Future Prospects**

5354    In this dissertation I have discussed research and development efforts towards the  
5355    development of a scalable CRES measurement technology that can be used to build a  
5356    CRES experiment at cubic-meter scales with sensitivity to neutrino masses of 40 meV.  
5357    The primary contributions of my dissertation are the development and analysis of signal  
5358    reconstruction algorithms for an antenna-based CRES experiment [62], which vital to  
5359    estimating the neutrino mass sensitivity of the experiment; the development of a synthetic  
5360    cyclotron radiation antenna (SYNCA) [78], which allowed for laboratory validation of  
5361    antenna array CRES simulation models [44]; and the development of an open-ended cavity  
5362    design compatible with atomic tritium for a cavity based CRES experiment. A measurable  
5363    impact of this work is the transition of the Project 8 collaboration's experimental plan  
5364    from an antenna array based approach to a cavity based approach, after my work played  
5365    a key role in demonstrating the significantly higher cost and complexity of the antenna  
5366    array experiment.

5367    The transition from antenna arrays to cavities requires a new set of demonstrator  
5368    experiments to make incremental progress towards a 40 meV measurement of the neutrino  
5369    mass. At the time of writing, the near-term plan of Project 8 is to design and construct a  
5370    small-scale cavity CRES experiment utilizing the 1 T magnet installed in the UW-Seattle.  
5371    This cavity is designed to have a TE011 resonance with a frequency of about 26 GHz with  
5372    a length-to-diameter ratio that mimics the larger cavities intended for the pilot-scale and  
5373    Phase IV experiments. The goal of this experiment is to demonstrate cavity CRES as  
5374    well as validate models of CRES systematics using electrons from  $^{83m}\text{Kr}$  and an electron  
5375    gun. Though the primary goal is demonstration, near-term physics measurements are  
5376    available in the form of high-resolution measurements of the  $^{83m}\text{Kr}$  conversion spectrum  
5377    of interest to the KATRIN collaboration.

5378    Furthermore, Project 8 is currently constructing a low-frequency CRES setup located  
5379    at Yale University to better understand the principles of cavity based CRES at lower

5380 magnetic fields. The Low, UHF Cavity Krypton Experiment at Yale (LUCKEY) is  
5381 a 1.5 GHz cavity CRES experiment the will use conversion electrons from  $^{83m}\text{Kr}$  to  
5382 perform CRES measurements at the lowest frequencies ever attempted with the technique.  
5383 LUCKEY will validate frequency scaling models developed by Project 8 and will pave  
5384 the way for the future Low-Frequency Apparatus (LFA), which will be a larger, 1 GHz  
5385 cavity CRES experiment that includes a molecular tritium source. The target for the  
5386 LFA is a measurement of the neutrino mass with a sensitivity of approximately 0.2 eV,  
5387 which will build towards the atomic pilot-scale CRES experiment.

5388 In parallel to the development of cavity CRES is the development of the atomic  
5389 tritium source. Recent demonstrations of the production of atomic hydrogen are excellent  
5390 steps towards the atomic tritium production needed for the pilot-scale experiment. One  
5391 area of future study includes the development of a more detailed understanding of the  
5392 efficiency of atomic hydrogen production. Near-term plans include the development  
5393 of a magnetic, evaporatively cooled beamline, as well as the prototyping of a Halbach  
5394 array atom trap. Nearly all the components of the atomic tritium system will require  
5395 demonstration before the complete system can be built. The long-term goal of the  
5396 atomic tritium work is to construct a full atomic tritium prototype that demonstrates  
5397 the production, cooling, trapping, and recycling of tritium at the rates needed for the  
5398 pilot-scale experiment.

5399 More broadly, the long-term goal of the Project 8 collaboration is to fully develop  
5400 both the atomic tritium and cavity CRES technologies so that both can be combined in  
5401 a pilot-scale CRES experiment. It is envisioned that this process will take approximately  
5402 10 years for both atomic tritium and cavity CRES. After these developments comes  
5403 the pilot-scale experiment which will be the first CRES experiment that simultaneously  
5404 demonstrates all the required technologies for Phase IV. Scaling to Phase IV with cavity  
5405 CRES will require the construction of multiple copies (approximately 10) of the pilot-scale  
5406 experiment to obtain sufficient statistics for 40 meV sensitivity.

5407 Development of the CRES experimental technique by Project 8 has led to new  
5408 experiments utilizing the CRES technique for basic physics research, such as the  $^6\text{He}$ -  
5409 CRES collaboration [107], and has also found applications as a new approach to x-ray  
5410 spectroscopy [108]. Recently, a new experimental effort called CRESDA has begun in  
5411 the UK to develop new quantum technologies applied to CRES measurements for the  
5412 neutrino mass [109]. This flourishing of new experimental efforts based on the CRES  
5413 technique is likely to continue as Project 8 continues to develop the technique towards  
5414 its neutrino mass measurement goal.

5415        The work described in this dissertation represents important R&D steps towards  
5416        a next-generation neutrino mass measurement with CRES. A direct neutrino mass  
5417        measurement, which sets both an upper and lower bound on the neutrino mass will  
5418        be important to several physics subfields. For example, fixing the neutrino mass scale  
5419        with an independent measurement will enable cosmological fits to use the neutrino mass  
5420        as a fixed parameter, which will allow current data to provide more information on  
5421        other parameters in cosmological models. Additionally, a precise measurement of the  
5422        neutrino mass scale will be important for constraining the energy-scales of possible new  
5423        physics responsible for the smallness of the neutrino mass relative to other standard  
5424        model particles.

# Bibliography

- [1] CAHN, R. N., D. A. DWYER, S. J. FREEDMAN, W. C. HAXTON, R. W. KADEL, Y. G. KOLOMENSKY, K. B. LUK, P. McDONALD, G. D. OREBI GANN, and A. W. P. POON (2013) “White Paper: Measuring the Neutrino Mass Hierarchy,” in *Snowmass 2013: Snowmass on the Mississippi*, 1307.5487.
- [2] AGOSTINI, M., G. BENATO, and J. DETWILER (2017) “Discovery probability of next-generation neutrinoless double-  $\beta$  decay experiments,” *Phys. Rev. D*, **96**(5), p. 053001, 1705.02996.
- [3] WENGER, N. C. and J. SMETANA (1972) “Hydrogen Density Measurements Using an Open-Ended Microwave Cavity,” *IEEE Transactions on Instrumentation and Measurement*, **21**(2), pp. 105–114.
- [4] WENGER, N. (1967) “Resonant Frequency of Open-Ended Cylindrical Cavity,” *IEEE Transactions on Microwave Theory and Techniques*, **15**(6), pp. 334–340.
- [5] DAS, A. and T. FERBEL (2003) *Introduction to Nuclear and Particle Physics*, World Scientific.
- [6] CURIE, P. (1898) “Sur une nouvelle substance fortement radioactive, contenue dans la pechblende,” *Comptes rendus de l’Academie des Sciences, Paris*, **127**, pp. 1215–1217.
- [7] RUTHERFORD, E. (1899) “Uranium radiation and the electrical conduction produced by it,” *Philos. Mag.*, **47**, p. 109.  
URL <https://cds.cern.ch/record/261896>
- [8] GERWARD, L. (1999) “Paul Villard and his Discovery of Gamma Rays,” *Physics in Perspective*, **1**, pp. 367–383.
- [9] BECQUEREL, H. (1900) “Deviation du rayonnement du radium dans un champ électrique,” *C.R.*, **130**, pp. 809–815.
- [10] D.Sc., E. R. M. and F. S. B.A. (1902) “XLI. The cause and nature of radioactivity.—Part I,” *The London, Edinburgh, and Dublin Philosophical Magazine and Journal of Science*, **4**(21), pp. 370–396, <https://doi.org/10.1080/14786440209462856>.  
URL <https://doi.org/10.1080/14786440209462856>

- 5455 [11] CHADWICK, J. (1914) *Intensitätsverteilung im magnetischen Spektrum der  $\beta$ -*  
5456 *Strahlen von Radium B+C*, Druck von Friedr. Vieweg und Sohn.  
5457 URL <https://books.google.com/books?id=8s8UmQEACAAJ>
- 5458 [12] BROWN, L. M. (1978) “The idea of the neutrino,” *Physics Today*, **31**(9).
- 5459 [13] PAULI, W. (1978) “Dear radioactive ladies and gentlemen,” *Phys. Today*, **31N9**,  
5460 p. 27.
- 5461 [14] AMALDI, E. (1984) “From the discovery of the neutron to the discovery of nuclear  
5462 fission,” *Physics Reports*, **111**(1), pp. 1–331.  
5463 URL <https://www.sciencedirect.com/science/article/pii/037015738490214X>
- 5465 [15] CHADWICK, J. (1932) “The existence of a neutron,” *Proceedings of the Royal  
5466 Society of London. Series A, Containing Papers of a Mathematical and Physical  
5467 Character*, **136**(830), pp. 692–708, <https://royalsocietypublishing.org/doi/pdf/10.1098/rspa.1932.0112>.  
5468 URL <https://royalsocietypublishing.org/doi/abs/10.1098/rspa.1932.0112>.
- 5469 [16] WILSON, F. L. (1968) “Fermi’s Theory of Beta Decay,” *American Journal of  
5470 Physics*, **36**(12), pp. 1150–1160, [https://pubs.aip.org/aapt/ajp/article-pdf/36/12/1150/11891052/1150\\_1\\_online.pdf](https://pubs.aip.org/aapt/ajp/article-pdf/36/12/1150/11891052/1150_1_online.pdf).  
5471 URL <https://doi.org/10.1119/1.1974382>
- 5475 [17] CRANE, H. R. and J. HALPERN (1938) “New Experimental Evidence for the  
5476 Existence of a Neutrino,” *Phys. Rev.*, **53**, pp. 789–794.  
5477 URL <https://link.aps.org/doi/10.1103/PhysRev.53.789>
- 5478 [18] COWAN, C. L., F. REINES, F. B. HARRISON, H. W. KRUSE, and A. D.  
5479 MC GUIRE (1956) “Detection of the Free Neutrino: a Confirmation,” *Science*,  
5480 **124**(3212), pp. 103–104, <https://www.science.org/doi/pdf/10.1126/science.124.3212.103>.  
5481 URL <https://www.science.org/doi/abs/10.1126/science.124.3212.103>
- 5483 [19] ANICIN, I. V. (2005) “The Neutrino - Its Past, Present and Future,” *arXiv e-prints*,  
5484 physics/0503172, physics/0503172.
- 5485 [20] DAVIS, R. (2003) “Nobel Lecture: A half-century with solar neutrinos,” *Rev. Mod.  
5486 Phys.*, **75**, pp. 985–994.
- 5487 [21] McDONALD, A. B. ET AL. (2002) “Direct evidence for neutrino flavor transfor-  
5488 mation from neutral-current interactions in SNO,” *AIP Conf. Proc.*, **646**(1), pp.  
5489 43–58.
- 5490 [22] FUKUDA, Y. ET AL. (1998) “Evidence for oscillation of atmospheric neutrinos,”  
5491 *Phys. Rev. Lett.*, **81**, pp. 1562–1567, hep-ex/9807003.

- 5492 [23] GIGANTI, C., S. LAVIGNAC, and M. ZITO (2018) “Neutrino oscillations: The rise  
 5493 of the PMNS paradigm,” *Prog. Part. Nucl. Phys.*, **98**, pp. 1–54, 1710.00715.
- 5494 [24] WORKMAN, R. L. and OTHERS (2022) “Review of Particle Physics,” *PTEP*, **2022**,  
 5495 p. 083C01.
- 5496 [25] AN, F. ET AL. (2016) “Neutrino Physics with JUNO,” *J. Phys. G*, **43**(3), p. 030401,  
 5497 1507.05613.
- 5498 [26] BIAN, J. ET AL. (2022) “Hyper-Kamiokande Experiment: A Snowmass White  
 5499 Paper,” in *Snowmass 2021*, 2203.02029.
- 5500 [27] ABI, B. ET AL. (2020) “Long-baseline neutrino oscillation physics potential of the  
 5501 DUNE experiment,” *Eur. Phys. J. C*, **80**(10), p. 978, 2006.16043.
- 5502 [28] ZUBER, K. (2020) *Neutrino Physics*, CRC Press.
- 5503 [29] XING, Z. Z. and S. ZHOU (2011) *Neutrinos in Particle Physics, Astronomy and*  
 5504 *Cosmology*, Springer.
- 5505 [30] MOHAPATRA, R. N. ET AL. (2007) “Theory of neutrinos: A White paper,” *Rept.  
 5506 Prog. Phys.*, **70**, pp. 1757–1867, hep-ph/0510213.
- 5507 [31] DE GOUVÉA, A. (2016) “Neutrino Mass Models,” *Ann. Rev. Nucl. Part. Sci.*, **66**,  
 5508 pp. 197–217.
- 5509 [32] WONG, Y. Y. Y. (2011) “Neutrino mass in cosmology: status and prospects,”  
 5510 *Ann. Rev. Nucl. Part. Sci.*, **61**, pp. 69–98, 1111.1436.
- 5511 [33] ADE, P. A. R. ET AL. (2016) “Planck 2015 results. XIII. Cosmological parameters,”  
 5512 *Astron. Astrophys.*, **594**, p. A13, 1502.01589.
- 5513 [34] CARLSTROM, J. ET AL. (2019) “CMB-S4,” in *Bulletin of the American Astronomical Society*, vol. 51, p. 209, 1908.01062.
- 5515 [35] ELLIOTT, S. R. and P. VOGEL (2002) “Double beta decay,” *Ann. Rev. Nucl. Part.  
 5516 Sci.*, **52**, pp. 115–151, hep-ph/0202264.
- 5517 [36] DOLINSKI, M. J., A. W. P. POON, and W. RODEJOHANN (2019) “Neutrinoless  
 5518 Double-Beta Decay: Status and Prospects,” *Ann. Rev. Nucl. Part. Sci.*, **69**, pp.  
 5519 219–251, 1902.04097.
- 5520 [37] FORMAGGIO, J. A., A. L. C. DE GOUVÉA, and R. G. H. ROBERTSON (2021)  
 5521 “Direct measurements of neutrino mass,” *Physics Reports*, **914**, pp. 1–54, direct  
 5522 measurements of neutrino mass.  
 5523 URL [https://www.sciencedirect.com/science/article/pii/  
 5524 S0370157321000636](https://www.sciencedirect.com/science/article/pii/S0370157321000636)

- 5525 [38] AKER, M. ET AL. (2022) “New Constraint on the Local Relic Neutrino Background  
5526 Overdensity with the First KATRIN Data Runs,” *Phys. Rev. Lett.*, **129**(1), p.  
5527 011806, 2202.04587.
- 5528 [39] FORMAGGIO, J. A., A. L. C. DE GOUVÊA, and R. G. H. ROBERTSON (2021)  
5529 “Direct Measurements of Neutrino Mass,” *Phys. Rept.*, **914**, pp. 1–54, 2102.00594.
- 5530 [40] MONREAL, B. and J. A. FORMAGGIO (2009) “Relativistic cyclotron radiation  
5531 detection of tritium decay electrons as a new technique for measuring the neutrino  
5532 mass,” *Phys. Rev. D*, **80**, p. 051301.  
5533 URL <https://link.aps.org/doi/10.1103/PhysRevD.80.051301>
- 5534 [41] ESFAHANI, A. A. ET AL. (2022) “The Project 8 Neutrino Mass Experiment,”  
5535 2203.07349.
- 5536 [42] ——— (2023) “Cyclotron Radiation Emission Spectroscopy of Electrons from  
5537 Tritium Beta Decay and  $^{83m}\text{Kr}$  Internal Conversion,” 2303.12055.
- 5538 [43] ——— (2023) “Tritium Beta Spectrum and Neutrino Mass Limit from Cyclotron  
5539 Radiation Emission Spectroscopy,” 2212.05048.
- 5540 [44] “Antenna Arrays for Physics Measurements with Large-scale CRES Detectors,” *In  
5541 preparation*.
- 5542 [45] NICHOLSON, T. ET AL. (2015) “Systematic evaluation of an atomic clock at 2 x  
5543 10-18 total uncertainty,” *Nature Communications*, **6**(6896).
- 5544 [46] HÄNSCH, T. W. (2006) “Nobel Lecture: Passion for precision,” *Rev. Mod. Phys.*,  
5545 **78**, pp. 1297–1309.  
5546 URL <https://link.aps.org/doi/10.1103/RevModPhys.78.1297>
- 5547 [47] GABOR, D. (1946) “Theory of communication. Part 1: The analysis of information,”  
5548 *Journal of the Institution of Electrical Engineers-part III: radio and communication  
5549 engineering*, **93**(26), pp. 429–441.
- 5550 [48] ESFAHANI ASHTARI, A. ET AL. (2022) “Viterbi decoding of CRES signals in  
5551 Project 8,” *New J. Phys.*, **24**(5), p. 053013, 2112.05265.
- 5552 [49] JACKSON, J. D. (1999) *Classical electrodynamics*, 3rd ed., Wiley, New York, NY.  
5553 URL <http://cdsweb.cern.ch/record/490457>
- 5554 [50] F.R.S., J. L. D. (1897) “LXIII. On the theory of the magnetic influence on  
5555 spectra; and on the radiation from moving ions,” *The London, Edinburgh, and  
5556 Dublin Philosophical Magazine and Journal of Science*, **44**(271), pp. 503–512,  
5557 <https://doi.org/10.1080/14786449708621095>.  
5558 URL <https://doi.org/10.1080/14786449708621095>

- 5559 [51] ESFAHANI, A. A. ET AL. (2022) “The Project 8 Neutrino Mass Experiment,” in  
5560 *2022 Snowmass Summer Study*, 2203.07349.
- 5561 [52] KRAUS, C. ET AL. (2005) “Final results from phase II of the Mainz neutrino mass  
5562 search in tritium beta decay,” *Eur. Phys. J. C*, **40**, pp. 447–468, [hep-ex/0412056](#).
- 5563 [53] ASEEV, V. N. ET AL. (2011) “An upper limit on electron antineutrino mass from  
5564 Troitsk experiment,” *Phys. Rev. D*, **84**, p. 112003, [1108.5034](#).
- 5565 [54] SAENZ, A., S. JONSELL, and P. FROELICH (2000) “Improved Molecular Final-  
5566 State Distribution of HeT+ for the  $\beta$ -Decay Process of T2,” *Phys. Rev. Lett.*, **84**(2),  
5567 p. 242.
- 5568 [55] BODINE, L. I., D. S. PARNO, and R. G. H. ROBERTSON (2015) “Assessment  
5569 of molecular effects on neutrino mass measurements from tritium  $\beta$  decay,” *Phys.  
5570 Rev. C*, **91**(3), p. 035505, [1502.03497](#).
- 5571 [56] ASNER, D. M. ET AL. (2015) “Single electron detection and spectroscopy via  
5572 relativistic cyclotron radiation,” *Phys. Rev. Lett.*, **114**(16), p. 162501, [1408.5362](#).
- 5573 [57] VÉNOS, D., J. SENTKERESTIOVÁ, O. DRAGOUN, M. SLEZÁK, M. RYŠAVÝ, and  
5574 A. ŠPALEK (2018) “Properties of 83mKr conversion electrons and their use in the  
5575 KATRIN experiment,” *JINST*, **13**(02), p. T02012.
- 5576 [58] LAGENDIJK, A., I. F. SILVERA, and B. J. VERHAAR (1986) “Spin exchange and  
5577 dipolar relaxation rates in atomic hydrogen: Lifetimes in magnetic traps,” *Phys.  
5578 Rev. B*, **33**, pp. 626–628.  
5579 URL <https://link.aps.org/doi/10.1103/PhysRevB.33.626>
- 5580 [59] SILVERA, I. and J. WALRAVEN (1986) “Spin-polarized atomic hydrogen,” *Prog.  
5581 Low Temp. Phys.*, **X**, pp. 139–370.
- 5582 [60] PRITCHARD, D. E. (1983) “Cooling Neutral Atoms in a Magnetic Trap for Precision  
5583 Spectroscopy,” *Phys. Rev. Lett.*, **51**, pp. 1336–1339.  
5584 URL <https://link.aps.org/doi/10.1103/PhysRevLett.51.1336>
- 5585 [61] HALBACH, K. (1980) “Design of permanent multipole magnets with oriented rare  
5586 earth cobalt material,” *Nuclear Instruments and Methods*, **169**(1), pp. 1–10.  
5587 URL <https://www.sciencedirect.com/science/article/pii/0029554X80900944>
- 5588 [62] “Real-time Signal Detection for Cyclotron Radiation Emission Spectroscopy Mea-  
5589 surements using Antenna Arrays,” *In preparation*.
- 5590 [63] FURSE, D. ET AL. (2017) “Kassiopeia: a modern, extensible C++ particle tracking  
5591 package,” *New Journal of Physics*, **19**(5), p. 053012.  
5592 URL <https://doi.org/10.1088/1367-2630/aa6950>

- 5594 [64] ESFAHANI, A. A. ET AL. (2019) “Electron radiated power in cyclotron radiation  
5595 emission spectroscopy experiments,” *Phys. Rev. C*, **99**, p. 055501.  
5596 URL <https://link.aps.org/doi/10.1103/PhysRevC.99.055501>
- 5597 [65] ASHTARI ESFAHANI, A. ET AL. (2019) “Locust: C++ software for simulation of  
5598 RF detection,” *New J. Phys.*, **21**, p. 113051, 1907.11124.
- 5599 [66] WIECHERT, E. (1901) “Elektrodynamische Elementargesetze,” .  
5600 URL <https://doi.org/10.1002/andp.19013090403>
- 5601 [67] LIÉARD, A. (1898) “Champ électrique et Magnétique,” *Léclairage électrique*, **16**(27-  
5602 29).
- 5603 [68] BALANIS, C. (2015) *Antenna Theory: Analysis and Design*, Wiley.  
5604 URL <https://books.google.com/books?id=PTFcCwAAQBAJ>
- 5605 [69] <https://www.ansys.com/products/electronics/ansys-hfss>.
- 5606 [70] [https://en.wikipedia.org/wiki/Linear\\_time-invariant\\_system](https://en.wikipedia.org/wiki/Linear_time-invariant_system).
- 5607 [71] NYQUIST, H. (1928) “Certain Topics in Telegraph Transmission Theory,” *Transactions of the American Institute of Electrical Engineers*, **47**(2), pp. 617–644.
- 5609 [72] BRUN, R. and F. RADEMAKERS (1997) “ROOT: An object oriented data analysis  
5610 framework,” *Nucl. Instrum. Meth. A*, **389**, pp. 81–86.
- 5611 [73] ASHTARI ESFAHANI, A. ET AL. (2021) “Bayesian analysis of a future  $\beta$  decay  
5612 experiment’s sensitivity to neutrino mass scale and ordering,” *Phys. Rev. C*, **103**,  
5613 p. 065501.  
5614 URL <https://link.aps.org/doi/10.1103/PhysRevC.103.065501>
- 5615 [74] KAY, S. (1998) *Fundamentals of Statistical Signal Processing: Detection Theory*,  
5616 Volume II, Pearson.
- 5617 [75] NEYMAN, J. and E. PEARSON (1933) “On the problem of the the most efficient  
5618 tests of statistical hypotheses,” *Phil. Trans. R. Soc. Lond. A*, **231**.
- 5619 [76] STUMPF, M. (2018) *Electromagnetic Reciprocity in Antenna Theory*, Wiley.
- 5620 [77] BUZINSKY, N. (2021) *Statistical Signal Processing and Detector Optimization in*  
5621 *Project 8*, Ph.D. thesis, Massachusetts Institute of Technology.
- 5622 [78] ESFAHANI, A. A. ET AL. (2023) “SYNCA: A Synthetic Cyclotron Antenna for  
5623 the Project 8 Collaboration,” *Journal of Instrumentation*, **18**(01), p. P01034.  
5624 URL <https://dx.doi.org/10.1088/1748-0221/18/01/P01034>
- 5625 [79] BISHOP, C. (2016) *Pattern Recognition and Machine Learning*, Springer.

- 5626 [80] PLEHN, T., A. BUTTER, B. DILLON, and C. KRAUSE (2022) “Modern Machine  
 5627 Learning for LHC Physicists,” 2211.01421.
- 5628 [81] GEORGE, D. and E. A. HUERTA (2018) “Deep Learning for Real-time Gravitational  
 5629 Wave Detection and Parameter Estimation: Results with Advanced LIGO Data,”  
 5630 *Phys. Lett. B*, **778**, pp. 64–70, 1711.03121.
- 5631 [82] GABBARD, H., C. MESSENGER, I. S. HENG, F. TONOLINI, and R. MURRAY-  
 5632 SMITH (2022) “Bayesian parameter estimation using conditional variational au-  
 5633 toencoders for gravitational-wave astronomy,” *Nature Phys.*, **18**(1), pp. 112–117,  
 5634 1909.06296.
- 5635 [83] REIMANN, R. (2022) “Project 8: R&D for a next-generation neutrino mass experi-  
 5636 ment,” *PoS, PANIC2021*, p. 283.
- 5637 [84] ASHTARI ESFAHANI, A. ET AL. (2020) “Cyclotron radiation emission spectroscopy  
 5638 signal classification with machine learning in project 8,” *New J. Phys.*, **22**(3), p.  
 5639 033004, 1909.08115.
- 5640 [85] BALANIS, C. A. (2016) *Antenna Theory: Analysis and Design, 4th Edition*, Wiley.
- 5641 [86] STANKOVIĆ, L. and D. MANDIC (2023) “Convolutional Neural Networks Demys-  
 5642 tified: A Matched Filtering Perspective-Based Tutorial,” *IEEE Transactions on*  
 5643 *Systems, Man, and Cybernetics: Systems*, **53**(6), pp. 3614–3628.
- 5644 [87] <https://www.nvidia.com/en-us/data-center/v100/>.
- 5645 [88] <https://www.nvidia.com/en-us/data-center/h100/>.
- 5646 [89] HE, K., X. ZHANG, S. REN, and J. SUN (2016) “Deep Residual Learning for  
 5647 Image Recognition,” in *2016 IEEE Conference on Computer Vision and Pattern*  
 5648 *Recognition (CVPR)*, pp. 770–778.
- 5649 [90] SIMONYAN, K. and A. ZISSERMAN (2015) “Very Deep Convolutional Networks  
 5650 for Large-Scale Image Recognition,” in *3rd International Conference on Learning*  
 5651 *Representations, ICLR 2015, San Diego, CA, USA, May 7-9, 2015, Conference*  
 5652 *Track Proceedings* (Y. Bengio and Y. LeCun, eds.).  
 5653 URL <http://arxiv.org/abs/1409.1556>
- 5654 [91] FRIIS, H. (1946) “A Note on a Simple Transmission Formula,” *Proceedings of the*  
 5655 *IRE*, **34**(5), pp. 254–256.
- 5656 [92] POZAR, D. M. (2005) *Microwave engineering; 3rd ed.*, Wiley, Hoboken, NJ.  
 5657 URL <https://cds.cern.ch/record/882338>
- 5658 [93] AKER, M. ET AL. (2022) “Direct neutrino-mass measurement with sub-electronvolt  
 5659 sensitivity,” *Nature Physics*, **18**(2), pp. 160–166.  
 5660 URL <https://doi.org/10.1038/s41567-021-01463-1>

- 5661 [94] MONREAL, B. and J. A. FORMAGGIO (2009) “Relativistic Cyclotron Radiation  
 5662 Detection of Tritium Decay Electrons as a New Technique for Measuring the  
 5663 Neutrino Mass,” *Phys. Rev. D*, **80**, p. 051301, 0904.2860.
- 5664 [95] ASHTARI ESFAHANI, A. ET AL. (2017) “Determining the neutrino mass with  
 5665 cyclotron radiation emission spectroscopy—Project 8,” *J. Phys. G*, **44**(5), p. 054004,  
 5666 1703.02037.
- 5667 [96] ESFAHANI, A. A. ET AL. (2022) “The Project 8 Neutrino Mass Experiment,” in  
 5668 *2022 Snowmass Summer Study*, 2203.07349.
- 5669 [97] ASHTARI ESFAHANI, A. ET AL. (2019) “Locust: C++ software for simulation of  
 5670 RF detection,” *New Journal of Physics*, **21**(11), p. 113051.  
 5671 URL <https://doi.org/10.1088/1367-2630/ab550d>
- 5672 [98] FURSE, D. ET AL. (2017) “Kassiopeia: a modern, extensible C++ particle tracking  
 5673 package,” *New Journal of Physics*, **19**(5), p. 053012.  
 5674 URL <https://doi.org/10.1088/1367-2630/aa6950>
- 5675 [99] BALANIS, C. (2011) *Modern Antenna Handbook*, Wiley.  
 5676 URL <https://books.google.com/books?id=UYpV8L8GNCwC>
- 5677 [100] WIRTH, W. (2001) *Radar Techniques Using Array Antennas*, Institution of Engi-  
 5678 neering and Technology.  
 5679 URL <https://books.google.com/books?id=ALht42gkzLsC>
- 5680 [101] BROWN, L. S., G. GABRIELSE, K. HELMERSON, and J. TAN (1985) “Cyclotron  
 5681 motion in a microwave cavity: Lifetime and frequency shifts,” *Phys. Rev. A*, **32**,  
 5682 pp. 3204–3218.  
 5683 URL <https://link.aps.org/doi/10.1103/PhysRevA.32.3204>
- 5684 [102] HANNEKE, D., S. FOGWELL HOOGERHEIDE, and G. GABRIELSE (2011) “Cavity  
 5685 control of a single-electron quantum cyclotron: Measuring the electron magnetic  
 5686 moment,” *Phys. Rev. A*, **83**, p. 052122.  
 5687 URL <https://link.aps.org/doi/10.1103/PhysRevA.83.052122>
- 5688 [103] HANNEKE, D. A. (2007) *Cavity control in a single-electron quantum cyclotron: an  
 5689 improved measurement of the electron magnetic moment*, Ph.D. thesis, Harvard U.
- 5690 [104] PURCELL, E. (1946) “Spontaneous Emission Probabilities at Radio Frequencies,”  
 5691 *Phys. Rev.*, **69**, pp. 674–674.  
 5692 URL <https://link.aps.org/doi/10.1103/PhysRev.69.674>
- 5693 [105] MOSKOWITZ, B. E. and J. ROGERS (1988) “ANALYSIS OF A MICROWAVE  
 5694 CAVITY DETECTOR COUPLED TO A NOISY AMPLIFIER,” *Nucl. Instrum.  
 5695 Meth. A*, **264**, pp. 445–452.

- 5696 [106] RAPIDIS, N. M. (2018) “Application of the Bead Perturbation Technique to a  
5697 Study of a Tunable 5 GHz Annular Cavity,” *Springer Proc. Phys.*, **211**, pp. 45–51,  
5698 [1708.04276](#).
- 5699 [107] BYRON, W. ET AL. (2022) “First observation of cyclotron radiation from MeV-scale  
5700  $e^{pm}$  following nuclear beta decay,” [2209.02870](#).
- 5701 [108] KAZKAZ, K. and N. WOOLLETT (2021) “Using Cyclotron Radiation Emission  
5702 for Ultra-high Resolution X-Ray Spectroscopy,” *New J. Phys.*, **23**(3), p. 033043,  
5703 [1911.05869](#).
- 5704 [109] CANNING, J. A. L., F. F. DEPPISCH, and W. PEI (2023) “Sensitivity of future  
5705 tritium decay experiments to New Physics,” *JHEP*, **03**, p. 144, [2212.06106](#).

5706

## Vita

5707

**Andrew Douglas Ziegler**

5708

### Education

5709

- Doctor of Philosophy, Physics, The Pennsylvania State University, University Park, Pennsylvania, USA, 2023
- Bachelor of Science, Physics, The University of Minnesota, Minneapolis, Minnesota, USA, 2017

5710

5711

5712

5713

### Selected Publications

5714

5715

- Astari Esfahani, A. et al. (2023) "Antenna Arrays for CRES-based Neutrino Mass Measurement", *Phys. Rev. C*, In preparation.
- Astari Esfahani, A. et al. (2023) "Real-time Signal Detection for Cyclotron Radiation Emission Spectroscopy Measurements using Antenna Arrays", *Journal of Instrumentation*, In preparation.
- Astari Esfahani, A. et al. (2023) "Tritium Beta Spectrum and Neutrino Mass Limit from cyclotron Radiation Emission Spectroscopy", *Phys. Rev. Lett.*, Accepted.
- Astari Esfahani, A. et al. (2022) "SYNCA: A Synthetic Cyclotron Antenna for the Project 8 Collaboration", *Journal of Instrumentation*, **18**(01).

5716

5717

5718

5719

5720

5721

5722

5723

### Selected Presentations

5724

5725

5726

- *New Developments in the CRES Technique for Neutrino Mass Measurement*, Invited Talk, Fall 2022 Meeting of the APS Division of Nuclear Physics, New Orleans, Louisiana, USA, 2022
- *Signal Detection Algorithms for Phase III of the Project 8 Experiment*, Contributed Talk, APS April Meeting 2022, New York, New York, USA, 2022
- *Synthetic Electron Antenna for Calibrating the Project 8 Neutrino Mass Experiment*, Contributed Talk, Fall 2021 Meeting of the APS Division of Nuclear Physics, Virtual, 2021

5727

5728

5729

5730

5731